

Hydrogen Atom Transfer Reactions and the Effects of Non-Redox Active Metal Cations

by

Jeffrey A. van Santen

B.Sc. Hons. Chemistry, The University of British Columbia, 2015

A THESIS SUBMITTED IN PARTIAL FULFILLMENT OF
THE REQUIREMENTS FOR THE DEGREE OF

MASTER OF SCIENCE

in

THE COLLEGE OF GRADUATE STUDIES

(Chemistry)

THE UNIVERSITY OF BRITISH COLUMBIA

(Okanagan)

December 2017

© Jeffrey A. van Santen, 2017

The undersigned certify that they have read, and recommend to the College of Graduate Studies for acceptance, a thesis entitled: HYDROGEN ATOM TRANSFER REACTIONS AND THE EFFECTS OF NON-REDOX ACTIVE METAL CATIONS submitted by JEFFREY A. VAN SANTEN in partial fulfilment of the requirements of the degree of Master of Science

Supervisor, Professor (please print name and faculty/school above the line)

Supervisory Committee Member, Professor (please print name and faculty/school above the line)

Supervisory Committee Member, Professor (please print name and faculty/school above the line)

University Examiner, Professor (please print name and faculty/school above the line)

External Examiner, Professor (please print name and faculty/school above the line)

(Date Submitted to Grad Studies)

Additional Committee Members include:

(please print name and faculty/school above the line)

(please print name and faculty/school above the line)

Abstract

Hydrogen atom transfer (HAT) reactions are a fundamental step in many biological processes, but can initiate the free-radical induced oxidation of cellular components. Although HAT reactions appear fundamentally elementary, there are many poorly understood factors that influence HAT. In this thesis, three aspects of HAT reactivity are investigated using quantum chemical techniques.

First, the importance of pre-reaction complex formation in considering the kinetics of HAT reactions were investigated. For a set of nearly-thermoneutral HAT reactions involving oxygen-centred radicals, the relationship between pre-reaction complex non-covalent binding energies and Arrhenius pre-exponential factors (A-factors) was investigated. It is demonstrated that for HAT reactions that take place through similar mechanisms, there is a strong correlation between pre-reaction complex binding energies and A-factors. This suggests that non-covalent interactions may directly affect the kinetics of certain HAT reactions.

Next, the relationship between bond dissociation energies (BDEs) and reaction rates for abstraction of a hydrogen from a C–H bond by the CumO[•] radical are investigated in the context of the Bell-Evans-Polanyi (BEP) principle. The applicability of the BEP principle is examined by exploring a hypothesis: If the BEP principle is a valid linear free-energy relationship, there should exist two linear relationships for BDE against the logarithm of HAT rate constant, one for incipient radicals that are allylic or benzylic, and one for alkyl radicals. It is demonstrated that there is a reasonably strong correlation for allylic/benzylic C–H bonds, but not

Abstract

for alkyl ones. The BEP principle should not be used for quantitative prediction, but remains useful as a conceptual framework.

Finally, the effect of non-redox active metal cations on HAT reactions involving small models for proteins and oxygen-centred radicals is studied. Previous experimental evidence demonstrated that Lewis acid-base interactions between metal cations and substrates can inhibit HAT reactions, and that the cations may serve as a form of chemo-protection in biological systems. The results herein demonstrate that metal-substrate interactions can deactivate certain CH bonds. Metal-radical interactions may promote HAT reactions. On the basis of these limited results, non-redox active metal cations might not act as natural chemo-protective agents.

Table of Contents

Abstract	iii
Table of Contents	vii
List of Tables	viii
List of Figures	x
List of Schemes	xiii
List of Symbols and Abbreviations	xiv
Acknowledgements	xvi
Chapter 1: Introduction	1
1.1 Background	1
1.2 Details of HAT reactions	4
1.3 Research goals	10
Chapter 2: Theory	17
2.1 The quantum mechanical approach	17
2.1.1 Spin and Spatial Orbitals	18
2.1.2 Slater determinants	20
2.1.3 The Hartree-Fock approximation	21
2.1.4 Basis sets	24
2.1.5 Post-Hartree-Fock methods	29
2.1.6 The complete basis set limit	33
2.1.7 Composite quantum chemistry methods	34
2.1.8 Density-functional theory	36
2.2 Applying theory to chemical problems	43
2.2.1 Geometry optimization	43
2.2.2 Molecular vibrations	44
2.2.3 Thermochemistry	46
2.2.4 Modelling solvent	49

TABLE OF CONTENTS

2.2.5 Rate constants and transition state theory	50
Chapter 3: The Relationship Between Arrhenius Pre-factors with Non-Covalent Binding	60
3.1 Introduction	60
3.2 Computational methods and details	63
3.3 Results and discussion	64
3.4 Summary	78
Chapter 4: Interrogation of the Bell-Evans-Polanyi Principle: Investigation of the Bond Dissociation Enthalpies Correlated with Hydrogen Atom Transfer Rate Constants	80
4.1 Introduction	80
4.2 Methods	86
4.2.1 Quantum chemical composite procedures	87
4.2.2 Transition state calculations	90
4.3 Comparison of composite method for the prediction of BDEs	91
4.4 Analysis of the Bell-Evans-Polanyi principle	101
4.5 Transition state analysis	105
4.6 Is the Bell-Evans-Polanyi principle valid?	110
Chapter 5: Do non-redox active metal cations have the potentials to behave as chemo-protective agents? The Effects on Metal Cations on HAT Reaction Barrier Heights	115
5.1 Introduction	115
5.2 Computational methods and details	128
5.3 Exploring the nature of metal cation substrate interactions	130
5.4 HAT reactions involving non-redox active metals	141
5.4.1 DMA	141
5.4.2 DIA	148
5.5 Summary	151
Chapter 6: Conclusions	154
References	159
Appendix	181
Appendix A: Chapter 3 Additional Data	182
Appendix B: Chapter 4 Additional Data	183
Appendix C: Chapter 5 Additional Data	187

TABLE OF CONTENTS

C.1	Benchmarking DFT based methods for the binding of alkali and al-	
	kaline earth metals to organic substrates and oxygen-centred radicals	187
C.1.1	Metal cation basis set convergence	189
C.1.2	High level results and evaluation of various density-functional	
	theory based methods	194
C.2	HAT reactions involving non-redox active metals	198
C.2.1	DMA + HO [•]	198
C.2.2	Strong hydrogen bond accepting substates	200

List of Tables

Table 3.1	Table of results for (nearly) thermoneutral reactions studied.	61
Table 4.1	Bond dissociation enthalpies of the species used to investigate the accuracy of composite methods.	92
Table 4.2	Reaction barrier heights for reactions of substrates with CumO [•] calculated in the gas phase at 298 K.	106
Table 5.1	Ionic concentrations inside a mammalian heart cell and in the blood plasma.	116
Table 5.2	Summary of rate constants for reactions of CumO [•] with various organic substrates in the presence of alkali and alkaline earth metal salts.	118
Table 5.3	Bond dissociation enthalpies of DMA, DMSO, MeCN, and DIA with and without metal cations.	134
Table 5.4	Calculated free energy (enthalpy) barrier for direct HAT from different C–H bonds in DMA by CumO [•] and BnO [•] , with and without NaCl.	142
Table 5.5	Calculated free energy (enthalpy) for direct HAT from different C–H bonds in DIA by CumO [•] , with and without NaCl. .	151
Table B.1	Summary of experimental rate constants and literature bond dissociation enthalpies.	185
Table C.1	Total energy of alkali and alkaline earth-metal cations. . . .	194
Table C.2	Benchmark gas-phase binding energies of alkali and alkaline earth-metals with small organic substrates and radicals. . . .	195
Table C.3	Evaluation of DFT-based methods for alkali and alkaline metal binding to organic substrates and radicals.	195
Table C.4	Comparison of single point and relaxed binding energies for alkali and alkaline metal binding with DFT-based methods. .	197
Table C.5	Calculated free energy (enthalpy) barrier for direct HAT from different C–H bonds in DMA by HO [•] , with and without NaCl.	199

LIST OF TABLES

Table C.6	Calculated free energy (enthalpy) barrier for HAT between DMSO and CumO [•] , and conventional HAT and radical H-atom donation with BnO [•] , with and without NaCl.	201
Table C.7	Calculated free energy (enthalpy) barrier for HAT between HMPA and TBPO with CumO [•] with and without NaCl.	206

List of Figures

Figure 1.1	A typical reaction coordinate diagram.	11
Figure 2.1	Schematic representation of a quantum mechanical composite method.	35
Figure 2.2	A reaction coordinate diagram for a generic reaction.	52
Figure 2.3	Quantum mechanical tunnelling occurs when a particle penetrates a reaction barrier, rather than surmounting it.	57
Figure 3.1	Plot of logarithm of A-factor against binding energy.	65
Figure 3.2	Three-dimensional structures of pre-reaction complexes 2 (TEMPO-H and 4-oxo-TEMPO) and 3 (di- <i>t</i> -butyl-hydroxylamine and di- <i>t</i> -butyl-nitroxyl).	68
Figure 3.3	Three-dimensional structure of pre-reaction complex 4 between 2,4,6-tri- <i>t</i> -butylphenol and 4- <i>t</i> -butylphenoxy.	70
Figure 3.4	Three-dimensional structures of pre-reaction complexes 8 (<i>t</i> -butylperoxy and phenol) and 9 (<i>t</i> -butylperoxy and 2-naphthol).	71
Figure 3.5	Three-dimensional structure of pre-reaction complex 10 between <i>t</i> -butylperoxy and α -tetralin peroxide.	73
Figure 3.6	Three-dimensional structure of pre-reaction complex 6 between <i>N,N</i> -diphenylhydroxylamine and <i>N,N</i> -diphenylnitroxyl.	75
Figure 3.7	Three-dimensional structure of pre-reaction complex 7 between 2-naphthol and phenoxy.	76
Figure 3.8	Three-dimensional structures of pre-reaction complexes 1 (2,4,6-tri- <i>t</i> -butylphenoxy and 2,4,6-tri- <i>t</i> -butylphenoxy) and 5 (2,4,6-tri- <i>t</i> -butylphenol and <i>t</i> -butylperoxy).	77
Figure 3.9	Reaction coordinate qualitatively illustrating the proposed mechanism for HAT in complexes 1 and 5.	77
Figure 4.1	Energy profiles for a series of related exothermic reactions illustrating the Bell-Evans-Polanyi principle.	81
Figure 4.2	Bell-Evans-Polanyi plot of experimental rate constants against literature BDEs.	85
Figure 4.3	Summary of deviations of BDEs from literature for composite quantum chemical methods.	98

LIST OF FIGURES

Figure 4.4	One-to-one plot of BDEs from literature and as calculated by the W1BD composite method.	99
Figure 4.5	One-to-one plot comparing BDEs calculated by ROCBS-QB3 to literature and W1BD BDEs.	100
Figure 4.6	Bell-Evans-Polanyi plot of experimental rate constants (normalized for the number of equivalent hydrogen atoms) for HAT between CumO [·] and substrates against BDEs calculated using the ROCBS-QB3 method.	102
Figure 4.7	Further breakdown of Bell-Evans-Polanyi plot of experimental rate constants (normalized for the number of equivalent hydrogen atoms) for HAT between CumO [·] and alkyl substrates against BDEs calculated using the ROCBS-QB3 method.	104
Figure 4.8	Structures of TS for HAT between CumO [·] and toluene with SOMO and HOMO.	107
Figure 4.9	Bell-Evans-Polanyi plot of calculated enthalpic barriers for HAT between CumO [·] and substrates against BDEs calculated using the ROCBS-QB3 method.	111
Figure 5.1	Plot of observed rate constant against concentration of DMF and DMA for reaction with CumO [·] at 298 K in the presence of 0.2 M Mg(ClO ₄) ₂	121
Figure 5.2	Plot of observed rate constant against concentration of DMA for reaction with CumO [·] at 298 K in the presence of 0.2 M NaClO ₄ and Mg(ClO ₄) ₂	123
Figure 5.3	Plot of observed rate constant against concentration of DIA for reaction with CumO [·] at 298 K in the presence of 0.2 M Mg(ClO ₄) ₂	124
Figure 5.4	Potential energy surface of binding energy between DMA and sodium cation and sodium chloride.	132
Figure 5.5	Potential energy surface of binding energy between DMA and magnesium cation and magnesium chloride.	133
Figure 5.6	Structures of the DMA-NaCl complex and associated radical complexes.	136
Figure 5.7	The resonance forms of DMA.	138
Figure 5.8	Structures of the DIA-NaCl complex and radical complex.	139
Figure 5.9	TS structures of HAT reaction between DMA and CumO [·] including and excluding NaCl.	145
Figure 5.10	TS structures of HAT reaction between DMA and BnO [·] including NaCl.	148
Figure 5.11	TS structures for HAT reaction between DIA and CumO [·] including NaCl.	152

LIST OF FIGURES

Figure A.1	Molecular orbitals of hydrogen peroxide-peroxyl self-exchange reaction TS complex, demonstrating a PCET mechanism.	182
Figure B.1	One-to-one plots of composite methods compared to literature and W1BD.	183
Figure B.2	One-to-one plots comparing experimental and calculated rate constants for HAT reactions between CumO [·] and various organic substrates.	186
Figure C.1	Basis set convergence for alkali and alkaline earth-metal cations.	191
Figure C.2	Basis set convergence for sodium and magnesium ions with core-correlation basis sets.	192
Figure C.3	Explicitly correlated basis set convergence for alkali and alkaline earth-metal cations.	193
Figure C.4	TS structures of HAT reaction between DMSO and CumO [·] , and the conventional HAT and radical H-atom donation reactions with BnO [·] excluding and including NaCl.	202
Figure C.5	Reaction profiles for HAT between HMPA with BnO [·] and TBPO with BnO [·]	205
Figure C.6	TS structures of HAT reaction between HMPA and TBPO with CumO [·] and BnO [·] including NaCl.	207

List of Schemes

1.1	Common reactions involved in protein oxidation.	3
1.2	Self-exchange reactions of the benzyl-toluene couple through direct HAT, and the phenoxyl-phenol couple through PCET.	6
1.3	Possible cisoid (stacked) and transoid TS structures for the benzyl-toluene couple, the peroxyt-toluene couple, and the iminoxyl-oxime couple.	9
1.4	Hyperconjugative overlap in tetrahydrofuran and the effect of non-redox active metal cations on the transition state complex.	15
4.1	Unimolecular decay of the cumyloxy radical.	87
4.2	Locally-dense basis set partitioning used in the calculation of BDEs.	89
4.3	A generic HAT transition state structures and possible resonance forms.	114
5.1	Chemical structures of the species studied herein.	127
C.1	Initial proposed benchmark set of substrates/radicals and metal cations.	188
C.2	Revised benchmark set of small substrates and cations.	190
C.3	The HAT reactions of DMSO with CumO [•] and BnO [•]	201

List of Symbols and Abbreviations

A-factor	Arrhenius pre-exponential factor
AO	atomic orbitals
ATP	adenosine triphosphate
BDE	bond dissociation enthalpy
BEP	Bell-Evans-Polanyi
BnO [•]	benzyloxy radical
BSIP	basis set incompleteness potential
CHD	1,4-cyclohexadiene
CumO [•]	cumyloxy radical
CBS	complete basis set
DABCO	diazobicyclo[2.2.2]octane
DFT	density-functional theory
DIA	<i>N,N</i> -diisobutylacetamide
DMA	<i>N,N</i> -dimethylacetamide
DMF	<i>N,N</i> -dimethylformamide
DMSO	dimethyl sulfoxide
E_a	activation energy
GGA	generalized-gradient approximation
GTO	Gaussian-type orbitals
\mathcal{H}	Hamiltonian operator
HAT	hydrogen atom transfer
HF	Hartree-Fock
HMPA	hexamethylphosphoramide
HOMO	highest-occupied molecular orbital
IP	ionization potential
k	rate constant
K	equilibrium constant
LDA	local-density approximation
LCAO	linear combination of atomic orbitals
LFER	linear free energy relationship
LFP	laser flash photolysis
LP	lone pair

List of Symbols and Abbreviations

LUMO	lowest occupied molecular orbital
MeCN	acetonitrile
MO	molecular orbital
MP	Møller-Plesset
NBO	natural bonding orbital
NCI	non-covalent interaction
NPA	natural population analysis
PCET	proton coupled electron transfer
PES	potential energy surface
QM	quantum mechanics
RDF	radial distribution function
ROS	reactive oxygen species
SOMO	singly occupied molecular orbitals
STO	Slater-type orbitals
TBPO	tributylphosphine
TEA	triethylamine
THF	tetrahydrofuran
TS	transition state
TST	transition state theory
XC	exchange-correlation
ZPE	zero-point vibrational energy
ΔG	Gibbs free energy of reaction
ΔG^\ddagger	Gibbs free energy barrier of reaction
ΔH	enthalpy of reaction
ΔH^\ddagger	enthalpic reaction barrier of reaction
ΔS	entropic change of reaction
∇^2	Laplacian operator

Acknowledgements

I would like to first express my deepest gratitude to my supervisor, Prof. Gino DiLabio, for his guidance throughout the course of my degree. His depth of knowledge and continuing enthusiasm were always there to support and inspire me. I am truly indebted to him and cannot say thank you enough. I would also like to thank all the past and current members of the DiLabio group, without whom the computational research path would have been exceedingly isolated. A special thank you to Dr. Alberto Otero de la Roza for all his help with many research and technical matters.

Thank you to Dr. Steve McNeil, Dr. Fred Menard, Dr. Paul Shipley, Dr. Jim Bailey, and Dr. Sandra Mecklenburg for their advice, knowledge, and dedication to teaching. Your collective efforts as instructors, mentors, and advisors have helped tremendously.

I would also like to thank my family for their endless support, encouragement, and love: Michael, Mama, Papa, Nicola, Rob, and Arlene. Words cannot express how much you all mean to me.

And finally I would like to thank Grace. Your never ending support and love have been fundamental to my success.

Chapter 1

Introduction

1.1 Background

Radicals are chemical species that tend to be highly reactive due to the presence of one or more unpaired electrons. Living systems depend on radical processes as part of normal metabolism¹ but biomaterials, such as proteins, are susceptible to radical-induced damage. Radical-induced oxidation of biomaterials has been implicated in a number of degenerative disease states, including cancer, Alzheimer's, Parkinson's, and multiple sclerosis.^{2–5}

In biological systems, radicals are derived from many sources. Exogenous sources include solar radiation and air pollutants, while endogenous sources include *in vivo* transition metal-ion redox processes, such as in the electron transport chain involved in cellular respiration.⁶ Some processes in the electron transport chain may transfer an electron to molecular oxygen, forming the superoxide anion ($O_2^{\cdot-}$). Superoxide is not a strong oxidant on its own, however it may become protonated to form the more reactive hydroperoxyl radical,⁷ or disproportionate spontaneously or catalytically through metalloenzymes such as superoxide dismutase, leading to the formation of highly reactive oxygen-centred radicals. Oxygen-centred radicals derive from reactions of O_2 with redox-active metals.¹

Oxygen-centred radicals, known as reactive oxygen species (ROSs) in biology, are particularly important and common due to the previously described nature of aerobic respiration. The ROSs that are of primary concern are the highly reac-

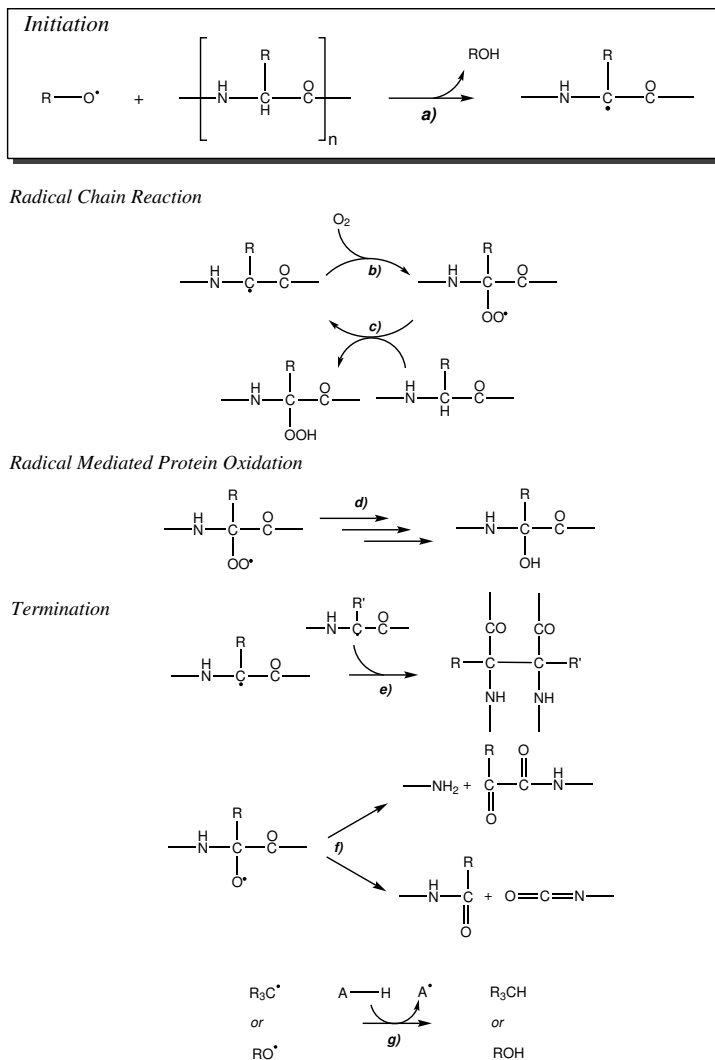
1.1. Background

tive hydroxyl radicals (HO^\bullet), alkoxy radicals (RO^\bullet), superoxide ($\text{HOO}^\bullet/\text{O}_2^{\cdot-}$), and peroxy radicals (ROO^\bullet).¹ The oxidation of proteins by ROSs occurs through a radical chain mechanism that has been studied experimentally in detail.^{8,9} This chain reaction occurs when an ROS initiates a radical chain reaction through hydrogen atom transfer (HAT), single electron transfer, or addition reactions with protein substrates, leading to rapid propagation and formation of new radicals. HAT is an extremely important reaction in the context of oxidative damage. The focus of my work is the development of an understanding of the fundamental chemistry involved in protein oxidation through studying small model systems.

Proteins are the most abundant biomaterial in most mammalian biological systems,¹⁰ thus understanding their degradation is essential to understanding degenerative disease. Because proteins are composed of as many as 20 natural amino acid side-chains, as well as the common peptide backbone, there are a large number of possible reactions. Some of the reactions involved in protein oxidation are shown in Scheme 1.1.

Initial abstraction (Reaction **a**) often occurs at the α -carbon position ($\alpha-\text{CH}$), forming a carbon-centred radical ($\alpha-\text{C}^\bullet$) that is partially delocalized in the π -system of the neighbouring amide and carbonyl groups. Studies have indicated that the stability of $\alpha-\text{C}^\bullet$ is determined by stereo-electronic effects related to the planarity of the amide group.¹¹ As such, steric bulk in the side-chains, as well as local protein structure (helix, sheet, etc.) can constrain radical geometries. For example, the most stable α -carbon radicals occur at glycine residues in antiparallel β -sheets, whereas other bulkier residues and secondary structures lead to loss of captodative stabilization.¹² Amino acid side-chains are also susceptible to oxidation. Those side-chains containing sulfur,¹³ as well as tyrosine (which has a fairly weak phenolic O-H bond of about 89 kcal mol⁻¹),¹⁴ are particularly susceptible to oxidation.

1.1. Background



Scheme 1.1: Common reactions involved in protein oxidation. The reactions are as follows: **a)** initiation of radical chain through abstraction by an oxygen-centred radical to generate an α -carbon-centred radical, **b)** radical addition of molecular oxygen, **c)** propagation of the radical chain reaction generating another α -carbon radical and a peroxide. **d)** Radical mediated protein oxidation proceeds through multiple steps involving oxygen centred radicals and molecular oxygens and results in the generation of a reduced amide (alcohol). Termination of the radical chain reaction can occur in several ways, including: **e)** cross-linking of two carbon-centred radicals, **f)** fragmentation of an oxygen-centred radical intermediate, or **g)** HAT with an antioxidant (AH).

1.2. Details of HAT reactions

Propagation of the radical chain reaction occurs through various processes. In the presence of molecular oxygen, rapid addition occurs at the newly formed α -C $^\bullet$ (Reaction **b**), generating a peroxy radical, which can carry forward through further HAT reactions (Reaction **c**).¹⁵ The mechanism involved in the radical mediated oxidation of proteins has been studied experimentally using techniques involving ionizing radiation.^{16,17} The course of this process is dependent on the availability of either singlet oxygen ($^1\text{O}_2$), or superoxide ($\text{O}_2^{\cdot-}$) or the protonated form, peroxy radical ($\cdot\text{OOH}$). A detailed analysis of this process is outside the scope of this thesis, but ultimately, these reactions lead to the generation of a hydroxyl-amide (Reaction **d**).

The radical chain reaction can be terminated through several mechanisms, including protein-protein cross-linking (Reaction **e**), or protein fragmentation (Reaction **f**). Reactions with antioxidants (A–H, Reaction **g**) also terminate the chain reaction by removing the radical from the protein system. The sum total of all these processes contribute to the accumulation of oxidized proteins that are associated with many degenerative diseases.¹⁸ HAT reactions, which are important steps in the initiation, propagation, and termination reactions of protein oxidation, are investigated through small molecular models in this thesis.

1.2 Details of HAT reactions

Developing an understanding of protein and other biomolecular oxidation requires an understanding of the deceptively simple HAT reactions involved. Formal HAT reactions are a fundamental radical chemical transformation that have been studied for more than a century.^{19,20} From an experimental perspective, HAT reactions that involve oxygen-centred radicals and non-radical organic substrates are reasonably well characterized: the effects of different solvents are well understood.²¹

1.2. Details of HAT reactions

However, the main challenge faced by many experiments is elucidating the mechanistic details of a reaction. This is a problem that can be examined by quantum chemistry, which is the approach that I shall take. Background on the theory used in this thesis is given in Chapter 2.

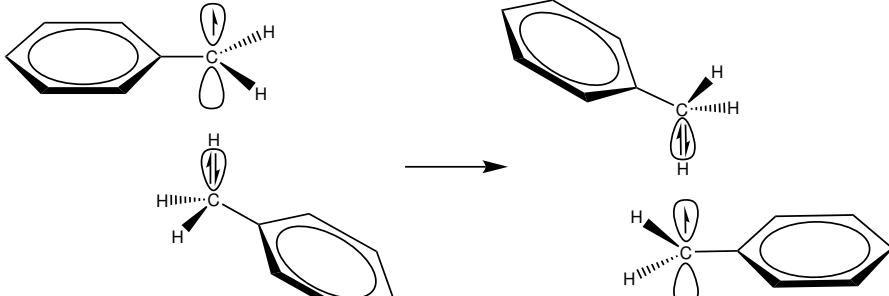
In order to investigate HAT reactions, we need to consider the mechanism in detail. For a simple HAT reaction, there exist several possible mechanisms by which this transformation can occur. The two most common concerted mechanisms are direct HAT and proton-coupled electron transfer (PCET). At the basic level, direct HAT involves the transfer of an electron and proton through the same set of acceptor/donor orbitals, while PCET involves the transfer of an electron and proton through different sets of orbitals. In practise, this distinction is poorly described, and is still an active topic of discussion in the literature.^{22–32}

The prototypical example demonstrating the difference between direct HAT to PCET comes from the computational work of Mayer et al.,²³ that describes the self-exchange reactions of benzyl-toluene and phenoxyl-phenol, shown in Scheme 1.2. These complexes are oriented so that the aromatic rings are anti relative to one another. In this geometry, the benzyl-toluene pair undergoes direct HAT, with the $2p - \pi$ orbital of the benzylic carbon radical oriented at the benzylic hydrogen on toluene. This is described as direct HAT, as the orbital containing the radical overlaps with the C–H σ^* anti-bonding orbital, and thus the transfer of the H atom occurs through the same set of orbitals (see Scheme 1.2 A).

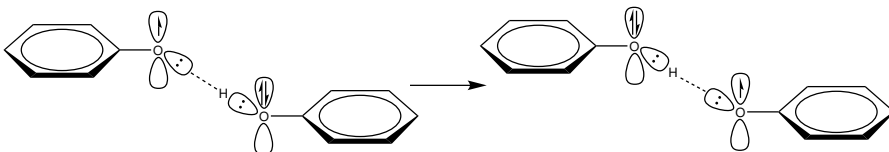
For the phenoxyl-phenol pair (see Scheme 1.2 B), a fairly strongly hydrogen bonded pre-reaction complex is first formed with a predicted gas-phase binding enthalpy of $-8.1\text{ kcal mol}^{-1}$. As a result of this strong interaction, the TS structure is such that the oxygen $2p$ -orbital of the phenoxy radical that nominally contains the unpaired e^- is perpendicular to the hydrogen bond. Therefore, in order to

1.2. Details of HAT reactions

A.



B.



Scheme 1.2: Self-exchange reactions of **A.** the benzyl-toluene couple through direct HAT, and **B.** the phenoxy-phenol couple through PCET.

undergo direct HAT, the hydrogen bond between the phenol OH and phenoxy O lone-pair (LP) must break, and a new, weaker hydrogen bond with the nominally O-centred radical must form. Alternatively, the hydrogen bonded pre-reaction complex geometry allows the orbital containing the radical to overlap with the $2p$ LP of the phenol moiety, and the conjugated aromatic π -systems in the TS complex. This overlap results in a TS complex with a singly occupied molecular orbital (SOMO) that is of π -symmetry and highly delocalized. Accordingly, the proton is transferred through the hydrogen bond and the electron is transferred through the π -system. This reaction has an enthalpic barrier height (ΔH^\ddagger) of 5.0 kcal mol^{-1} relative to the hydrogen bonded complex, so that the barrier is 3.1 kcal mol^{-1} below the separated reactants.

The work by Mayer et al.²³ suggests that hydrogen bonding is a necessary, but not sufficient, condition for PCET to occur. This then implies that PCET is not possible between molecules that do not possess hydrogen bonding moieties,

1.2. Details of HAT reactions

such as carbon atoms. Work by other authors has shown this to be untrue.^{26,33} In particular, DiLabio and Johnson²⁶ demonstrated that Mayer et al.²³ neglected the important contributions of $\pi - \pi$ interactions and LP- π interactions. Computational studies revealed the existence of a TS structure for the benzyl-toluene couple that is 3.7 kcal mol⁻¹ lower in energy than previously reported. This structure has the aromatic rings in an optimal “parallel-displaced” or “stacked” conformation, as observed in the benzene-benzene non-covalently bound dimer.³⁴ Analysis of the TS structure highest occupied molecular orbital (HOMO) reveals bonding character between the two π -systems, while the SOMO shows anti-bonding character between the π -systems, as well as both C–H bonds. Thus, there exists a net partial bonding interaction between the two π -systems, opening up an additional electronic channel for electron transfer to occur, while the overlap between the C–H σ^* orbital and the singly occupied C p -orbital allows for proton transfer. DiLabio and Johnson also suggested that the phenol-phenoxy couple also prefers a π -stacked TS structure, and compared this to a structural analogue, a naturally occurring tyrosyl-tyrosine couple in the RNR enzyme, in which the HAT reaction proceeds through a PCET mechanism. Other authors have confirmed the existence of a π -stacked TS structure for the phenol-phenoxy couple.^{31,32,35}

Hammes-Schiffer has argued that molecular orbital based analysis is insufficient to describe the distinction between PCET and HAT mechanisms, as it is not always conclusive.^{31,36} Instead, Hammes-Schiffer has proposed the use of quantitative diagnostics that measure the non-adiabatic effects of a reaction, that is, the breakdown of the Born-Oppenheimer approximation.^{31,35} Under these criteria, electronically non-adiabatic and adiabatic proton-transfer occur for PCET and HAT mechanisms, respectively. This was demonstrated using the non-stacked TS structures for the self-exchange reactions of the phenol-phenoxy and benzyl-toluene couples. To com-

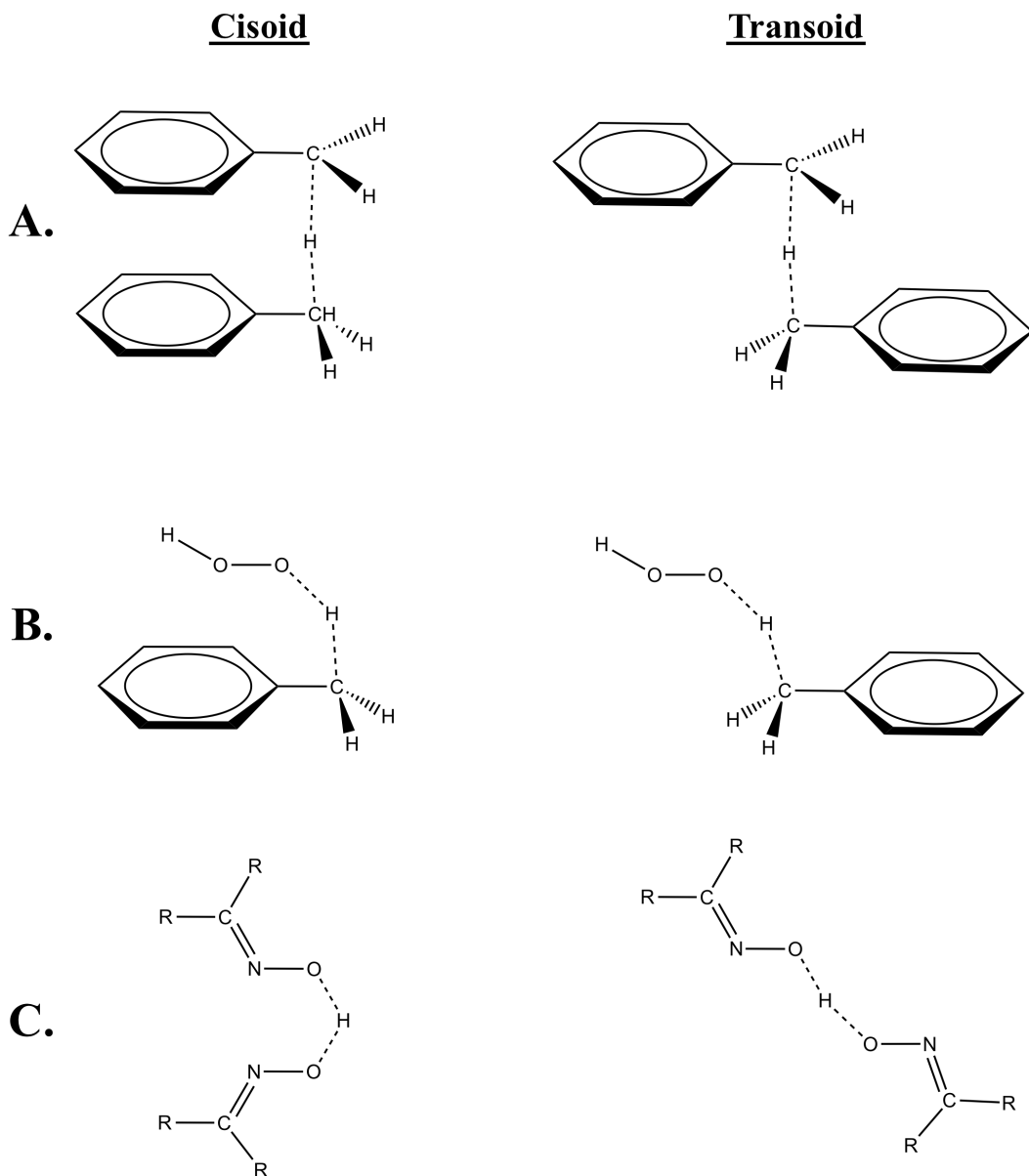
1.2. Details of HAT reactions

plicate the matter further, work by Inagaki et al.³⁷ and Muñoz-Rugeles et al.³² has demonstrated that in the favoured stacked TS structures for the above self-exchange reactions, there are no non-adiabatic effects. This can be interpreted in two different ways: Firstly, π - π -stacking changes the mechanism of the phenol-phenoxy self-exchange reaction from PCET to HAT, as suggested by Inagaki et al.³⁷ Alternatively, Muñoz-Rugeles et al.³² demonstrated that π - π -stacking orbital interactions can “turn off” non-adiabatic effects, while the electron and proton are transferred through different sets of acceptor and donor orbitals, thus fitting within the definition of a PCET mechanism. While this highlights the active discussion of the HAT/PCET field, in this work I shall utilize the latter interpretation, which treats MO overlap as a qualifier for the PCET mechanism.

HAT can also occur through a PCET mechanism for species that have LP- π or LP-LP overlap in the TS complex.^{26,38} DiLabio and Johnson²⁶ showed that the formal HAT reaction between phenol and the *t*-butyl peroxy radical exhibits orbital overlap between the non-radical O-lone pair of *t*-butyl peroxy and the aromatic π -system of phenol in the lowest energy cisoid TS complex. As with the benzyl-toluene couple, there is both a bonding interaction in the HOMO of the TS structure, and an anti-bonding interaction in the SOMO of the TS structure. Therefore, there exists a net partial bonding interaction that allows electron transfer through the LP- π interaction and proton transfer through the hydrogen bond. DiLabio and Ingold³⁸ also showed that iminoxyl-oxime self-exchange reactions occur through a five-centred PCET TS complex. The lowest energy transition states for iminoxyl-oxime couples are cisoid, such that the LPs of the nitrogen centres overlap, opening a channel for electron transfer, while proton transfer occurs between the two oxygen centres. Examples of cisoid and transoid TS structures are shown in Scheme 1.3.

Bearing in mind there is not an obvious way to explore the related differences

1.2. Details of HAT reactions



Scheme 1.3: Possible cisoid (stacked) and transoid TS structures for **A.** the benzyl-toluene couple, **B.** the peroxyxyl-toluene couple, and **C.** the iminoxyl-oxime couple.

1.3. Research goals

in mechanism experimentally, computational examination of formal HAT reactions enables analysis of the mechanism of these reactions. Herein, I shall consider the existence of these mechanisms on a continuum: Reactions where an unambiguous π - π stacked PCET TS structure is formed (for example the $\text{PhO}^\bullet + \text{PhOH}$ self-exchange reaction) have the most PCET character, and therefore have the lowest reaction barriers; while reactions where an unambiguous direct HAT TS structure is formed (for example the $\text{CH}_3^\bullet + \text{CH}_4$ self-exchange reaction) have the most HAT character, and therefore have the highest reaction barriers. In the middle are PCET reactions that may occur through either LP- π (more PCET character) or LP-LP interactions (less PCET character). The use of this analysis provides important insight into the electronic behaviour of these reactions. In this vein, the investigation of the physico-chemical nature of HAT reactions shall be the central theme of this thesis.

1.3 Research goals

Consider for a moment the potential energy surface (PES) for an arbitrary chemical reaction. Theoretical methods can be used to generate a full PES. However, this quickly becomes computationally unfeasible as the number of atoms in a system increases. Typically this problem can be simplified by examining only the relevant degrees of freedom. Often, the two most important coordinates can be isolated, giving a three-dimensional PES. Furthermore, in chemistry we often simplify this problem to two dimensions using the so-called intrinsic reaction coordinate, which is the lowest energy cross section of a higher dimension PES. This yields a reaction coordinate diagram, as is illustrated below in Figure 1.1.

In a typical reaction coordinate diagram, the reactants begin to interact and form a pre-reaction complex. Given sufficient energy, the reaction will proceed over the

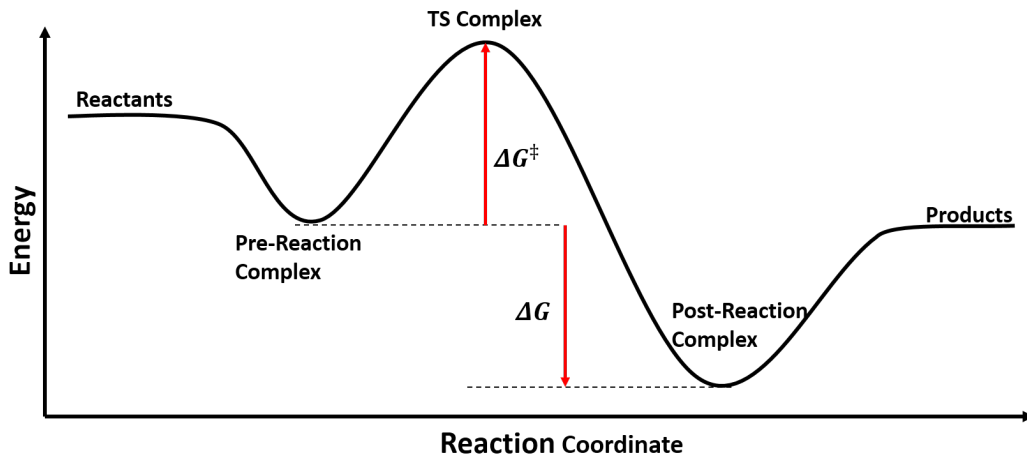


Figure 1.1: A typical reaction coordinate diagram.

top of the energy barrier through a TS complex. After the chemical transformation is completed, a post-reaction complex is formed and then the products separate. This is a somewhat simplified description, as it only broadly describes a chemical transformation. In particular, the roles of substrate-radical and substrate-radical-medium interactions along the reaction coordinate are not fully described. This is in fact a key point, as a thorough understanding of these interactions continues to be lacking in the literature.

Consequently, recent work from our group, in collaboration with our experimental colleagues at the University of Rome Tor Vergata, has focused on the importance of substrate-radical interactions in determining the kinetics of HAT reactions. Specifically, it has been shown that the three-dimensional structures of oxygen-centred radicals, as well as the organic substrates, impact the nature of the interactions involved in HAT reaction pathways.³⁹ In our work, we utilize primarily the benzyloxy (BnO[•]) and cumyloxy (CumO[•]) radicals, which serve as proxies for biological oxygen-centred radicals. This is primarily due to the fact that reactions involving BnO[•] and CumO[•] are relatively long lived in solution, and can be mon-

1.3. Research goals

itored using time-resolved laser flash photolysis (LFP) techniques. These radicals are somewhat different than biologically relevant radicals such as HO[•], and as a result, the reactivity trends pertaining to the substrates can be somewhat masked by the properties of the radical, such as steric bulk,⁴⁰ or non-covalent binding.⁴¹ Nonetheless, through a careful combination of theoretical and experimental techniques, reactions involving BnO[•] and CumO[•] with a variety of organic substrates have been used to develop a great deal of insight with respect to the role of structure in both the radicals and substrates, and resulting intermolecular interactions.

With respect to the work in this thesis, in Chapter 3 the importance of the left-hand side of Figure 1.1 shall be examined by studying how the pre-reaction complex impacts HAT reactions. There has been limited investigation of the importance of pre-reaction complex formation for HAT reaction.⁴² This is problematic, as oxygen-centred radicals can hydrogen bond with substrates as both acceptors and donors.⁴³ These hydrogen bonding interactions, in addition to the other non-covalent interactions between the radical and substrate, lead to the formation of a pre-reaction complex. Accordingly, the formation of a pre-reaction complex is a fundamental step in the model systems that have been used to study HAT.

The specific aim of Chapter 3 is to investigate the effects of non-covalent binding in the pre-reaction complex, with respect to the well-known, but phenomenological, Arrhenius equation. As of yet, there is no framework that relates the non-covalently bound pre-reaction complex to kinetic results. I ask the simple question: Does there exist a direct correlation between the Arrhenius pre-factor and the non-covalent binding that occurs in the pre-reaction complex formed for HAT reactions? To address this question, I examine the non-covalent binding in the pre-reaction complex in a series of related HAT reactions. Arrhenius parameters for the systems of interest in this work were previously tabulated,³⁸ and consist of thermoneutral or nearly

1.3. Research goals

thermoneutral reactions involving the formation and destruction of oxygen-centred radicals. These reactions are related to the phenol-phenoxy self-exchange reaction, where a relatively strong pre-reaction complex is expected.

Then in Chapter 4, the right-hand side of Figure 1.1 is considered, where the effects of bond dissociation enthalpies (BDEs) on HAT rate constants are examined. BDEs are central to the understanding of reactions with respect to thermodynamics. In addition to this, there exists a tremendous amount of literature in which BDEs are linked to chemical reactivity, especially for HAT reactions.^{19,25,44–46} There is a linear free energy relationship (LFER) called the Bell-Evans-Polanyi (BEP) principle,^{47,48} which states that the difference in activation energy (E_a) for two related reactions is proportional to the differences in reaction enthalpy (ΔH):

$$E_a = E_0 + \alpha\Delta H \quad (1.1)$$

where E_0 is the activation energy of a reference reaction, and α , a constant that characterizes the position of the TS along the reaction coordinate. This relationship has been generally used to compare larger families of reactions. Despite the widespread use of the BEP principle, the validity of this relationship is not well described.

I probe the generality of the BEP principle for a series of HAT reactions from C–H bonds, with the aim to determine how generally it may be applied. This is achieved by relating accurate, theoretically determined C–H BDEs for species that undergo abstraction at the appropriate C–H position, to the experimentally determined HAT rate constants. HAT reaction rate constants depends on many factors. However, by using rate constants determined under specific conditions (LFP with CumO[•] in acetonitrile at 298K), the differences in reactivity depend mainly on the differences in chemical properties of the substrates of interest. Therefore, if the

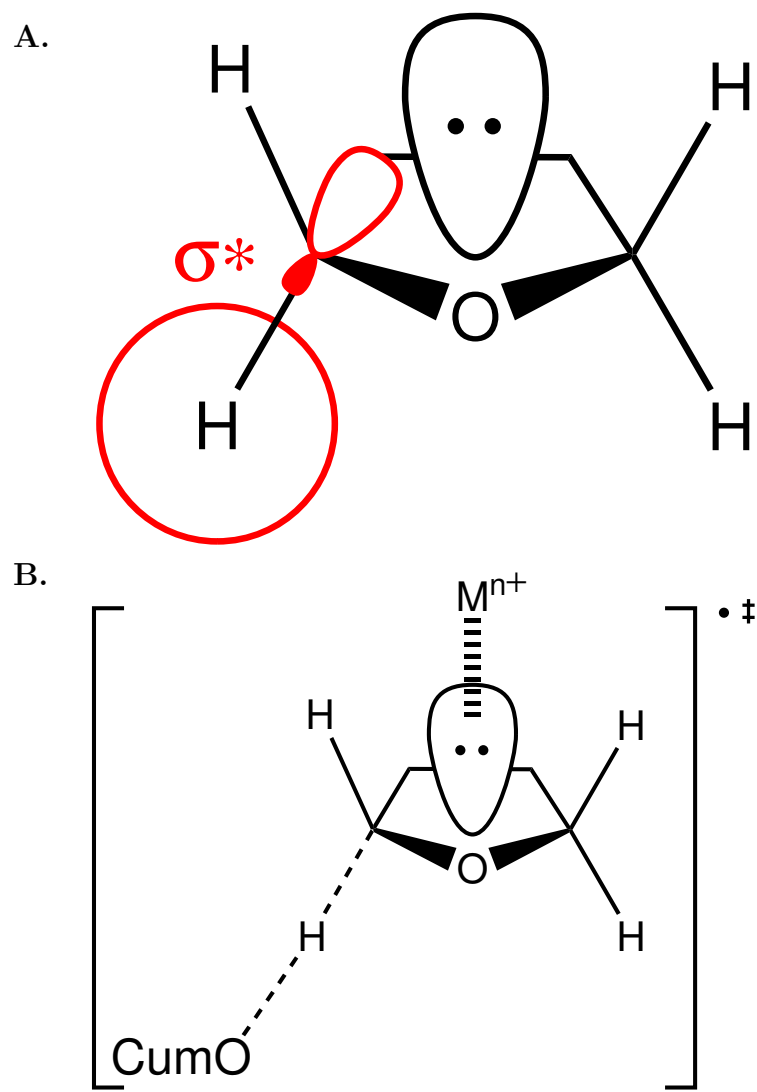
1.3. Research goals

BEP relation is valid, there should exist two relationships for C–H bonds: one in which the incipient radical is delocalized into a π -system (benzylic-allylic), and the other in which the remaining alkyl radicals are largely localized.

Finally, recent experimental results show that non-redox active metal cations, which are found ubiquitously in biological systems, have an inhibitory effect on HAT reactions involving oxygen-centred radicals. This has been demonstrated experimentally for substrates that undergo abstraction from sites adjacent to heteroatoms (e.g. amines, amides, and ethers). Under various stoichiometric ratios, these metal cations have effects ranging from full inhibition to partial deactivation of HAT reactivity.^{49–51} This effect has been attributed partially to the effects of hyperconjugative overlap. Take for example tetrahydrofuran (THF), shown in Scheme 1.4. In the absence of other species, there exists C–H bond weakening hyperconjugative overlap of electron density from one of the oxygen LPs and the adjacent C–H σ^* anti-bonding orbitals. The interaction of a metal cation with the oxygen LPs removes electron density from the C–H σ^* , thus increasing the C–H bond strength. As a result, the reactivity of this bond is decreased, as observed from the experimentally-measured 3.2-fold decrease in the rate constant for HAT with CumO $^\bullet$ in acetonitrile from $5.8 \times 10^6 \text{ M}^{-1}\text{s}^{-1}$ to $1.8 \times 10^6 \text{ M}^{-1}\text{s}^{-1}$ in the presence of 1.0 M Mg(ClO₄)₂.⁴⁹

The nature of the interactions between non-redox active metal cations and organic substrates is poorly understood. This problem is explored in Chapter 5, with the aim to understand the fundamental physico-chemical properties that lead to the observed trends in reactivity. The experimentally observed effects have led us to hypothesize that the presence of non-redox active metal cations has a chemo-protective effect against the radical-induced oxidation of biomaterials such as proteins.

In using theory to study HAT reactions, I hope to contribute to a better understanding of the fundamental properties that govern these reactions, and thus



Scheme 1.4: **A.** Hyperconjugative overlap in tetrahydrofuran. **B.** The non-redox active metal cation accepts electron density from the heteroatom lone pair, reducing overlap with the C–H σ^* anti-bonding orbital, and increasing the C–H bond strength, thus destabilizing the TS complex.

1.3. Research goals

develop insights into the many important biological processes in which HAT takes place.

Chapter 2

Theory

2.1 The quantum mechanical approach

The fundamental properties governing all of chemistry are dictated by the quantum mechanical wave functions, Ψ . Therefore, in quantum chemistry we seek solutions to the non-relativistic time-independent Schrödinger equation

$$\mathcal{H} |\Psi\rangle = E |\Psi\rangle \quad (2.1)$$

where \mathcal{H} is the Hamiltonian operator for a system of nuclei and electrons, and Ψ is the wave function, defined as the set of eigenvectors with energy eigenvalues E .⁵² For a system with N electrons and M nuclei, the full Hamiltonian in atomic units is

$$\begin{aligned} \mathcal{H} = & -\sum_{i=1}^N \frac{1}{2} \nabla_i^2 - \sum_{A=1}^M \frac{1}{2M_A} \nabla_A^2 - \sum_{i=1}^M \sum_{A=1}^M \frac{Z_A}{r_{iA}} \\ & + \sum_{i=1}^N \sum_{j>i}^N \frac{1}{r_{ij}} + \sum_{A=1}^M \sum_{B>A}^M \frac{Z_A Z_B}{R_{AB}} \end{aligned} \quad (2.2)$$

In this equation, Z_A is the atomic number of nucleus A with a mass M_A divided by the mass of an electron. The Laplacian operators ∇_i^2 and ∇_A^2 represent differentiation with respect to the coordinates of the i th electron and A th nucleus. The first and second terms are the kinetic energies of the electrons and nuclei, respectively.

2.1. The quantum mechanical approach

The third term represents the Coulomb attraction between electrons and nuclei with distance r_{iA} . The fourth and fifth terms represent repulsion between two electrons with distance r_{ij} , and between two nuclei with distance R_{AB} , respectively.

Nuclei move slowly relative to electrons, due to their much greater mass. This is the central pillar of the Born-Oppenheimer approximation that is nearly always applied in molecular electronic structure calculations. The application of this approximation allows for the simplification of Equation 2.2: using a separation of electronic and nuclear variables, the second term for nuclear kinetic energy is solved separately. Also, the last term of nuclear repulsion is constant, and thus is generally ignored. This leaves us with the electronic Hamiltonian

$$\mathcal{H}_{elec} = - \sum_{i=1}^N \frac{1}{2} \nabla_i^2 - \sum_{i=1}^M \sum_{A=1}^M \frac{Z_A}{r_{iA}} + \sum_{i=1}^N \sum_{j>i}^N \frac{1}{r_{ij}} \quad (2.3)$$

Unfortunately, it is only possible to exactly solve the Schrödinger equation for the full electronic Hamiltonian \mathcal{H}_{elec} in the simplest of cases: when there is only one electron (H , H_2^+ , He^+ , Li^{2+} , etc). Note that since we will always work within the Born-Oppenheimer approximation, the subscript *elec* is usually dropped. In order to proceed to systems with multiple electrons, we must make further approximations.

2.1.1 Spin and Spatial Orbitals

We will refer to the wave function of a single particle as an orbital. Naturally then, as we will deal with electrons in molecules, we shall refer to their wave functions as molecular orbitals (MOs). To fully describe electrons we must consider a spatial and spin component to the overall wave function. A spatial orbital $\psi_i(\mathbf{r})$, is a function of the position vector \mathbf{r} , and describes the distribution of an electron in all space. It is usually assumed that spatial MOs form an orthonormal set such that

$$\langle \psi_i(\mathbf{r}) | \psi_j(\mathbf{r}) \rangle = \int d\mathbf{r} \psi_i^*(\mathbf{r}) \psi_j(\mathbf{r}) = \delta_{ij} \quad (2.4)$$

where the left-hand side is standard Dirac *bra-ket* notation representing the same integral in the middle. The right-hand side of Equation 2.4 is the standard Kronecker delta.

The spin of an electron is represented by two orthonormal functions $\alpha(\omega)$ and $\beta(\omega)$, or spin-up and spin-down. If a wave function describes both the spatial distribution and spin of an electron it is a spin orbital, $\chi_i(\mathbf{x})$, where \mathbf{x} represents both the spatial distribution and spin coordination of an electron ($\mathbf{x} = \{\mathbf{r}, \omega\}$). Since $\psi_i(\mathbf{r})$ and $\alpha(\omega)/\beta(\omega)$ are orthonormal, so too is $\chi_i(\mathbf{x})$

$$\langle \chi_i(\mathbf{x}) | \chi_j(\mathbf{x}) \rangle = \delta_{ij} \quad (2.5)$$

The first steps towards describing an N electron wave function come from the work in the late 1920s by Hartree. The early *Hartree method* took an approach in which the wave function of N non-interacting electrons (Ψ^{HP}) is described by the product of N spin orbitals, known as a *Hartree product*:

$$\Psi^{HP}(\mathbf{x}_1, \mathbf{x}_2, \dots, \mathbf{x}_N) = \chi_i(\mathbf{x}_1) \chi_j(\mathbf{x}_2) \dots \chi_k(\mathbf{x}_N) \quad (2.6)$$

In such a system the Hamiltonian has the form of a sum of N independent operators

$$\mathcal{H} = \sum_{i=1}^N \hat{h}(i) \quad (2.7)$$

where $\hat{h}(i)$ is

$$\hat{h}(i) = -\frac{1}{2} \nabla_i^2 + V(\mathbf{r}_i) \quad (2.8)$$

2.1. The quantum mechanical approach

such that the first term describes an electron's kinetic energy, and the second term describes potential felt by a single electron. If we consider the case that ignores electron-electron repulsion, then V describes only the nuclear-electron attraction. Alternatively, the electron-electron repulsion may be included as an average potential.

Solutions to the Schrödinger equation for this system of non-interacting electrons are facile to obtain as each $h(i)$ depends only on the variables of $\chi_i(\mathbf{x}_i)$, so that

$$\mathcal{H} |\Psi^{HP}\rangle = E |\Psi^{HP}\rangle \quad (2.9)$$

gives an eigenvalue energy solution E that is the sum of N spin orbital energies ε_i

$$E = \varepsilon_1 + \varepsilon_2 + \cdots + \varepsilon_N \quad (2.10)$$

While this theory does allow one to calculate energies for an N electron system, it has a basic deficiency: the antisymmetry principle of wave functions is not obeyed. The antisymmetry principle states that the electronic wave function must change sign (be antisymmetric) with respect to the exchange of spacial and spin coordinate of any two electrons. Hartree accounted for this by nominally applying the Pauli exclusion principle. However, this description is still incomplete in the sense that it does not describe the statistical nature of quantum particles.

2.1.2 Slater determinants

In order to satisfy the antisymmetry principle, a linear combination of Hartree products can be taken. Although the method was first utilized independently by Heisenberg⁵³ and Dirac,⁵⁴ this method is called a *Slater determinant* after Slater.⁵⁵ For an N electron system, a Slater determinant is written as

$$\Psi(\mathbf{x}_1, \dots, \mathbf{x}_N) = \frac{1}{\sqrt{N!}} \begin{vmatrix} \chi_i(\mathbf{x}_1) & \chi_j(\mathbf{x}_1) & \cdots & \chi_k(\mathbf{x}_1) \\ \chi_i(\mathbf{x}_2) & \chi_j(\mathbf{x}_2) & \cdots & \chi_k(\mathbf{x}_2) \\ \vdots & \vdots & \ddots & \vdots \\ \chi_i(\mathbf{x}_N) & \chi_j(\mathbf{x}_N) & \cdots & \chi_k(\mathbf{x}_N) \end{vmatrix} \quad (2.11)$$

where $1/\sqrt{(N!)}$ is a normalization factor. This simple mathematical trick ensures antisymmetry since the interchange of two electrons requires the exchange of two rows in the determinant, which changes the sign. Normally the short-hand form, which implicitly includes the normalization factor and assumes the ordering of electrons is $\mathbf{x}_1, \mathbf{x}_2, \dots, \mathbf{x}_N$, is written as only the diagonal elements of the determinant:

$$\Psi(\mathbf{x}_1, \mathbf{x}_2, \dots, \mathbf{x}_N) = |\chi_i \chi_j \cdots \chi_k\rangle \quad (2.12)$$

Slater determinants are completely dependent on the spin orbitals from which it is formed, to within a sign. Therefore, Slater determinants also form an orthonormal set. Additionally, the introduction of antisymmetry into the Hartree product incorporates so-called *exchange correlation*. This means that the motion of two electrons with parallel spin are correlated because each spin-orbital can only contain one electron. However, since the motion of electrons with opposite spin are not correlated, a single determinant wave function is said to be uncorrelated.

2.1.3 The Hartree-Fock approximation

Now that we have a method for describing many-electron wave functions, we can consider the computation of molecular properties. The cornerstone of quantum chemistry is the *Hartree-Fock method* (HF), otherwise known as the self-consistent field method. The main principle of the HF method is to approximate electron-electron interactions with an average potential. We begin with a single Slater de-

2.1. The quantum mechanical approach

terminant for an N electron system in the ground state:

$$|\Psi_0\rangle = |\chi_1\chi_2 \dots \chi_N\rangle \quad (2.13)$$

By applying the variational method to the Schrödinger equation, we hope to find the lowest possible ground state energy, E_0 . One applies the variational principle by choosing a trial wave function (ϕ) dependent on some number of parameters. These parameters are optimized so that the expectation value of the energy is minimized:

$$E_0 \leq \langle \phi | \mathcal{H} | \phi \rangle \quad (2.14)$$

The trial wave function minimizes E_0 only when $\phi = \Psi_0$, the ground state wave function.

Within the Hartree-Fock approximation, we approximate the full electronic Hamiltonian \mathcal{H} with a related operator \hat{H}_0 :

$$\hat{H}_0 = \sum_{i=1}^N \hat{f}(i) \quad (2.15)$$

where $\hat{f}(i)$ is the Fock operator of the $i - th$ electron, defined as

$$\hat{f}(i) = -\frac{1}{2}\nabla_i^2 + \sum_{A=1}^M \frac{Z_A}{r_{iA}} + v^{HF}(i) \quad (2.16)$$

The first two terms are the non-interacting one electron Hamiltonian, $\hat{h}(i)$. The third term, $v^{HF}(i)$, is the average potential experienced by each electron in the presence of other electrons.

With these approximations, the quantum problem is now reduced to solving the eigenvalue Hartree-Fock equation of the form

$$\hat{f}(i)\chi(\mathbf{x}_i) = \epsilon_i\chi(\mathbf{x}_i) \quad (2.17)$$

Solving Equation 2.17 directly is computationally very challenging, as there are infinite possible solutions. However in 1951, Roothaan⁵⁶ demonstrated that the problem can be simplified by expanding each spin orbital into a linear combination of a known finite number K basis functions:

$$\chi_i = \sum_{\mu=1}^K C_{\mu,i} \phi_{\mu} \quad (2.18)$$

where $C_{\mu,i}$ is a weighting coefficient and ϕ_{μ} is a basis function. As K approaches ∞ , the set $\{\phi_{\mu}\}$ becomes more complete and the energy approaches the so-called *Hartree-Fock limit*, or the exact energy in the Hartree-Fock approximation. One is, however, always limited to a finite number of basis functions, leaving deficiencies in the desired wave function Ψ_0 .

The expansion of spin orbitals into a basis allows Equation 2.17 to be written in terms of the *Roothaan matrix equation*

$$\mathbf{FC} = \mathbf{SC}\varepsilon \quad (2.19)$$

where $\mathbf{F} = \sum_{l,m} \langle \chi_l | \hat{f}(i) | \chi_m \rangle$ is the Fock matrix, $\mathbf{S} = \sum_{l,m} = \langle \chi_l | \chi_m \rangle$ is the orbital overlap matrix. \mathbf{C} is the orbital coefficient matrix, and ε is the diagonal matrix of orbital energies ε_i , which are generally the desire solutions. By performing a transformation of basis to an orthonormal basis, the overlap matrix \mathbf{S} becomes the identity matrix $\mathbb{1}$, and simplifies the problem. Thus, utilizing Equation 2.19 reduces the problem to the of diagonalization \mathbf{F} . Unfortunately, this must be done iteratively, as \mathbf{F} depends on its own solution, hence the name self-consistent field method.

2.1.4 Basis sets

Choosing optimal basis functions can help significantly in terms of determining the ground state wave function Ψ_0 . Quantum chemists rely on the choice of *basis sets*, defined as the vector space in which an ab initio problem is defined. Basis sets usually refer to the set of one particle functions, which are used to form MOs in a linear combination of atomic orbitals (LCAO-MO) like approach. For a system with N electrons, the LCAO-MO approach gives $N/2$ occupied orbitals in the ground state. The remaining basis functions in a set are combined to give *virtual* (unoccupied) orbitals.

Early basis sets were composed of *Slater-type orbitals* (STOs), due to their resemblance to the atom orbitals (AOs) of the hydrogen atom. These are functions of the form

$$\phi_i^{STO}(\zeta, n, a, b, c, x, y, z) = N r^{n-1} e^{-\zeta r} x^a y^b z^c \quad (2.20)$$

where N is a normalization constant, ζ is a constant related to the effective nuclear charge of the nucleus, r is the distance of the electron from the atomic nucleus, n is a natural number that plays the role of the principal quantum number, and x , y , and z are Cartesian coordinates. The angular component $x^a y^b z^c$ describes the shape of the function, such that if $a+b+c=0$ ϕ_i^{STO} is of *s*-type; if $a+b+c = 1$, ϕ_i^{STO} is of *p*-type, and so forth. Although STOs approximate the long and short range behaviour of atomic orbitals correctly, performing integration with these functions is computationally very demanding, due primarily to the complexity of the integrals involved describing in electron-electron interactions.

In order to make the integration over orbitals computationally efficient, modern basis sets are almost exclusively composed of *Gaussian-type orbitals* (GTOs), which

can generally be represented as

$$\phi_i^{GTO}(\alpha, a, b, c, x, y, z) = Ne^{-\alpha r^2} x^a y^b z^c \quad (2.21)$$

where N is a normalization constant, α is the orbital exponent coefficient, x , y , and z are Cartesian coordinates, r is the radius ($r^2 = x^2 + y^2 + z^2$), and the angular portion is described the same as in an STO. It takes a linear combination of several GTOs to represent the same function as an STO. These linear combinations of GTOS are known as *contracted GTOs* (CGTO) with n GTOs combined as

$$\phi_i^{CTGO}(\alpha, a, b, c, x, y, z) = N \sum_{i=1}^n c_i e^{-\alpha r^2} x^a y^b z^c \quad (2.22)$$

where c_i is referred to as the contraction coefficient that describes the weighting of each GTO. Although it requires more GTOs than STOs to accurately describe the atomic orbitals, the integrals can be computed 4–5 times faster, and thus calculations involving GTOs are much more efficient.⁵⁷

Basis set nomenclature

Standard basis sets are composed of basis functions used to represent atomic orbitals where each basis function is a CGTO composed of several GTOs. A *minimal basis set* is one in which each AO is represented by a single basis function. To more accurately represent AOs, more basis functions should be used, although basis set size needs to be balanced with computational cost. Larger basis sets are referred to by their cardinal number, the number of basis functions that represent each AO. When two basis functions are used to represent each AO, this is called a *double-zeta* basis set. If three basis functions represent each AO, this is called a *triple-zeta* basis set. Generalized, a basis set is N -zeta in size when N basis functions are used per

AO.

A *split-valence* basis set is one in which a single basis function is used to represent each core AO, while more basis functions are used to represent the valence AOs. Constructing basis sets in this way can help reduce the computational cost while still accurately representing the electrons that are most important to chemistry.

Additional basis functions are often added to basis sets in order to correctly describe molecular properties. *Polarization functions* are basis functions that are one or more angular momentum channels greater than the natural electronic configuration of an atom. For example, a single *p*-type basis function can be added to the minimal basis of a hydrogen atom. Polarization functions are essential to accurately describe chemical bonding, as the presence of other atoms distorts the spherical symmetry of a single atom's AOs.⁵⁸ *Diffuse functions* are basis functions that extend further into space, typically by the inclusion of a very shallow Gaussian function (small ζ exponent). Diffuse functions are necessary to accurately describe anions, very electronegative atoms, and large systems in which non-covalent interactions (NCIs) are important.

Commonly used basis sets

A large number of basis sets currently exist in the literature.⁵⁹ While not all basis sets are created equally, we shall briefly consider four of the most commonly used basis sets used in quantum chemistry.

Pople-style basis sets

Perhaps the most utilized basis sets in chemistry are those arising from the group of Pople.^{60–62} These basis sets were defined by minimizing the HF energy. The earliest of these basis sets are the minimal STO-*NG* basis sets, where *N* describes the number of GTOs that go into each contraction.

2.1. The quantum mechanical approach

The practise of using minimal basis sets has diminished significantly as technology has advanced, thus these basis sets are largely considered out of date. It is more common to utilize the split-valence basis sets, denoted as $n - ijG$ or $n - ijkG$ for double and triple zeta split-valence basis sets, respectively. In this system of notation, n represents the number of GTOs that describe the core AOs, and i, j, k describe the number of GTOs for contractions in the valence AOs. Polarization functions are denoted either with asterisks or with the specific shell and number of functions that are being added. Diffuse functions are denoted with either a single or double “+”, indicating diffuse s and p -type functions for non-hydrogen atoms, and the addition of diffuse s -type functions for hydrogen, respectively. For example, the $6-31+G(d,p) \equiv 6-31+G^{**}$ double-zeta basis set for C and H is one that has: 6 GTOs per core AO, 3 GTOs for the first valence set of AOs, and 1 GTO for the second, along with s and p diffuse functions of the heavy atoms, a single d polarization function of heavy atoms, and a single p polarization function of hydrogen atoms.

Correlation consistent basis sets

Post-Hartree-Fock methods (*vide infra*) are commonly used in quantum chemistry. In 1989, Dunning^{63–65} identified that the use of basis sets optimized for HF were inappropriate for post-HF methods. The basis sets that came from Dunning and co-workers, which are referred to as “correlation consistent” basis sets are commonly used in, but not limited to, state of the art wave function calculations. These basis sets are said to be correlation consistent as they treat electron correlation (*vide infra*) in a manner that systematically approached the complete basis set limit. Correlation consistent basis sets are denoted as “cc-VNZ”, where $N=2(D),3(T),4(Q),5,6,\dots$ is the cardinal number of the basis set. These are large sets containing polarization functions by default and can be additionally augmented with diffuse functions, denoted by the prefix “aug.” A variant of these basis sets

2.1. The quantum mechanical approach

that are used for including core-correlation are denoted by “cc-pCVNZ”.⁶⁶ A commonly used basis set is aug-cc-pVTZ, which is a triple-zeta basis set with implicit polarization functions and specified diffuse functions on all atoms.

Polarization consistent basis sets

The polarization consistent basis sets have been developed by Jensen and coworkers.^{67–70} The polarization consistent basis sets have been developed to systematically complete basis set limit in density-functional theory calculations through the use of higher order polarization functions. The notation adopted is “pc- X ”, where X is the cardinal number of the basis set minus one (i.e. $X = N-1$). Polarization functions are included by default in these basis sets, and additional diffuse functions can be specified with the same “aug” prefix used for the correlation consistent basis sets.

Ahlrich basis sets

The last basis sets we will mention are those developed by Ahlrich and coworkers.^{71,72} These are the “Def2” basis sets, named as such because they are the second generation of default basis set in the Turbomole quantum chemistry package.⁷³ Additionally, these basis sets have been developed so that consistent errors are obtained for nearly every element on the periodic table: a unique trait among modern basis sets. The nomenclature for these basis sets is fairly straightforward where either SV is used for split valence, or NZ is used for cardinal number. Addition of polarization and diffuse functions is specified with a P and D, respectively. For example, Def2-SVP is the basis set of split-valence double-zeta quality with polarization functions; Def2-TZVP is the triple-zeta basis set with polarization functions; Def2-QZVPD is the quadruple-zeta basis set with polarization and diffuse functions.

2.1.5 Post-Hartree-Fock methods

The HF method gives an approximation to the ground state wave function of a molecule for a reasonable computational cost (scaling with N^4 number of basis function). There is however, a lack of the complete description of *dynamical electron correlation*,⁷⁴ and thus significant deviations from experimental results can be observed. Dynamical electron correlation is a measure of how much one electron's movement is affected by the motion of other electrons. As described previously, the HF method includes correlation through the average electron field potential term, however this field is in general, not static, thus correlation must be treated directly in order to obtain accurate results. The majority of methods take the HF wave function Ψ_0 as the starting point. The correlation energy is defined as the difference between the exact energy and the HF energy:

$$E_{corr} = E_{exact} - E_0 \quad (2.23)$$

E_{corr} is the difference between the full non-relativistic energy from the Schrödinger equation, E_{exact} , and a reference ground state energy E_0 , usually the HF energy.

We shall briefly consider two important methods for accounting for electron correlation and obtaining E_{corr} : Møller-Plesset perturbation theory, and the related configuration interaction and coupled cluster theories.

Møller-Plesset perturbation theory

Møller-Plesset (MP) perturbation theory is a special case of Rayleigh-Schrödinger perturbation theory in which the Hamiltonian for a system can be approximated by

$$\hat{H} = \hat{H}_0 + \lambda \hat{V} \quad (2.24)$$

2.1. The quantum mechanical approach

where \hat{H}_0 is an unperturbed Hamiltonian, \hat{V} is a small perturbation, and λ is an arbitrary parameter that controls the size of the perturbation. The perturbed wave function and energy are expressed as a power series in λ :

$$\Psi = \lim_{m \rightarrow \infty} \sum_{i=0}^m \lambda^i \Psi^{(i)} \quad (2.25)$$

$$E = \lim_{m \rightarrow \infty} \sum_{i=0}^m \lambda^i E^{(i)} \quad (2.26)$$

The MP method applies perturbations to HF by defining a *shifted* Fock operator \hat{H}_0 and *correlation potential* \hat{V} as

$$\hat{H}_0 = \hat{F} + \langle \phi_0 | (\hat{H} - \hat{F}) | \phi_0 \rangle \quad (2.27)$$

$$\hat{V} = \hat{H} - \hat{H}_0 \quad (2.28)$$

where ϕ_0 is the ground state Slater determinant of the Fock operator.

Within this formulation, the zeroth-order energy is the expectation of \hat{H} , which gives the HF energy. The first-order energy is

$$E_{MP1} = \langle \phi_0 | \hat{V} | \phi_0 \rangle = 0 \quad (2.29)$$

by Brillouin's Theorem of singly excited determinants. Thus, the first useful correction occurs at the second order of perturbation, which is known as MP2. Additional orders of perturbation are referred to as MP3, MP4, *etc.* The MP2 method has been popular in quantum chemistry because it scales with N^5 number of basis functions and is a significant improvement on the treatment of electron correlation compared to HF. One may expect higher order of perturbation theory to more accurately de-

2.1. The quantum mechanical approach

scribe a system. Practically however, the expansions used in MPN theory do not in all cases converge smoothly to a limit with higher order of perturbation.⁷⁵ As a result, for molecular properties calculated with MP3 or higher are not guaranteed to give more accurate results than MP2.

Configuration interaction and coupled cluster theory

The solutions to the HF method give a single determinant wave function that only describes the ground state electronic configuration. Configuration interaction (CI) is a post-HF method that describes a linear combination of Slater determinants to more accurately represent a system's wave function. The additional Slater determinants represent excited electronic configurations and can be singly excited (S), doubly excited (D), and so forth. This is represented as follows:

$$|\Psi\rangle = \left(1 + \sum_{j=1}^N C_j\right) |\phi_0\rangle \quad (2.30)$$

where C_j are operators that describes the j -th excitations of electrons. If all possible excitations are included in the CI equation, this is referred to as *full CI* (FCI). Extending FCI to an infinite basis set gives the exact solution to the Schrödinger equation.

Coupled cluster (CC) theory⁷⁶ is a similar approach to CI, but uses the so-called *exponential ansatz*

$$|\Psi\rangle = e^{\hat{T}} |\phi_0\rangle \quad (2.31)$$

where \hat{T} is the cluster operator, defined by n -electron excitation operators \hat{T}_n :

$$\hat{T} = \hat{T}_1 + \hat{T}_2 + \hat{T}_3 + \dots \quad (2.32)$$

2.1. The quantum mechanical approach

Within the exponential ansatz, $e^{\hat{T}}$ is usually truncated and expanded in a Taylor series. For example, truncation at the \hat{T}_2 excitation operator gives

$$\begin{aligned} |\Psi\rangle &= e^{\hat{T}_1 + \hat{T}_2} |\phi_0\rangle \\ &= (1 + \hat{T}_1 + \hat{T}_2 + \frac{1}{2!} \hat{T}_1^2 + \hat{T}_1 \hat{T}_2 + \frac{1}{2!} \hat{T}_2^2 + \dots) |\phi_0\rangle \end{aligned} \quad (2.33)$$

Considering both CI and CC with single and double excitation (CISD and CCSD), the wave functions will include similar excitations, however inclusion of cross terms ($\hat{T}_1 \hat{T}_2$) in CCSD implicitly includes higher excitation levels. Additionally, the use of the exponential operator makes the CC formulation *size consistent*, which is the largest short coming of the CI method. Size consistency refers to the additivity of energies for an ensemble of molecules. That is, for a pair of molecules A and B, their energies must follow the relation

$$E_{AB}(r \rightarrow \infty) = E_A + E_B \quad (2.34)$$

Size consistency is a necessary requirement of a theoretical treatment to treat systems of molecules accurately. It is for this reason that CC has superseded CI as the dominant highly correlated method in quantum chemistry.

The inclusion of higher order excitations become less important with increasing orders of excitation; however, the inclusion of triples is often found to be necessary for the accurate description of electron correlation (i.e. CCSDT). The computation of triples is prohibitively expensive in all but the simplest of systems, thus approximations based on perturbation theory are often used instead. The most commonly used perturbative triples method is CCSD(T), where the parenthesis indicate the use of perturbative arguments. Note also that traditionally, the use of CCSD(T) implies excitation of only the valence electrons, unless otherwise stated.

2.1. The quantum mechanical approach

CCSD(T) is commonly referred to as the *gold standard* in quantum chemistry and is often used to obtain benchmark quality results for thermochemistry and NCIs.⁷⁷ However, CCSD(T) scales with N^7 number of basis functions, and is thus significantly more computationally expensive than HF or MP2, restricting its application to small systems of molecules. Quadratic configuration interaction (QCI) is closely related to CC, except that it uses quadratic operators in place of exponential ones. QCISD(T) and CCSD(T) gives very similar results.⁷⁸

2.1.6 The complete basis set limit

Complete basis set extrapolation

In accordance with the variational principle, the energy obtained by a particular method will always be greater than or equal to the exact energy. The exact energy can only be achieved with an infinite basis set, a value known as the *complete basis set* (CBS) limit.⁷⁹ Since this is computationally infeasible, specific approaches have been developed to approximate the CBS limit. Specifically, molecular properties calculated using the HF and post-HF methods have been shown to asymptotically approach the CBS limit in a smooth manner when appropriate basis sets are used. Therefore, to obtain results estimating a molecular property at the CBS limit ($Y(\infty)$), properties can be fit to three-parameter^{80,81} or two-parameter functions:^{82,83}

$$Y(x) = Y(\infty) + Ae^{-x/B} \quad (2.35)$$

$$Y(x) = Y(\infty) + A/x^3 \quad (2.36)$$

where the molecular property as a function of basis set cardinal number $Y(x)$ is

2.1. The quantum mechanical approach

fit using parameters A and B . Typically calculations of this nature are performed using the correlation consistent basis sets (cc-pVNZ), however there is evidence that for DFT based calculations, the polarization consistent basis sets (pc- X) more rapidly approach the CBS limit for some molecular properties.⁸⁴ The true *gold standard* in quantum chemistry is referred to as CCSD(T)/CBS, which typically means CCSD(T) with complete basis set extrapolation with aug-cc-pVNZ basis sets, where $N=D$, T, Q, or 5. Although extrapolation is useful for approximating highly accurate results, there is an inherent amount of uncertainty associated with the final fitted results, which may be unclear from the nomenclature.

Explicit correlation methods

A new technique that is gaining popularity among post-HF methods is the inclusion of so called *explicit correlation*.^{85,86} The introduction of additional functions dependent on inter-electronic distance coordinates allows for explicit correlation of electrons.⁸⁷ As a result the dynamical correlation of electrons is treated more accurately with reduced basis sets, therefore accurate results can be achieved at a reduced computational cost. Basis set extrapolation can also be performed on explicitly correlated results: this is quickly becoming the standard approach.⁸⁸

2.1.7 Composite quantum chemistry methods

In order to calculate thermochemical and kinetic properties that are within a sub-kcal mol⁻¹ range of experiment, multistep *ab initio* procedures that are referred to as *composite methods* have been developed.⁸⁹ These procedures work by including important energy terms that contribute to molecular properties. Generally, composite methods make use of a combination of low correlation methods with large basis sets and high correlation methods with small basis sets, as is illustrated

2.1. The quantum mechanical approach

in Figure 2.1. Some of the relevant energy terms include: core-valence, relativistic, spin-orbital, Born-Oppenheimer, and zero-point vibrational energy corrections. There exist many composite methods, each of which makes use of a variety of quantum mechanical (QM) methods and different basis set extrapolation techniques in order to best approximate energy terms that are relevant, with the ultimate goal of achieving the exact energy of a system. In this work, I have made use of several composite methods including: the G4 and G4(MP2) methods,^{90,91} CBS-QB3 and CBS-APNO methods,^{92–94} and the W1BD method.⁹⁵ A description of these methods will be provided in Chapter 4.

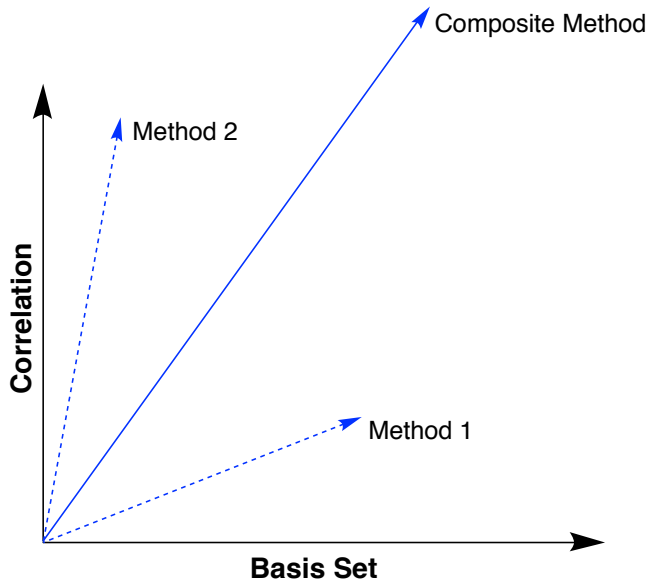


Figure 2.1: Schematic representation of a quantum mechanical composite method. The exact energy can only be achieved at the limits of an infinite basis set and complete correlation. Using a combination of Method 1 (low correlation/large basis set) and Method 2 (high correlation/small basis set), the composite method approaches the exact energy.

2.1.8 Density-functional theory

Density-functional theory (DFT) is the most popular quantum chemical method applied to date. It relies on the two Hohenberg-Kohn theorems, the first of which states that there exists a unique electron density ρ that defines the properties of a many-electron system. The second theorem defines an energy functional of the electron density and demonstrates that the correct ground state electron density minimizes the energy functional through the variational theorem.^{96,97} These theorems alone do not provide the solutions to the Schrödinger equation.

It wasn't until the formulation of Kohn-Sham DFT⁹⁸ that the theory began gaining ground as a useful quantum theory. Kohn-Sham DFT scales formally with N^3 number of electrons⁷⁴ which is better than HF by a factor of N . In addition, DFT is a complete theory like FCI; however, there is no straightforward way to determine the correct functionals of the electron density as the exact form of the functionals is unknown. Nonetheless, the drive for the development of the correct density-functional has been one of the main endeavours in quantum chemistry in the last two decades.

The framework behind conventional DFT is built into the description of the full energy functional E :

$$E[\rho] = T_{ni}[\rho] + V_{ne}[\rho] + V_{ee}[\rho] + \Delta T[\rho] + \Delta V_{ee}[\rho] \quad (2.37)$$

where T_{ni} is the kinetic energy of non-interacting electrons, V_{ne} is the potential of nuclear-electron interactions, and V_{ee} is the classical electron-electron repulsion. The last two terms are collectively referred to as the exchange-correlation (XC) functionals, where ΔT is the dynamical correlation term, and ΔV_{ee} is the non-classical correction to electron-electron repulsion. All the functionals, except the

2.1. The quantum mechanical approach

XC functionals have an exact form. It is therefore the XC functionals in which there is currently empiricism.

The ultimate goal in describing XC functionals is to find the “correct” XC functional that gives the exact energy of a system from the electron density. At this point, this must be done using approximations, for which there are several degrees of complexity. These approaches follow a hierarchical scheme, commonly referred to as the “Jacob’s ladder” of DFT.⁹⁹ The first rung represents the simplest approximation that is known as local-density approximations (LDAs), which approximate the exchange-correlation density at a given point by the electron density at that same point. The form of these functionals is:

$$E_{XC}^{LDA} = \int \rho(\mathbf{r}) \varepsilon_{XC}(\rho(\mathbf{r})) d\mathbf{r} \quad (2.38)$$

where $\varepsilon_{XC}(\rho(\mathbf{r}))$ is the exchange-correlation energy per particle (energy density) of a uniform electron gas of density $\rho(\mathbf{r})$. This approximation is overly simple and applies only when the electron density is constant at all points, and are thus not generally applied in chemical problems. Nonetheless, LDA based approaches are commonly employed in solid state physics.

The second rung on the ladder corresponds to generalized-gradient approximation (GGA) based functionals, which are still amongst some of the most popular density-functionals. GGAs depend on both the electron density and the gradient of the electron density at a point:

$$E_{XC}^{GGA} = \int \rho(\mathbf{r}) \varepsilon_{XC}^{GGA}(\rho(\mathbf{r}), \nabla \rho(\mathbf{r})) d\mathbf{r} \quad (2.39)$$

where, $\varepsilon(\rho(\mathbf{r}), \nabla \rho(\mathbf{r})) d\mathbf{r}$ is the energy density associated with a given GGA. GGA functionals provide a substantial improvement over LDAs, and most are constructed

2.1. The quantum mechanical approach

so that they correct the LDA energy:

$$\varepsilon_{XC}^{GGA}(\rho(\mathbf{r}), \nabla\rho(\mathbf{r})) = \varepsilon_{XC}^{LDA}(\rho(\mathbf{r}))d\mathbf{r} + \Delta\varepsilon_{XC}\left(\frac{\nabla\rho(\mathbf{r})}{\rho^{4/3}(\mathbf{r})}\right) \quad (2.40)$$

A step above GGAs on the third rung of the ladder are meta-GGAs, which depend on the electron density, as well as the first derivative of electron density at a point, and the kinetic-energy density, $\tau(\mathbf{r})$, defined as:

$$\tau(\mathbf{r}) = \sum_i^{\text{occupied}} \frac{1}{2} |\nabla\chi_i(\mathbf{r})|^2 \quad (2.41)$$

where $\chi_i(\mathbf{r})$ are the self-consistently determined Kohn-Sham orbitals. Meta-GGAs improve upon the accuracy of GGAs at a comparable cost.⁷⁴

The XC functionals described up to this point (LDAs, GGAs, meta-GGAs) depend only on the electron density and derivatives of the electron density. The fourth and fifth rungs of the ladder improve upon the prior functionals by inclusion of terms dependent on additional properties. While these approaches improve upon the accuracy of these functionals, they come with an increase in computational cost. On the fourth rung sit functionals that depend to some percentage on the HF exact exchange. When the ratio of HF exchange is fixed, these functionals are termed hybrid functionals. Alternatively, functionals are said to be range-separated corrected if a different amount of exact-exchange to describe long and short-range behaviours. In the cases of hybrid and range-separated functionals, the added computational cost comes from the calculation of the HF exact exchange (N^4).

Alternatively, one can describe the fourth rung functionals as depending upon the properties of the occupied molecular orbitals. The fifth rung then, is said to depend on the properties of unoccupied molecular orbitals. These functionals are typically referred to as double-hybrids, and incorporated correlation energy from

2.1. The quantum mechanical approach

a post-HF method, typically MP2.¹⁰⁰ Double-hybrid DFT methods are once again more accurate than the lower rung methods, however, calculating the MP2 correlation energy is considerably more computationally demanding than traditional DFT approaches. Therefore, double-hybrid DFT methods have not gained popularity in the literature.

There are many published XC functionals. Fortunately, there is a fairly standard system of nomenclature, such that density functionals are described as *exchange functional-correlation functional*. The most commonly used density functional is the B3-LYP, which uses the 3-parameter hybrid exchange functional of Becke,¹⁰¹ and the correlation functional of Lee, Yang, and Parr.¹⁰² There are also standalone functionals that have built in exchange and correlation functionals. A common example of these are the Minnesota family of functionals from the Truhlar group.^{103,104}

Aside from the problem of choosing density-functionals, solving DFT is computationally very similar to the HF method. Within Kohn-Sham (KS) DFT, we define a fictitious system of non-interacting electrons with the same electron density as the real system. This is achieved by the use of a Hamiltonian in which there is an effective local potential, $V_s(\mathbf{r})$:

$$\hat{H}_s = -\frac{1}{2} \sum_i^N \nabla_i^2 | \sum_i^N V_S(\mathbf{r}_i) \quad (2.42)$$

The ground state wave function of this non-interacting Hamiltonian is represented by a single Slater determinant with spin orbitals (χ), completely analogous to the HF problem. These spin orbitals, referred to as *Kohn-Sham orbitals* are determined by

$$\hat{h}_i^{KS} \chi_i = \varepsilon_i \chi_i \quad (2.43)$$

2.1. The quantum mechanical approach

where the one-electron Kohn-Sham operator \hat{h}^{KS} is defined as

$$\hat{h}_i^{KS} = -\frac{1}{2}\nabla^2 + V_s(\mathbf{r}) \quad (2.44)$$

It is crucial to realize that this procedure does not give us the exact energy of a system, but rather is used to determine an electron density that represents our real system. The connection between this fictitious system comes from the chose of the effective potential such that the density of our real system is a result of summing over the squared moduli of the KS orbitals:

$$\rho(\mathbf{r}) = \sum_i |\chi_i|^2 \quad (2.45)$$

Once again in analogy to HF theory, one applies the variational principle to minimize the total energy functional in Equation 2.37 with respect to χ . The effective potential that variationally minimizes the energy is given by¹⁰⁵

$$\begin{aligned} V_s(\mathbf{r}) &= \frac{\delta J[\rho]}{\rho(\mathbf{r})} + \frac{\delta E_{XC}[\rho]}{\delta \rho(\mathbf{r})} + \sum_A^M \frac{Z_A}{r_{iA}} \\ &= \int \frac{\rho(\mathbf{r}_2)}{r_{12}} + V_{XC} + \sum_A^M \frac{Z_A}{r_{iA}} \end{aligned} \quad (2.46)$$

where the first term describes the Coulombic potential between two electrons, the last term is the potential between the electron and each nucleus. The middle term is once again the unknown XC potential. The electron density obtained from the fictitious system of non-interacting particles is finally used in Equation 2.37 to find the total energy of the system. Since $V_s(\mathbf{r})$ depends on the electron density, these equation must be solved iteratively, as with HF theory. Note however, that if the exact form of $E_{XC}[\rho]$ was known, this method would give the exact ground state

electron density of the system, and thus the exact energy.

Challenges for density-functional theory methods

Pure DFT has low computational cost and potentially good accuracy, hence its popularity as a quantum chemical treatment. However, there are several problems that common DFT methods experience that lead to erroneous results in many cases.¹⁰⁶ It is well established that traditional DFT methods completely fail at describing non-covalent interactions.^{107,108} This shortcoming leads to poor descriptions of chemistry beyond equilibrium geometries, including transition states. Fortunately, there are several methods that can correct for this problem, commonly through the addition of an energy correction term E_{disp} to the DFT energy E_{DFT} , as

$$E_{tot} = E_{DFT} + E_{disp} \quad (2.47)$$

It is common to employ the empirical D3 pair-wise correction of Grimme,¹⁰⁹ paired with of the Becke-Johnson damping function,¹¹⁰ denoted as D3(BJ). This correction works by calculating the dispersion interactions between all pairs of atoms A and B separated by distance R_{AB} , with the following equation:

$$E_{disp} = \sum_{A>B} \frac{C_6^{AB}}{R_{AB}^6} f_6(R_{AB}) + s_8 \frac{C_8^{AB}}{R_{AB}^8} f_8(R_{AB}) \quad (2.48)$$

where C_6 and C_8 are dispersion coefficients, s_8 is an empirically determined scaling parameter, and f_n are the damping functions that limit the range of dispersion correction, avoiding near singularities at small R_{AB} . Another approach to correcting for dispersion is to add parameters directly to the functional, as is the case in the Minnesota functionals.^{103,103} Both of these empirical corrections have the benefit

2.1. The quantum mechanical approach

of adding negligible computational time, but must be parametrized for each DFT method with which they are employed.

Another striking issue with DFT is the unphysical ability of an electron to interact with itself, termed *self-interaction error*. This is most obvious in what is known as *delocalization error*, which is a result of many-electrons interacting with themselves, or many-electron self-interaction error. In HF theory, self-interaction error is exactly cancelled, thus DFT methods that have a high portion of HF exchange in their formulation are able to account for this issue. Consider for a moment a one electron system: there should be exactly zero electron correlation. In terms of the energy functionals shown in Equation 2.37, the electronic repulsion term $V_{ee}[\rho]$ should cancel exactly with the XC term ($V_{ee}[\rho] = -E_{XC}[\rho]$).⁷⁴ Unfortunately, all pure DFT methods fail to reproduce this expected behaviour. An obvious manifestation of delocalization error is the incorrect treatment of charge-transfer in intramolecular interactions,^{111,112} as well as in transition state complexes. Even for the simplest HAT reaction $\text{H}_2 + \text{H}^\bullet \longrightarrow \text{H}^\bullet + \text{H}_2$, the calculated barrier height is underestimated by 8–9 kcal mol⁻¹ using a GGA functional.¹¹³ Charge-transfer occurs when a fraction of an electron is transferred between molecular entities. Specifically, charge-transfer is mistreated at longer ranges, thus either high percentage exact exchange hybrid functionals, or range-separated functionals are suggested for systems in which charge-transfer may occur.

As is the case for most experimental methods, identifying the correct theoretical methods requires the careful consideration of the problem at hand. Choosing a DFT based method requires calibration. However, once a method has been tested and is known to provide reasonably accurate results, DFT methods have the ability to help understand chemical problem with relatively low computational costs.

2.2 Applying theory to chemical problems

2.2.1 Geometry optimization

All QM methods depend parametrically on the geometry of a molecular system. That is the electronic energy of a system depends on the positions of the nuclei. While the wave functions can describe any arbitrary geometry, we are typically only interested in certain geometries of a molecule. These geometries of interest are normally stationary states along the PES of a system, that is, points where the gradient of energy with respect to nuclear coordinates is zero. Therefore, we perform *geometry optimization* calculations to determine these points.

Molecular systems have complex PESs. For a non-linear molecule, the nuclear PES has $3N-6$ dimensions, where N is the number of nuclei present.¹¹⁴ In geometry optimization, we seek the local minima (reactants, products, or intermediates) and local maxima (TS complexes). Consider only local minima for a moment. Often complex molecules have more than one possible conformation, and each conformation represents a different local minimum along the PES. It is therefore important to ensure the correct conformation, typically the lowest energy structure (global minimum), is used when approaching chemical problems.

In order to efficiently perform geometry optimization, numerical analysis techniques are employed. All geometry optimization methods follow the same general framework.¹¹⁵ First, energy and necessary derivatives are computed from an initial geometry. Second, the geometry is modified to step towards the nearest stationary state. And lastly, some test is performed to determine if the new geometry is near enough to the stationary state along the PES. The most efficient method to do this is the *Newton method*, in which the energy is expanded in a Taylor series (truncated at the second order point) about the current point, \mathbf{x}_0 :

$$E(\mathbf{x}) = E_0 + \mathbf{g}_0 \Delta \mathbf{x} + \frac{1}{2} \Delta \mathbf{x} \mathbf{H}_0 \Delta \mathbf{x} \quad (2.49)$$

where E_0 , \mathbf{g}_0 , and \mathbf{H}_0 are the energy, gradient (Jacobian), and second derivative (Hessian) at point \mathbf{x}_0 , and $\Delta \mathbf{x} = \mathbf{x}_i - \mathbf{x}_0$. The aim of the Newton method is to minimize the gradient of the Taylor expansion, $\mathbf{g}(\mathbf{x})$, such that

$$\mathbf{g}(\mathbf{x}) = \mathbf{g}_0 + \mathbf{H}_0 \Delta \mathbf{x} \quad (2.50)$$

Solving for $\Delta \mathbf{x}$ gives the so-called Newton step that leads to minimization:

$$\Delta \mathbf{x} = -\mathbf{H}_0^{-1} \mathbf{g}_0 \quad (2.51)$$

The analytic computation of the Hessian is very expensive, especially for large systems. Therefore, to simplify the problem at the beginning of geometry optimization, the Hessian matrix is approximated and updated at each step in the optimization, using clever algorithms.¹¹⁵ This is called the *quasi-Newton method*, and is the default optimization routine in the Gaussian¹¹⁶ quantum chemistry package, as well as many other quantum chemistry packages.

Some additional caution must be taken in optimizing molecular structures. Normal algorithms that optimize structures stop when the gradient of energy is sufficiently close to zero; however, often PES can be flat or very shallow in regions and structures that are not fully optimized can be obtained. To avoid this, geometries are always subject to molecular vibration analysis.

2.2.2 Molecular vibrations

The computation of molecular vibrations can be performed simply given a set of molecular coordinates.¹¹⁷ Assuming a non-linear molecule, we start with $3N-6$

2.2. Applying theory to chemical problems

internal coordinates that are non-coupled (orthogonal). We then apply the *harmonic approximation*, in which we assume each normal mode follows Hooke's Law

$$F = kx \quad (2.52)$$

where F is the force, k is the force constant, and x is the displacement along one normal mode's coordinates. This approximation assumes the PES along the normal mode is parabolic, which in general is not true, but is a good approximation near the minima. Deviations from this approximation are known as *anharmonicity*. In practise, however, at normal temperatures ($\sim 298\text{K}$) the harmonic approximation is sufficient to describe molecular vibrations as displacements are assumed to be small.

Typically to obtain molecular frequencies, one computes the mass-weighted Hessian matrix elements F_{ij}

$$F_{ij} = \frac{1}{\sqrt{m_i m_j}} \mathbf{H}_{ij} \quad (2.53)$$

where the partial derivatives of internal coordinates x_i of the potential energy U are taken for $3N$ atoms with mass m . One then seeks to diagonalize this $3N \times 3N$ matrix to obtain eigenvalues λ_i , which describe the force constant of each normal mode. The harmonic frequencies ν_i are then obtained by

$$\nu_i = \frac{\sqrt{\lambda_i}}{2\pi} \quad (2.54)$$

and the lowest 6 modes are then discarded to account for $3N-6$ translations and rotations. These lowest energy modes generally correspond the internal rotations, and thus must be discarded to correctly obtain thermochemical corrections.

From these frequencies, the *zero-point vibrational energy* (ZPE, E_{ZPE}) is calculated:

$$E_{ZPE} = \sum_{i=1}^{3N-6} \frac{h\nu_i}{2} \quad (2.55)$$

The ZPE is an important quantum correction to the classical potential, giving the electronic potential energy

$$U = E_{elec} + E_{ZPE} \quad (2.56)$$

where E_{elec} is the QM electronic energy.

If a normal mode describes a non-minimum along the PES, the energy gradient will be negative (imaginary) instead of positive. Only energy maxima or saddle-points (TS structures) should have a single imaginary mode. Therefore, if a non-TS molecular structure calculation yields one or more imaginary modes, the geometry optimization has yielded a structure that is not at minimum on the PES. In this situation additional steps must be taken to find a corrected structure.

2.2.3 Thermochemistry

Up until this point we have been viewing molecules from a microscopic perspective; however, this is not useful for describing properties of bulk systems. Fortunately, fundamental statistical thermodynamics can be used to approximately describe a system in bulk.^{118,119} We approximate our system as an ensemble of non-interacting particles: using the Ideal Gas approximation. Within statistical thermodynamics, the fundamental starting point is the partition function Q ,¹²⁰ from which all thermodynamic properties can be calculated. For our ensemble, the molecular partition function is

$$Q = \sum_J e^{\varepsilon_j / k_B T} \quad (2.57)$$

2.2. Applying theory to chemical problems

where a Boltzmann distribution of j energy states ε is taken at temperature T , and k_B is the Boltzmann constant. All calculations herein are defined under conditions of temperature $T = 298.15$ K and pressure $P = 1$ atm, and concentration = 1 M.

Normally, the molecular partition function is decomposed into contributions from translational, vibrational, rotational, and electronic motion:

$$Q = q_{trans}q_{vib}q_{rot}q_{elec} \quad (2.58)$$

The equation describing the translational partition function q_{trans} is

$$q_{trans} = \left(\frac{2\pi m k_B T}{h^2} \right)^{3/2} \frac{k_B T}{P} \quad (2.59)$$

where m is the mass of the molecule, h is Planck's constants.

The vibrational partition function q_{vib} depends on the contributions of each of K vibrational modes. Only the $3N - 6$ (or $3N - 5$ for linear molecules) real vibrational modes of a molecule are considered, and imaginary frequencies are ignored. Therefore, for molecules that possess an imaginary frequency this thermodynamic analysis is invalid. TS complexes do possess a single imaginary frequency that is ignored, as it is assumed to not contribute to the overall vibrational partition function as no formal bond is said to be formed in the acceptor-donor system. Each vibrational mode has a characteristic vibrational electronic temperature, $\Theta_{\nu,K} = h\nu/k_B$, and the partition function is

$$q_{vib} = \prod_K \frac{e^{-\Theta_{\nu,K}/2T}}{1 - e^{-\Theta_{\nu,K}/T}} \quad (2.60)$$

The rotational partition function depends on the geometry of a system. For a single atom $q_{rot}=1$. For a linear molecule, the rotational partition function is

$$q_{rot} = \frac{1}{\sigma_r} \left(\frac{T}{\Theta_r} \right) \quad (2.61)$$

where σ_r is the symmetry number for rotation that depends on the molecular symmetry, and $\Theta_r = h^2/8\pi^2Ik_B$. I is the moment of inertia. Finally, for a non-linear polyatomic molecule, the rotational partition function is

$$q_{rot} = \frac{\sqrt{\pi}}{\sigma_r} \left(\frac{T^{3/2}}{\sqrt{\Theta_{r,x}\Theta_{r,y}\Theta_{r,z}}} \right) \quad (2.62)$$

where $\Theta_{r,x}$, $\Theta_{r,y}$, and $\Theta_{r,z}$ describe contributions of the moment of inertia in each of the x, y, and z-planes.

Finally, we make an important assumption that electronic contributions are assumed to exist in only the ground state, as excited states are generally safely assumed to be much larger than k_BT in energy. The full electronic partition function is

$$q_{elec} = \sum_{i=0} \omega_i e^{-\epsilon_i/k_BT} \quad (2.63)$$

where ω is the degeneracy of an energy level with energy ϵ . Applying our assumption, and by setting the ground state energy $\epsilon_0 = 0$, our problem simplifies dramatically, such that $q_{elec} = \omega_0$, which is simply the spin multiplicity of the molecule.

We now have all the information needed to calculate the thermodynamic quantities we are interested in. In chemistry we are concerned with the Gibbs free energy G , which is defined by the entropy S and enthalpy H as

$$G = H - TS \quad (2.64)$$

From each of the partition functions, the entropy of a system with N moles, $S_{tot} = S_{trans} + S_{vib} + S_{rot} + S_{elec}$, is calculated using the relation

$$S = Nk_B + Nk_B \ln \left(\frac{Q}{N} \right) + Nk_B T \left(\frac{\partial \ln Q}{\partial T} \right)_V \quad (2.65)$$

Similarly, the internal energy of a system, $E_{int,tot} = E_{int,trans} + E_{int,vib} + E_{int,rot} + E_{int,elec}$, is given by the relation

$$E_{int} = Nk_B T^2 \left(\frac{\partial \ln Q}{\partial T} \right)_V \quad (2.66)$$

Finally, the enthalpy is obtained from

$$H_{tot} = E_{int,tot} + k_B T \quad (2.67)$$

Using very simple statistical thermodynamic arguments, the properties of a bulk system are easily computed. It is important to emphasize that these results are for particles in the gas phase, thus additional steps must be taken if one desires to compare results to experiments performed in solvent.

2.2.4 Modelling solvent

It is in principle possible to include solvent molecules explicitly in QM calculations: this is in practise, extremely cost prohibitive. In order to approximate the important contributions of solvation, so-called *implicit continuum solvent models* are generally employed.^{74,121} Mathematically, one describes this as

$$\hat{H}^{tot}(\mathbf{r}_m) = \hat{H}^{mol}(\mathbf{r}_m) + \hat{V}^{mol+sol}(\mathbf{r}_m) \quad (2.68)$$

where a perturbation $\hat{V}^{mol+sol}$ dependent only on the coordinates of the solute (\mathbf{r}_m ; thus implicit) is applied to the Hamiltonian of the solute. The perturbation term is composed of interaction operators that contribute to the net free energy:

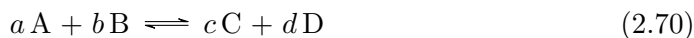
$$G_{solv} = G_{cavity} + G_{electrostatic} + G_{dispersion} + G_{repulsion} + G_{solv\ kinetic} \quad (2.69)$$

where the total solvation free energy G_{solv} contains terms from: the formation of a solvation cavity G_{cavity} , the electrostatic interactions between solvent and solute $G_{electrostatic}$, the dispersion interactions between solvent and solute $G_{dispersion}$, the QM exchange repulsion between solvent and solute $G_{repulsion}$, and the movement of solvent molecules $G_{solv\ kinetic}$.

A widely used model for solvation comes from the Truhlar group, and is known as SMD.¹²² The main parameter in implicit solvent models is the solvent dielectric constant (ϵ) with contributions from surface tension and the solvent-solute interface. SMD also includes terms that depend on the electron density of the solute. While many other implicit solvent models require the use of the same QM method as they were parametrized,¹²³ SMD is a *universal* model that was parametrized using several QM methods. Therefore, it does not require the use of a specific QM method and can be applied broadly in both single point energy and geometry optimization calculations.

2.2.5 Rate constants and transition state theory

In the discussion of chemical kinetics, the rate (r) of a reaction involving two species



is determined by the *rate law*, which can generally be described as

$$r = \frac{1}{c} \frac{dC}{dt} = \frac{1}{d} \frac{dD}{dt} = k[A]^\alpha[B]^\beta \quad (2.71)$$

where k is the rate constant, t is time, A, B, C , and D are chemical species with stoichiometric coefficients a, b, c , and d , α and β are the order of the reaction with respect to reactants A and B, and k is the rate constant. Computational chemistry is in general, not useful for determining rate laws: this must be done experimentally. Where computational studies can be useful, is in determining reaction mechanisms, and how the reaction barrier height can be altered. In doing so, we focus entirely on k .

Most chemists are intimately familiar with the phenomenological *Arrhenius equation*

$$k_{Arr} = A e^{-E_a/RT} \quad (2.72)$$

where A is a constant, R is the gas constant, and E_a is the *activation energy*, which is an experimental measure of the reaction barrier height. This equation dates back to the 1880s, when Arrhenius noticed that the reactions depended more heavily on temperature than was intuitive, and thus introduced the A constant, known often as the Arrhenius pre-factor.¹²⁴ The Arrhenius pre-factor is an empirical measure of the frequency of collisions which have the correct orientation for a reaction to occur. From the perspective of theory, Equation 2.72 has little meaning as the parameters are empirical. Thus, to study rate constants theoretically we must turn to *transition state theory*.

Transition state theory

The study of transition state theory (TST) originates in the 1930s, and was developed primarily by Eyring.^{124,125} In TST we focus on the TS complex, which is defined as a transient species that exists at the top of the energy barrier of a reaction. If we consider the same reaction in Equation 2.70, and set all the coefficients to 1, then TST states the reaction proceeds in two steps, the first of which includes a quasi-equilibrium between the reactants and TS complex



with an equilibrium constant (K_c^\ddagger) expression

$$K_c^\ddagger = \frac{[AB^\ddagger]/c^\circ}{[A]/c^\circ[B]/c^\circ} \quad (2.74)$$

where c° is the standard-state concentration (normally taken to be 1 M).

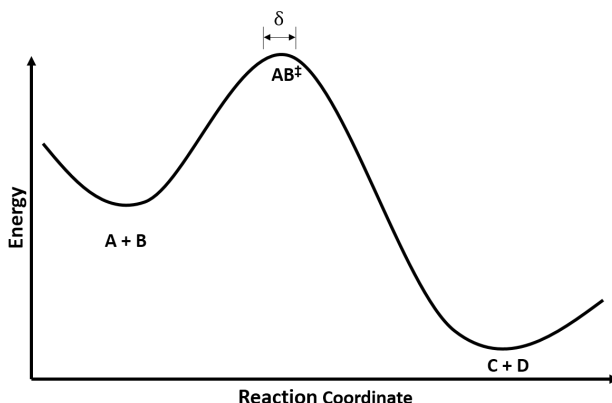


Figure 2.2: A reaction coordinate diagram for the reaction of Equation 2.73. The TS complex is defined to exist in the small region δ on top of the reaction barrier.

In TST, we define the TS complex to exist within a small region of width δ on top of the reaction barrier (Figure 2.2). From the second step of the reaction in

2.2. Applying theory to chemical problems

Equation 2.73, we can define a reaction rate dependent on the concentration $[AB^\ddagger]$ and v_c , a factor that defines the frequency with which the complexes proceed over the barrier:

$$r = v_c[AB^\ddagger] \quad (2.75)$$

From Equations 2.70 and 2.73, we now have two equivalent expressions for the reaction rate, which allows us to derive the following

$$r = k[A][B] = v_c[AB^\ddagger] \quad (2.76)$$

and solving Equation 2.74 for $[AB^\ddagger]$ results in

$$r = v_c \frac{[A][B]K_c^\ddagger}{c^\circ} \quad (2.77)$$

or

$$k = \frac{v_c K_c^\ddagger}{c^\circ} \quad (2.78)$$

We must now invoke statistical thermodynamics to make sense of Equation 2.78. We can rewrite the equilibrium expression K_c^\ddagger in terms of partition functions of each molecular species:

$$K_c^\ddagger = \frac{[AB^\ddagger]/c^\circ}{[A]/c^\circ[B]/c^\circ} = \frac{(q^\ddagger/V)c^\circ}{(q_A/V)(q_b/V)} \quad (2.79)$$

where V is the volume, and q_A , q_B , and q^\ddagger are the partition functions of A, B, and AB^\ddagger , respectively.

Since we have defined the reaction to be occurring with one degree of freedom, the translational partition function q_{trans} can be defined as

$$q_{trans} = \frac{\sqrt{2\pi m^\ddagger k_B T}}{h} \delta \quad (2.80)$$

where m^\ddagger is the mass of the TS complex. The partition function of the TS complex can be written as the product $q^\ddagger = q_{trans} q_{int}^\ddagger$, where the second term accounts for all remaining degrees of freedom of the TS complex. We can use this and rewrite Equations 2.79 and 2.78 as

$$K_c^\ddagger = \frac{\sqrt{2\pi m^\ddagger k_B T}}{h} \delta \frac{(q_{int}^\ddagger/V)c^\circ}{(q_A/V)(q_b/V)} \quad (2.81)$$

and

$$k = v_c \frac{\sqrt{2\pi m^\ddagger k_B T}}{hc^\circ} \delta \frac{(q_{int}^\ddagger/V)c^\circ}{(q_A/V)(q_b/V)} \quad (2.82)$$

We are now left with the two terms v_c and δ that are ill-defined. However, the product of these two terms is the average speed at which the TS complex crosses the barrier, $\langle u_{TS} \rangle = v_c \delta$. A Maxwell-Boltzmann distribution is used to calculate the value of $\langle u_{TS} \rangle$:

$$\langle u_{TS} \rangle = \left(\frac{m^\ddagger}{2\pi k_B T} \right)^{1/2} \int_0^\infty ue^{-m^\ddagger u^2/2k_B T} du = \left(\frac{m^\ddagger}{2\pi k_B T m^\ddagger} \right)^{1/2} \quad (2.83)$$

Substituting Equation 2.83 into Equation 2.82 for $v_c \delta$ yields

$$k = \frac{\sqrt{k_B T}}{hc^\circ} \frac{(q_{int}^\ddagger/V)c^\circ}{(q_A/V)(q_b/V)} = \frac{k_B T}{hc^\circ} K_c^\ddagger \quad (2.84)$$

We now define the standard Gibbs free energy of activation ($\Delta^\ddagger G^\circ$) to be the change in Gibbs free energy in going from reactants to TS. The thermodynamical expression is

$$\Delta^\ddagger G^\circ = -RT \ln K_c^\ddagger \quad (2.85)$$

which can be substituted into Equation 2.84

$$k = \frac{k_B T}{h c^\circ} e^{-\Delta^\ddagger G^\circ / RT} \quad (2.86)$$

The standard Gibbs free energy of activation can be expressed in terms of enthalpy and entropy as

$$\Delta^\ddagger G^\circ = \Delta^\ddagger H^\circ - T \Delta^\ddagger S^\circ \quad (2.87)$$

which upon substitution gives the equation

$$k = \frac{k_B T}{h c^\circ} e^{\Delta^\ddagger S^\circ / R} e^{-\Delta^\ddagger H^\circ / RT} \quad (2.88)$$

At this point, we can draw a direct comparison to the Arrhenius equation (Equation 2.72) by expressing E_a in terms of $\Delta^\ddagger H^\circ$ and A in terms of $\Delta^\ddagger S^\circ$. We must differentiate the natural logarithm of Equation 2.84, as well as Equation 2.72 (assuming that A is independent of temperature):

$$\frac{d \ln k}{dT} = \frac{1}{T} + \frac{d \ln K_c^\ddagger}{dT} \quad (2.89)$$

$$\frac{d \ln k_{Arr}}{dT} = \frac{E_a}{RT^2} \quad (2.90)$$

Next, we use the fact that $d \ln K_c/dT = \Delta U^\circ / RT^2$ for an ideal gas, then Equation 2.89 becomes

$$\frac{d \ln k}{dT} = \frac{1}{T} + \frac{\Delta^\ddagger U^\circ}{RT^2} \quad (2.91)$$

Additionally, $\Delta^\ddagger H^\circ = \Delta^\ddagger U^\circ + RT\Delta^\ddagger n$ ($\Delta^\ddagger n = 1$), so Equation 2.91 can be rewritten as

$$\frac{d \ln k}{dT} = \frac{\Delta^\ddagger H^\circ + 2RT}{RT^2} \quad (2.92)$$

Therefore, by comparison of Equation 2.92 and 2.90, we get

$$E_a = \Delta^\ddagger H^\circ + 2RT \quad (2.93)$$

which then converts Equation 2.88 into the form

$$k = \frac{e^2 k_B T}{hc^\circ} e^{\Delta^\ddagger S^\circ / R} e^{-E_a / RT} \quad (2.94)$$

Therefore, a natural statistical thermodynamical picture of the Arrhenius equation arises from TST, and the Arrhenius pre-factor A can be expressed as

$$A = \frac{e^2 k_B T}{hc^\circ} e^{\Delta^\ddagger S^\circ / R} \quad (2.95)$$

In practise, we use the form of Equation 2.86 to compute the rate constant of a reaction, which we shall denote as k_{TST} . The conventional TST makes an assumption that the reaction coordinate is static along the lowest energy pathway. This can be corrected by the use of *variational transition state theory*.¹²⁶ We shall not consider variational TST in this work, as with careful application, conventional TST does a remarkably good job at accounting for the magnitude and temperature dependence of a wide range of reactions.¹²⁵ Additionally, if one makes corrections for *QM tunnelling*, conventional TST can easily give a more complete description of

the rate constant.

Quantum mechanical tunnelling

Atoms are quantum mechanical particles, and are thus subject to the probabilistic behaviours observed at the microscopic level. QM tunnelling refers to the ability of particles to penetrate the reaction barrier, rather than surmounting it classically (Figure 2.3). While all reactions are subject to QM tunnelling, we will show that due to the low mass of the hydrogen atom, QM tunnelling can play a significant role in HAT reactions.

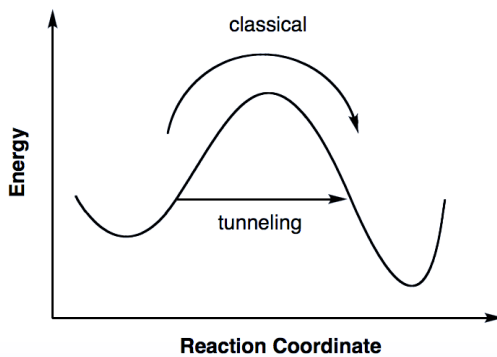


Figure 2.3: Quantum mechanical tunnelling occurs when a particle penetrates a reaction barrier, rather than surmounting it.

In order to determine the effects of scattering, one must find transmission coefficients (κ) by solving the Schrödinger equation.⁵² This is done by approximating the reaction barrier with an analytical potential, thus simplifying the problem mathematically. The earliest model potentials were introduced by Bell, who used a parabolic function to approximate the reaction barrier.¹²⁷ To obtain κ , and thus the observed rate constant (k_{obs}), the following equations were used:

$$k_{obs} = \kappa A e^{-E_a/RT} \quad (2.96)$$

$$\kappa = \frac{e^\alpha}{\beta - \alpha} \left(\beta e^{-\alpha} - \alpha e^{-\beta} \right) \quad (2.97)$$

$$\alpha = E_a/RT \quad (2.98)$$

$$\beta = \frac{2a\pi^2(2mE_a)^{1/2}}{h} \quad (2.99)$$

where the Arrhenius equation was used to estimate the rate constant, m is the mass of the tunnelling particle, and $2a$ is the width of the barrier. Since the equation is dependent on the mass of the particle, tunnelling occurs more often when lighter particles are involved. As a consequence, tunnelling is more common in HAT reactions than other atom transfer reactions. Also, the height and width of the barrier are important factors in determining the contributions to tunnelling: reactions with small barriers have low tunnelling contributions; narrow barriers result in higher tunnelling contributions.

The Bell model is a poor representation of an actual reaction barrier. One that is a much better approximation is the *Eckart potential*.¹²⁸ The form of this potential is

$$V = -\frac{Ay}{1-y} - \frac{By}{1-y^2} \quad (2.100)$$

$$y = -e^{2\pi x/L} \quad (2.101)$$

where x is the variable along the reaction coordinate and L is called the characteristic length. If $A = 0$ the potential becomes a symmetric function, further simplifying the problem; however, most reactions do not have a symmetric potential. A , B and

2.2. Applying theory to chemical problems

L are related to the change in barrier height in the forward and reverse direction, ΔV_1 and ΔV_2 , respectively:

$$A = \Delta V_1 - \Delta V_2 \quad (2.102)$$

$$B = ((\Delta V_1)^{1/2} + (\Delta V_2)^{1/2})^2 \quad (2.103)$$

$$\frac{L}{2\pi} = \left(-\frac{2}{F^*}\right)^{1/2} \left[\frac{1}{(\Delta V_1)^{1/2}} + \frac{1}{(\Delta V_2)^{1/2}} \right]^{-1} \quad (2.104)$$

where $F^* = d^2V/dx^2$ evaluated at the maximum of the potential. In this formulation, V is a placeholder energy. Note that if a reaction is endoergic, tunnelling does not occur. Alternatively, one says tunnelling only occurs in exoergic or energy-neutral reactions.

The solutions to the Schrödinger equation for the Eckart potential are analytical, thus the transmission coefficient κ can easily be computed using standard numerical techniques. These tunnelling corrections will be applied, where applicable as

$$k_{calc} = \kappa k_{TST} = \kappa \frac{k_B T}{\hbar c^\circ} e^{-\Delta^\ddagger G^\circ} \quad (2.105)$$

Chapter 3

The Relationship Between Arrhenius Pre-factors with Non-Covalent Binding

3.1 Introduction

DiLabio and Ingold³⁸ previously investigated the formal HAT reaction of the iminoxyl/oxime self-exchange reaction. In that paper, they compiled a table of parameters from the phenomenological Arrhenius equation for a series of interesting reactions, which appear here in Table 3.1.^{42,129–135} These are thermoneutral hydrogen atom self-exchange reactions involving oxygen-centered radicals, and other nearly thermoneutral reactions involving the destruction and formation of oxygen-centered radicals, reactions 3.1 and 3.2, respectively:



Although it is well known that reactions of this nature involve remarkably low activation energies (E_a),^{136–139} the Arrhenius pre-exponential factors (A), or as they shall be referred to herein, *A-factors*, as a well as rate constants, span a wide range (summarized in Table 3.1): The measured A-factors range from $10^{3.5}\text{--}10^{8.3}$ M⁻¹s⁻¹ and the rate constants range from $10\text{--}10\times 10^7$ M⁻¹s⁻¹. In the past, this range has

3.1. Introduction

Table 3.1: Table of results for (nearly) thermoneutral reactions studied. Units for ΔH , E_a , and calculated pre-reaction complex binding energy (BE) are kcal mol⁻¹, log A are log M⁻¹s⁻¹, and k are M⁻¹s⁻¹. References to the original literature are included with the Complex ID number. [†]Calculated binding energies involve structures that could not be fully optimized and contain one or more small imaginary frequencies. Adapted with permission from Reference 38. Copyright (2005) American Chemical Society.

ID	RO [•] /R'O [•]	ROH	ΔH	log A	E_a	k	BE
1 ⁴²			0.0	3.7	1.2	3.3×10^2	-10.8
2 ¹²⁹			-2.0	3.8	3.8	10	-14.8
3 ⁴²			0.0	5.1	3.5	3.3×10^2	-10.1 [†]
4 ^{130,131}			4.2	5.5	4.8	93	-10.0 [†]
5 ¹³²			-7.0	4.2	0.5	7×10^3	-6.5
6 ⁴²			0.0	>7	-	$>10^7$	-13.6 [†]
7 ¹³³			-2.2	8.3	2.3	4×10^6	-8.6
8 ¹³⁴			0.3	7.2	5.2	3×10^3	-5.5 [†]
9 ¹³⁴			-1.9	6.4	2.6	3×10^4	-5.6 [†]
10 ¹³⁵			1.4	6.0	4.5	7×10^2	-8.0 [†]

been attributed to steric shielding around the oxygen atoms, resulting in a larger entropic barriers.³⁸ Importantly, it was noted that the degree of steric shielding on the oxygen atom appears to play an important role in the order of the A-factor;

3.1. Introduction

systems with greater bulk have lower A-factors, while non-shielded systems have larger A-factors.

Stereo-electronic effects are known to play an important role in HAT, and have been studied extensively.^{40,140–146} Although the abstraction of a specific hydrogen atom may be more thermodynamically favourable than others on a given substrate, if it is not accessible due to steric constraints, abstraction will not occur at this site. Otherwise, additional steric bulk can lead to significant reductions in reactivity, through destabilization of the TS complex, or by forcing additional processes involving conformational changes in order to reach the appropriate TS structure. For example, in reactions of tertiary acetamides with CumO[•],¹⁴⁶ where abstraction occurs mainly from C–H bonds α to the nitrogen atom, a two-fold decrease in the rate constant (normalized for the number of equivalent hydrogen atoms) is observed in going from *N,N*-dimethylacetamide to *N,N*-diisobutylacetamide ($k_H = 2.0 \times 10^5$ and $7.8 \times 10^4 \text{ M}^{-1}\text{s}^{-1}$, respectively). The decrease in rate constant is attributed to the steric clash between the methyl groups of CumO[•] and the isobutyl groups of *N,N*-diisobutylacetamide.

As all of the reactions in Table 3.1 are nearly thermoneutral, thermochemical effects on the rates of reaction are expected to be minimal. Therefore, the large degree of variance in their rate constants (k) is somewhat surprising. These reactions are closely related to the self-exchange reaction between phenol and phenoxyl,²³ in which a strong molecule-radical pre-reaction complex akin to those listed in Table 3.1 is formed, ca. 10 kcal mol⁻¹ below the separated reactants. It is therefore expected that most, if not all, of the systems in Table 3.1 should exhibit a similar molecule-radical complex; granted, the strength of the interaction will vary because of steric repulsion. As such, it is plausible that the strength of this interaction may directly influence the rate of formal hydrogen atom transfer.

3.2. Computational methods and details

Currently, there has been no comprehensive investigation of the relationship between the pre-reaction complex and the kinetics of a reaction. On the basis of the reaction data in Table 3.1, we ask the question: *Do A-factors have a correlation with non-covalent binding energies of the pre-reaction complex?* This is a reasonable question as non-covalent binding and steric hinderance represent a loss of degrees of freedom and therefore entropy,ⁱ which ultimately determines the A-factor magnitude. If the answer to the question is yes, then non-covalent binding may be useful as a diagnostic for the “looseness” or “tightness” of a TS complex, in addition to providing an important link between theory and experiment.

3.2 Computational methods and details

Density-functional theory (DFT) calculations were carried out using the Gaussian-09 software package.¹¹⁶ Care was taken to obtain minimum energy structures through detailed conformational analysis. For this, the BLYP density-functional^{102,147} was utilized, paired with the empirical D3 dispersion correction¹⁰⁹ with the recommended Becke-Johnson damping functions,¹¹⁰ as well as our groups’ own basis set incompleteness potentials (BSIPs),¹⁴⁸ and minimal MINIs basis sets.¹⁴⁹ The use of minimal basis sets corrected for basis set incompleteness allows DFT-based methods to be used efficiently in performing a large number of calculations. Minimum energy conformers of the monomers (substrates and radicals) were first obtained by manual manipulation of the necessary dihedral bond angles, followed by geometry optimization and vibrational analysis.

The lowest energy radicals and substrates were combined to generate the appropriate pre-reaction complexes. These pre-reaction complexes were subject to confor-

ⁱRecall from Equation 2.95 that the A-factor can be related to TST such that the primary variable is entropy ($\Delta^\ddagger S^\circ$).

3.2. Computational methods and details

mational analysis using the same BLYP-D3(BJ)-BSIP/MINIs method. Geometries were initially manipulated by hand. It became apparent that manual manipulation resulted in an unsatisfactory exploration of the conformational space. To solve this, all the necessary dihedral angles were scanned systematically using a combination of scripts.¹⁵⁰ All manipulated geometries were subject to optimization. For each complex, the top 5–10 complex geometries were subject to further optimization using a higher level of theory (BLYP-D3(BJ)-BSIP/pc-1) to obtain the final minimum energy pre-reaction complex structures. Due to the free rotation of groups such as *t*-butyl and methyl, some of the optimized pre-reaction complex structures contain small imaginary frequencies, and thus do not represent proper stationary states. Several measures were taken to resolve this; no resolution was obtained in many cases. Regardless, the complexes adequately represent the pre-reaction complex and differences in “true” binding energies can likely be ignored.

To obtain accurate pre-reaction complex binding energies, the substrates and complexes were subject to single-point energy calculations using the LC- ω PBE long-range corrected density functional^{151,152} with D3(BJ) dispersion corrections and pc-2 basis sets with *f*-type basis functions removed (pc-2-spd).¹⁵³ This method was selected on the recommendation of work by Johnson et al.¹⁵³, which demonstrated the accuracy of this method for the calculation of NCIs. On the basis of the reported mean absolute error in Reference 153 for the S66 benchmark set of sixty-six different non-covalently interacting dimers,¹⁵⁴ the calculated binding energies reported herein from the LC- ω PBE-D3(BJ)/pc-2-spd level of theory carry an estimated 0.2 kcal mol⁻¹ margin of error.

3.3 Results and discussion

The theoretically determined electronic binding energies calculated for the lowest energy pre-reaction complex of each system are listed in Table 3.1. The logarithm of A-factor against binding energy was plotted, as shown in Figure 3.1. The overall correlation is quite poor ($R^2 = 0.33$), however much of the data is grouped about a single, well correlated line ($R^2 = 0.95$). The intercept of the fitted line that corresponds to zero binding energy is 8.63, a value that is in line with what has been cited as the expected A-factor for HAT reactions, *viz.* $10^{8.5 \pm 0.5} \text{ M}^{-1}\text{s}^{-1}$.¹⁵⁵ These results suggest that the observed correlation is genuine, that is, NCIs may have an impact on A-factors. I shall demonstrate that the data that do not correlate are reasonable outliers. In fact, using simple rationale I shall demonstrate that different regimes of steric bulk results in different mechanistic processes leading to the TS complex.

In order to understand the deviations from the expected linear trend of A-factor against pre-reaction complex binding energies, it is important to consider the specific reaction mechanisms taking place. Recall from Chapter 1 that we are focussed on two important possible reaction mechanisms, namely direct HAT and PCET.

For direct HAT to occur, the SOMO of the radical must overlap with the O-H σ^* anti-bonding orbital. In the case of hydrogen abstraction from a phenolic compound, this may require the rotation of the hydrogen atom donating hydroxyl group out of the plane. The rotation of a phenolic hydroxyl group has an energy barrier that follows a $\cos^2 \theta$ relationship.¹⁵⁶ As a reference point, the rotational barrier of phenol¹⁵⁷ is 3.1 kcal mol⁻¹, thus sterically hindered phenols may have a greater rotational barrier. For a PCET mechanism to occur, there are two possible geometries: The nominally singly-occupied O 2p-orbital of the radical can overlap with the corresponding oxygen LP 2p-orbital, as seen in the work of Mayer et al.²³. Alterna-

3.3. Results and discussion

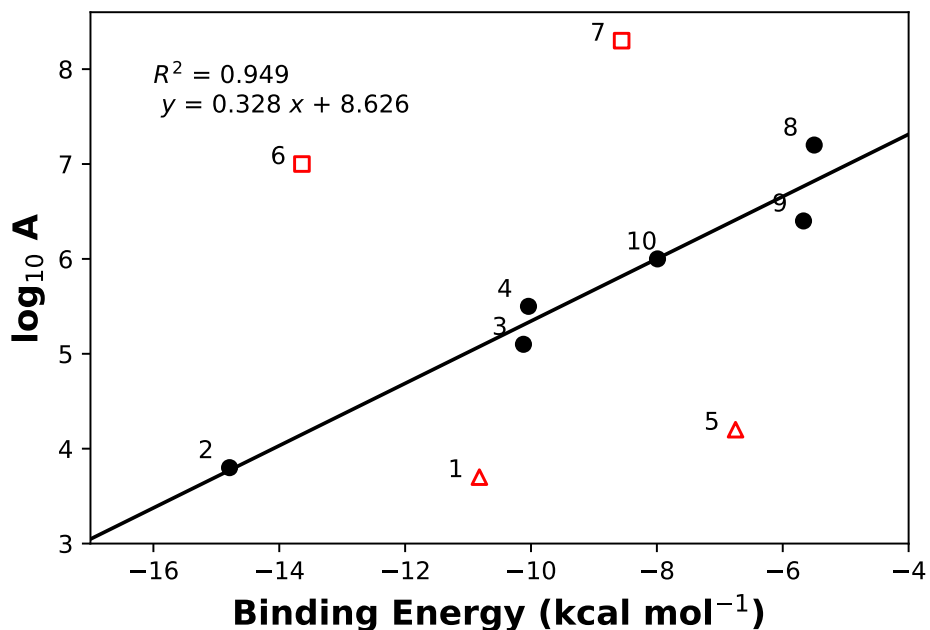


Figure 3.1: Plot of logarithm of A-factor against binding energy. Only the black points were included in the line fitting (slope = 0.328 kcal mol⁻¹, intercept = 8.626 kcal mol⁻¹, and $R^2 = 0.949$). Red points with open faced markers indicate outliers, *vide infra*. The inclusion of complexes 1, 5, and 7 result in an $R^2=0.334$. Complex 6 is always omitted from line fitting as the experimental A-factor is approximate.

3.3. Results and discussion

tively, a LP- π , LP-LP, or π - π bonding overlap between the radical and substrate can occur, as seen in the work of DiLabio and Ingold³⁸, and DiLabio and Johnson²⁶.

As described in Chapter 1, there remains no clear physical criteria to distinguish direct HAT from PCET, a topic of active discussion in the literature.^{22–32} One possible solution is consider the existence of these mechanisms on a continuum; the rate constant (and thus A-factor) for formal HAT (k_{HAT}) can be described as a combination of the rate constants direct HAT (k_{direct}) and PCET (k_{PCET}) mechanisms, i.e.:

$$k_{HAT} = k_{direct} + k_{PCET} \quad (3.3)$$

Before elaborating on Equation 3.3, we must first discuss the role of the pre-reaction complexes in formal HAT reactions. As a radical and substrate approach sufficient proximity for a reaction to take place, NCIs lead to the formation of a weakly-bound complex. If this complex has the appropriate geometry for a hydrogen transfer to occur, it is considered a pre-reaction complex, otherwise it is considered an initial encounter complex. An initial encounter complex must pass over an additional energy barrier to reach the appropriate pre-reaction complex. With respect to the species in Table 3.1, the complexes formed involve various degrees of π - π , LP- π , and LP-LP interactions, which contribute to the weakly attractive, dispersion interactions. Furthermore, these same orbital interactions in the TS complex can lead to the formation of an additional electronic channel, enabling contributions of a PCET mechanism to the overall mechanism.^{26,38} Returning now to Equation 3.3, the different types of orbital interactions may control the contributions of k_{PCET} to the overall rate constants. Our hypothesis, which cannot be tested until a quantitative diagnostic for PCET vs HAT is developed, is that π - π interactions contribute to a PCET dominated mechanism ($k_{HAT} \approx k_{PCET}$). On the other hand, LP-LP

3.3. Results and discussion

interactions are weaker and thus PCET of this nature contributes only weakly to the overall mechanism.

While the data herein explore only the geometries of the pre-reaction complexes involved in the hydrogen transfer reactions, the presumptive TS structures will have similar structures and more importantly, orbital interactions. Therefore, by considering the similarities between pre-reaction and TS complexes, it is possible to rationalize the deviations from the observed trendline in Figure 3.1.

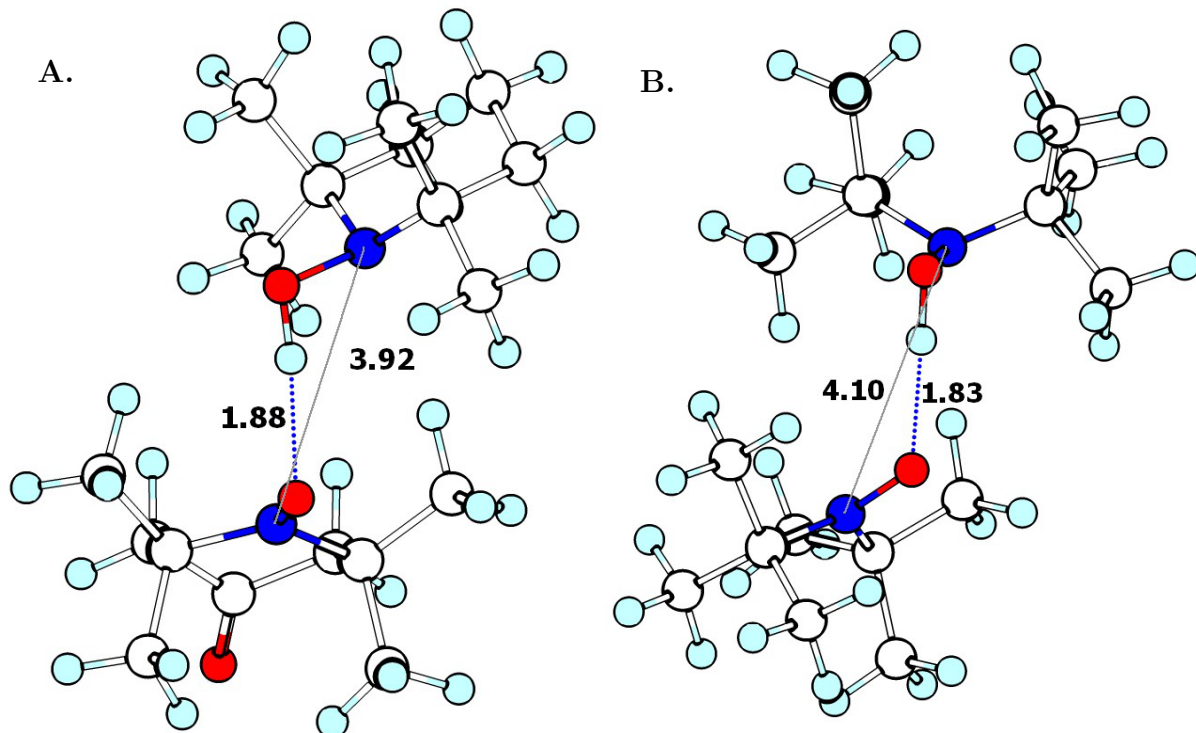


Figure 3.2: Three-dimensional structures of **A** complex 2 (TEMPO-H and 4-oxo-TEMPO) and **B** complex 3 (di-*t*-butyl-hydroxylamine and di-*t*-butyl-nitroxyl). Bond distances are shown in units of Å. The elements are coloured as white for carbon, light blue for hydrogen, red for oxygen, and blue for nitrogen.

I shall begin by examining the points that fall on the expected line, complexes 2–4 and 8–10. The examination of all these pre-reaction complexes reveals that an additional rearrangement that has a moderate energetic barrier is required in order

3.3. Results and discussion

for the hydrogen transfer to proceed. Complexes 2 and 3 are shown in Figure 3.2, and are very similar in structure. Both are hydroxylamine-nitroxyl couples with similar degrees of steric bulk adjacent to the reacting centres. The *t*-butyl groups of 3, and the methyl groups of 2 (the NO-ON dihedral angles are 65° and 68°, respectively) prevent the overlap of the N LP orbitals in of the NO-H-ON frameworks to allow for PCET. Thus, while the presumptive TS structure may have some degree of LP-LP orbital interaction, the overall mechanism is dominated by direct HAT.

In the most stable stacked conformation, complex 4, as seen in Figure 3.3, steric clash of the para-position *t*-butyl groups obstructs π-π overlap between the aromatic rings. It is likely that this steric clash does not allow any significant orbital interaction, suggesting that the reaction is dominated by direct HAT. In order to react via direct HAT, the hydroxyl group must rotate farther out of the aromatic plane, or the bulky para-position *t*-butyl groups must come into close proximity. Alternatively, an open conformation for complex 4 is possible, which lies ca. 2 kcal mol⁻¹ higher in energy than the stacked complex, a result that is also consistent with the observed trend-line. From the open conformation, PCET is still not possible due to the steric bulk of the ortho-position *t*-butyl groups of the radical, thus this reaction likely also proceeds through a direct HAT mechanism. For complex 4, steric clash prevents π-π orbital intactions, therefore the reaction proceeds through a direct HAT dominated mechanism.

Complexes 8 and 9 are similar systems, in which *t*-BuOO[•] reacts with unhindered phenolic substrates. As seen by the structures in Figure 3.4, the bound complexes are somewhat dissimilar. The hydroxyl group of complex 8 is rotated out of the plane 24°, while in complex 9 the hydroxyl group lies entirely in the plane. It is likely that the larger aromatic system of 2-naphthol results in a larger OH rotational barrier. Therefore, the most favourable conformation for this complex places

3.3. Results and discussion

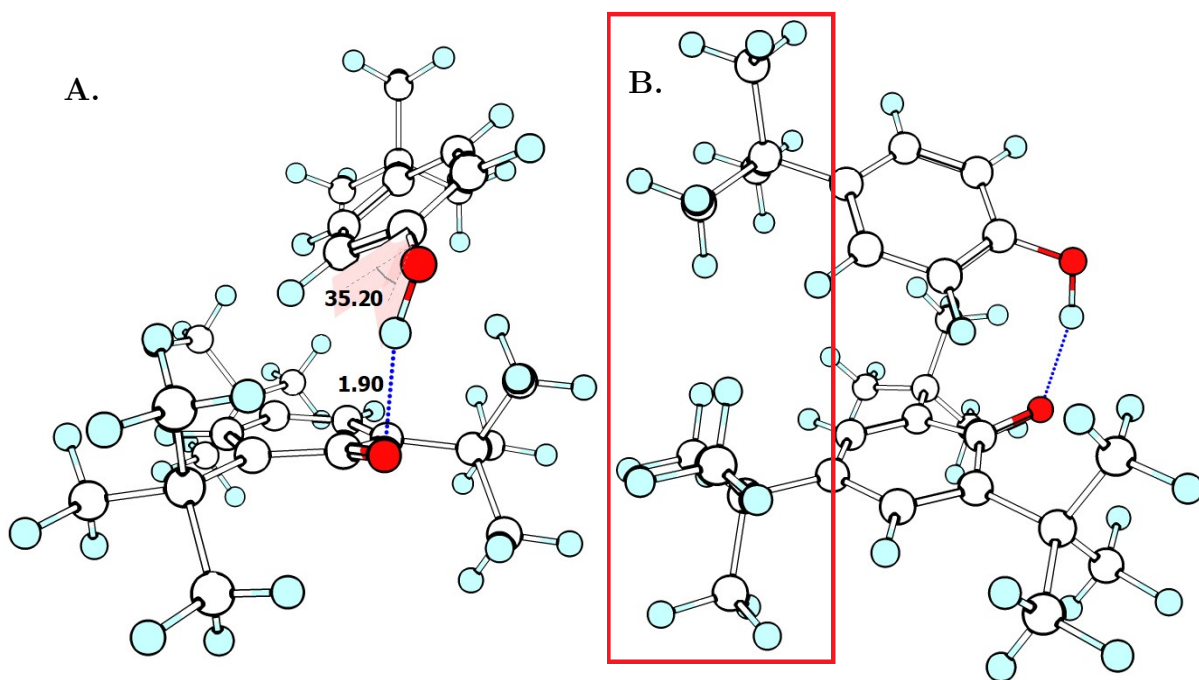


Figure 3.3: Three-dimensional structure of pre-reaction complex 4 between 2,4,6-tri-*t*-butylphenol and 4-*t*-butylphenoxyl. **A** demonstrates the hydrogen bond distances in units of Å, and the out-of-plane rotation by 35.2° of the phenolic hydroxyl group. **B** demonstrates the steric clash (highlighted by red box) between the para-position *t*-butyl groups. The elements are coloured as white for carbon, light blue for hydrogen, and red for oxygen.

3.3. Results and discussion

the phenolic hydroxyl group entirely in the plane. In complex 9, there is also a weak hydrogen bond between the C–H bond in the ortho-position and the non-radical O-centre of *t*–BuOO[•], contributing further to the stabilization of the planar conformation. Complex 8 was previously studied by DiLabio and Johnson²⁶, where it was demonstrated that a partial bonding interaction exists between the peroxyLP and phenolic π -system in the TS complex. However, this interaction is likely weak and thus contributes weakly to the overall rate constant. That is, k_{HAT} is dominated by k_{direct} . Also, although the pre-reaction complexes are somewhat dissimilar, the conformational changes necessary to reach the TS complex, similar to that reported in reference 26, are likely not dramatically different in terms of energetic barriers. Any small differences result in noise in the observed trend.

Complex 10, shown in Figure 3.5 is unique in that it is the only reaction between a peroxide and a peroxy radical. Therefore, this system represents the best case scenario for LP-LP overlap to occur. The self-exchange reaction between HOO[•] and HOOH can be considered the simplest reference for the reaction of α -tetralin peroxide with *t*-butylperoxyl. To the best of my knowledge, the mechanism of the hydroperoxyhydrogen peroxide couple has not been characterized as either PCET or direct HAT previously in the literature, although the TS structure has been previously reported.¹⁵⁸ Using this structure, calculations reveal a LP-LP interaction leading to partial bonding in the TS, i.e. a PCET mechanism. (See Appendix A, Figure A.1). The hydroperoxyhydrogen peroxide couple contains a H–O–O–H dihedral angle of 90°, so that the two non-reacting hydrogen atoms oriented 180° away from one another. Orienting substituents directly away from one another is likely the most stable TS structure for all peroxy-peroxide formal HAT reactions.

The orientation of *t*-butylperoxyl and α -tetralin peroxide at exactly 180° away from one another is unfavourable in complex 10, due to steric clash. Nonetheless,

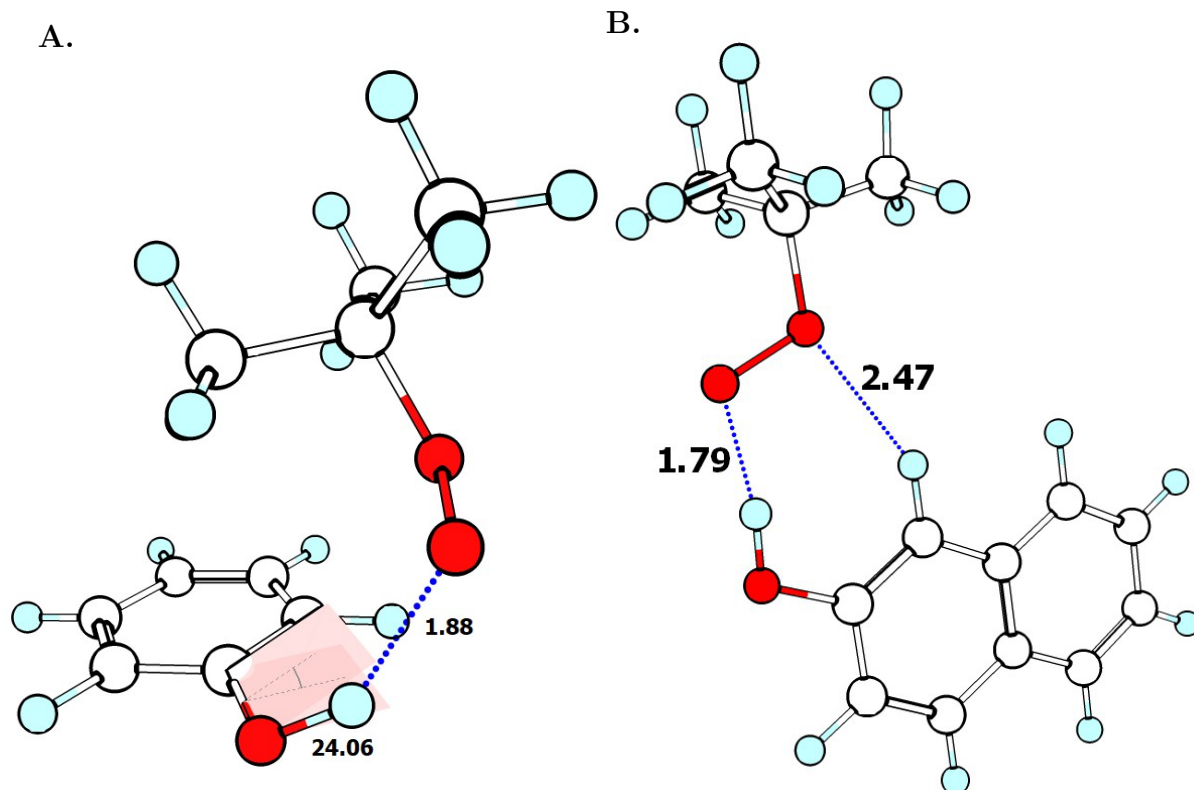


Figure 3.4: Three-dimensional structures of pre-reaction **A** complex 8 (*t*-butylperoxy and phenol) and **B** complex 9 (*t*-butylperoxy and 2-naphthol). Bond distances are shown in units of Å. Complex 8 has an out of plane rotation of the phenolic hydroxyl group of 24.1° . The elements are coloured as white for carbon, light blue for hydrogen, and red for oxygen.

3.3. Results and discussion

there may still be some LP-LP overlap contributing to a weak k_{PCET} contribution to k_{HAT} . On the basis of our hypothesis, LP-LP interactions do not allow for PCET to contribute strongly to the overall mechanism. This will require additional investigation. For complex 10, k_{HAT} is dominated by k_{direct} .

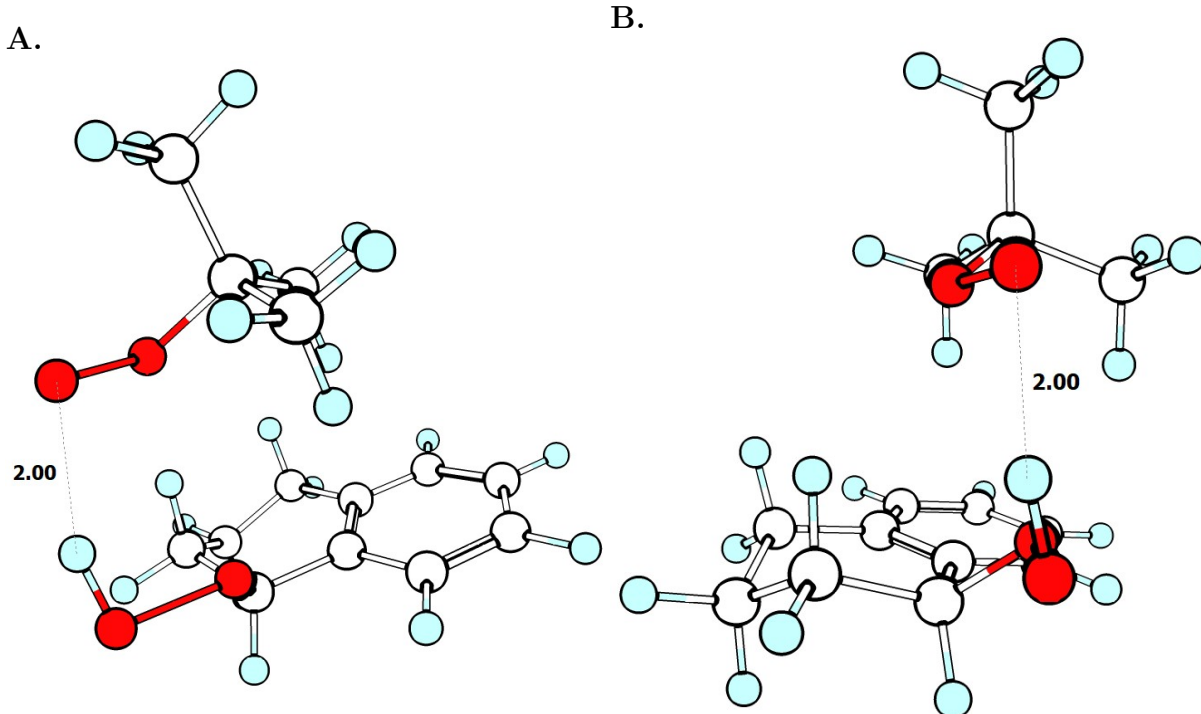


Figure 3.5: Three-dimensional structure of pre-reaction complex 10 between *t*-butylperoxy and α -tetralin peroxide. **A** demonstrates the hydrogen bond distances in units of Å. **B** demonstrates the likely steric clash preventing strong LP-LP overlap. The elements are coloured as white for carbon, light blue for hydrogen, and red for oxygen.

Once again, complexes 2–4 and 8–10 follow the observed trend. In all cases, these complexes may have some PCET contribution to k_{HAT} through either LP- π or LP-LP orbital overlap. Interpretation of Figure 3.1 in this manner allows for two possible explanations. The simplest is that all these complexes proceed through a mechanism in which $k_{HAT} \approx k_{direct}$ ($k_{PCET} \ll k_{direct}$). In this case, the A-factor is a direct reflection of k_{HAT} and this the pre-reaction complex binding energy correlates

3.3. Results and discussion

well with the A-factor.

Alternatively, there may be increasing contributions of PCET leading to an increase in the A-factor. This effect can be rationalized on the basis of a stronger interaction in the case of LP- π overlap, as compared to LP-LP overlap. Within this framework, complexes 2, 3, and 4 may have little or no overlap due to steric clashing, and complexes 8 and 9 have a higher A-factor than complex 10 due to LP- π vs. LP-LP overlap. Further work is necessary to discern this effect.

Consider next the points that sit above the trendline, complexes 6 and 7, shown in Figure 3.6 and Figure 3.7. The A-factor for complex 6 is approximate and thus does not get factored into the line fitting. In both cases, the non-covalently bound complexes are in a slipped-parallel π -stacked conformation, allowing for π - π orbital overlap. Complex 7 in particular is very similar to the phenol-phenoxy couple, except with 2-naphthol instead of phenol. In both cases, the π -stacked pre-reaction complex is very close to the presumptive TS structure. Therefore, it is possible to infer that both of these reactions take place through mechanism in which k_{PCET} is dominant. The key difference from the points that fall on the trendline is that $k_{HAT} \approx k_{PCET}$.

Lastly, consider the points that fall below the trendline, complexes 1 and 5. In both cases, a high degree of steric repulsion likely does not allow for a PCET mechanism through orbital overlap. It is important to study the “encounter complex” that represents the first pre-reaction complex, i.e. prior to any reorganization, as this will be the complex that affects the A-factor with regards to simple collision theory. Complex 1 is the self-exchange reaction between the very bulky 2,4,6-tri-*t*-butylphenol/2,4,6-tri-*t*-butylphenoxy couple, as seen in Figure 3.8 A. As a result of steric shielding around the reaction centres, the encounter complex is stacked to maximize dispersion interactions, but does not have a hydrogen bond. Therefore,

3.3. Results and discussion

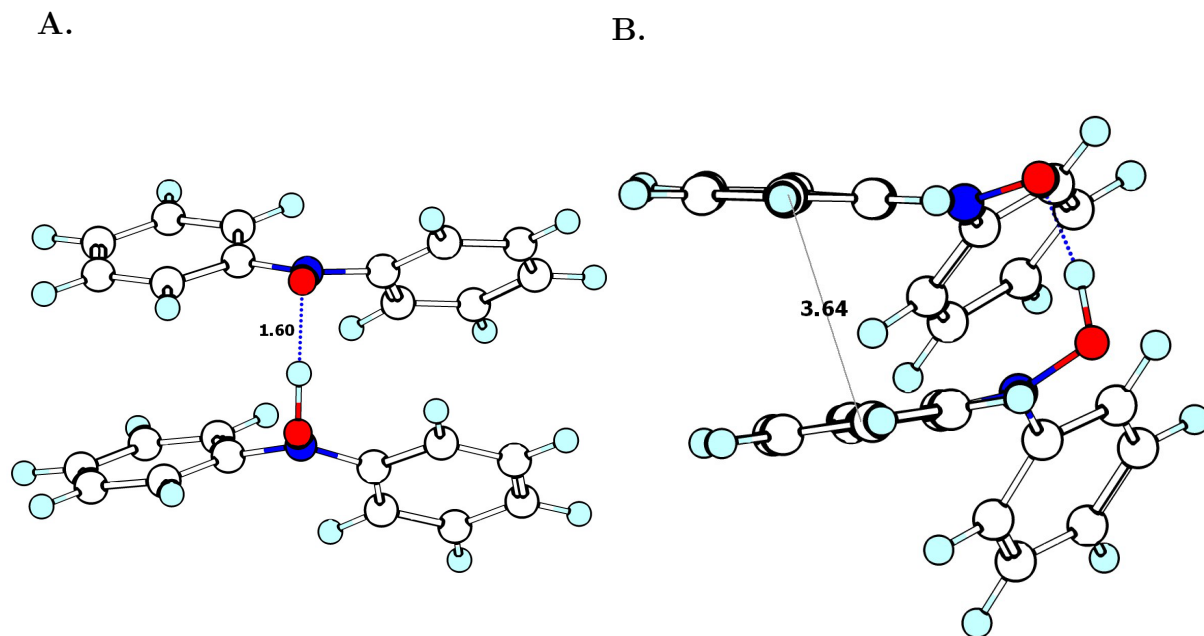


Figure 3.6: Three-dimensional structures of pre-reaction complex 6 between *N,N*-diphenylhydroxylamine and *N,N*-diphenylnitroxyl. **A** demonstrates the hydrogen bonding interaction while **B** demonstrates the $\pi\text{-}\pi$ interaction. Distances in unit of Å and angles are shown in degrees. The elements are coloured as white for carbon, light blue for hydrogen, blue for nitrogen, and red for oxygen.

3.3. Results and discussion

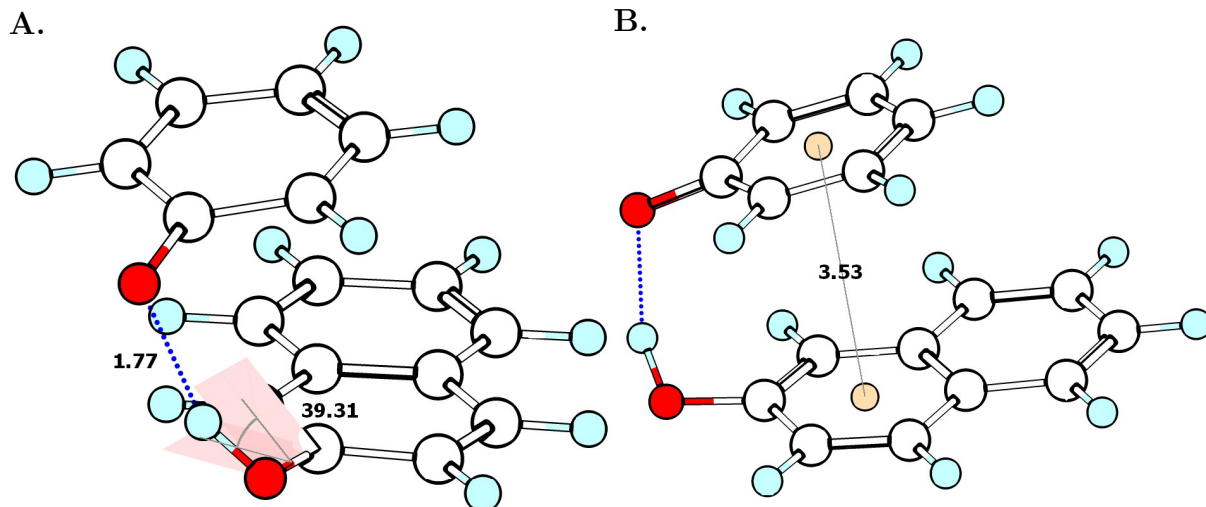


Figure 3.7: Three-dimensional structures of pre-reaction complex 7 between 2-naphthol and phenoxy. **A** demonstrates the hydrogen bonding interaction while **B** demonstrates the π - π interaction. Distances in unit of Å and angles are shown in degrees. The elements are coloured as white for carbon, light blue for hydrogen, and red for oxygen.

an additional rearrangement is required in order to get to the presumptive TS structure. That is, there must be a higher-energy hydrogen-bonded pre-reaction complex that leads to the direct HAT mechanism. Note however, that there is a barrier to rotation of the hydroxyl group to 90° out of the plane for direct HAT to occur.

Complex 5 is the 2,4,6-tri-*t*-butylphenol/*t*-butylperoxy reaction couple. The encounter pre-reaction complex also does not contain a hydrogen bond. As with complex 1, an encounter complex without a hydrogen bond must form first. However, in complex 5 there is less steric clashing. As a result the formation of a hydrogen bond is favourable and the “true” pre-reaction complex is about 0.7 kcal mol⁻¹ more stable than the encounter complex. In contrast, for complex 1 the true pre-reaction complex is about 0.6 kcal mol⁻¹ less stable than the encounter complex. Note also that there is a barrier to rotationⁱⁱ of the hydroxyl group that can be estimated as about 4.1 kcal mol⁻¹. This is illustrated schematically in Figure 3.9.

ⁱⁱCalculated as the difference in energy between the in-plane and out-of-plane structures of 2,4,6-

3.3. Results and discussion

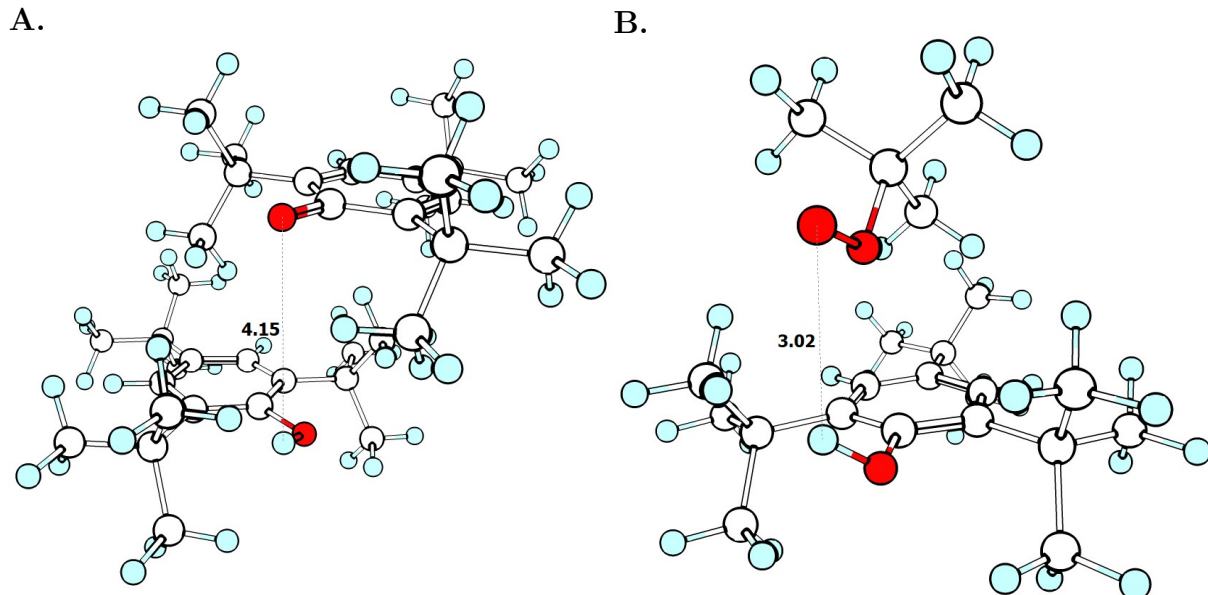


Figure 3.8: Three-dimensional structures of pre-reaction **A** complex 1 (2,4,6-tri-*t*-butylphenoxy and 2,4,6-tri-*t*-butylphenoxy) and **B** complex 5 (2,4,6-tri-*t*-butylphenol and *t*-butylperoxy). Distances in unit of Å and angles are shown in degrees. The elements are coloured as white for carbon, light blue for hydrogen, and red for oxygen.

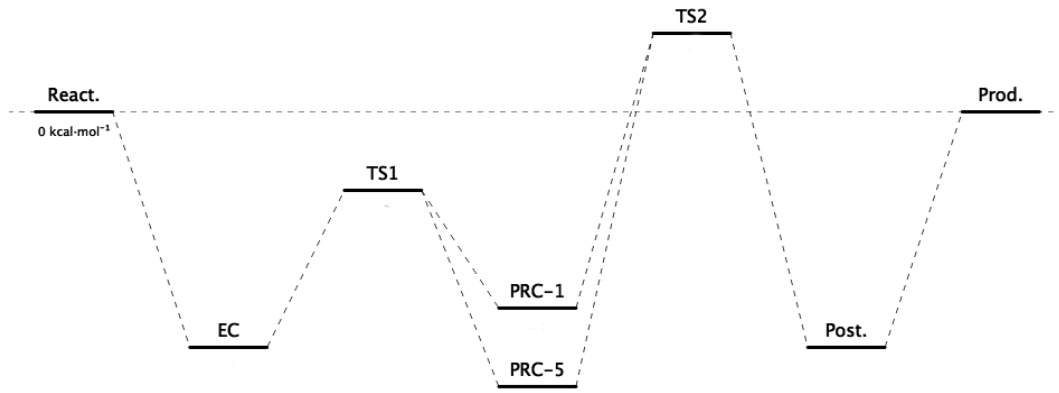


Figure 3.9: Reaction coordinate qualitatively illustrating the proposed mechanism for HAT in complexes 1 and 5. React. = reactants, EC = encounter complex, PRC-1/5. = true pre-reaction complex 1/5, TS1 = transition state associated with out-of-plane rotation of the OH group, TS2 = (presumptive) TS associated with HAT, Post. = post-reaction complex, Prod. = products.

3.4. Summary

For both complex 1 and 5, steric clashing prevents significant π - π overlap or LP- π overlap. Therefore, the reactions likely proceed through a direct HAT dominated mechanism ($k_{HAT} \approx k_{direct}$). One might then expect these data to fall on the trendline, however the formation of an encounter complex that does not lead directly to HAT results in a different overall process from the other complexes. As a result of the necessary initial process complex 1 and 5 have lower A-factors as fewer collisions are likely to lead to successful formal HAT.

3.4 Summary

In this investigation, a series of thermoneutral or nearly thermoneutral HAT reactions were considered. I have plotted the logarithm of experimentally determined A-factors against the theoretically determined electronic binding energies. These results demonstrate that the A-factors for (nearly) thermoneutral HAT reactions correlate to some extent with the pre-reaction complex binding energies, given that the reactions proceed through similar mechanisms and energetically similar pathways. The results herein can be sorted into three bins by considering the contributions of k_{direct} and k_{PCET} to the overall transformation, k_{HAT} :

1. Complexes that have weak k_{PCET} contributions due to either LP-LP or LP- π orbital overlap, and are therefore dominated by k_{direct} . This is the case for the data that fall on the trendline.
2. Complexes in which k_{PCET} is the dominant contribution to k_{HAT} , as is the case for complexes 6 and 7.
3. Complexes in which the encounter complex does not lead directly to the HAT TS complex, as was the case for complexes 1 and 5.

tri-*t*-butylphenol at the LC- ω PBE-D3/6-311+G(2d,2p) level of theory.

3.4. Summary

These results indicate that different regimes of electronic and steric interactions lead to different chemical processes in seemingly similar reactions. As a result, non-covalent binding can be used as a metric for kinetics parameters, however, it cannot describe in full the entropic factors that contribute to the A-factor. One must first consider the mechanistic details in which formal HAT occurs.

Additional work is necessary to extend these results. In particular, the main question that remains is whether π - π PCET is “better” than other forms of orbital overlap. To answer this a larger sample of data points, and a diagnostic for PCET must be used. Regardless, the results herein represent a novel attempt to link theory and experiment. Given that obtaining the full PES for large molecules is currently computationally impractical, these results serve as a seed for developing a fundamental understanding of complex formal HAT reactions.

Chapter 4

Interrogation of the Bell-Evans-Polanyi Principle: Investigation of the Bond Dissociation Enthalpies Correlated with Hydrogen Atom Transfer Rate Constants

4.1 Introduction

The Bell-Evans-Polanyi (BEP) principle is a conceptual framework that states, for two closely related reactions, the difference in activation energy is proportional to the difference in their enthalpies of reaction.^{47,48,159} This is commonly expressed as the linear free energy relationship (LFER): $E_a = E_0 + \alpha\Delta H$ (Equation 1.1). Initially, the BEP principle was used as a simple model to explain the Brønsted catalysis law, which states that the stronger an acid is, the faster the catalyzed reaction will proceed.¹⁶⁰ A key assumption associated with the BEP principle is that the position of the TS along the reaction coordinate is the same for all reactions. The relationship is described schematically in Figure 4.1: the more stable the product, the lower the reaction barrier.

A modern utilization of the BEP principle is to estimate rate constants of related reactions. The main purpose of LFERs is to apply understanding of known systems to new systems in order to develop novel chemical insight. For example, much

4.1. Introduction

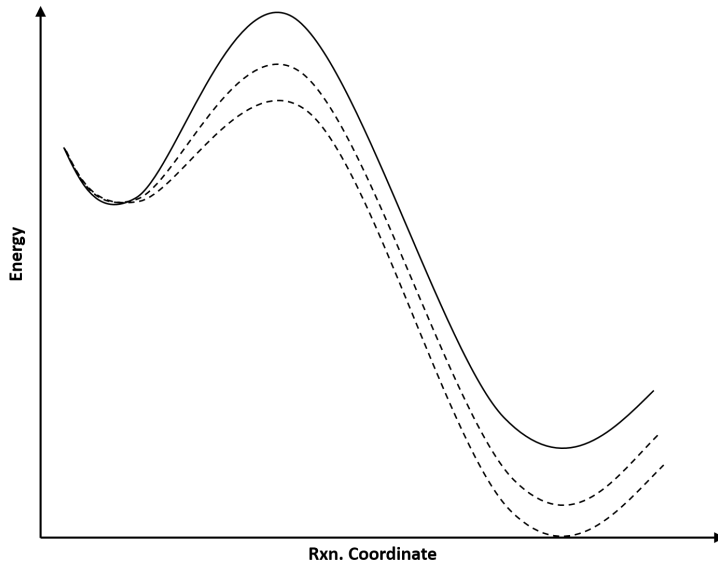


Figure 4.1: Energy profiles for a series of related exothermic reactions illustrating the Bell-Evans-Polanyi principle.

of our groups' work focuses on studying simple protein models. By thoroughly investigating small systems with ab initio approaches, it is possible to extrapolate the fundamental concepts to large-scale systems. Furthermore, if one can establish that there exists a LFER between activation energy and bond strength for a specific model, then the difference in bond dissociation enthalpy (BDE) can be used to estimate HAT reaction rates in a large-scale protein system.

The application of the BEP principle in HAT reactions, utilizes the relationship between the logarithm of the rate constant (k_H) and the BDEs: $\log(k_H) = \alpha\Delta H + \text{constant}$. For HAT reactions involving abstraction by CumO $^\bullet$, the enthalpy of reaction (ΔH) is directly related to the strength of the breaking bond: $\Delta H = \text{BDE}(\text{C}-\text{H}) - \text{BDE}(\text{CumO}-\text{H})$. If the relationship holds for a series of related HAT reactions, then BDEs should correlate with the activation energy (Equation 1.1). It would then stand to reason that an increase in bond strength represents a destabilization in the TS complex, and thus a decrease in reaction rate. This concept

4.1. Introduction

is also important for the work in Chapter 5, where the interaction of non-redox active metal cations results in an increase in effective bond strength, and decrease in rate constant. It is also important to note that if the BEP principle breaks down for reactions that appear related, then additional physico-chemical factors, such as non-covalent binding (*viz.* Chapter 3), or stereo-electronics may be influencing the reaction barrier.

An interesting application of the BEP principle is the work of Pratt et al.¹⁶¹, in which the free radical oxidation of unsaturated lipids was examined. They studied the correlation of theoretically determined allylic or benzylic C–H and C–OO[•] bond strengths with experimentally-measured HAT rate constants and O₂ addition rate constants, respectively. BEP plots (log k vs. BDE) for a large range of polyunsaturated fatty acid models show good correlation ($R^2 = 0.92$) for C–OO[•] bonds examined, and reasonable correlation ($R^2 = 0.82$) for C–H bonds. This demonstrates that factors which affect BDEs also affect reaction barrier height, in line with the BEP principle. Additionally, these results provide the ability to predict rate constants for HAT and oxygen addition reactions related to unsaturated lipid models, by means of calculating BDEs. Another area of research in which the BEP principle is often applied is heterogenous catalysis.¹⁶²

There is a significant gap in the literature on the BEP principle: there are no criteria for how broadly the BEP principle can be utilized. In fact, the theoretical validity of the BEP relationship has come into question, and a call has been made to theoreticians for a detailed analysis of the BEP principle.¹⁶³ In this work, I explore the relationship between BDEs and log(k_H). In order to achieve this, I have studied HAT reactions involving the abstraction of C–H bonds by CumO[•] under the same experimental conditions, for which many rate constants have been published.^{140,141,143,144,164–167} Additional unpublished rate constants have been provided

4.1. Introduction

by our experimental colleagues in Rome. The substrates of interest are diverse in nature and include branched and cyclic alkanes, linear and cyclic amines and ethers, and substrates with allylic or benzylic C–H bonds. The BDEs for these substrates range from \sim 76–100 kcal mol $^{-1}$. The experimentally determined rate constants are listed in Appendix B, Table B.1.

The above studies, as well as many others, have used CumO $^{\cdot}$ and the closely related *t*-butoxyl radical (*t*-BuO $^{\cdot}$) as models for reactive oxygen-centred radicals in studying oxidative damage of biological macromolecules,^{168–170} as well as in studying the mechanism and efficiency of antioxidants.^{171–175} Using these radicals to study biomolecular oxidation has an important caveat: The fundamental chemistry of these radicals is less well understood than is often assumed.^{40,41,176}

The BDE of CumO–H is 106.7 kcal mol $^{-1}$, a value that is larger than all the C–H bonds studied herein.¹⁷⁷ Therefore, HAT reactions involving CumO $^{\cdot}$ and the organic substrates of interest are all exothermic on the order of 5–32 kcal mol $^{-1}$. Hammond’s postulate¹⁷⁸ states that the transition states for these HAT reaction should most closely resemble the reactants in structure (i.e. an early TS), and the BEP α values should all be less than 0.5.¹⁷⁹ If the BEP principle holds as a LFER, the substrates should be considered as if the BDEs were controlled by substituent effects. For example, if one considers methane as the reference C–H bond model, the BDE of toluene should reflect the effect of replacing one hydrogen with a phenyl group. This is also the basis for schemes that utilize group additivity to predict molecular heats of formation.¹⁵⁵

Considering this group additivity-like approach, our colleague in Rome, Massimo Bietti, hypothesized that there should exist two general BEP relations for C–H bond: one in which the incipient radical is delocalized into a π -system (benzylic or allylic), and one in which the remaining alkyl radicals are largely localized. Plotting

4.1. Introduction

the experimental rate constants against literature BDEs (Figure 4.2) there appears to be evidence for the two BEP relations.

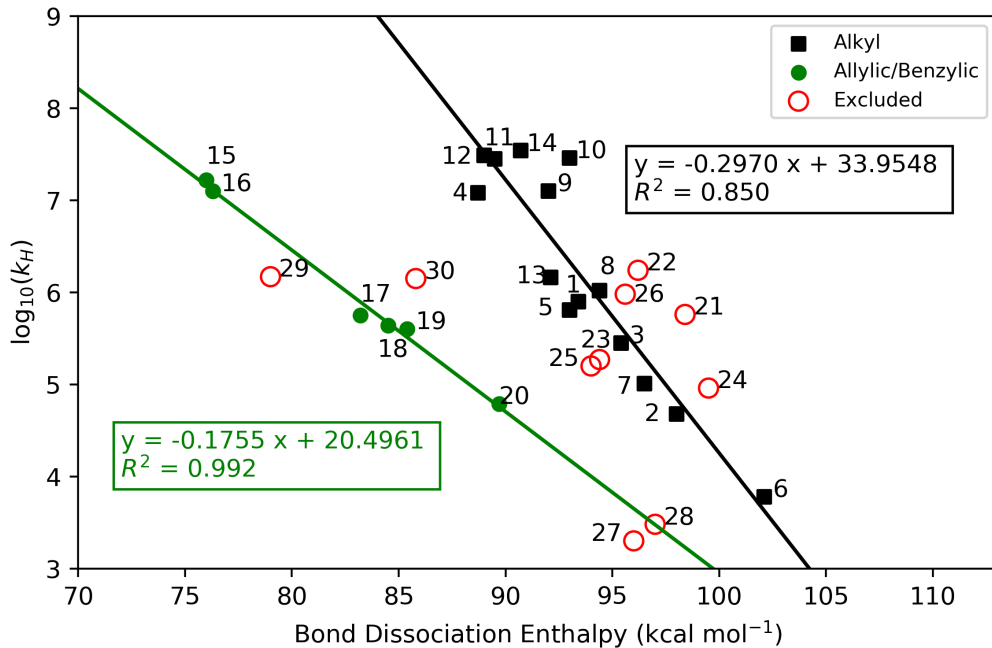
There is a considerable amount of scatter in Figure 4.2, thus possible outliers were excluded from the initial linear-regression analysis. The scatter may be due to differences in experimental procedures in the measurement of BDEs, which were determined using a large number of different experimental techniques. A great deal of data exists in the literature, much of which has conveniently been compiled in the *de facto* reference for BDEs: the *Handbook of Bond Dissociation Energies in Organic Compounds*.¹⁸⁰ However, caution must be taken with experimentally determined BDEs, as not all experimental methods give reliable data. For example, BDEs from the Bordwell¹⁸¹ thermochemical cycle are possibly unreliable.^{144,182} This was demonstrated for the BDE of dimethyl sulfoxide (DMSO), for which the experimentally determined BDE is about 8 kcal mol⁻¹ lower than the best computational estimate.¹⁴⁴ Therefore, quantum chemistry is a useful tool for studying BDEs, as it is relatively simple to compute BDEs. The BDE for an arbitrary X–H bond is given by:

$$\Delta H(BDE) = H(X^\bullet) + H(H^\bullet) - H(X-H) \quad (4.1)$$

where $\Delta H(BDE)$ is the BDE, and the right-hand terms are the enthalpies of the radical product, the hydrogen atom, and the substrate, respectively. By computing the most accurate BDEs possible, we are able to discern if the BEP principle holds for C–H bond hydrogen abstraction by CumO[•].

Many DFT-based methods have been shown to give reasonably reliable relative BDEs, that is, the difference in BDE from a reference molecule (often CH₄).^{183–185} However, highly correlated wave function based methods are required to predict chemically accurate (sub-kcal mol⁻¹) BDEs. For this purpose, we shall use com-

4.1. Introduction



1	1,4-diazobicyclo[2.2.2]octane	2	2,2-dimethylbutane
3	2,2-dimethylbutane	4	Benzaldehyde
5	Diethyl ether	6	Dimethyl sulfoxide
7	Dioxane	8	Hexamethylphosphoramide
9	Morpholine	10	Piperazine
11	Piperidine	12	Pyrroldiine
13	Tetrahydrofuran	14	Triethylamine
15	1,4-cyclohexadiene	16	9,10-dihydroanthracene
17	Cumene	18	Diphenylmethane
19	Ethylbenzen	20	Toluene
21	Adamantane (2°)	22	Adamantane (3°)
23	Cycloheptane	24	Cyclohexane
25	Cyclooctane	26	Cyclopentane
27	Acetone	28	Acetonitrile
29	Benzyl alcohol	30	Dibenzyl ether

Figure 4.2: Bell-Evans-Polanyi plot of experimental rate constants (normalized for the number of equivalent hydrogen atoms) for HAT between CumO[·] and substrates against weakest literature C–H BDEs of the substrates. BDEs for dimethyl sulfoxide and hexamethylphosphoramide are from Ref. 144, while all other BDEs are from Ref. 180. Points 21–26 and 29–30 were excluded from linear regression as possible outliers.

4.2. Methods

posite quantum chemical procedures. Unfortunately, due to the computational cost of some of these procedures, calculations are often limited to small molecules. For instance, Chan and Radom¹⁸⁴ recently published a diverse set of high-level BDEs for small molecules with at most 5 heavy (non-hydrogen) atoms. There is a lack of literature that compares the ability of common composite methods to predict accurate C–H BDEs for relatively large molecules. Therefore, another aim of the work is to determine that composite procedure can be used to calculate accurate BDEs for relatively large molecules.

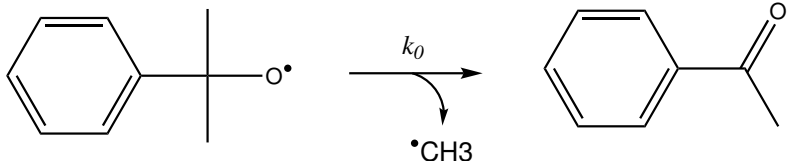
4.2 Methods

Experimental rate constants were either provided from unpublished results from our colleagues in Rome, or come from literature sources.^{140,141,143,144,164–167} All rate constants come from laser flash photolysis (LFP) experiments of CumO[•] with the substrates of interest. Nitrogen or argon saturated acetonitrile solvent and ambient conditions (298 K and 1 atm) were used in all cases. For those results that are unpublished, CumO[•] is generated by laser pulses at either 266 nm or 355 nm in solutions of excess dicumyl peroxide. Many of the literature results are also from the Bietti group, where the same procedure is used. Other results may have small variations in experimental details; all results are well time-resolved.

Observed rate constants (k_{obs}) are generally obtained from 2–8 averaged trials, which are reproducible to within 5%. Transient absorption decay traces of CumO[•] monitored at 485 nm are used to determine k_{obs} . The observed rate constant is plotted against concentration of substrate to provide the bimolecular HAT rate constant (k_H) as the slope ($k_{obs} = k_0 + k_H[\text{substrate}]$). The CumO[•] radical decays unimolecularly through the β -scission of a methyl group, giving acetophenone and a methyl radical, as shown in Scheme 4.1. The unimolecular decay rate constant^{186,187}

4.2. Methods

for CumO[•] (k_0) in acetonitrile is on the order of $6.3 \times 10^5 \text{ s}^{-1}$ at 298 K.



Scheme 4.1: Unimolecular decay of the cumyloxy radical.

All quantum chemical calculations were performed using the Gaussian 09 software package.¹¹⁶ Several composite quantum chemical methods that are implemented in Gaussian 09 were used in this work: W1BD, CBS-QB3 and the restricted open-shell variant ROCBS-QB3, CBS-APNO, G4 and the MP2 variant G4(MP2). An approach using ROCCSD(T) with locally-dense basis sets^{188,189} (LDBS) was also utilized in order to approximate W1BD results. Each of these methods is briefly described below.

4.2.1 Quantum chemical composite procedures

W1BD

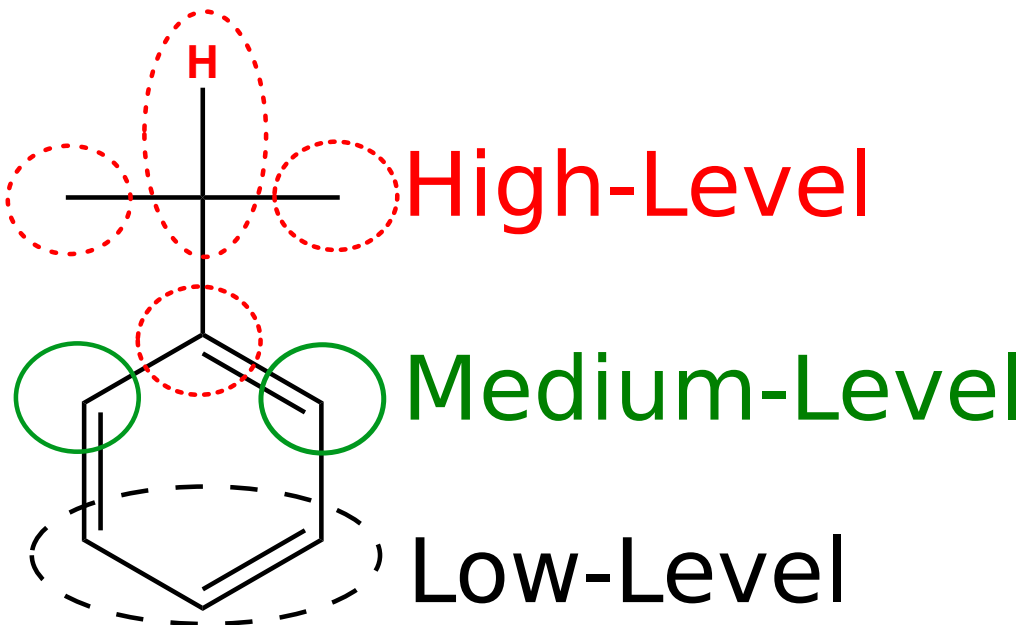
The highest-accuracy method used is W1BD, which employs seven different calculations to obtain highly-correlated electronic energies, as well as thermochemically corrected quantities. This method is very computationally expensive, and thus cannot be applied to the larger species of interest in this work. Geometries and thermochemical corrections come from DFT-based B3LYP calculations with nearly complete cc-pVTZ+d basis sets. A frequency scaling factor of 0.985 is used to obtain thermochemical corrections. The electronic energy comes from several additive corrections involving the Brueckner Doubles⁹⁵ (BD) variation of coupled cluster and large basis sets extrapolated to the complete basis set limit. Corrections for core-electron correlation and relativistic contributions are computed using an

4.2. Methods

uncontracted variant of the cc-pVTZ+2df basis sets, known as MTsmall.¹⁹⁰

LDBS approach

Locally-dense basis sets have been used in the past to calculated BDEs for relatively large molecules.^{188,189,191} The principle behind LDBS is to use large basis sets to treat the atomic centres that are directly involved in the chemistry taking place, and use progressively smaller basis sets for “remote” portions of the molecule, thus taking advantage of error cancellation. We chose a method that best approximates W1BD results for a small subset of molecules. The scheme utilized herein involves geometry optimization and scaled frequency calculations from DFT-based B3LYP/cc-pVTZ+d, as used in the W1BD procedure. Single-point energy calculations are then performed using ROCCSD(T) and an LDBS partitioning scheme we denote as pc-3/3/2/1, demonstrated in Scheme 4.2, using the polarization consistent basis sets.⁶⁷



Scheme 4.2: Locally-dense basis set partitioning used in the calculation of BDEs. The scheme is referred to as pc-3/3/2/1, where for the shown cumene molecule, the centre of C–H cleavage and the immediately adjacent groups are treated with high-level pc-3 basis sets. The next groups are treated with medium-level pc-2 basis sets, and all other atoms/groups are treated with low-level pc-1 basis sets.

CBS methods

The Complete Basis Set (CBS) methods of Petersson and colleagues^{92–94,192} are widely used because of the relatively low computational cost (compared to other composite procedures), and well-established accuracy.^{193,194} CBS-QB3^{92,93} utilizes DFT-based B3LYP optimization and scaled frequencies (factor = 0.990) with modified triple-zeta Pople style basis sets. Electronic energies are obtained by extrapolating medium basis set MP2 single point energy calculations to the complete basis set limit, along with corrections for electron correlation from MP4(SQD) and CCSD(T). Small empirical corrections are added to achieve more accurate results compared to the parametrization sets.¹⁹⁵ ROCBS-QB3 is a similar procedure to CBS-QB3, except spin-restricted wave functions are used in place of unrestricted wave functions.

4.2. Methods

This is done to eliminate spin contamination, and the use of a restricted open-shell definition has been shown to produce more accurate BDEs.¹⁸³ The (RO)CBS-QB3 methods have been implemented for the first, second, and third periods of elements.

G_n methods

The Gaussian-*n* (G_n) series of methods originates from the Pople group,¹⁹⁶ and G4 is the fourth generation. G4 utilizes moderately large basis sets and extrapolation techniques with CCSD(T) calculations to obtain highly correlated electronic energies. G4(MP2) uses MP2 in place of CCSD(T) and is thus less computationally expensive, but also gives a less complete description of electron correlation. Both methods use the B3LYP/6-31(2df,p) level of theory for optimization and frequency calculations with a frequency scaling factor of 0.9854. G4 results have been described as generally on par with CBS-QB3 results,^{193,194} but calculations are more computationally expensive.

4.2.2 Transition state calculations

Calculations were performed to identify the lowest energy TS complex of several reactions between CumO[•] and organic substrates. In all cases cisoid and transoid conformations were explored. All optimization calculations were performed at the B3LYP-D3(BJ)/6-31+G* level of theory, followed by single-point energy calculations at the B3LYP-D3(BJ)/6-311+G(2d,2p) level of theory with the SMD continuum solvent model¹²² to approximate acetonitrile solvent effects. Transition states were visualized using the Chemcraft program¹⁹⁷ to confirm a single imaginary frequency connecting reactants to products. In some cases, a small secondary imaginary frequency was observed, indicating a TS complex that is not fully optimized. Necessary steps were taken to re-optimize the structures and eliminate

4.3. Comparison of composite method for the prediction of BDEs

the small imaginary frequencies, but this was not always successful. Nonetheless, I am confident the structures reported herein sufficiently represent the true TS complex geometries and relative energies. Results from structures that are not fully optimized are indicated appropriately as such.

4.3 Comparison of composite method for the prediction of BDEs

In order to determine the best method for BEP principle analysis, and to investigate which is the most efficient yet accurate composite method, the BDEs of 50 species have been calculated. This set of species contains a wide variety of chemical functionalities with BDEs ranging from 75–113 kcal mol⁻¹, thus this set may be described as a comprehensive test of these methods for C–H BDEs. Given that W1BD is the most accurate method used, these results have been used for comparison to other composite methods. However, due to computational cost restrictions, BDEs for only 33 out of the 50 species studied could be calculated using W1BD; hard disk capacity was insufficient for large systems. Therefore, literature BDEs from Luo¹⁸⁰ for the 49 species that have literature values in the set are also used for comparison. The literature and calculated BDEs are listed in Table 4.1.

4.3. Comparison of composite method for the prediction of BDEs

Table 4.1: Bond dissociation enthalpies of the species used to investigate the accuracy of composite methods. Structures show an explicit C–H bond for that which is cleaved. All values are in kcal mol⁻¹. Statistics are listed at the bottom of the table.

Molecule	Structure	Lit.	W1BD	ROCBS-QB3	G4
1,3-pentadiene		83.0	82.9	81.7	81.6
1,4-cyclohexadiene		76.0	76.3	75.0	75.2
1,4-diazabicyclo[2.2.2]-octane		93.4		98.8	96.7
1,4-pentadiene		76.6	76.2	75.0	75.1
2,2-dimethylbutane		98.0	99.3	99.3	97.5
2,3-dimethylbutane		95.4	97.8	97.8	96.2
2-methylbutane		95.8	97.3	97.1	95.9
9,10-dihydroanthracene		76.3		78.1	
Acetaldehyde		94.3	95.9	95.7	94.9

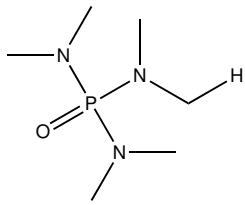
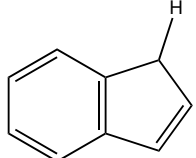
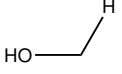
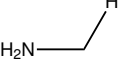
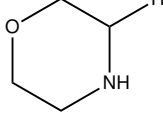
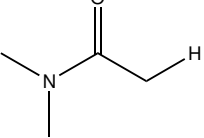
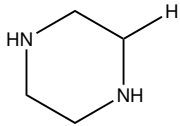
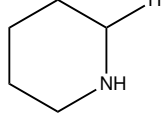
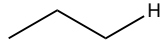
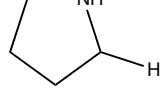
4.3. Comparison of composite method for the prediction of BDEs

Acetone		96.0	96.9	96.7
Acetonitrile		97.0	96.9	96.6
Adamantane (2°)		98.4		100.4
Adamantane (3°)		96.2		99.9
Benzaldehyde		88.7		91.4
Benzene		112.9	113.1	113.0
Benzyl Alcohol		79.0		83.2
Cumene		83.2		86.9
Cycloheptane		94.0		95.8
Cyclohexane		99.5	99.2	99.3
Cyclooctane		94.4		92.4
				90.2

4.3. Comparison of composite method for the prediction of BDEs

Cyclopentane		95.6	96.3	96.3	95.6
Cyclopropane		106.3	109.0	109.2	108.2
Dibenzyl ether		85.8		82.7	
Diethyl ether		93.0	95.3	95.5	93.8
Dimethylamine		94.2	92.6	92.8	92.0
Dimethylsulfoxide		94.0	102.0	102.3	100.9
Dioxane		96.5	97.3	97.6	95.7
Diphenylmethane		84.5		82.8	
Ethane		100.5	101.3	101.5	100.7
Ethylbenzene		85.4		87.6	87.6
Ethylene		110.9	110.8	110.9	109.9
Fluorene		82.0		81.9	
Formaldehyde		88.0	88.6	88.9	88.2

4.3. Comparison of composite method for the prediction of BDEs

Hexamethyl-phosphoramide				93.9	
Indene		83.0	80.1	79.0	
Methane		105.0	105.0	105.2	104.5
Methanol		96.1	96.4	96.8	96.0
Methylamine		93.9	93.1	93.3	92.7
Morpholine		92.0		93.3	91.8
N,N-dimethylacetamide		91.4	99.6	99.5	97.6
Piperazine		93.0	93.4	93.5	91.9
Piperidine		89.5	92.1	92.2	90.7
Propane		100.9	101.6	101.8	100.7
Pyrrolidine		89.0	90.8	90.7	89.5

4.3. Comparison of composite method for the prediction of BDEs

		Lit.	W1BD	ROCBS-QB3	G4
Tetrahydro-2H-pyran		96.0	96.3	96.5	94.7
Tetrahydrofuran		92.1	93.7	93.8	92.2
Toluene		89.7	90.5	89.7	89.8
Trichloromethane		93.8	93.5	93.7	92.4
Triethylamine		90.7		91.2	89.4
Trifluormethane		106.4	107.2	107.4	105.8
Statistics		Lit.	W1BD	ROCBS-QB3	G4
Number of BDEs	(N)	49	33	50	43
<i>Relative to Literature Values</i>					
MAE			0.82	1.64	1.21
Max. Error			1.59	3.15	4.19
Min. Error			-8.22	-8.25	-6.86
<i>Relative to W1BD Values</i>					
MAE (W1BD)				0.18	0.70
Max. Error				1.26	2.05
Min. Error				-0.35	0.37

4.3. Comparison of composite method for the prediction of BDEs

Mean absolute error (MAE) is used to assess the quality of computational methods, where errors are calculated with respect to benchmark values for a given data set.¹⁹⁸ The MAE is calculated as

$$\text{MAE} = \frac{1}{N} \sum |E_{ref} - E_{calc}| \quad (4.2)$$

where, for a set of N reference values, the MAE is the average of the mean differences of the reference energy (E_{ref}) and the calculated value (E_{calc}). The MAE with respect to W1BD and literature shall be reported herein as “ MAE_{W1BD} ($\text{MAE}_{\text{Lit.}}$)”. An additional semi-quantitative metric that I used to evaluate the accuracy of composite procedures to reproduce experimental results is a bar chart that summarizes the number of deviations from literature within given error ranges. This bar chart is reported in Figure 4.3. Note that calculations for some species with some methods failed to converge, thus number of BDEs out of 49 are also shown in Figure 4.3. Also, an alternative method that I shall utilize for reporting these data is through the use of one-to-one plots, in which BDEs from two methods are directly compared. An ideal plot should have a slope = 1 and y-intercept = 0.

Comparing W1BD results to literature, the MAE is 0.82 kcal mol⁻¹, and the majority of the data match to within 1–2 kcal mol⁻¹ of literature. Thus, W1BD is largely consistent with the literature values. Additionally, the one-to-one plots comparing W1BD to literature in Figure 4.4 show reasonable agreement with slope of 0.98 and a y-intercept of 2.35. There are two notable outliers: DMSOⁱⁱⁱ and *N,N*-dimethylacetamide, for which experiment underestimates the BDEs by -8.0 and -8.2 kcal mol⁻¹, respectively. DMSO and *N,N*-dimethylacetamide are consistently outliers amongst all composite methods, suggesting the literature BDEs are incorrect.

ⁱⁱⁱThe experimental BDE for dimethyl sulfoxide was previously identified as being inaccurate by

4.3. Comparison of composite method for the prediction of BDEs

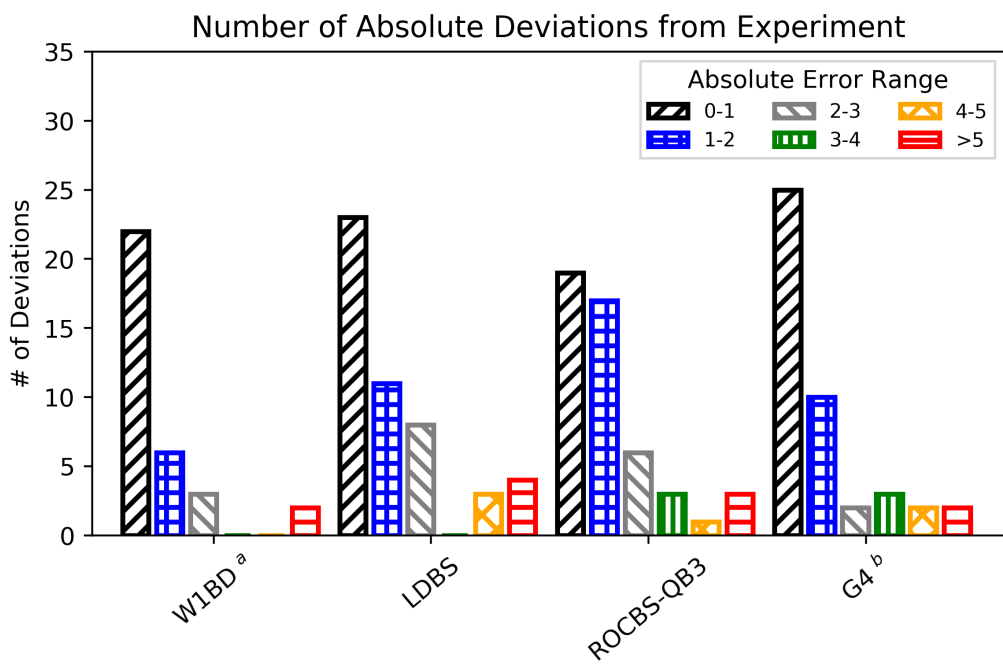


Figure 4.3: Summary of deviations of BDEs from literature or composite quantum chemical methods. Errors are units of kcal mol^{-1} and are relative to Ref. 180. ^a Includes BDEs for 33/49 substrates. ^b Includes BDEs for 40/49 substrates.

4.3. Comparison of composite method for the prediction of BDEs

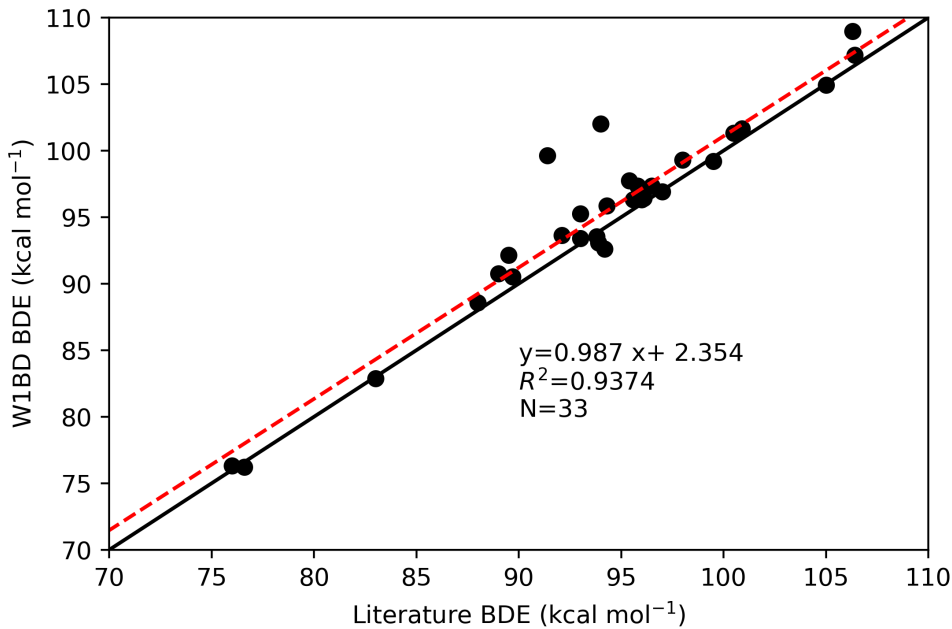


Figure 4.4: One-to-one plot of BDEs from literature¹⁸⁰ and as calculated by the W1BD composite method. The red dashed-line represents the least squares line of best fit, while black line represents a perfect one-to-one correlation.

The method that gives the best combined agreement with W1BD and literature is ROCBS-QB3 with an MAE from W1BD (literature) = 0.18 (1.64) kcal mol^{-1} . It is also apparent, from the one-to-one plots in Figure 4.5, that ROCBS-QB3 matches well with literature and experiment. In comparison, CBS-QB3 has an MAE = 0.32 (1.88) kcal mol^{-1} , while CBS-APNO has an MAE = 0.20 (1.40) kcal mol^{-1} . The LDBS approach also performs well with an MAE = 0.22 (1.60) kcal mol^{-1} . The G4 method deviates from the W1BD reference by about 0.5 kcal mol^{-1} more, however, it appears to give reasonable agreement with experimental results (MAE = 0.70 (1.21) mol). The use of the MP2 variant of G4 gives somewhat questionable results, with an MAE of 0.88 (1.60) kcal mol^{-1} , as well as a large outlier of 6.2 kcal mol^{-1}

Salamone et al.¹⁴⁴

4.3. Comparison of composite method for the prediction of BDEs

that is not present in the other data from composite methods. One-to-one plots of all other methods are presented in Appendix B.

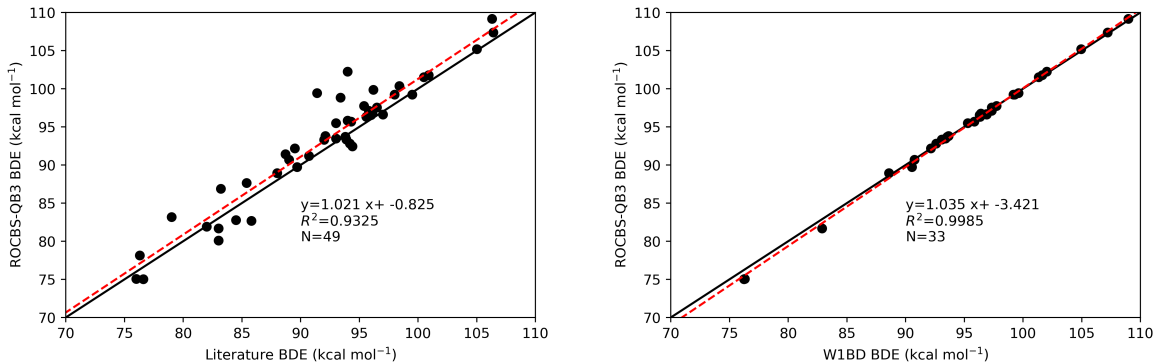


Figure 4.5: One-to-one plot comparing calculated BDEs calculated by the ROCBS-QB3 to reference literature¹⁸⁰ and W1BD BDE values, respectively. The red dashed-line represents the least squares line of best fit, while black line represents a perfect one-to-one correlation.

In summary, ROCBS-QB3 performs best for the calculation of C–H BDEs while G4(MP2) performs worst. Given these data, and considering the relative computational cost, I recommend the ROCBS-QB3 for the calculation of accurate BDEs, particularly for large molecules for which more expensive computational methods are not possible. Importantly, we can now confidently continue investigating the BEP relationships using reliably calculated BDE data from the ROCBS-QB3 method. Furthermore, these results can be extended to even larger systems as the ROCBS-QB3 approach is one of the least computationally-expensive composite methods. For example, calculations on the cyclohexane molecule take about 20 minutes using ROCBS-QB3 on SGI Altix compute nodes with 6 processors and 8 GB RAM, while G4 takes approximately 27 times longer, the LDBS approach takes about 500 times longer, and W1BD takes about 1100 times longer.

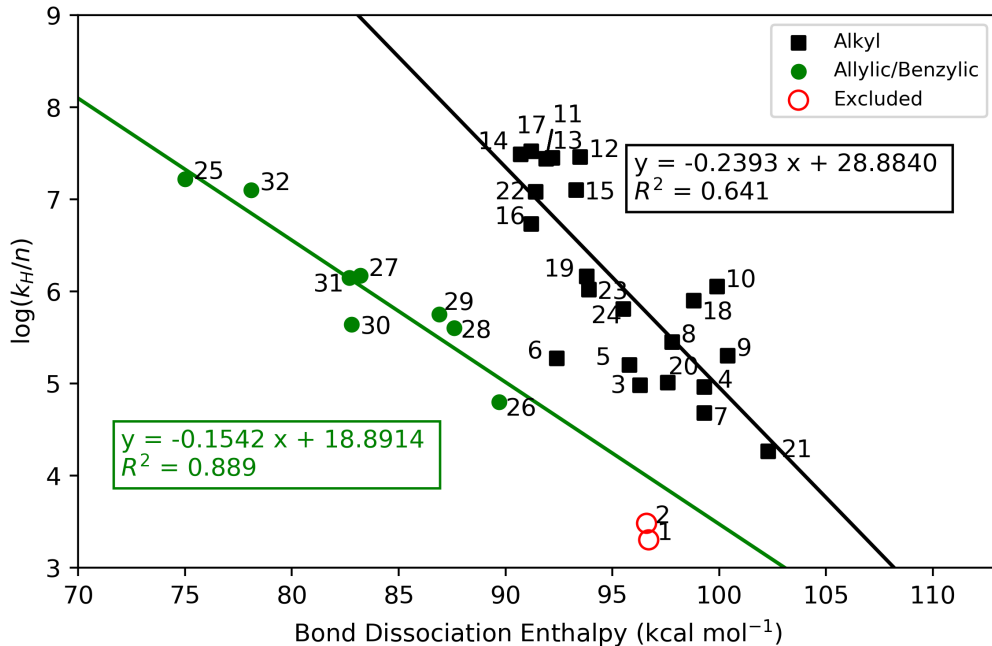
4.4 Analysis of the Bell-Evans-Polanyi principle

We turn now to the application of accurate BDEs to the BEP principle. Experimental HAT rate constants have been collected for 32 reactions involving CumO[•] and organic substrates. The BEP plot of the logarithm of rate constants divided by the number of equivalent H atoms (i.e. normalized) against BDEs is shown in Figure 4.6.

As with the experimental results in Figure 4.2, there clearly exists two distinct regions in Figure 4.6. This is congruent with the initial hypothesis that there should exist two linear relations: one for allylic/benzylic C–H bonds, and another for alkyl C–H bonds. However, there remains a considerable amount of scatter in the data, thus correlation of the expected BEP relations is poor. For the allylic/benzylic series of C–H BDEs, for which bond scissions results in a radical that is delocalized, the coefficient of determination is $R^2 = 0.89$. This result is consistent with work of Pratt et al.,¹⁶¹ which obtained an $R^2 = 0.82$ from the BEP plot for the abstraction of C–H bonds from models for unsaturated fatty acids. Most of the rate constants used in the work of Pratt et al. are for the abstraction of C–H by peroxy radicals, which were obtained through an experimental method that gives estimated HAT rate constants with large associated errors. Thus, they suggested that the degree of scatter is associated with experimental errors. The same however cannot be said for the rate constants associated with this work. Therefore, there may be additional physico-chemical factors at play.

The alkyl C–H BDEs show very weak correlation with CumO[•] HAT rate constants, with an $R^2 = 0.63$. One possibility is that applying the BEP principle to such a large grouping of substrates is inappropriate. Thus, I have re-plotted this data in Figure 4.7, breaking the data into several smaller chemical groupings: cyclic alkanes, other alkanes (branched and adamantine), hydrogen bond donating (H-

4.4. Analysis of the Bell-Evans-Polanyi principle



1	Acetone	2	Acetonitrile
3	Cyclopentane	4	Cyclohexane
5	Cycloheptane	6	Cyclooctane
7	2,2-dimethylbutane	8	2,3-dimethylbutane
9	Adamantane (2°)	10	Adamantane (3°)
11	Diethyl amine	12	Piperazine
13	Piperidine	14	Pyrrolidine
15	Morpholine	16	Propylamine
17	Triethylamine	18	1,4-diazobicyclo[2.2.2]octane
19	Tetrahydrofuran	20	Dioxane
21	Dimethyl sulfoxide	22	Benzaldehyde
23	Hexamethylphosphoramide	24	Diethyl ether
25	1,4-cyclohexadiene	26	Toluene
27	Benzyl alcohol	28	Ethylbenzene
29	Cumene	30	Diphenylmethane
31	Dibenzyl ether	32	9,10-dihydroanthracene

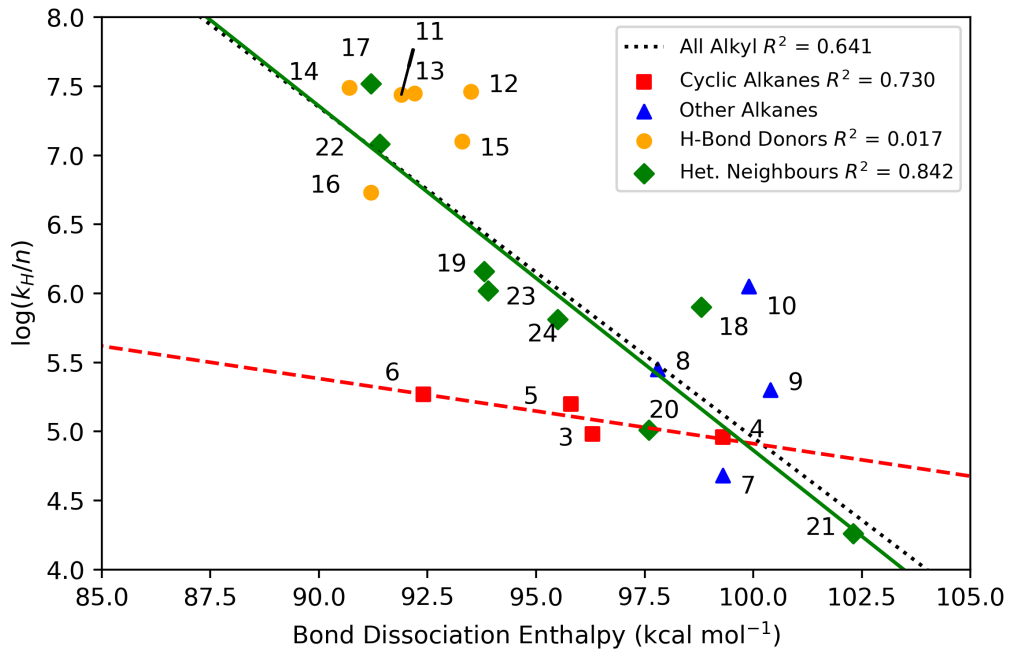
Figure 4.6: Bell-Evans-Polanyi plot of experimental rate constants (normalized for the number of equivalent hydrogen atoms) for HAT between CumO[·] and substrates against BDEs calculated using the ROCBS-QB3 method. Acetone and acetonitrile are note included in fitting as the experimental rate constants are approximate.

4.4. Analysis of the Bell-Evans-Polanyi principle

Bond Donors) species, and other C–H bonds with heteroatom neighbours (Het. Neighbours). Doing so appears to reveal one reasonably well-correlated trend for C–H bonds with heteroatom neighbours ($R^2 = 0.84$). There are two data points for the tertiary amines (triethylamine and 1,4-diazobicyclo[2.2.2]octane) that do not fit well with the expected trend, however it is unclear why they do not fit into the other points in the heteroatomic neighbours trend. Excluding points for the tertiary amines results in an $R^2 = 0.92$.

The cyclic alkanes are somewhat poorly correlated ($R^2 = 0.73$). Within the “other alkanes” grouping there are two branched alkanes, 2,3-dimethylbutane and 2,2-dimethylbutane, as well as the secondary and tertiary C–H positions of adamantane. There may be a separate correlation for each of these, but there are too few data points to make this assertion. Extremely poor correlation is observed for both the hydrogen bond donating species ($R^2 = 0.02$). This is likely due to the formation of a hydrogen bonded pre-reaction complex that does not allow for HAT to occur without some subsequent rearrangement (See Chapter 3). In general, there are no evident reasons on the basis of group-additivity based arguments that explain the poor correlations observed. Thus, the lack of simple relationships is perhaps evidence against the validity of the BEP principle. However, before making any conclusions, we must consider if there are any explanations that arise from examining the transition state structures.

4.4. Analysis of the Bell-Evans-Polanyi principle



3	Cyclopentane	4	Cyclohexane
5	Cycloheptane	6	Cyclooctane
7	2,2-dimethylbutane	8	2,3-dimethylbutane
9	Adamantane (2°)	10	Adamantane (3°)
11	Diethyl amine	12	Piperazine
13	Piperidine	14	Pyrrolidine
15	Morpholine	16	Propylamine
17	Triethylamine	18	1,4-diazobicyclo[2.2.2]octane
19	Tetrahydrofuran	20	Dioxane
21	Dimethyl sulfoxide	22	Benzaldehyde
23	Hexamethylphosphoramide	24	Diethyl ether

Figure 4.7: Further breakdown of Bell-Evans-Polanyi plot of experimental rate constants (normalized for the number of equivalent hydrogen atoms) for HAT between CumO[•] and substrates.

4.5 Transition state analysis

In order to determine if there are any reasons for the breakdown of the BEP principle, I have calculated TS structures for 20 of the reactions at the B3LYP-D3(BJ)/6-311+G(2d,2p)//B3LYP-D3(BJ)/6-31+G* level of theory. Note that the inclusion of the SMD continuum solvent model decreases the agreement in calculated rate constant with experiment, and so gas-phase results are reported herein (See Appendix B, Figure B.2). The experimental and calculated HAT reaction rate constants (k_H) agree reasonably well (within 2 orders of magnitude) and are listed in Table 4.2, along with the free-energy barrier heights (ΔG^\ddagger) and the decomposition into enthalpic and entropic terms: $\Delta G^\ddagger = \Delta H^\ddagger - T\Delta S^\ddagger$.

First, consider some general features associated with the TS complexes listed in Table 4.2. One factor that may lead to deviations from the BEP principle is the possibility for different HAT reaction mechanisms, i.e. direct HAT or PCET. Consider first the reaction of toluene with CumO[•]. As this reaction is similar to the self-exchange reaction of the benzyl-toluene couple as described by DiLabio and Johnson,²⁶ one might expect the reaction to proceed via PCET. The lowest-energy TS complex has a partially π -stacked conformation with the rings oriented approximately 40° relative to one another. Examination of the SOMO and HOMO reveals no π - π partial bonding interaction, as can be seen in Figure 4.8. The electron density of the SOMO is largely localized on the toluene portion of the complex. This is likely due to the additional non-conjugated carbon centre of CumO[•], which prevents an additional electron channel for PCET to occur. Therefore, this reaction takes place through direct HAT, as has been previously described.¹⁴⁰ This behaviour is specific to the CumO[•] radical, thus all the reactions likely also take place through a direct HAT dominant mechanism, and this should not factor into the deviations in the observed BEP principle relationships.

4.5. Transition state analysis

Table 4.2: Reaction barrier heights for reactions of substrates with CumO[•] calculated in the gas phase at 298 K at the B3LYP-D3(BJ)/6-311+G(2d,2p)//B3LYP-D3(BJ)/6-31+G* level of theory. Rate constants are in units of M⁻¹s⁻¹, while all other values are in units of kcal mol⁻¹. ID numbers match those in Figure 4.6. [†]TS structure could not be fully optimized and contains a small additional imaginary frequency.

ID	Substrate	$k_H(\text{expt.})$	$k_H(\text{calc.})$	ΔG^\ddagger	ΔH^\ddagger	$-T\Delta S^\ddagger$
Excluded						
1	Acetone	$< 1 \times 10^4$	2.8×10^2	14.1	0.1	14.0
2	Acetonitrile	$< 1 \times 10^4$	2.9×10^2	14.1	2.6	11.5
Cyclic Alkanes						
3	Cyclopentane [†]	9.5×10^5	5.5×10^4	11.0	-2.0	13.0
4	Cyclohexane	1.1×10^6	5.8×10^4	10.9	-1.1	12.1
6	Cyclooctane [†]	3.0×10^6	2.7×10^4	11.4	-2.7	14.1
Other Alkanes						
7	2,2-dimethylbutane	9.5×10^4	1.1×10^6	9.2	-1.2	10.4
8	2,3-dimethylbutane	5.6×10^5	2.5×10^6	8.7	-3.3	12.0
9	Adamantane (2°)	6.9×10^6	2.0×10^5	10.2	-1.8	12.0
10	Adamantane (3°)	6.9×10^6	1.1×10^7	7.9	-3.9	11.8
H-Bond Donor						
11	Diethylamine	1.1×10^8	8.2×10^9	3.9	-9.1	13.0
Heteroatom Neighbours						
18	1,4-diazobicyclo[2.2.2]octane	9.6×10^6	5.1×10^7	6.9	-5.3	12.3
20	Dioxane	8.2×10^5	1.2×10^7	7.8	-4.0	11.8
21	Dimethyl sulfoxide	1.8×10^4	2.7×10^4	11.4	-0.5	11.9
22	Benzaldehyde [†]	1.2×10^7	2.5×10^7	7.4	-5.6	12.9
23	Hexamethylphosphoramide	1.9×10^7	3.9×10^7	7.1	-7.3	14.4
24	Diethyl ether	2.6×10^6	5.9×10^7	6.8	-4.6	11.4
Allylic/Benzylic						
25	1,4-cyclohexadiene	6.6×10^7	1.1×10^8	6.5	-6.5	13.0
26	Toluene	1.8×10^5	2.0×10^5	10.2	-3.5	13.7
29	Cumene	5.6×10^5	1.9×10^7	7.5	-5.8	13.3
30	Diphenylmethane [†]	8.7×10^5	1.8×10^6	8.9	-5.6	14.5
32	9,10-dihydroanthracene [†]	5.0×10^7	2.2×10^8	6.1	-8.5	14.6

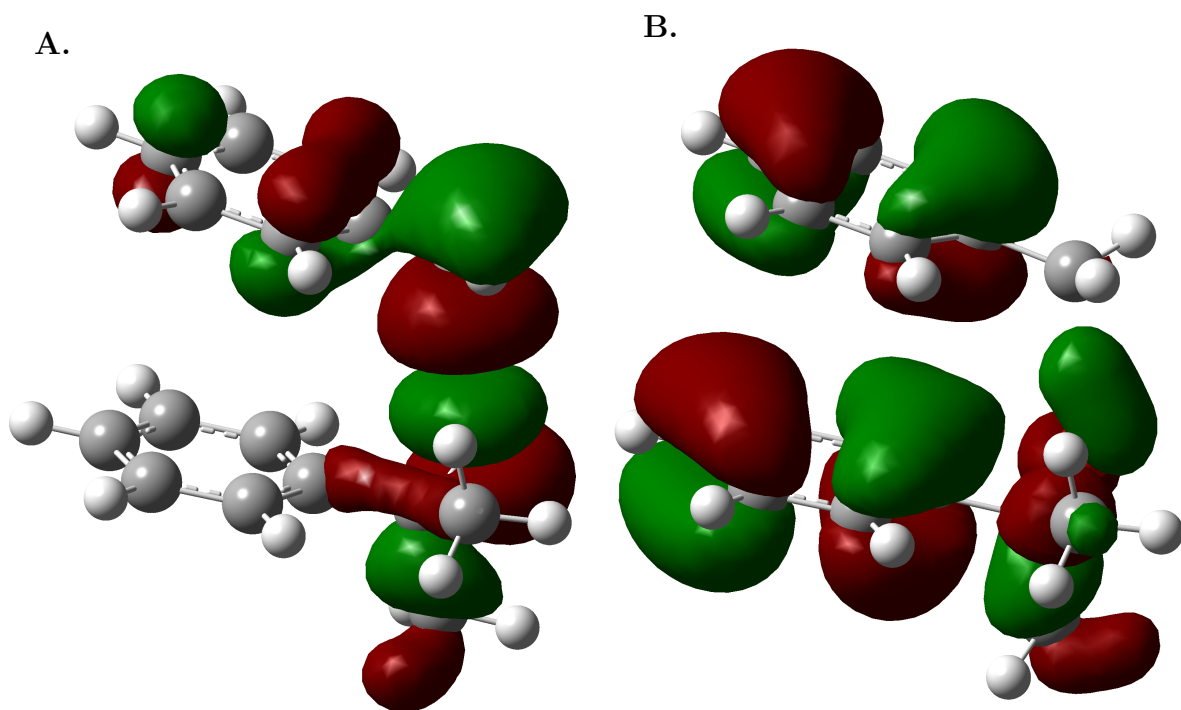


Figure 4.8: Structures of TS for HAT between CumO[•] and toluene with **A.** SOMO and **B.** HOMO. The elements are coloured as grey for carbon, white for hydrogen, and red for oxygen. MOs are shown with an isovalue of $0.02 \text{ } e^-/\text{\AA}^3$.

4.5. Transition state analysis

For all of the TS structures of the reactions in Table 4.2, a conformation that maximizes non-covalent interactions while minimizing steric repulsion is adopted. In the cases of acetone, acetonitrile, hexamethylphosphoramide (HMPA), and DMSO, a very weak hydrogen bonding interaction is formed between the X=O (or C≡N for acetonitrile) moieties and the C–H of the methyl of CumO[•]. In all but two cases, this involves a cisoid (partially-stacked) complex so that dispersion interactions are maximized. The two outliers are benzaldehyde and cyclooctane. In order for benzaldehyde to adopt a cisoid TS structure, there are two possibilities. First, a T-shaped conformation could be adopted, rather than a slipped-parallel π -stacked conformation. On the basis of the benzene-benzene non-covalently bound dimer,³⁴ the T-shaped conformation is very slightly favourable compared to the π -stacked conformation by circa 0.1 kcal mol^{−1}. However, forming the T-shaped TS structure would require a rotation of nearly 90° of the C(CH₃)₂O[•] of CumO[•], which has a predicted energetic cost^{iv} of 4.2 kcal mol^{−1}, and so this conformation is unlikely. On the other hand, the C(CH₃)₂O[•] of CumO[•] could rotate to accommodate a partially slipped-parallel π -stacking conformation in the TS complex. Note that I was unable to obtain TS structures for either of the described possible cisoid conformations for the benzaldehyde-CumO[•] TS complex, as geometry optimization calculations did not converge. For cyclooctane, the difference in free energy between the cisoid and transoid TS structures is 1.8 kcal mol^{−1}. Both structures contain a secondary small imaginary frequency, and thus do not represent true TS structures. The reason for the transoid TS structure being more stable is somewhat unclear, but it is possible that the non-optimal nature of the TS structures is the cause. Furthermore, it is possible that the cyclooctane molecule undergoes a conformational change in forming the TS complex that was not accounted for in these calculations. Cyclooctane

4.5. Transition state analysis

has many conformations that are close in relative energy.¹⁹⁹

TS complex structures and mechanism aside, there is one striking feature in the reaction barriers calculated for HAT reactions involving CumO[•]: all the reactions studied are entropy-controlled at 298 K. This means that the free-energy barrier, and thus rate constant, is controlled by the entropic contributions, rather than the enthalpic contributions, i.e., $-T\Delta S^\ddagger > \Delta H^\ddagger$. From the results in Table 4.2, it can be said that $-T\Delta S^\ddagger >> \Delta H^\ddagger$ for hydrogen abstraction by CumO[•]. One interpretation of these results is that CumO[•] is so highly reactive that HAT is governed by trajectory, orientation, and degrees of freedom, factors that are normally associated with the A-factor in Arrhenius theory. In fact, in many cases, ΔH^\ddagger is calculated to be negative with respect to the separated reactants. This implies that a pre-reaction complex is formed, which, as was demonstrated in Chapter 3, can have significance on HAT reactivity with respect to the magnitude of the A-factor. Pre-reaction complex structures were not calculated in this work. In some cases the systems have been studied in combined experimental and theoretical work. Some examples of previously calculated CumO[•] + substrate pre-reaction complex binding enthalpies are: HMPA^v $\Delta H \approx -6$ kcal mol⁻¹, DMSO $\Delta H \approx -5$ kcal mol⁻¹, and 1,4-diazobicyclo[2.2.2]octane (DABCO)⁴¹ $\Delta H \approx -0.1$ kcal mol⁻¹. Note that the calculated enthalpic barrier herein is -5.3 kcal mol⁻¹ for DABCO, a result that can be ascribed to differences in computational methods. In Ref. 41, no dispersion correction was used, thus accounting for a less stable TS complex and pre-reaction complex. The calculated difference in enthalpy from pre-reaction complex to TS complex for DABCO was found to be only 1.0 kcal mol⁻¹.

The fact that hydrogen abstraction by CumO[•] is entropy-controlled is perhaps unsurprising, given the work of Finn et al.⁴⁰, which demonstrated that HAT re-

^{iv}Calculated at the B3LYP-D3(BJ)/6-311+G(2d,2p) level of theory.

^vDMSO and HMPA were studied in Ref. 144 at the B3LYP-DCP²⁰⁰/6-31+G(2d,2p) level of theory

4.6. Is the Bell-Evans-Polanyi principle valid?

actions involving various organic substrates and the closely related radical $t\text{-BuO}^\bullet$ are also entropy-controlled at room temperature. Furthermore, it has been shown that CumO^\bullet and $t\text{-BuO}^\bullet$ display very similar hydrogen atom abstraction reactivities.^{140,201–203} It is surprising then that these radicals remain so often applied as proxies for reactive oxygen species in kinetic studies. Future work should use extreme caution in applying CumO^\bullet and $t\text{-BuO}^\bullet$ as chemical probes, as has been noted in the past.^{40,41,140} Note also that it is uncommon to encounter entropy-controlled reactions in organic chemistry, and they are often associated with non-Arrhenius kinetic behaviour. Other examples of reported entropy-controlled reactions include the addition of a carbene across a multiple bond,^{204,205} and radical-radical recombination reactions.²⁰⁶

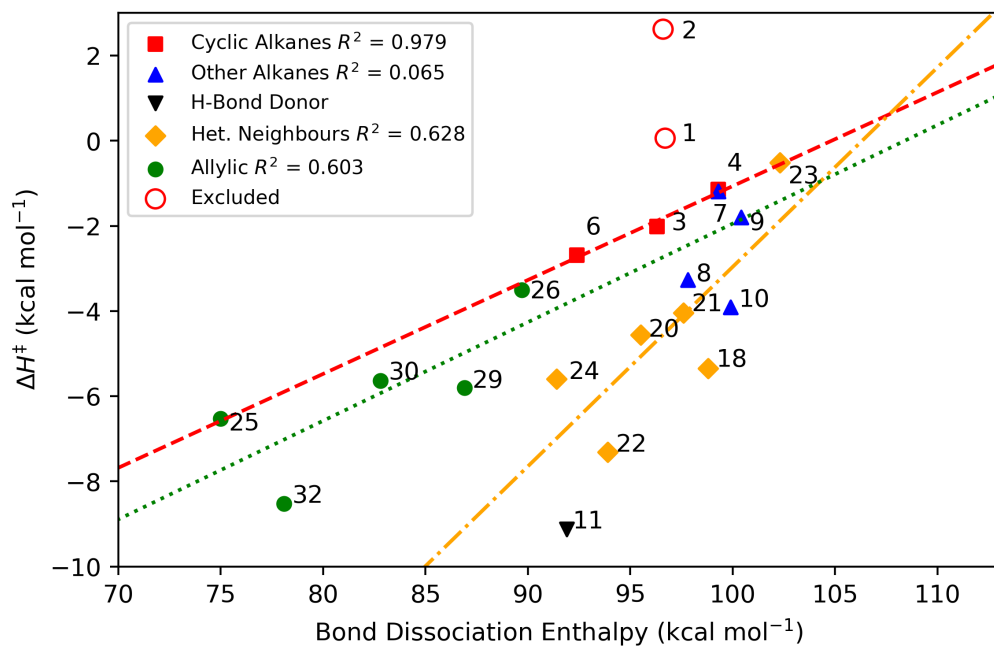
Classical physical organic chemical literature can explain why the reactions that are entropy-controlled do not follow “normal” LFERs.²⁰⁷ Blackadder and Hinshelwood²⁰⁸ defined three classifications for different types of LFERs, the first of which applies to the BEP principle: A series of reactions with constant entropy are controlled by enthalpy changes that are based on electronic effects that do not affect the form of the TS. Therefore, reaction rates that involve non-isoentropic TS complex formation will not correlate with bond strengths, as is observed herein. It seems prudent at this point to suggest that expecting reactions to be isoentropic with respect to transition state formation is an over-simplification, especially given the number of factors that contribute to entropy in solvent phase chemistry.

4.6 Is the Bell-Evans-Polanyi principle valid?

The question still remains whether the BEP principle is valid or not. Recall from Equation 2.93 that E_a is related directly to ΔH^\ddagger . Thus, if the BEP principle still holds for HAT reactions between CumO^\bullet and organic substrates, then the cal-

4.6. Is the Bell-Evans-Polanyi principle valid?

culated values of ΔH^\ddagger should be a function of C–H BDE. These data are plotted in Figure 4.9.



1	Acetone	2	Acetonitrile
3	Cyclopentane	4	Cyclohexane
6	Cyclooctane	7	2,2-dimethylbutane
8	2,3-dimethylbutane	9	Adamantane (2°)
10	Adamantane (3°)	11	Diethyl amine
18	1,4-diazobicyclo[2.2.2]octane	20	Dioxane
21	Dimethyl sulfoxide	22	Benzaldehyde
23	Hexamethylphosphoramide	24	Diethyl ether
25	1,4-cyclohexadiene	26	Toluene
29	Cumene	30	Diphenylmethane
32	9,10-dihydroanthracene		

Figure 4.9: Bell-Evans-Polanyi plot of calculated enthalpic barriers for HAT between CumO[•] and substrates against BDEs calculated using the ROCBS-QB3 method.

Perhaps unsurprisingly at this point, there is once again a great deal of scatter in the data. The cyclic alkanes fit into a linear relationship that is very well correlated ($R^2 = 0.98$). However, all other chemical groupings show very poor correla-

4.6. Is the Bell-Evans-Polanyi principle valid?

tion. Therefore, the correlation seen for the cycloalkanes is an adventitious example of the BEP principle showing a linear relation between ΔH^\ddagger and BDE. Even the substrates with allylic/benzylic C–H bonds show only weak correlation in a BEP relation ($R^2 = 0.63$), although the experimental results show a reasonable correlation between $\log(k_H/n)$ and calculated BDEs. Therefore, the experimental results are likely serendipitous, especially considering the reactions are entropy-controlled and non-isoentropic.

Further analysis of the allylic/benzylic relation demonstrates a clear breakdown in the BEP principle. If one begins with toluene with a BDE of 89.7 kcal mol⁻¹ and ΔH^\ddagger of -3.5 kcal mol⁻¹, then the addition of two methyl substituents forms cumene, with a BDE of 86.9 kcal mol⁻¹ and ΔH^\ddagger of -5.8 kcal mol⁻¹, indicating the relative stabilization of the TS by substituents. However, if one adds another phenyl group instead of two methyl groups, diphenylmethane is obtained, which has a BDE of 82.8 kcal mol⁻¹. This indicates that phenyl is a better radical stabilizing group, however ΔH^\ddagger is -5.6 kcal mol⁻¹, which is slightly higher than that of cumene. The difference can be partially attributed then to differences in progress along the reaction coordinate. Evidence of this difference is the spin density localized on the O-centre of CumO[•] in the TS complex, which should go to zero as the reactants move to products. The O[•] spin densities are 0.477 e⁻, 0.528 e⁻, and 0.518 e⁻ for toluene, cumene, and diphenylmethane, respectively. Therefore, the progress along the reaction coordinate is furthest for toluene, and progressively less far for diphenylmethane and cumene. Note, that the O[•] spin densities for cyclopentane, cyclohexane, and cyclooctane are 0.455 e⁻, 0.452 e⁻, and 0.458 e⁻, respectively. Therefore the progress along the reaction coordinate for the cycloalkanes is roughly the same, which may explain the R^2 of nearly 1.

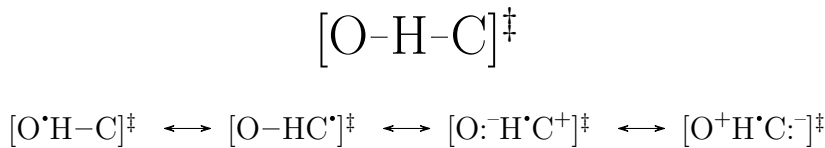
Such contradictory data makes it very difficult to draw any conclusions. Instead,

4.6. Is the Bell-Evans-Polanyi principle valid?

I shall make some suggestions as to why the BEP principle is an incomplete theoretical construct for describing the HAT reaction of CumO[•] with organic substrates:

1. HAT reactions between CumO[•] and these organic substrates may be decidedly exothermic, resulting in reactions with no enthalpic barrier associated with the breaking of a C–H bonds and the formation of an O–H bond. This is supported by the fact that the calculated enthalpic barriers are all very low or even negative. Therefore, any remaining nominal activation energy is a result of stereo-electronic interactions between CumO[•] and the substrate. The high reactivity of CumO[•] also suggests that abstraction from the weakest bond in a substrate will not always occur. The site of abstraction will most likely be determined by the orientation of the substrate upon collision. This is likely an additional reason why $\log k_H/n$ does not correlate with the calculated C–H BDEs.
2. Polar effects have been shown to be extremely important in the stability of the TS complex.²⁰⁹ The species involved in HAT reactions are often neutral radicals, thus the influence of charge transfer in the TS complex can have important implications. Consider the TS of a generic HAT reaction in Scheme 4.3, there are four obvious resonance forms. Oxygen-centred radicals are electrophilic in nature, thus the importance of the third resonance structure increases. The BEP principle does not account for polarity in the TS complex, as these effects are not captured by the BDE of the substrate, thus ΔH^\ddagger does not correlate well with BDE. This issue was addressed by Roberts and Steel²¹⁰, who suggested an extension of the BEP principle to include simple empirical parameters that capture the polar effects in the transition state.

4.6. Is the Bell-Evans-Polanyi principle valid?



Scheme 4.3: A generic HAT transition state structures and possible resonance forms.

3. The BEP principle is an over-simplification that does not capture nearly enough of the physics associated with the deceptively complex hydrogen abstraction reactivity of CumO[•] (or *t*-BuO[•]). Therefore, I suggest that the BEP principle should not be used as a tool for predicting activation energies or rate constants. One method that has been popularized by Mayer is the use of Marcus cross-relations.²⁹ This predictive method has also been used to explain reactions that have negative enthalpic barriers.¹²⁹ An alternative approach is that of Zavitsas, that predicts activation energies based on so-called “triplet repulsion”^{vi} and radical delocalization.^{211,212} It is clear from the analysis herein that the BEP principle is valid only as a conceptual framework, rather than a broadly applied linear relationship.

^{vi}Zavitsas uses the term “triplet repulsion” to describe repulsion between the parallel spins of the hydrogen atom acceptor and donor atoms ($\uparrow\downarrow\uparrow$ or $\downarrow\uparrow\downarrow$) in the TS complex.

Chapter 5

Do non-redox active metal cations have the potentials to behave as chemo-protective agents? The Effects on Metal Cations on HAT Reaction Barrier Heights

5.1 Introduction

Metal cations are ubiquitous in biological systems and play an important role in biological function. As such, there is a great deal of interest in studying metals in biological systems. Proteins in particular are often associated with metals, and in the worldwide Protein Data Bank,^{213,214} over one-third of crystal structures contain metals. Redox active metals, such as copper and iron, act as co-factors in metalloenzymes for important catalytic processes.²¹⁵

Non-redox active metal cations are equally as important in biological function as redox active metals, where they are essential to protein structure and function, along with cellular and neuronal signalling.²¹⁶ Sodium and calcium ions are most abundant extracellularly, while potassium and magnesium are dominant inside of cells. Specific ionic concentrations vary dramatically depending on physiological conditions; estimates for equilibrium concentrations in both mammalian heart cells²¹⁷ and blood plasma²¹⁸ are listed in Table 5.1. As sodium and magnesium are the

5.1. Introduction

most abundant alkali and alkaline earth metals found in biologically relevant systems, they are of prime interest for my investigation.

Table 5.1: Ionic concentrations inside a mammalian heart cell and in the blood plasma. Concentrations are in units of mM. Values are rounded to one significant figure. Data are from Ref. 217 and 218.

Ion Conc.	Mammalian Cells	Blood Plasma
Na ⁺	10	100–200
Mg ²⁺	10	1
K ⁺	100	4
Ca ²⁺	0.1	2

Extensive crystallographic surveys indicate that metals bind predominantly to oxygen centres in proteins.^{219–221} Divalent metals are most often found bound directly to proteins. Calcium binds anywhere from 4 to 6 binding sites in protein crystal structures, while magnesium binds only 1 or 2. Monovalent metals, on the other hand, are often heavily solvated and so they appear in solvent cavities of proteins, although sodium or potassium are sometimes found bound directly to carbonyl or carboxylate oxygen centres.²¹³

A great deal of research has focussed on Ca²⁺ in the context of reactive oxygen-centred radical production.²²² Specifically, Ca²⁺ ions are important in the mitochondria, where, depending on physiological conditions and concentrations, they can act as inhibitors or promoters of free-radical production in the electron transport chain.²²³ One explanation is that Ca²⁺ induce conformational changes of the proteins involved in the electron transport chain that are responsible for radical generation.²²⁴ Mitochondrial free-radicals, when present in moderate amounts, can act as cell signalling molecules to activate pro-growth responses.²²⁵ However, “dysfunctional” mitochondria can produce excess radicals leading to oxidative damage that has been linked to degenerative diseases.

Given the significant importance alkali and alkaline earth metals play in biolog-

5.1. Introduction

ical systems, their impact on protein oxidation must be considered. However, until recently, kinetic studies of protein oxidation have not investigated the mechanistic role of non-redox active metals. In a series of three papers,^{49–51} Bietti and colleagues showed that alkali and alkaline earth metals have an inhibitory effect on HAT reactions involving CumO[•] and organic substrates. Some of the experimental rate constants from these papers are summarized in Table 5.2. All rate constants were obtained by time-resolved LFP in nitrogen or argon-saturated acetonitrile (MeCN) at 298 K, as was previously described in Section 4.2. The experimental results have been rationalized on the basis of Lewis acidic metal cation interactions with Lewis basic substrates.

For hydrocarbons, cyclic ethers, and tertiary amines, rate constants for hydrogen abstraction by CumO[•] in the presence of excess concentrations of lithium and magnesium salts were measured.⁴⁹ In the presence of LiClO₄ and Mg(ClO₄)₂, the rate of abstraction by CumO[•] from 1,4-cyclohexadiene (CHD) increases very slightly. Since CHD has no Lewis basic centres, the increase in HAT rate constant was explained on the basis of metal cation interactions with CumO[•], very slightly increasing the hydrogen abstraction ability by withdrawing electron density from the aromatic ring. Metal cations were also shown to increase the unimolecular decay of CumO[•] by β -scission (See Section 4.2). The largest kinetic effect was observed with LiClO₄ with $k_\beta = 1.8 \times 10^6 \text{ s}^{-1}$, which is a roughly 3-fold increase as compared to the rate in MeCN at 298 K ($k_\beta = 6.3 \times 10^5 \text{ s}^{-1}$).¹⁸⁷ This effect is significantly less than the observed kinetic solvent effect on CumO[•] β -scission measured in H₂O or 2,2,2-trifluoroethanol ($k_\beta = 1.0 \times 10^7$ and $6.1 \times 10^6 \text{ s}^{-1}$, respectively).^{226,227} Therefore, the kinetic effects of these alkali and alkaline metal salts interacting via Lewis acid-base interactions with the oxygen-centre of CumO[•] are less than the effects of hydrogen-bonding by solvents.

5.1. Introduction

Table 5.2: Summary of rate constants for reactions of CumO[•] with various organic substrates in the presence of alkali and alkaline earth metal salts.

Substrate	Conditions	k_H ($M^{-1}s^{-1}$)	$k_H(\text{MeCN})/k_H(M^{n+})$
1,4-cyclohexadiene (CHD)		6.7×10^7	
	LiClO ₄ 1.0 M	7.5×10^7	0.89
	Mg(ClO ₄) ₂ 1.0 M	7.0×10^7	0.96
tetrahydrofuran (THF)		5.7×10^6	
	LiClO ₄ 1.0 M	2.9×10^6	1.7
	LiOTf 1.0 M	2.8×10^6	2.0
triethylamine (TEA)	Mg(ClO ₄) ₂ 1.0 M	1.8×10^6	3.2
		2.0×10^8	
	LiClO ₄ 1.0 M	9.4×10^7	2.1
<i>N,N</i> -dimethylformamide (DMF)	Mg(ClO ₄) ₂ 0.005 M	$< 1 \times 10^6$	>200
		1.2×10^6	
	LiClO ₄ 0.5 M	$k_{H1} = 8.9 \times 10^5$ $k_{H2} = 1.5 \times 10^6$	1.3 0.80
<i>N,N</i> -dimethylacetamide (DMA)	NaClO ₄ 0.2 M	$k_{H1} = 9.6 \times 10^5$ $k_{H2} = 1.4 \times 10^6$	1.3 0.86
	Mg(ClO ₄) ₂ 0.2 M	$k_{H1} = 5.8 \times 10^5$ $k_{H2} = 1.1 \times 10^6$	2.1 1.1
	Ca(ClO ₄) ₂ 0.2 M	$k_{H1} = 1.0 \times 10^6$ 1.2×10^6	0.83
	LiClO ₄ 0.2 M	$k_{H1} = 8.5 \times 10^5$ $k_{H2} = 1.5 \times 10^6$	1.4 0.8
	NaClO ₄ 0.2 M	$k_{H1} = 1.1 \times 10^6$ $k_{H2} = 1.3 \times 10^6$	1.1 0.92
	Mg(ClO ₄) ₂ 0.2 M	$k_{H1} = 4.7 \times 10^5$ $k_{H2} = 2.4 \times 10^5$ $k_{H3} = 1.1 \times 10^6$	2.6 5.0 1.1
	Ca(ClO ₄) ₂ 0.2 M	$k_{H1} = 1.2 \times 10^6$	1.0

5.1. Introduction

Next, the HAT rate constants for abstraction from tetrahydrofuran (THF) decrease in the presence of non-redox active metal salts. Both LiClO₄ and LiOTf decrease k_H by a factor of about 2, indicating the nature of the counter-anion plays a negligible role in the Lewis acid-base interactions between metal cations and substrates. The addition of Mg(ClO₄)₂ has a greater effect on HAT reactivity, decreasing k_H by a factor of 3. The magnesium ion is a stronger Lewis acid than lithium,²²⁸ supporting the notion of Lewis acid-base interactions between the oxygen lone-pair and the metal cations. The decrease in k_H has been partially attributed to the reduction in electron density in the C–H σ^* anti-bonding orbital which is normally present due to hyperconjugative overlap with the neighbouring oxygen lone-pair (See Scheme 1.4), as a consequence of the metal cation withdrawing electron density from the oxygen lone-pair.

A 2-fold decrease in k_H for the tertiary amine, triethylamine (TEA), is observed upon the addition of LiClO₄, for which an analogous orbital interaction explanation is also appropriate. Interestingly, the addition of 1.0 M Mg(ClO₄)₂ was reported to immediately form a precipitate. This precipitate was identified as the formation of a strong TEA-Mg²⁺ Lewis acid-base adduct. This observation is once again consistent with the stronger Lewis acidity of Mg²⁺ as compared to Li⁺, and also the significantly greater Lewis basicity of TEA vs THF.^{49,229} It was also pointed out that MeCN will competitively bind with metal cations, but it is a weaker Lewis base than both THF and TEA. Measurements of k_H for HAT between CumO[•] and TEA in the presence of 0.005 M Mg(ClO₄)₂ were successful only up until [TEA] = 9.6 mM, at which point a precipitate began to form. Nonetheless, an upper limit to the hydrogen abstraction rate constant was estimated as $k_H < 1 \times 10^6 \text{ M}^{-1}\text{s}^{-1}$, or at least a 200 fold decrease relative to no metal salt. Very similar results for bulkier tertiary amines were also obtained. Thus, the addition of strong Lewis acids in the

5.1. Introduction

presence of Lewis basic sites on hydrogen atom donors can deactivate C–H bonds.

Next, we turn to the more relevant models for the work of this thesis, the tertiary amides *N,N*-dimethylformamide (DMF) and *N,N*-dimethylacetamide (DMA). As with THF, normal hyperconjugative overlap between the conjugated amide π -system and the adjacent C–H σ^* anti-bonding orbitals weakens the C–H bonds. Therefore, metal binding to the amide oxygen-centre should result in a decrease in this orbital interaction, strengthen the C–H bonds, and decrease HAT reactivity. In their study, Salamone et al.⁵⁰ measured CumO $^\bullet$ abstraction rate constants from DMF and DMA in the presence of stoichiometric equivalents of LiClO₄, LiOTf, NaClO₄, Mg(ClO₄)₂, and Ca(ClO₄)₂ (in contrast to the excess used in Reference 49). Figure 5.1a,b shows the plots of k_{obs} against [substrate] for the reactions of CumO $^\bullet$ with DMF and DMA in MeCN containing 0.2 M Mg(ClO₄)₂, respectively. For both DMF and DMA, there are three distinct regions in the plots: weak C–H bond activation for $[amide]/[Mg^{2+}] \leq 2$, followed by strong C–H bond deactivation for $2 < [amide]/[Mg^{2+}] \leq 4$, and no deactivation for $[amide]/[Mg^{2+}] < 4$.

The addition of both LiClO₄ and LiOTf decrease to a similar extent the rate constants for abstraction from DMF and DMA by CumO $^\bullet$. However, in contrast to Mg(ClO₄)₂, the lithium salts strongly deactivate C–H bonds for 2 equivalents, followed by weak deactivation for another 2 equivalents, and no deactivation for $[amide]/[Li^+] < 4$. Salamone et al. were not able to give a clear cut explanation, but suggest that the different patterns are a result of differences in charge density, which is greater for Mg²⁺ than Li⁺, as well as different coordination geometries of the two ions. A coordination number of 4 is most common for Li⁺, while an octahedral geometry with the coordination of 6 ligands is almost always observed for Mg²⁺.^{230,231} As a result, interactions of the ions with solvent and counter-anions were suggested to be more important for Mg²⁺ than Li⁺.

5.1. Introduction

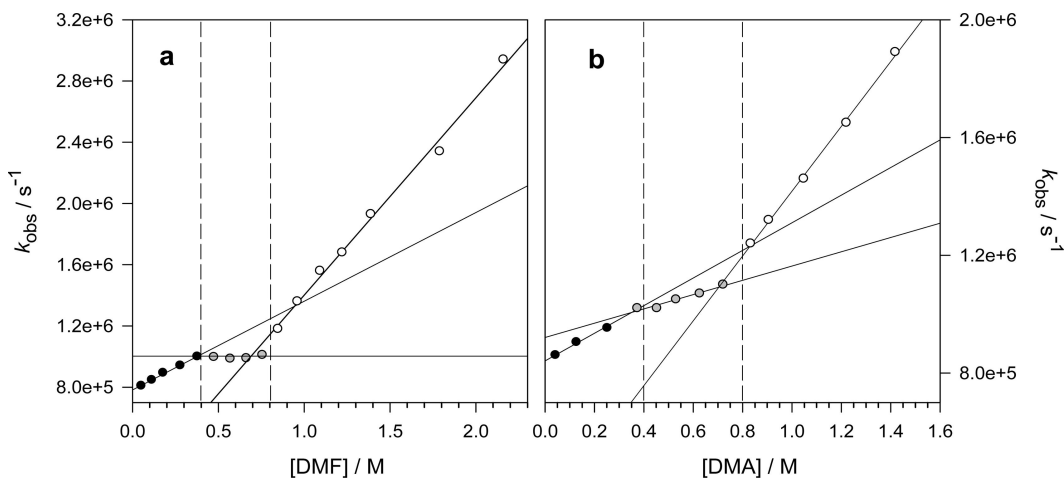


Figure 5.1: **a)** Plot of observed rate constant against concentration of DMF for reaction with CumO[•] at 298 K in the presence of 0.2 M Mg(ClO₄)₂. 0–0.4 M [DMF] range (black circles), $k_{H1} = 5.8 \times 10^5 \text{ M}^{-1}\text{s}^{-1}$; 0.8–2.2 M [DMF] range (white circles), $k_{H2} = 1.3 \times 10^6 \text{ M}^{-1}\text{s}^{-1}$. **b)** Plot of observed rate constant against concentration of DMA for reaction with CumO[•] at 298 K in the presence of 0.2 M Mg(ClO₄)₂. 0–0.4 M [DMA] range (black circles), $k_{H1} = 4.7 \times 10^5 \text{ M}^{-1}\text{s}^{-1}$; 0.4–0.8 M [DMA] range (grey circles), $k_{H2} = 2.4 \times 10^5 \text{ M}^{-1}\text{s}^{-1}$; 0.8–2.2 M [DMA] range (white circles), $k_{H3} = 1.1 \times 10^6 \text{ M}^{-1}\text{s}^{-1}$. Reprinted with permission from Reference 50. Copyright 2015 American Chemical Society.

5.1. Introduction

NaClO_4 and $\text{Ca}(\text{ClO}_4)_2$ influence HAT between CumO^\bullet and DMA to different extents than both LiClO_4 and $\text{Mg}(\text{ClO}_4)_2$. Figure 5.2a,b shows the plots of k_{obs} against [substrate] for the reactions of CumO^\bullet with DMA in MeCN containing 0.2 M NaClO_4 and $\text{Mg}(\text{ClO}_4)_2$, respectively. For NaClO_4 , an almost negligible deactivation of C–H bonds is observed for up to 4 equivalents of DMA. This was explained on the basis of the weaker Lewis acidity of Na^+ as compared to Li^+ . With regards to $\text{Ca}(\text{ClO}_4)_2$, binding to DMA fully deactivates C–H bond abstraction up to 4 equivalents of DMA. The first region of Figure 5.2b ($[\text{DMA}] = 0\text{--}0.2 \text{ M}$, black circles) represents the decrease in k_β of CumO^\bullet as Ca^{2+} preferentially binds to DMA over CumO^\bullet . Interestingly, for both DMF and DMA, the same experiments in dimethyl sulfoxide (DMSO) solvent show no inhibition of HAT reactivity by metal cations. This was rationalized on the basis of the stronger Lewis basicity of DMSO as compared to both MeCN and the amides, thus the metals preferentially bind the solvent rather than amide substrate.

Finally, Salamone et al.⁵¹ examined the effects of substrate structure on HAT reaction between CumO^\bullet and sterically bulky tertiary alkanamides in the presence of alkali and alkaline earth metal ions. For *N,N*-dialkylacetamides, the steric bulk of the *N*-alkyl groups was previously characterized.¹⁴⁶ Steric repulsion between CumO^\bullet and the *N*-alkyl groups can decreases the HAT rate constant, as evident by the 3-fold decrease in k_H in going from DMA to *N,N*-diisobutylacetamide (DIA; 1.2×10^6 and $3.1 \times 10^5 \text{ M}^{-1}\text{s}^{-1}$, respectively). For reactions of CumO^\bullet with DIA addition of 0.2 M LiClO_4 or $\text{Ca}(\text{ClO}_4)_2$ to results in the same trends in C–H bond deactivation observed for DMA. This indicates that the influence of metal cation-substrate binding is not significantly influenced by the steric bulk of *N*-alkyl groups. The same is true for the addition of 0.2 M $\text{Mg}(\text{ClO}_4)_2$ to abstraction from DIA by CumO^\bullet , as shown in Figure 5.3. Once again, a slight decrease in reactivity is observed for

5.1. Introduction

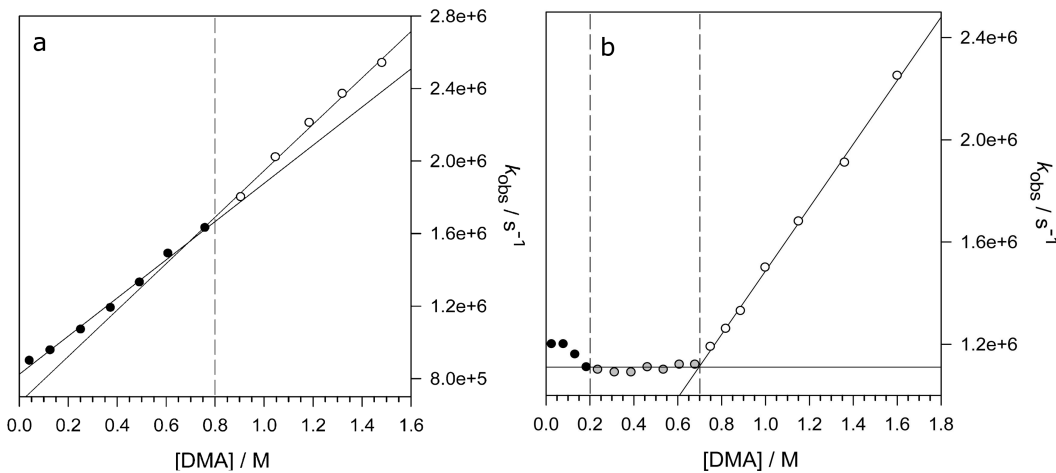


Figure 5.2: **a)** Plot of observed rate constant against concentration of DMA for reaction with CumO[•] at 298 K in the presence of 0.2 M NaClO₄. 0–0.8 M [DMA] range (black circles), $k_{H1} = 9.6 \times 10^5 \text{ M}^{-1}\text{s}^{-1}$; 0.8–1.4 M [DMA] range (white circles), $k_{H2} = 1.4 \times 10^6 \text{ M}^{-1}\text{s}^{-1}$. **b)** Plot of observed rate constant against concentration of DMA for reaction with CumO[•] at 298 K in the presence of 0.2 M Ca(ClO₄)₂. 0.8–1.7 M [DMA] range (white circles), $k_{H1} = 1.2 \times 10^6 \text{ M}^{-1}\text{s}^{-1}$. Adapted with permission from Reference 50. Copyright 2015 American Chemical Society.

the first 2 equivalents of DIA, followed by strong C–H bond deactivation for an additional two equivalents, and no deactivation beyond that. No additional insight was provided by Salamone et al. as to the reason for this reactivity. The plausible explanation provided was once again that Mg²⁺ has a high charge density. These results show that Lewis acid-base interactions between alkali or alkaline earth metal cations can greatly depress hydrogen abstraction by alkoxy radicals.

With these results in mind, I am interested in the possibility that alkali and alkaline earth metal cations found in biological system can protect C–H bonds in proteins from HAT to reactive oxygen-centred radicals. However, the experimental results do not answer some of the key physico-chemical determinants that may make this possible. Specifically, I have composed several important research questions that remain unclear from the experimental results.

The first question I have is one of methodology: Can DFT-based methods can ac-

5.1. Introduction

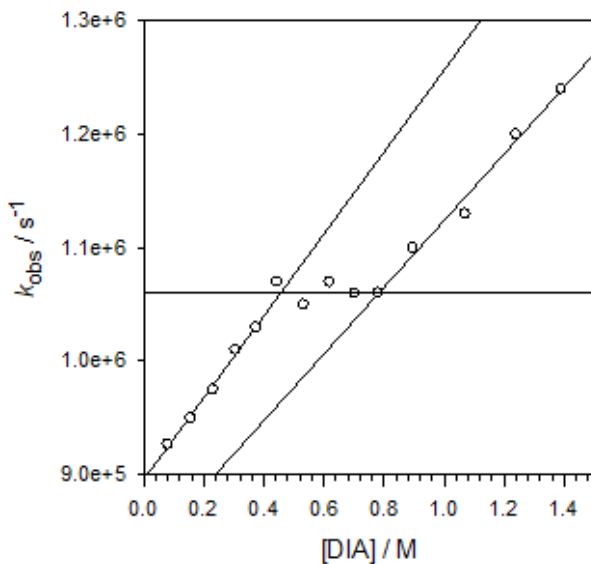


Figure 5.3: Plot of observed rate constant against concentration of DIA for reaction with CumO[•] at 298 K in the presence of 0.2 M Mg(ClO₄)₂. 0–0.4 M [DIA] range, $k_{H1} = 3.6 \times 10^5 \text{ M}^{-1}\text{s}^{-1}$; 0.8–1.4 M [DIA] range, $k_{H2} = 2.9 \times 10^5 \text{ M}^{-1}\text{s}^{-1}$. Reprinted from Tetrahedron, 72, Salamone et al., Hydrogen atom transfer from tertiary alkanamides to the cumyloxy radical. The role of substrate structure on alkali and alkaline earth metal ion induced CH bond deactivation, 7757–7763, 2016, with permission from Elsevier.

5.1. Introduction

curately treat alkali/alkaline metal cation binding to organic substrates or radicals? There exists limited ab initio data describing these interactions.^{232–235} Therefore, I have conducted a benchmark quality study involving Li⁺, Na⁺, Mg²⁺, K⁺, and Ca²⁺. To the best of my knowledge, this represents the first systematic benchmark study of these metal cations with both organic substrates and radicals.

Secondly, the nature of the binding of metal ions to substrates is still poorly described, especially given the odd stoichiometric effects observed for Mg(ClO₄)₂ with alkylamides. Specifically, I wish to address the range of these interactions, and how much the metals effect the C–H being broken. To address this I have utilized both Na⁺ and Mg²⁺ in my calculations. These metal ions were chosen to capture the large differences in Lewis acidity and ion size associated with these third-period ions, and because they are two of the most biologically relevant metal ions.

Thirdly, I address the effect that metal ions have on the HAT barrier heights. Experiments demonstrate that under certain conditions, the presence of metal ions can decrease HAT reactivity. If metal ions do effectively increase C–H bond strengths, this will be a contributing factor to the free energy barrier as per the BEP principle^{47,48} (see Chapter 4). There will likely be additional factors such as polarization in the TS complex, or other effects of possible charge transfer from the substrate to metal ions (or vice versa). To investigate this, I have primarily studied HAT reactions involving DMA and oxygen-centred radicals. Given there are only experimental data for CumO[·], this is the primary subject. However, I was interested in structural differences of the oxygen-centred radical, thus I have utilized BnO[·] as well, which differs significantly in that it has the ability to form strong pre-reaction complexes with hydrogen bond accepting substrates.^{144,166} I also investigated the effect metal cations have on the abstraction from DMA by the more biologically relevant hydroxyl radical (See Appendix C). I have also performed calculations with

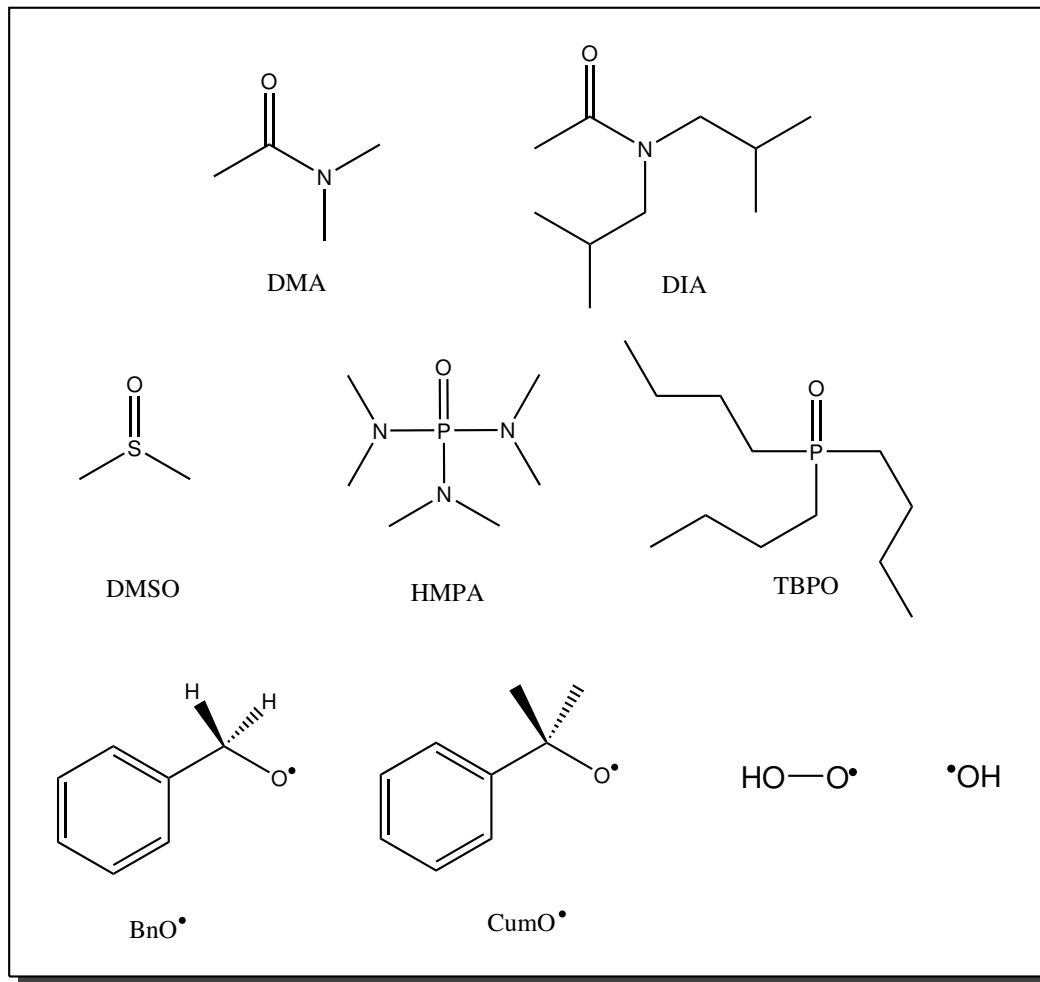
5.1. Introduction

the bulkier DIA substrate and CumO[•] to verify whether or not steric bulk does have an influence on the ability of a metal cation to affect HAT reactions.

Finally, given that reactions of DMA with CumO[•] in the presence of metal salts show no deactivation, I was interested in studying the reactivity of alkoxy radicals with strong Lewis bases. Strong Lewis basic compounds are important as they are often used as solvents in physical organic chemical experiments. Furthermore, strong Lewis acids are common in biological systems. Specifically, phosphates represent an important functionality as part of the DNA backbone, as well being important in adenosine triphosphate (ATP), the so-called “energy currency.” Sulfur containing amino acids are also susceptible to oxidation into sulfoxides and disulfoxides.²³⁶ Therefore, understanding the HAT reactivity of strong Lewis basic compounds with oxygen-centred radicals also contributes to the understanding of oxidative stress in biological systems.

HAT reactions involving alkoxy radicals and strong Lewis bases have been previously studied,^{144,237} and can possess interesting and unusual chemical reactivity. For instance, we recently showed that for the HAT reaction between BnO[•] and DMSO, BnO[•] acts as a hydrogen atom donor rather the acceptor.²³⁷ In light of this, I examined the effect of metal cations on the expected HAT reactivity between CumO[•] and DMSO, as well as the radical H-atom donation reactivity between BnO[•] and DMSO. I also performed calculations to determine the effects of metal cations and if there exists reverse reactivity for two other strong Lewis basic substrates: hexamethylphosphoramide (HMPA) and tributylphosphine oxide (TBPO). These results are reported in Appendix C. The chemical structures of all the species studies herein are shown Scheme 5.1.

5.1. Introduction



Scheme 5.1: Chemical structures of the species studied herein.

5.2 Computational methods and details

All quantum mechanical calculations were performed using either the Gaussian 09 software package,¹¹⁶ or the TURBOMOLE software package.⁷³ Detailed benchmark studies of metal cation-substrate interactions were carried out, the full data and discussion of which is presented in Appendix C. Calculations for the benchmark quality data of metal binding to substrates were first optimized at the LC- ω PBE-D3(BJ)/6-31+G(2d,2p) level of theory,^{109,110,151,152} and later re-optimized with larger 6-311+G(3df,3pd) basis sets. Single-point energy calculations were then carried out using the coupled cluster methodology with single, double and perturbative triples with full core correlation, CCSD(T,Full), and various basis sets. Final benchmark quality binding energies have been calculated using the F12* explicitly correlated method with Def2-QZVPPD primary basis sets and Def2-QZVPP auxiliary basis sets required for the resolution-of-the-identity (RI) approximation as implemented in TURBOMOLE. The RI approximation is used to reduce the computational cost associated with calculating MO integrals.²³⁸ A total of 31 different DFT-based methods with nearly complete 6-311+G(3df,3pd) and moderate sized 6-31+G(2d,2p) basis sets were tested both by single-point energy calculations on the LC- ω PBE-D3(BJ)/6-311+G(3df,3pd) optimized reference structures. Geometry optimization calculations starting from the reference structures were also performed for three of the best performing DFT-based method, in order to verify their ability to capture the minimum energy bound structures. The final DFT-based method selected from this benchmark work is M05-2X.¹⁰³

To test the effects of metal cations on HAT barrier heights, calculations were first performed for the reactions not involving metal cations. Geometry optimizations were performed at the M05-2X/6-31+G** level of theory. Transition state (TS) structures were obtained by first freezing the abstraction donor-hydrogen-acceptor

5.2. Computational methods and details

bond lengths with multiple initial orientations. The frozen bonds were then relaxed to obtain the final TS structures, which were then used to identify the appropriate pre- and post-reaction complexes. All structures were subjected to harmonic vibrational frequency calculations, which were visualized using the Chemcraft program¹⁹⁷ to verify minima (or saddle-points with a single imaginary frequency connecting reactants to products for TS structures). Single-point energy calculations were performed at the M05-2X/6-311+G(2d,2p) level of theory. The effects of MeCN solvent were estimated by inclusion of the SMD¹²² continuum solvent model in single-point energy calculations.

The inclusion of metal cations into the TS structures proved to be technically challenging. It was my expectation that I could simply include metal cations and necessary counter-anions into the minimum energy complex structures and re-optimize; this was not the case. TS structures were once again obtained by constrained optimization with the inclusion of the metal cation and counter-anion and freezing the abstraction donor-hydrogen-acceptor bond lengths, providing a guess TS structure. However, in most cases the force constants (which are necessary for a TS optimization calculation) from the guess TS structure were not representative of the true TS structure, thus force constants were recalculated for every step along the optimization, using the “CalcAll” keyword in Gaussian. This is a very computationally expensive procedure. Even using this method, many TS structures including metal cations failed to converge. Therefore, guess TS structures that contain a single imaginary frequency connecting reactants to products are used in place. This technique provides genuine TS structures, although they may not be the TS associated with the minimum energy reaction pathway. Nonetheless, the guess TS structure can be used to provide an estimate of the reaction barrier height that are verified with calculations that were successful. Where available, final TS structures

5.3. Exploring the nature of metal cation substrate interactions

were used to identify the appropriate pre- and post-reaction complexes.

Natural bond order (NBO) and natural population analysis (NPA) were utilized in order to investigate the electronic structures involved in the HAT reactions and the effects of metal cation binding.^{239–241} Version 3.1 of the NBO software package,²⁴² as implemented in the Gaussian 09 package was used in all cases.¹¹⁶ NBO analysis provides a means for estimating the physical effects of chemically intuitive orbital interactions while NPA charges are a means for calculating the occupancies and charges of atomic centres.^{243,244}

5.3 Exploring the nature of metal cation substrate interactions

The first step to understanding the effect non-redox active metal have on HAT reaction barrier heights is investigating the nature of the binding interaction. Figure 5.4a,b show the potential energy surfaces (PESs) of the binding of sodium ion, and sodium chloride to DMA, respectively. There are three surfaces in each plot representing the same potential energy surface in the gas-phase (black circles), and in an SMD¹²² continuum solvent field of MeCN (grey squares) or water (white circles). For both sodium ion and sodium chloride, the gas-phase PES demonstrates strong binding with respect to a solvated system. This is indicated by a much deeper well than both solvents and a long-range interaction that does not tail off within 6 Å due to the lack of screening. This underscores the importance of including solvent effects in studying the effects of metal cations. Interestingly, for the effects of water compared to MeCN solvent appears to be quite small. In both cases the difference between the minimum of the water PES is about 2.5 kcal mol⁻¹. Furthermore, the minimum of the PES well in all cases falls at about the same distance (2.1–2.2 Å) in

5.3. Exploring the nature of metal cation substrate interactions

the gas-phase and in both solvents. The small differences in binding interactions indicate that the effects as measured in MeCN may also apply to the more biologically relevant aqueous system.

For both the ion and the salt of sodium in water and MeCN, the binding interaction only approaches zero slowly. Even at 6 Å, the predicted binding energy of DMA in water with Na^+ and NaCl are 1.1 and 0.7 kcal mol⁻¹, respectively. This is an indication that M05-2X-SMD does not properly capture long-range interactions of DMA with sodium. This may be a result of not fully capturing the screening effect of solvent. Nonetheless, at a distance of 5 Å, which corresponds well with the size of the first solvation shell of the sodium ion,²⁴⁵ the interaction between DMA and sodium is nearly zero. This result is consistent with literature that studies the Hofmeister series, where it has been shown that biologically relevant cations are only able to influence their immediate solvation shell.^{246,247} Furthermore, Heyda et al.²⁴⁸ utilized molecular dynamics simulations of *N*-methylacetamide in aqueous solutions of NaCl, NaBr, KCl, and KBr to obtain radial distribution functions (RDFs). The RDFs are in agreement with the calculated PESs in that the most probable distance to find Na^+ from the amidic oxygen-centre is at about 2–2.5 Å separation. Heyda et al. also showed that Na^+ binds more strongly with the amide than K^+ , and that the nature of the halide counteranion does not contribute significantly to the overall interaction. This is consistent with the results of Salamone et al., which showed that the nature of the counteranion plays a negligible role to the effect on rate constants.⁴⁹ The calculated binding energies of NaCl and NaClO_4^- to DMA are very similar in magnitude (-16.0 and -18.1 kcal mol⁻¹, respectively). From these results it is possible to draw an important conclusion: The use of Cl^- in the calculations may reasonably reflect the trends observed by Salamone et al. with ClO_4^- and OTf^- .

5.3. Exploring the nature of metal cation substrate interactions

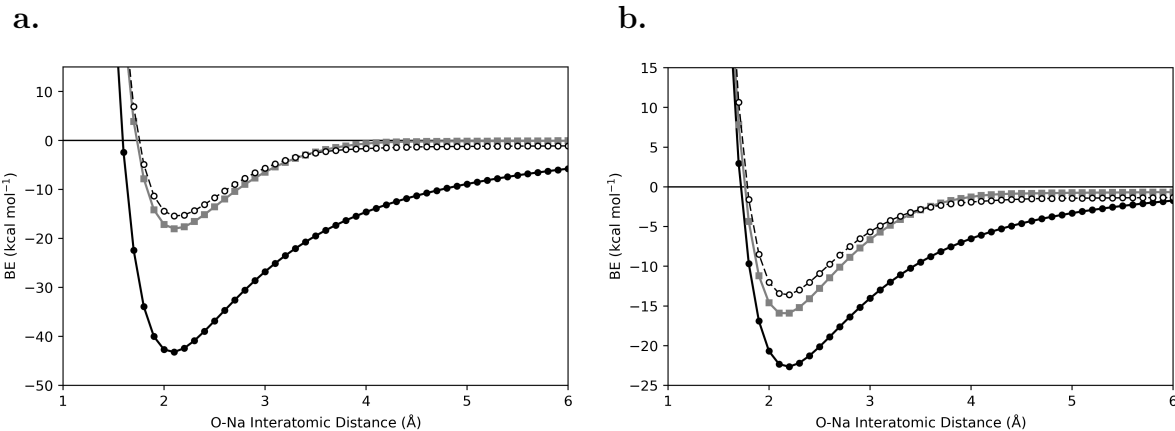


Figure 5.4: Potential energy surface of binding energy between DMA and **a**) sodium cation and **b**) sodium chloride as a function of O-Na interaction distance (Å). The black line and points represent gas-phase results, the grey squares and line is in continuum MeCN solvent, and white circles and dashed line is in continuum water solvent. Calculated as a rigid scan from the M05-2X/6-31+G** minimized complex structure at the M05-2X/6-311+G(2d,2p) level of theory with the SMD solvent model.

Figure 5.5a,b show the PESs of the binding of magnesium ion and magnesium dichloride to DMA, respectively. As is the case for Na^+ , the gas-phase PES of Mg^{2+} is very strongly bound. In fact, the binding energy does not asymptotically approach zero. At an O-Mg distance of 12 Å, there is calculated binding interaction of -48.5 kcal mol⁻¹, which is actually greater than at 6 Å by about 5 kcal mol⁻¹. This is a result of the the ionization potentials (IP) of the metals with respect to that of DMA. The experimental IP^{249–251} of DMA is 8.8–9.2 eV, the first IP of Na is 5.1 eV, and the second IP of Mg is 15.0 eV (calculated with M05-2X/6-311+G(2d,2p) = 8.9, 5.0, and 14.9 eV, respectively). In a solvated system, magnesium ions exist invariably in the +2 oxidation state. However, due to nature of the IPs, DFT-based methods prefer to transfer charge, resulting in a non-convergent binding interaction between DMA and Mg^{2+} , but not for Na^+ .

5.3. Exploring the nature of metal cation substrate interactions

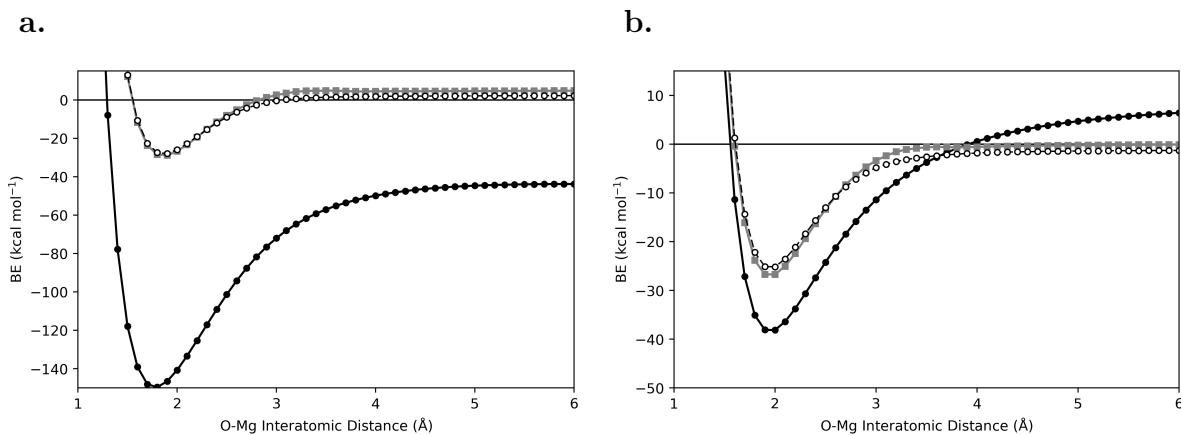


Figure 5.5: Potential energy surface of binding energy between DMA and **a)** magnesium cation and **b)** magnesium chloride as a function of O-Mg interaction distance (\AA). The black line and points represent gas-phase results, the grey squares and line is in continuum MeCN solvent, and white circles and dashed line is in continuum water solvent. Calculated as a rigid scan from the M05-2X/6-31+G** minimized complex structure at the M05-2X/6-311+G(2d,2p) level of theory with the SMD solvent model.

The inclusion of MeCN and water solvent appear at first glance to alleviate this problem. Note however that both PESs cross over zero binding at about 3 \AA , indicating there is still charge transfer to some extent. Additionally, for magnesium chloride in the gas-phase, there also appears to be charge transfer occurring, as evident by the PES crossing zero just below 4 \AA . On the other hand, the inclusion of either water or MeCN solvent with MgCl_2 give reasonable PESs with a binding interaction of about -25 kcal mol⁻¹ for both water and MeCN, and a tailing off at about 3 \AA , or slightly larger than the size of the first hydration shell of Mg^{2+} (ca. 2 \AA).²⁵² Therefore, studying the effects of magnesium on HAT reaction barriers may be possible using MgCl_2 . Given the difficulties with Mg in general, I elected to focus only on NaCl for future considerations.

Next, I performed calculations to determine if the interaction of metal cations

5.3. Exploring the nature of metal cation substrate interactions

systematically increase the bond strengths of C–H bonds in the models of interest in this work. This effect is hypothesized to occur due to a decrease in electron density in the C–H σ^* orbital, which is normally present due to hyperconjugative overlap. The BDEs for several substrates in the presence of Na^+ and NaCl are listed in Table 5.3. The ROCBS-QB3 BDEs for each of the substrates is included to demonstrate that the relative order of BDEs for substrates with multiple C–H bonds is reasonable. The BDE for an arbitrary metal substrate complex ($\text{M}\cdots\text{X}-\text{H}$) can be calculated as:

$$BDE = E(\text{M}\cdots\text{X}\cdot) + E(\text{H}\cdot) - E(\text{M}\cdots\text{X}-\text{H}) \quad (5.1)$$

Table 5.3: Bond dissociation enthalpies of DMA, DMSO, MeCN, and DIA with Na^+ , NaCl, and without metal cations (Bare) calculated at the M05-2X-SMD(MeCN)/6-311+G(2d,2p)//M05-2X/6-31+G** level of theory. ROCBS-QB3-SMD(MeCN) BDEs without metals are included for reference. All values are in kcal mol⁻¹.

Substrate	ROCBS-QB3		M05-2X	
	Bare	Bare	Na^+	NaCl
DMA (acetyl)	101.0	98.5	97.8	98.4
DMA (cis)	94.8	92.2	93.2	94.0
DMA (trans)	94.3	91.6	92.8	92.6
DMSO	104.3	103.4	104.4	103.7
MeCN	99.0	97.4	98.3	98.1
DIA (acetyl)	99.7	97.8	97.5	97.7
DIA (α -cis)	97.0	95.7	96.5	95.3
DIA (β -cis)	98.3	96.4	94.8	93.1
DIA (α -trans)	94.6	93.0	93.8	94.0
DIA (β -trans)	97.3	95.3	95.5	95.5

For DMA, the *N*-methyl groups cis and trans relative to the carbonyl are the weakest, and therefore most thermodynamically favourable for abstraction. Salamone et al.¹⁶⁶ showed that both $\text{BnO}\cdot$ and $\text{CumO}\cdot$ prefer to abstract from the *N*-methyl groups of DMA, rather than the acetyl group. The complexation of Na^+ increases the cis BDE by 1.0 kcal mol⁻¹ and the trans BDE by 1.2 kcal mol⁻¹. The

5.3. Exploring the nature of metal cation substrate interactions

complexation of NaCl to DMA increases the cis BDE by 1.8 kcal mol⁻¹ and the trans BDE by 1.0 kcal mol⁻¹. One would expect the greater positive charge of the sodium cation (as compared to the sodium moiety of NaCl) to have a greater effect on the BDEs. However, these calculations indicate this may not always be the case. Specifically, the cis BDE is 0.8 kcal mol⁻¹ weaker for the DMA–NaCl complex as compared to the DMA–Na⁺ complex. These results, which are inconsistent with the hypothesis, can be explained by additional analysis of both the parent and radical complexes. The structures of the DMA-NaCl complex and three possible radical complexes are shown in Figure 5.6a-d.

NBO analysis can be used that give a qualitative description based on perturbation theory of the energy contribution of specific NBO interactions.²⁴⁴ Using NBO analysis on DMA, the estimated effect of hyperconjugative overlap reveals a weakening of the *N*-methyl C–H bonds by approximately 5.6 and 5.9 kcal mol⁻¹ for the cis and trans positions, respectively. Upon complexation of Na⁺, the bond weakening effects become 3.7 and 4.1 kcal mol⁻¹ for the cis and trans positions, respectively. Therefore, from an NBO perspective, the cis and trans *N*-methyl bond strengths can be described as strengthening upon complexation of Na⁺. Furthermore, the predicted effect of hyperconjugative overlap in the DMA–NaCl complex are 5.4 and 5.5 kcal mol⁻¹ for the cis and trans positions, respectively. Again, from an NBO perspective, the complexation of NaCl can be said to strengthen the *N*-methyl C–H bonds in DMA, but not as much as Na⁺. NBO analysis of the parent complexes thus supports the hypothesis.

However, BDEs can be affected by both parent and radical stability. The hypothesis considers only the stability of the parent molecule, where complexation of a metal cation stabilizes the parent by withdrawing electron density from an anti-bonding orbital. In the case of complexation of NaCl, secondary interactions

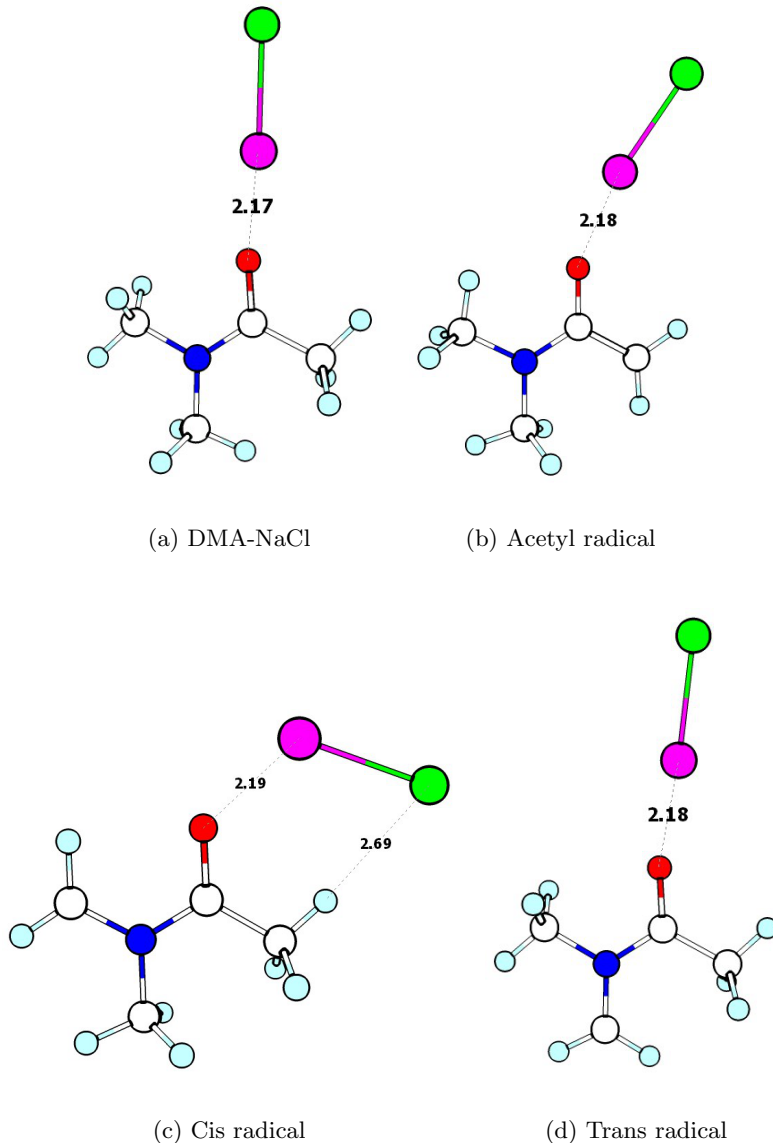


Figure 5.6: Structures of **a** the DMA-NaCl complex, **b** the DMA-NaCl acetyl radical complex, **c** the DMA-NaCl cis radical complex, and **d** the DMA-NaCl trans radical complex. Key interaction distances are shown in units of Å. Element colour key: white is carbon, light blue is hydrogen, red is oxygen, blue is nitrogen, purple is sodium, and green is chlorine.

5.3. Exploring the nature of metal cation substrate interactions

between the Cl moiety of NaCl and the radical can result in the destabilization of the radical complex and a further increase in the predicted C–H BDE. This is the case for the cis-DMA-NaCl radical complex (Figure 5.6c). The Cl moiety of NaCl is attracted to the partial positive charge of the acetyl hydrogen of DMA, which is greater than the partial charge on the cis *N*-methyl hydrogens ($0.25\text{ }e^-$ vs. $0.21\text{ }e^-$). This leads to the donation of electron density from Cl to the C–H σ^* orbital. NBO estimates this orbital interaction to amount to about 1 kcal mol^{-1} of bond weakening. Therefore, the hypothesis is incomplete in that it does not account for radical complex stability. Furthermore, with respect to TS complexes, additional interactions may further complicate the picture.

Interestingly, the predicted BDE for the acetyl position of DMA decreases, rather than increasing as hypothesized, with both Na^+ and NaCl. This can be attributed to the change in electronic structure associated with the complex. Consider the two possible resonance forms of DMA shown in Figure 5.7. Glendening and Hrabal²⁵³ utilized natural resonance theory to estimate that the right-hand resonance structure in the closely related formamide contributes about 30% to the overall resonance hybrid. On the other hand, NBO analysis predicts a bond order in DMA of 1.5 between the C and O and the C and N. Nonetheless, the complexation of DMA to Na^+ slightly increases the contribution of the zwitterionic form, resulting in a decrease in electron density at the carbonyl carbon. This is evidenced by the increase in NPA charge at the carbonyl carbon from +0.72 in DMA to +0.74 in the DMA- Na^+ complex. The partially positively-charged carbon centre inductively withdraws electron density, stabilizing the acetyl radical. This increases the π -bonding character between the two carbon centres, and decreases the effective BDE.

The observed inductive effects also manifest in the decrease in the carbonyl-acetyl C–C bond lengths in the acetyl radical, which decrease from 1.457 \AA to 1.443 \AA .

5.3. Exploring the nature of metal cation substrate interactions

Å upon complexation of Na^+ . Complexation of NaCl results in a bond length of 1.451 Å. These results are consistent with the ordering of the calculated acetyl BDEs ($\text{DMA} > \text{DMA}-\text{NaCl} > \text{DMA}-\text{Na}^+$). On the other hand, the amidic nitrogen becomes net more positive upon complexation of either Na^+ or NaCl, but still has an NPA charge that is negative. As a result, there is no inductive stabilization effect for the *N*-methyl radical complexes.

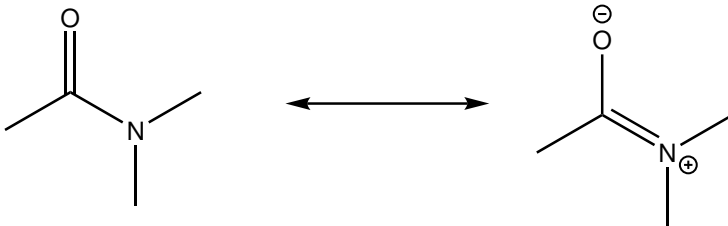


Figure 5.7: The resonance forms of DMA.

For MeCN and DMSO the complexation of either Na^+ or NaCl results in an increase in C–H BDE. In MeCN, the electron density in the C–H σ^* anti-bonding orbital decreases as a result of the interaction between Na and the nitrogen centre. DMSO has a non-Lewis electronic structure, making it difficult to analyze orbital interactions of valence-bond orbitals. Nonetheless, there is normally hyperconjugative overlap between the sulfur centre and the C–H σ^* anti-bonding orbitals, which was confirmed by NBO analysis. The electron density in the C–H σ^* orbital decreases as a result of the interaction of Na^+ with the oxygen-centre of DMSO.

Upon complexation of NaCl, the BDEs of the more sterically bulky amide substrate DIA follow the same trend that is observed as for DMA: The acetyl C–H BDE decreases due to inductive stabilization, while the C–H bonds α to the amidic nitrogen centre increase as a result of decreased C–H σ^* occupancy. Alkoxy radicals are not expected to abstract from C–H BDEs of the bonds β to the nitrogen centre in DIA or other longer chain *N*-alkyl amides, as the incipient radical is not

5.3. Exploring the nature of metal cation substrate interactions

stabilized by the amidic π -system. However, due to steric repulsion, the α -radicals of DIA cannot lie directly plane of allowing conjugation with the π -system. As such the α -C–H BDEs of DIA are greater than those of DMA by 2–3 kcal mol^{−1}, and are closer to the β -C–H BDEs than perhaps expected. The effects of sodium binding to the amidic oxygen are almost nil for the β -trans C–H bond of DIA, but there is a significant decrease in the β -cis C–H BDE. Figure 5.8a,b shows the structures of the DIA-NaCl complex and the β -cis radical complex, where it can be seen that the metal cation interacts with both the oxygen-centre and the carbon-centred radical. This interaction stabilizes the radical complex and thus decreases the effective BDE; this interaction is likely not possible in the TS structure and is not expected to contribute to a reduction of the barrier height.

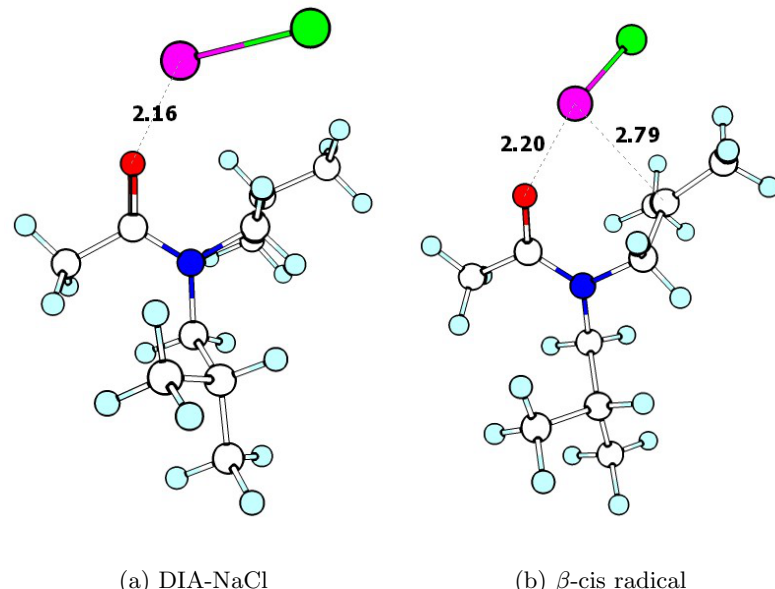


Figure 5.8: Structures of **a** the DMA-NaCl complex, **b** the DIA-NaCl β -cis radical complex. Key interaction distances are shown in units of Å. Element colour key: white is carbon, light blue is hydrogen, red is oxygen, blue is nitrogen, purple is sodium, and green is chlorine.

5.3. Exploring the nature of metal cation substrate interactions

All of these results together confirm that specific metal-substrate interactions can increase the effective BDEs of abstractable C–H bonds by decreasing C–H σ^* occupancy. However, this is complicated by the possibility for secondary interactions between the metal or counter-anion with the formed radicals. Furthermore, additional factors such as induction can alter the effects. It appears that for C–H bonds α to atoms with LPs that hyperconjugatively overlap with the C–H σ^* anti-bonding orbital, the complexation of non-redox active metals increases the C–H bond strength. However, if the C–H bond is adjacent to an electron-poor centre, such as the carbon of a carbonyl, metal complexation actually decreases the bond strength slightly by stabilizing the carbon-centred radical. In the context of HAT reaction barrier heights, increasing the effective C–H bond strength should decrease the reaction-rate slightly by destabilizing the TS complex. However, there are other important factors to consider such as how the metal effects the dipole moment in the TS complex. Furthermore, it is important to note that experiments showed that NaClO₄ did not significantly affect the HAT rate constants for reactions between CumO[•] and organic substrates. Therefore, the effects observed herein likely are an exaggeration of what is truly occurring *in situ*. Nonetheless, these theoretical calculations may be useful in developing an understanding of the subtle nature of the effects of non-redox active metal cations on HAT reactions in general.

With regards to the implications these results have on protein systems, since abstraction occurs predominantly from an α -C–H bonds, it is likely that the nature of the amino acid, and the three dimensional structure of the protein will have significant importance. As the geometry of the peptide backbone becomes more strained by steric interactions, the α hydrogen will become more difficult to abstract, as might be exemplified by the higher C–H BDEs in DIA as compared to DMA. In the absence of secondary interactions, alkali or alkaline earth-metals are able to

5.4. HAT reactions involving non-redox active metals

bind to a given carbonyl site on the surface of a protein, they may exert a chemo-protective effect by increasing the BDE of an adjacent C–H bond. However, the complexity of biological systems makes the absence of secondary interaction unlikely. Therefore, the possibility for chemo-protection to occur is remote.

5.4 HAT reactions involving non-redox active metals

5.4.1 DMA

Hydrogen abstraction reactions involving the oxygen-centred radicals BnO^\bullet and CumO^\bullet and DMA in MeCN have been previously investigated experimentally and theoretically.¹⁶⁶ The HAT reaction between DMA and BnO^\bullet was determined to occur predominantly through a direct HAT mechanism from the *N*-methyl group cis relative to the carbonyl, and is kinetically limited by the formation of a strong pre-reaction complex between the relatively acid α -C-H of BnO^\bullet and the amidic oxygen centre. On the other hand, CumO^\bullet cannot form a strong hydrogen-bonding interaction, and thus forms a non-specific dispersion-bound pre-reaction complexes. Abstraction by CumO^\bullet still takes place from one of the *N*-methyl groups, but the rate constant is 2 orders of magnitude less than for BnO^\bullet . Recall that the inclusion of metal salts in reactions of DMA with CumO^\bullet were previously investigated.⁵⁰ On the basis of the exaggerated effects observed in the changes in BDEs and the technical difficulties associated with these studies, the goal of this work is not to reproduce experimental results, but rather, develop insights into the possible changes that can occur as a result of metal salt addition to HAT reactions.

Herein, I have calculated the reaction barrier heights for all three abstractable positions of DMA for HAT reactions involving CumO^\bullet and BnO^\bullet , both with and without NaCl. These data are summarized in Table 5.4. Perhaps alarmingly, the

5.4. HAT reactions involving non-redox active metals

free energy barriers calculated at the M05-2X-SMD(MeCN)/6-311+G(2d,2p)//M05-2X/6-31+G** are systematically higher than those previously calculated by about 8.5 kcal mol⁻¹.¹⁶⁶ The previously calculated results were in reasonable agreement with experimental results. The reason for this discrepancy is unclear, given that M05-2X has previously been used successfully to calculate accurate HAT rate constants.²⁵⁴ Furthermore, the optimized minimum energy structures from both methods do not differ significantly, with the exception of slightly shorter abstracting C–H partial bonds and slightly elongated O–H partial bonds in the TS structures excluding NaCl (ca. 0.03 to 0.05 Å). However, the relative ranking and differences in energies for the reaction barrier heights for the different C–H bonds are consistent with previous results. Therefore, although these results cannot be used to predict rate constants, they are useful for studying the change in barrier height due to the complexation of NaCl.

Table 5.4: Calculated free energy (enthalpy) barrier ($\Delta G(H)^\ddagger$, kcal mol⁻¹) for direct HAT from different C–H bonds in DMA by CumO[•] and BnO[•], with and without NaCl. The change in barrier height ($\Delta\Delta G(H)^\ddagger$) is calculated relative to the same abstraction site without the inclusion of NaCl. All barrier heights are relative to separated reactants (or complexed DMA-NaCl) and were calculated at the M05-2X-SMD(MeCN)/6-311+G(2d,2p)//M05-2X/6-31+G** level of theory.

Reaction	Abstraction Site	$\Delta G(H)^\ddagger$	$\Delta\Delta G(H)^\ddagger$
DMA + CumO [•]	trans	17.3(3.4)	
	cis	17.5(3.8)	
	acetyl	21.6(7.5)	
DMA-NaCl + CumO [•]	trans	20.3(3.7)	3.0(0.3)
	cis	18.4(1.2)	0.9(-2.6)
	acetyl	21.0(4.3)	-0.6(-3.2)
DMA + BnO [•]	trans	16.5(3.7)	
	cis	17.5(3.6)	
	acetyl	20.8(7.8)	
DMA-NaCl + BnO [•]	trans	18.6(1.7)	2.1(-2.0)
	cis	17.8(4.7)	0.3(1.1)
	acetyl	22.0(4.7)	1.2(-3.1)

5.4. HAT reactions involving non-redox active metals

Focussing first on the barrier heights for HAT between DMA and CumO[•], the results of complexation with NaCl is variable. For each of the acetyl, cis, and trans C–H bond positions of DMA, there are three distinct effects upon complexation of NaCl. For the trans position, both the free energy and enthalpic barriers increase, for the cis position the free energy barrier increases and the enthalpic barrier decreases, and for the acetyl position both the free energy and enthalpic barriers decrease. The reasons for this can be understood by examining the TS structures, which are shown in Figure 5.9a-f.

First, note for all the TS structures in Figure 5.9, the complexation of NaCl results in a shortening of the O–H bond that is being formed as a result of the HAT reaction. This indicates that the TS structure shifts towards the product side along the reaction coordinate as a results of interactions with NaCl. By Hammond’s postulate,¹⁷⁸ this indicates a more endothermic reaction, giving evidence for increased reaction barrier heights.

For the TS structure representing abstraction from the trans position (relative to the carbonyl) C–H bond of DMA by CumO[•] (Figure 5.9a), there is a calculated 0.3 kcal mol⁻¹ increase in ΔH^\ddagger , which is somewhat less than the predicted increase in BDE of 1.0 kcal mol⁻¹. This result is consistent with the BEP principle, as the change in ΔH^\ddagger is necessarily less than or equal to the change in ΔH due to the constant α in Equation 1.1. This difference can possibly be ascribed to the effect of charge transfer: NPA indicates a 0.04 e^- transfer from DMA to NaCl. As a result, there is less electron density available for hyperconjugative donation to the C–H σ^* orbital, and thus there is a lesser effect upon ΔH^\ddagger . Furthermore, TSs for HAT between C–H bond and oxygen-centred radicals are characterized by a degree of charge separation.²⁰⁹ NPA indicates that in the trans position TS structure excluding NaCl the charge transfer from DMA to CumO[•] is 0.24 e^- , but

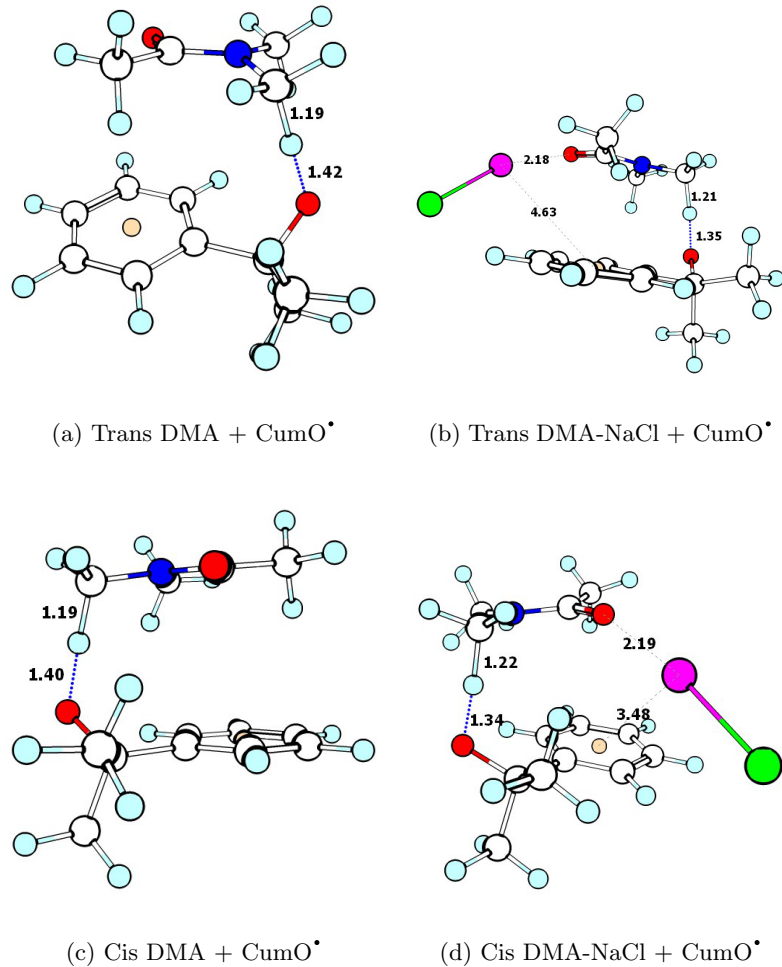


Figure 5.9: Continued on following page.

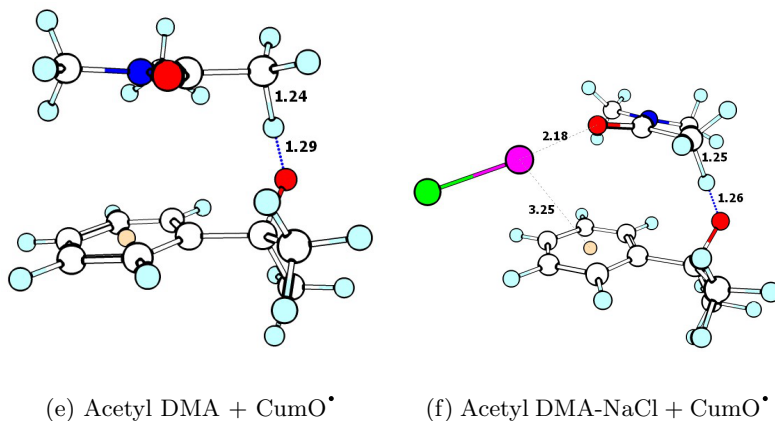


Figure 5.9: TS structures of HAT reaction between DMA and CumO[•] including NaCl for different C–H bonds: **a** trans, **b** trans with NaCl, **c** cis, **d** cis with NaCl, **e** acetyl, and **f** acetyl with NaCl. Key interatomic distances are shown in units of Å. Element colour key: white is carbon, light blue is hydrogen, red is oxygen, blue is nitrogen, purple is sodium, green is chlorine, and peach is a dummy atom in the centre of an aromatic ring.

the charge transfer increases with the inclusion of NaCl to $0.26\text{ }e^-$. This increased charge separation results in a lower enthalpic barrier than expected solely on the basis of the increase in C–H BDE. While orbital analysis does not indicate any PCET type orbital interactions, charge separation between DMA and CumO[•] in the TS structure may be considered as a partial ionization of the hydrogen atom. Therefore, by increasing charge separation in the TS structure, it becomes easier to abstract the hydrogen atom as there is an increase in the proton-transfer like character of the hydrogen atom. The increase in ΔG^\ddagger is 3.0 kcal mol^{-1} , therefore the complexation of metal cations increases the entropic penalty in forming the TS structure.

In the abstraction at the cis position C–H bond of DMA by CumO[•], there is a calculated 2.6 kcal mol⁻¹ decrease in ΔH^\ddagger and an increase of 0.9 kcal mol⁻¹ in ΔG^\ddagger . The decrease in enthalpic barrier is inconsistent with the predicted increase in BDE

5.4. HAT reactions involving non-redox active metals

of $1.8 \text{ kcal mol}^{-1}$ upon complexation with NaCl. The TS structure in Figure 5.9c shows a possible long range interaction between Na and the aromatic ring of CumO $^{\cdot}$ that draws electron density and increases the reactivity. Additionally, NPA predicts a $0.07 e^-$ charge transfer between DMA and Na. The combination of these two factors stabilizes the TS and decreases ΔH^{\ddagger} . The entropic penalty associated with complexation of NaCl results in an increase in the free energy barrier.

Abstraction by CumO $^{\cdot}$ from the acetyl C–H bond of DMA was previously described as being a minor reaction pathway.¹⁶⁶ In light of the reduction in BDE at the acetyl position of amides, it may be reasonable to expect the reaction barrier to decrease. This indeed appears to be the net effect of complexation of NaCl to DMA, as ΔH^{\ddagger} decreases by $3.1 \text{ kcal mol}^{-1}$ and ΔG^{\ddagger} decreases by $0.6 \text{ kcal mol}^{-1}$. Figure 5.9f shows that in the TS structure, Na interacts with the aromatic system of CumO $^{\cdot}$, which also stabilizes the TS and decreases the barrier, but not enough to make it the lowest barrier.

For HAT between DMA and BnO $^{\cdot}$, the interaction between NaCl and BnO $^{\cdot}$, are stronger as compared to CumO $^{\cdot}$, as indicated by the shorter distance between Na and the centre of the aromatic ring, as shown in Figure 5.10a-f. Note that, as in reactions with CumO $^{\cdot}$, the O–H partial bond in the TS structures are shorter upon complexation with NaCl, indicating greater product-like character in the TS complex. This shorter distance is likely possible due to the easier rotation of DMA relative to BnO $^{\cdot}$, as compared to CumO $^{\cdot}$. As a result, the enthalpic barriers for the abstraction from DMA by BnO $^{\cdot}$ decrease upon complexation of NaCl to both the acetyl and trans position C–H bonds. For the cis position C–H bond of DMA, the enthalpic barrier increases.

This can be explained on the basis of the presence of an interaction between Cl and the α -C–H bond of BnO $^{\cdot}$. While Na withdraws electron density from the

5.4. HAT reactions involving non-redox active metals

aromatic system of BnO^\bullet , Cl is able to donate electron density back to BnO^\bullet , counteracting the effect of the interaction of Na. Charge analysis confirms this, such that the NPA charge on Cl in the cis position abstraction TS complex is -0.88 e^- , as compared to -0.91 e^- in abstraction from the trans position. As a result, the enthalpic barrier increases as predicted on the basis of the increase of the cis position C–H BDE of DMA.

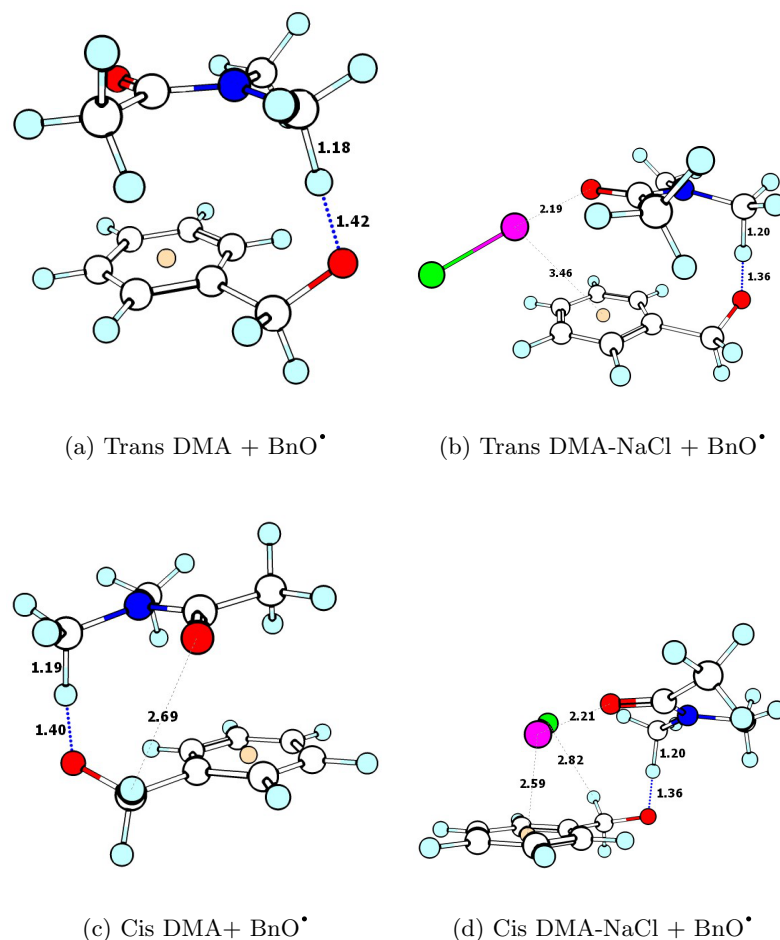


Figure 5.10: Continued on following page.

For both CumO^\bullet and BnO^\bullet , the presence of possible secondary interactions be-

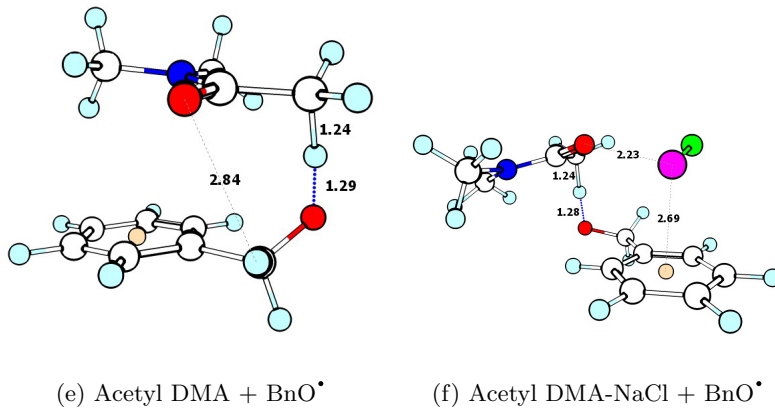


Figure 5.10: TS structures of HAT reaction between DMA and BnO^\bullet including NaCl for different C–H bonds: **a** trans, **b** trans with NaCl, **c** cis, **d** cis with NaCl, **e** acetyl, and **f** acetyl with NaCl. Key interatomic distances are shown in units of Å. Element colour key: white is carbon, light blue is hydrogen, red is oxygen, blue is nitrogen, purple is sodium, green is chlorine, and peach is a dummy atom in the centre of an aromatic ring.

tween NaCl and the radicals obfuscates the results. Therefore, in order to determine if non-redox active metal cations may act as chemo-protective agents in biological systems, I have performed calculation involving the more biologically relevant HO^\bullet radical. Although there is no literature value for k_H of the HAT reaction between DMA and HO^\bullet , I have used the Snelgrove-Ingold equation²⁵⁵ to estimate the rate constant as $1.5 \times 10^{10} \text{ M}^{-1}\text{s}^{-1}$, which is two and five orders of magnitude greater than BnO^\bullet and CumO^\bullet , respectively. Unfortunately, I was unsuccessful in performing full optimization calculations in the presence of the metal salt. Therefore, I have listed these preliminary results and the analysis thereof in Appendix C.

5.4.2 DIA

Next, to study the effect steric bulk has on the HAT reactions between amides and oxygen-centred radical, I have performed a study of HAT between DIA and

5.4. HAT reactions involving non-redox active metals

CumO[•]. The HAT reaction between DIA and CumO[•] was previously studied by Salamone et al.¹⁴⁶, but only the α -N-alkyl positions were studied theoretically. Since the BDEs for α - and β -N-alkyl C–H positions are relatively close in energy, I calculated the reaction barriers for these positions as well. The calculated free energy (enthalpic) barriers excluding and including NaCl are listed in Table 5.5. Interestingly the predicted reaction barriers for abstraction of the β -positions of DIA are lower than the α -positions. By applying the Boltzmann distribution about 69% of abstractions by CumO[•] from DIA will take place from either the cis- or trans- β positions of DIA. Therefore, abstraction from bulky amides by bulky oxygen-centred radicals are likely controlled by steric considerations. Note also that many of the TS optimizations were not successful with the inclusion of NaCl and in which case “guess” TS structures have been used to estimate the barrier heights. The TS structures for the HAT reaction between DIA and CumO[•] including NaCl are shown in Figure 5.11.

As was observed in the barrier height calculations involving NaCl with DMA with BnO[•] and CumO[•], the results vary depending on the presence or absence of secondary interactions of Na with CumO[•]. For the β -cis and acetyl position of DIA (Figure 5.11d-e), ΔH^\ddagger decreases by 2.3 and 0.2 kcal mol⁻¹, respectively, as a result of relatively long range interactions of Na with the aromatic system of CumO[•]. For abstraction from the α -cis position of DIA (Figure 5.11b), Na is able to interact with both the amidic oxygen lone pair, and a lone pair on the oxygen of CumO[•], resulting in a significant decrease in ΔH^\ddagger by 7.8 kcal mol⁻¹.

For the α -trans position there is no interaction between Na and CumO[•], yet the complexation of NaCl to DIA results in a 2.5 kcal mol⁻¹ decrease in ΔG^\ddagger . Comparing the TS structures including and excluding NaCl, there is very little difference. Therefore, it is likely that the “guess” TS structure including NaCl does

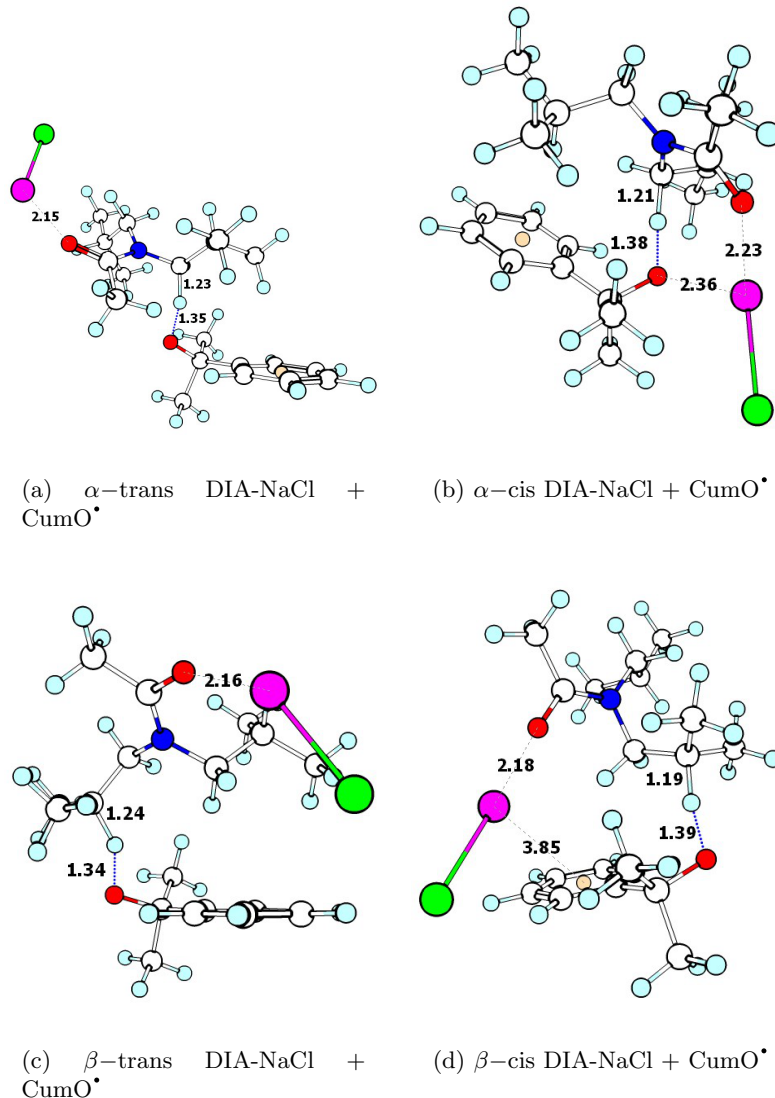


Figure 5.11: Continued on following page.

5.5. Summary

Table 5.5: Calculated free energy (enthalpy) ($\Delta G(H)^\ddagger$, kcal mol⁻¹) for direct HAT from different C–H bonds in DIA by CumO[•], with and without NaCl. The change in barrier height ($\Delta\Delta G(H)^\ddagger$) is calculated relative to the same abstraction site without the inclusion of NaCl. All barrier heights are relative to separated reactants (or complexed DIA-NaCl) and were calculated at the M05-2X-SMD(MeCN)/6-311+G(2d,2p)//M05-2X/6-31+G** level of theory. *Indicates estimated barrier based on “guess” TS structure.

Reaction	Abstraction Site	$\Delta G(H)^\ddagger$	$\Delta\Delta G(H)^\ddagger$
DIA + CumO [•]	α -trans	19.5(6.2)	
	α -cis	19.1(5.4)	
	β -trans	18.6(6.0)	
	β -cis	18.4(6.5)	
	acetyl	19.1(7.4)	
DIA-NaCl + CumO [•]	α -trans*	17.0(3.9)	-2.5(-2.3)
	α -cis*	12.7(-2.4)	-6.4(-7.8)
	β -trans	19.8(6.8)	0.7(1.4)
	β -trans*	19.6(6.9)	0.5(1.5)
	β -cis*	16.8(4.2)	-1.6(-2.3)
	acetyl*	17.8(3.8)	0.8(-0.1)
	acetyl	17.9(3.7)	0.9(-0.2)

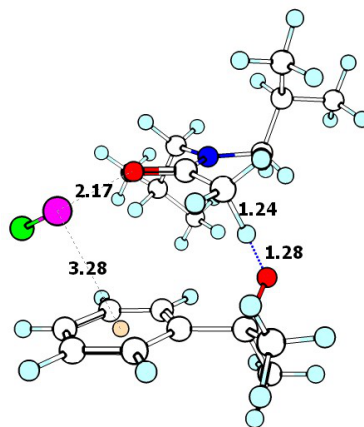
not appropriately represent the “true” TS structure for this particular abstraction site. Note that this may also be the case in other systems.

Abstraction by CumO[•] from the β -trans position of DIA does not allow for an interaction between both the amidic oxygen and CumO[•]. However, there should be no effect from decreased electron density in the C–H σ^* orbital. Consequently, ΔH^\ddagger increases by 1.4 kcal mol⁻¹ as a result of the effect of 0.04 e^- charge transfer from DIA to Na in the TS structure.

5.5 Summary

In this investigation, the effects of non-redox active metal cations upon the barrier heights of HAT reactions between small models for proteins with oxygen-centred radicals were studied. I began by examining the effects of the complexation

5.5. Summary



(e) Acetyl DIA-NaCl + CumO[•]

Figure 5.11: TS structures for HAT reactions between DIA and CumO[•] including NaCl for different C–H bonds: **a** α -trans, **b** α -cis, **c** β -trans, **d** β -cis, and **e** acetyl. Key interatomic distances are shown in units of Å. Element colour key: white is carbon, light blue is hydrogen, red is oxygen, blue is nitrogen, purple is sodium, green is chlorine, and peach is a dummy atom in the centre of an aromatic ring.

of NaCl upon the C–H bond strengths of the substrates of interest in this work. This in particular is central to the hypothesis of this work: complexation of a non-redox active metal to a heteroatom of a substrate reduces the electron density donated to adjacent C–H σ^* orbitals, increasing the C–H bond strength. By the BEP principle (See Chapter 4), the HAT reaction barrier height increases as a function of the C–H BDE.

Specific metal-substrate interactions can increase the effective C–H BDEs in the parent molecule, but this is complicated by the possibility for metal-radical interactions following bond cleavage. Metal-radical interaction can either increase or decrease C–H BDEs depending on the nature of the orbital interactions of the product radical and metal cation. The aforementioned hypothesis does not take into account the effects of metal-radical interaction.

5.5. Summary

Next, I studied the effects of metal complexation on the HAT reaction barrier heights. I calculated the barrier heights for two small models for proteins, DMA and DIA, including and excluding NaCl, with two different oxygen-centred radical, BnO[•] and CumO[•]. In the absence of any secondary interactions in the TS complex, the enthalpic HAT reaction barrier increases as a results of metal complexation. However, in the event of interactions between either the sodium or chlorine moieties with the oxygen-centred radical or extensions of the substrate in the TS complex, the effect of complexation can increase or decrease the barrier height, depending on the specific interaction. This further motivates the idea that the central hypothesis is incomplete in describing the effects of non-redox active metals on HAT reaction barrier heights.

The results obtained herein do not align with those from experiment. Recall that previous experimental results for the HAT reaction between DMA and CumO[•] demonstrated clear inhibition upon the addition of alkali and alkaline earth-metal salts. There are several possible explanations for this discrepancy: The models used herein may not properly capture the behaviour of bulk systems with respect to solvation or stoichiometry (the binding of multiple amide substrates to a single metal cation). Another possible explanation is the use of Cl⁻ as a counteranion herein, whereas ClO₄⁻ and OTf⁻ were utilized in experiment; the nature of the counteranion may play a larger roll than has been previously demonstrated.

The sum of these results suggests that non-redox active metal cations may not always deactivate C–H bonds in complex chemical environments. Therefore, on the basis of these limited results, it seems unlikely that a natural chemo-protective effect is observed due to the presence of alkali and alkaline earth-metal cations in protein or other biological systems. Additional work should be carried out to corroborate these results.

Chapter 6

Conclusions

HAT reactions are amongst the simplest radical chemical transformations. This can be deceiving, as there are many poorly understood factors that influence HAT. It is important to develop a full understanding of HAT reactions as they are a fundamental step in many biochemical processes. The radical-induced oxidation of biomaterials is often triggered by HAT reactions, and has been implicated in a number of degenerative disease states. In this thesis, three aspects of HAT reactivity were explored using quantum chemical techniques.

First, the role of non-covalent binding in the pre-reaction complex of HAT reactions was investigated. In particular, the relationship between the calculated pre-reaction complex binding energies and experimentally determined Arrhenius pre-exponential factors (A-factors) was examined for a series of thermoneutral or nearly thermoneutral reactions involving the formation and destruction of oxygen-centred radicals. The interpretation of the results of this investigation relies on an assumption: the mechanism for formal HAT, which is normally described as either direct HAT or PCET, exists on a continuum that is described by Equation 3.3.

It was demonstrated that there may be a correlation between A-factors and pre-reaction complex binding energies for (nearly) thermoneutral HAT reactions given that the reactions follow similar reaction mechanisms. This is an important caveat, as it is clear that binding energies do not serve as a diagnostic for fully describing all the entropic contributions to A-factors. Specifically, for a set of ten self-exchange and pseudo-self-exchange reaction, six out of ten of the reactions studied share similar

reaction mechanisms, and there is a strong correlation ($R^2 = 0.949$) of pre-reaction complex binding energies with A-factors. In order to apply this analysis to further systems, future work should aim at determining a quantitative diagnostic for the contributions of PCET and direct HAT to the overall hydrogen transfer reaction mechanism.

Next, the validity of the Bell-Evans-Polanyi (BEP) principle was investigated by analyzing a series of HAT reactions in which a hydrogen atom is abstracted from a carbon centre by the CumO[•] radical. A hypothesis on the basis of group-additivity states that if the BEP principle is valid, there should exist two linear relationships for C–H bonds, namely, one in which the incipient radical is delocalized into a π -system (benzylic or allylic), and the other in which the remaining alkyl radicals are largely localized. Detailed analysis of experimentally determined $\log(k_H/n)$ plotted against theoretically determined C–H BDEs demonstrated that there was reasonable correlation ($R^2 = 0.889$) in the case of allylic/benzylic substrates, however the correlation was not strong for all other alkyl substrates ($R^2 = 0.641$). Breaking the larger group of alkyl substrates into smaller chemical groups suggested that specific groups of alkyl containing species (e.g. cyclic alkanes and alkyl group with heteroatomic neighbours) may demonstrate linear relationships, however more data are needed to support this.

To explore this further, calculations were performed to determine the structures of relevant transition state complexes and reaction barrier heights. It was demonstrated that HAT reactions involving CumO[•] likely proceed through a mechanism that is dominated by direct HAT. As a result differences in mechanistic details may be ruled as a factor contributing to the observed poor correlation. Decomposition of the free energy barrier heights revealed that HAT reactions involving CumO[•] are entropy-controlled ($-T\Delta S^\ddagger \gg \Delta H^\ddagger$), and non-isoentropic. It is established in the

Chapter 6. Conclusions

literature that entropy-controlled processes do not follow LFERs consistently.²⁰⁷ Therefore, while these results do not invalidate the BEP principle as a LFER, it is apparent that the model is an over-simplification of the complexity associated with HAT reactions involving CumO[•]. This is likely to be the case for many HAT reactions. As a result, the BEP principle should not be used to as a quantitative prediction tool, but should remain a conceptual framework to qualitatively describe changes in reaction rates.

Finally, recent experimental evidence demonstrated that non-redox active metal cations can have an inhibitory effect on HAT reactions involving oxygen-centred radicals. As these metals are found ubiquitously in biological systems, it was suggested that this may be a form of chemo-protection against radical induced oxidation of biomaterials, in particular proteins. It was previously reported that the mechanism for this inhibition relies on C–H bond deactivation, which may be the result of a metal cation binding to a substrate. Herein, I sought to determine the exact mechanism by which this occurs. It was previously hypothesized that the metal bound to the substrate via an electron rich centre, such as the oxygen of a carbonyl. Then, electron density is withdrawn from a neighbouring C–H σ^* orbital, which is normally populated through hyperconjugation. Withdrawing electron density from the C–H σ^* orbital strengthens the bond, and thus the HAT reaction barrier height may increase, as per the BEP principle.

Two amides, DMA and DIA, were used as small models for protein systems. The calculated C–H BDEs of these substrates both with and without metal cations demonstrate that specific metal-substrate interactions can increase the effective C–H BDEs in the parent molecule. The calculated *N*-methyl C–H BDEs of DMA increase by an average of 1.4 kcal mol^{−1} upon complexation of NaCl. This is however complicated by the fact that the product radical can also interact with the metal

Chapter 6. Conclusions

cation, which can either increase or decrease the BDE. For example, the acetyl C–H BDE of DMA decreases by 0.1 kcal mol⁻¹ upon complexation of NaCl. As a result of metal-radical interaction, BDEs may not properly reflect the effect metal cations have on HAT barrier heights.

The hypothesis that C–H bond strengths are increased by interactions of the metal cation with the substrate does not account for interactions of that metal with species other than the substrate. This became abundantly obvious in calculating the reaction barrier heights including NaCl of DMA and DIA with the radicals CumO[•] and BnO[•]. Specifically, the predicted changes in barrier heights as a result of binding of NaCl to the substrate were found to both increase and decrease. For the HAT reaction of DMA and CumO[•] including NaCl, the predicted reaction barrier height for abstraction from an *N*-methyl hydrogen trans to the carbonyl increases as there are no interactions of NaCl with CumO[•]. However, for abstraction from an *N*-methyl cis to the carbonyl decrease as a result of a charge transfer interaction between NaCl and CumO[•]. Analysis of the interactions of NaCl with both the radical and extensions of the substrate demonstrated that secondary interaction can either stabilize or destabilize the TS complex.

The aforementioned hypothesis does not account for secondary interactions, however it was based on experimental results which demonstrate that alkali and alkaline earth metal salts do inhibit HAT reactions of amides with CumO[•]. The results obtained herein do not support the hypothesis. An explanation for this discrepancy remains unclear, however I have speculated that this may be a result of problems with the model chosen. Specifically, the experimental data suggests that stoichiometric ratios of substrates and metal cations are somehow related to the inhibitory effect. No multiple coordinating stoichiometries were considered herein.

Furthermore, the complexity of protein systems increases the likelihood that

Chapter 6. Conclusions

alkali and alkaline earth metal cations will interact not only with a single peptide moiety in a protein environment. On the basis of these limited results, it is possible that these metal cations may not serve as natural chemo-protective agents against radical induced oxidation in biological systems.

There is one important theme that arises from all the results in this thesis: HAT reactions appear deceptively simple. In each chapter, an attempt was made to make a generalization about the physico-chemical properties of HAT reactions. In each case, some properties of HAT reactivity were elucidated, while further questions arose. This work sets the stage for further research into three important aspects as HAT reactivity.

References

- [1] Halliwell, B.; Gutteridge, J. M. *Free Radicals in Biology and Medicine*, 4th ed.; Oxford University Press, 2015.
- [2] Barnham, K. J.; Masters, C. L.; Bush, A. I. Neurodegenerative diseases and oxidative stress. *Nat. Rev. Drug Discovery* **2004**, *3*, 205–214.
- [3] Valko, M.; Leibfritz, D.; Moncol, J.; Cronin, M. T. D.; Mazur, M.; Telser, J. Free radicals and antioxidants in normal physiological functions and human disease. *Int. J. Biochem. Cell Biol.* **2007**, *39*, 44–84.
- [4] Hwang, O. Role of oxidative stress in Parkinson’s disease. *Exp. Neurol.* **2013**, *22*, 11–17.
- [5] Halliwell, B. Oxidative stress and cancer: have we moved forward? *Biochem. J.* **2007**, *401*, 1–11.
- [6] Turrens, J. F. Mitochondrial formation of reactive oxygen species. *J. Physiol.* **2003**, *552*, 335–344.
- [7] Kozmér, Z.; Arany, E.; Alapi, T.; Takács, E.; Wojnárovits, L.; Dombi, A. Determination of the rate constant of hydroperoxyl radical reaction with phenol. *Radiat. Phys. Chem.* **2014**, *102*, 135–138.
- [8] Berlett, B. S.; Stadtman, E. R. Protein Oxidation in Aging, Disease, and Oxidative Stress. *J. Biol. Chem.* **1997**, *272*, 20313–20316.
- [9] Davies, M. J. Protein oxidation and peroxidation. *Biochem. J.* **2016**, *473*, 805–825.
- [10] Davies, M. J. The oxidative environment and protein damage. *Biochim. Biophys. Acta* **2005**, *1703*, 93–109.
- [11] Salamone, M.; Basili, F.; Mele, R.; Cianfanelli, M.; Bietti, M. Reactions of the cumyloxy radical with secondary amides. The influence of steric and stereo-electronic effects on the hydrogen atom transfer reactivity and selectivity. *Org. Lett.* **2014**, *16*, 6444–6447.
- [12] Rauk, A.; Armstrong, D. A. Influence of β -Sheet Structure on the Susceptibility of Proteins to Backbone Oxidative Damage: Preference for α C-Centered

References

- Radical Formation at Glycine Residues of Antiparallel β -Sheets. *J. Am. Chem. Soc.* **2000**, *122*, 4185–4192.
- [13] Stadtman, E. R. Role of oxidant species in aging. *Curr. Med. Chem.* **2004**, *11*, 1105–1112.
- [14] Mulder, P.; Korth, H.-G.; Pratt, D. A.; DiLabio, G. A.; Valgimigli, L.; Pedulli, G. F.; Ingold, K. U. Critical Re-evaluation of the O-H Bond Dissociation Enthalpy in Phenol. *J. Phys. Chem. A* **2005**, *109*, 2647–2655.
- [15] Stadtman, E. R.; Levine, R. L. Free radical-mediated oxidation of free amino acids and amino acid residues in proteins. *Amino Acids* **2003**, *25*, 207–218.
- [16] Garrison, W. M.; Jayko, M.; Bennett, W. Radiation-induced oxidation of protein in aqueous solution. *Radiat. Res.* **1962**, *16*, 483–502.
- [17] Garrison, W. M. Reaction mechanisms in the radiolysis of peptides, polypeptides, and proteins. *Chem. Rev.* **1987**, *87*, 381–398.
- [18] Halliwell, B. Oxidative stress and neurodegeneration: where are we now? *J. Neurochem.* **2006**, *97*, 1634–1658.
- [19] Kochi, J., Ed. *Free Radicals, Vols. 1 and 2*; Wiley, 1973.
- [20] Parsons, A. F. *An Introduction to Free Radical Chemistry*, 1st ed.; Wiley-Blackwell, 2000.
- [21] Litwinienko, G.; Ingold, K. U. Solvent Effects on the Rates and Mechanisms of Reaction of Phenols with Free Radicals. *Acc. Chem. Res.* **2007**, *40*, 222–230.
- [22] Cukier, R. I.; Nocera, D. G. Proton-coupled electron transfer. *Annu. Rev. Phys. Chem.* **1998**, *49*, 337–369.
- [23] Mayer, J. M.; Hrovat, D. A.; Thomas, J. L.; Borden, W. T. Proton-coupled electron transfer versus hydrogen atom transfer in benzyl/toluene, methoxyl/methanol, and phenoxy/phenol self-exchange reactions. *J. Am. Chem. Soc.* **2002**, *124*, 11142–11147.
- [24] Stubbe, J.; Nocera, D. G.; Yee, C. S.; Chang, M. C. Radical initiation in the class I ribonucleotide reductase: long-range proton-coupled electron transfer? *Chem. Rev.* **2003**, *103*, 2167–2202.
- [25] Mayer, J. M. Proton-coupled electron transfer: a reaction chemist's view. *Annu. Rev. Phys. Chem.* **2004**, *55*, 363–390.
- [26] DiLabio, G. A.; Johnson, E. R. Lone Pair- π and π - π Interactions Play an Important Role in Proton-Coupled Electron Transfer Reactions. *J. Am. Chem. Soc.* **2007**, *129*, 6199–6203.

References

- [27] Huynh, M. H. V.; Meyer, T. J. Proton-coupled electron transfer. *Chem. Rev.* **2007**, *107*, 5004–5064.
- [28] Hammes-Schiffer, S.; Soudackov, A. V. Proton-coupled electron transfer in solution, proteins, and electrochemistry. *J. Phys. Chem. B* **2008**, *112*, 14108–14123.
- [29] Mayer, J. M. Understanding hydrogen atom transfer: from bond strengths to Marcus theory. *Acc. Chem. Res.* **2010**, *44*, 36–46.
- [30] Weinberg, D. R.; Gagliardi, C. J.; Hull, J. F.; Murphy, C. F.; Kent, C. A.; Westlake, B. C.; Paul, A.; Ess, D. H.; McCafferty, D. G.; Meyer, T. J. Proton-coupled electron transfer. *Chem. Rev.* **2012**, *112*, 4016–4093.
- [31] Hammes-Schiffer, S. Proton-coupled electron transfer: Moving together and charging forward. *J. Am. Chem. Soc.* **2015**, *137*, 8860–8871.
- [32] Muñoz-Rugeles, L.; Galano, A.; Alvarez-Idaboy, J. R. Non-Covalent π - π Stacking Interactions Turn Off Non-Adiabatic Effects in Proton-Coupled Electron Transfer Reactions. *Phys. Chem. Chem. Phys.* **2017**, *19*, 6969–6972.
- [33] Hatcher, E.; Soudackov, A. V.; Hammes-Schiffer, S. Proton-coupled electron transfer in soybean lipoxygenase: dynamical behavior and temperature dependence of kinetic isotope effects. *J. Am. Chem. Soc.* **2007**, *129*, 187–196.
- [34] Sinnokrot, M. O.; Valeev, E. F.; Sherrill, C. D. Estimates of the Ab Initio Limit for π - π Interactions: The Benzene Dimer. *J. Am. Chem. Soc.* **2002**, *124*, 10887–10893.
- [35] Sirjoosinh, A.; Hammes-Schiffer, S. Proton-coupled electron transfer versus hydrogen atom transfer: generation of charge-localized diabatic states. *J. Phys. Chem. A* **2011**, *115*, 2367–2377.
- [36] Skone, J. H.; Soudackov, A. V.; Hammes-Schiffer, S. Calculation of Vibronic Couplings for Phenoxy/Phenol and Benzyl/Toluene Self-Exchange Reactions: Implications for Proton-Coupled Electron Transfer Mechanisms. *J. Am. Chem. Soc.* **2006**, *128*, 16655–16663.
- [37] Inagaki, T.; Yamamoto, T.; Kato, S. Proton-coupled electron transfer of the phenoxy/phenol couple: Effect of Hartree-Fock exchange on transition structures. *J. Comp. Chem.* **2011**, *32*, 3081–3091.
- [38] DiLabio, G. A.; Ingold, K. U. A Theoretical Study of the Iminoxy/Oxime Self-Exchange Reaction. A Five-Center, Cyclic Proton-Coupled Electron Transfer. *J. Am. Chem. Soc.* **2005**, *127*, 6693–6699.

References

- [39] Salamone, M.; Bietti, M. Tuning Reactivity and Selectivity in Hydrogen Atom Transfer from Aliphatic C–H Bonds to Alkoxyl Radicals: Role of Structural and Medium Effects. *Acc. Chem. Res.* **2015**, *48*, 2895–2903.
- [40] Finn, M.; Friedline, R.; Suleman, N. K.; Wohl, C. J.; Tanko, J. M. Chemistry of the t-Butoxyl Radical: Evidence that Most Hydrogen Abstractions from Carbon are Entropy-Controlled. *J. Am. Chem. Soc.* **2004**, *126*, 7578–7584.
- [41] Salamone, M.; Anastasi, G.; Bietti, M.; DiLabio, G. A. Diffusion Controlled Hydrogen Atom Abstraction from Tertiary Amines by the Benzyloxyl Radical. The Importance of C–H/N Hydrogen Bonding. *Org. Lett.* **2011**, *13*, 260–263.
- [42] Kreilick, R. W.; Weissman, S. I. Hydrogen Atom Transfer between Free Radicals and Their Diamagnetic Precursors. *J. Am. Chem. Soc.* **1966**, *88*, 2645–2652.
- [43] Johnson, E. R.; DiLabio, G. A. Radicals as hydrogen bond donors and acceptors. *Interdiscip. Sci.* **2009**, *1*, 133–140.
- [44] Tedder, J. M. Which factors determine the reactivity and regioselectivity of free radical substitution and addition reactions? *Angew. Chem. Int. Ed.* **1982**, *21*, 401–410.
- [45] Wijtmans, M.; Pratt, D. A.; Valgimigli, L.; DiLabio, G. A.; Pedulli, G. F.; Porter, N. A. 6-Amino-3-Pyridinols: Towards Diffusion-Controlled Chain-Breaking Antioxidants. *Angew. Chem. Int. Ed.* **2003**, *42*, 4370–4373.
- [46] Pratt, D. A.; DiLabio, G. A.; Mulder, P.; Ingold, K. U. Bond Strengths of Toluenes, Anilines, and Phenols: To Hammett or Not. *Acc. Chem. Res.* **2004**, *37*, 334–340.
- [47] Bell, R. P. The Theory of Reactions Involving Proton Transfers. *Proc. R. Soc. A* **1936**, *154*, 414–429.
- [48] Evans, M. G.; Polanyi, M. Inertia and driving force of chemical reactions. *Trans. Faraday Soc.* **1938**, *34*, 11–24.
- [49] Salamone, M.; Mangiacapra, L.; DiLabio, G. A.; Bietti, M. Effect of Metal Ions on the Reactions of the Cumyloxyl Radical with Hydrogen Atom Donors. Fine Control on Hydrogen Abstraction Reactivity Determined by Lewis Acid–Base Interactions. *J. Am. Chem. Soc.* **2013**, *135*, 415–423.
- [50] Salamone, M.; Carboni, G.; Mangiacapra, L.; Bietti, M. Binding to Redox-Inactive Alkali and Alkaline Earth Metal Ions Strongly Deactivates the C–H Bonds of Tertiary Amides toward Hydrogen Atom Transfer to Reactive Oxygen Centered Radicals. *J. Org. Chem.* **2015**, *80*, 9214–9223.

References

- [51] Salamone, M.; Mangiacapra, L.; Carboni, G.; Bietti, M. Hydrogen atom transfer from tertiary alkanamides to the cumyloxyl radical. The role of substrate structure on alkali and alkaline earth metal ion induced C–H bond deactivation. *Tetrahedron* **2016**, *72*, 7757–7763.
- [52] Griffiths, D. J. *Introduction to Quantum Mechanics*, 2nd ed.; Cambridge University Press, 2016.
- [53] Heisenberg, W. Mehrkörperproblem und Resonanz in der Quantenmechanik. *Z. Phys.* **1926**, *38*, 411–426.
- [54] Dirac, P. A. M. On the Theory of Quantum Mechanics. *Proc. R. Soc. A* **1926**, *112*, 661–677.
- [55] Slater, J. C. The Theory of Complex Spectra. *Phys. Rev.* **1929**, *34*, 1293–1322.
- [56] Roothaan, C. C. J. New Developments in Molecular Orbital Theory. *Rev. Mod. Phys.* **1951**, *23*, 69–89.
- [57] Gill, P. M. *Advances in Quantum Chemistry*; Elsevier, 1994; pp 141–205.
- [58] Szabo, A.; Ostlund, N. S. *Modern Quantum Chemistry: Intro to Advanced Electronic Structure Theory*; Dover Publications, 1996.
- [59] Jensen, F. Atomic orbital basis sets. *WIREs Comput. Mol. Sci.* **2012**, *3*, 273–295.
- [60] Hehre, W. J.; Stewart, R. F.; Pople, J. A. Self-Consistent Molecular Orbital Methods. I. Use of Gaussian Expansions of Slater-Type Atomic Orbitals. *J. Chem. Phys.* **1969**, *51*, 2657–2664.
- [61] Ditchfield, R.; Hehre, W. J.; Pople, J. A. Self-Consistent Molecular Orbital Methods. IX. An Extended Gaussian-Type Basis for Molecular Orbital Studies of Organic Molecules. *J. Chem. Phys.* **1971**, *54*, 724–728.
- [62] Hehre, W. J.; Ditchfield, R.; Pople, J. A. Self-Consistent Molecular-Orbital Methods. XII. Further Extensions of Gaussian-Type Basis Sets for Use in Molecular-Orbital Studies of Organic Molecules. *J. Chem. Phys.* **1972**, *56*, 2257–2261.
- [63] Dunning, T. H., Jr Gaussian basis sets for use in correlated molecular calculations. I. The atoms boron through neon and hydrogen. *J. Chem. Phys.* **1989**, *90*, 1007–1023.
- [64] Kendall, R. A.; Dunning, T. H., Jr.; Harrison, R. J. Electron affinities of the first-row atoms revisited. Systematic basis sets and wave functions. *J. Chem. Phys.* **1992**, *96*, 6792–6806.

References

- [65] Woon, D. E.; Dunning, T. H., Jr Gaussian basis sets for use in correlated molecular calculations. IV. Calculation of static electrical response properties. *J. Chem. Phys.* **1994**, *100*, 2975–2988.
- [66] Peterson, K. A.; Dunning, T. H., Jr. Accurate correlation consistent basis sets for molecular core-valence correlation effects: The second row atoms Al-Ar, and the first row atoms B-Ne revisited. *J. Chem. Phys.* **2002**, *117*, 10548–10560.
- [67] Jensen, F. Polarization consistent basis sets: I. Principles. *J. Chem. Phys.* **2001**, *115*, 9113–9125.
- [68] Jensen, F. Polarization consistent basis sets. II. Estimating the KohnSham basis set limit. *J. Chem. Phys.* **2002**, *116*, 7372–7279.
- [69] Jensen, F. Polarization consistent basis sets. III. The importance of diffuse functions. *J. Chem. Phys.* **2002**, *117*, 9234–9240.
- [70] Jensen, F. Polarization consistent basis sets. IV. The basis set convergence of equilibrium geometries, harmonic vibrational frequencies, and intensities. *J. Chem. Phys.* **2003**, *118*, 2459–2463.
- [71] Schäfer, A.; Horn, H.; Ahlrichs, R. Fully optimized contracted Gaussian basis sets for atoms Li to Kr. *J. Chem. Phys.* **1992**, *97*, 2571–2577.
- [72] Weigend, F.; Ahlrichs, R. Balanced basis sets of split valence, triple zeta valence and quadruple zeta valence quality for H to Rn: Design and assessment of accuracy. *Phys. Chem. Chem. Phys.* **2005**, *7*, 3297–3305.
- [73] TURBOMOLE V6.3 2011, a development of University of Karlsruhe and Forschungszentrum Karlsruhe GmbH, 1989-2007, TURBOMOLE GmbH, since 2007; available from <http://www.turbomole.com>.
- [74] Cramer, C. J. *Essentials of Computational Chemistry*, 2nd ed.; John Wiley & Sons, 2004.
- [75] Leininger, M. L.; Allen, W. D.; Schaefer, H. F.; Sherrill, C. D. Is Möller–Plesset perturbation theory a convergent ab initio method? *J. Chem. Phys.* **2000**, *112*, 9213–9222.
- [76] Crawford, T. D.; Schaefer, H. F. In *Reviews in Computational Chemistry*; Lipkowitz, K. B., Ed.; Wiley-Blackwell, 2000; Vol. 14; pp 33–136.
- [77] Levine, I. N. *Quantum Chemistry*, 7th ed.; Prentice Hall, 2013.
- [78] Pople, J. A.; Head-Gordon, M.; Raghavachari, K. Quadratic configuration interaction. A general technique for determining electron correlation energies. *J. Chem. Phys.* **1987**, *87*, 5968–5975.

References

- [79] Truhlar, D. G. Basis-set extrapolation. *Chem. Phys. Lett.* **1998**, *294*, 45–48.
- [80] Feller, D. Application of systematic sequences of wave functions to the water dimer. *J. Chem. Phys.* **1992**, *96*, 6104–6114.
- [81] Feller, D. The use of systematic sequences of wave functions for estimating the complete basis set, full configuration interaction limit in water. *J. Chem. Phys.* **1993**, *98*, 7059–7071.
- [82] Helgaker, T.; Klopper, W.; Koch, H.; Noga, J. Basis-set convergence of correlated calculations on water. *J. Chem. Phys.* **1997**, *106*, 9639–9646.
- [83] Halkier, A.; Helgaker, T.; Jørgensen, P.; Klopper, W.; Koch, H.; Olsen, J.; Wilson, A. K. Basis-set convergence in correlated calculations on Ne, N₂, and H₂O. *Chem. Phys. Lett.* **1998**, *286*, 243–252.
- [84] Kupka, T.; Lim, C. Polarization-Consistent versus Correlation-Consistent Basis Sets in Predicting Molecular and Spectroscopic Properties. *J. Phys. Chem. A* **2007**, *111*, 1927–1932.
- [85] Shiozaki, T.; Kamiya, M.; Hirata, S.; Valeev, E. F. Explicitly correlated coupled-cluster singles and doubles method based on complete diagrammatic equations. *J. Chem. Phys.* **2008**, *129*, 071101.
- [86] Köhn, A.; Richings, G. W.; Tew, D. P. Implementation of the full explicitly correlated coupled-cluster singles and doubles model CCSD-F12 with optimally reduced auxiliary basis dependence. *J. Chem. Phys.* **2008**, *129*, 201103.
- [87] Ten-no, S.; Noga, J. Explicitly correlated electronic structure theory from R12/F12 anstze. *WIREs Comput. Mol. Sci.* **2012**, *2*, 114–125.
- [88] Feller, D. Benchmarks of improved complete basis set extrapolation schemes designed for standard CCSD(T) atomization energies. *J. Chem. Phys.* **2013**, *138*, 074103.
- [89] Karton, A. A computational chemist's guide to accurate thermochemistry for organic molecules. *WIREs Comput. Mol. Sci.* **2016**, *6*, 292–310.
- [90] Curtiss, L. A.; Redfern, P. C.; Raghavachari, K. Gaussian-4 theory. *J. Chem. Phys.* **2007**, *126*, 084108.
- [91] Curtiss, L. A.; Redfern, P. C.; Raghavachari, K. Gaussian-4 theory using reduced order perturbation theory. *J. Chem. Phys.* **2007**, *127*, 124105.
- [92] Montgomery, J. A.; Frisch, M. J.; Ochterski, J. W.; Petersson, G. A. A complete basis set model chemistry. VI. Use of density functional geometries and frequencies. *J. Chem. Phys.* **1999**, *110*, 2822–2827.

References

- [93] Montgomery, J. A.; Frisch, M. J.; Ochterski, J. W.; Petersson, G. A. A complete basis set model chemistry. VII. Use of the minimum population localization method. *J. Chem. Phys.* **2000**, *112*, 6532–6542.
- [94] Ochterski, J. W.; Petersson, G. A.; Montgomery, J. A. A complete basis set model chemistry. V. Extensions to six or more heavy atoms. *J. Chem. Phys.* **1996**, *104*, 2598–2619.
- [95] Barnes, E. C.; Petersson, G. A.; Montgomery, J. A.; Frisch, M. J.; Martin, J. M. L. Unrestricted Coupled Cluster and Brueckner Doubles Variations of W1 Theory. *J. Chem. Theory Comput.* **2009**, *5*, 2687–2693.
- [96] Hohenberg, P.; Kohn, W. Inhomogeneous Electron Gas. *Phys. Rev.* **1964**, *136*, B864–B871.
- [97] Koch, W.; Holthausen, M. C. *A Chemist's Guide to Density Functional Theory*; Wiley-VCH, 2000.
- [98] Kohn, W.; Sham, L. J. Self-Consistent Equations Including Exchange and Correlation Effects. *Phys. Rev.* **1965**, *140*, A1133–A1138.
- [99] Perdew, J. P.; Ruzsinszky, A.; Tao, J.; Staroverov, V. N.; Scuseria, G. E.; Csonka, G. I. Prescription for the design and selection of density functional approximations: More constraint satisfaction with fewer fits. *J. Chem. Phys.* **2005**, *123*, 062201.
- [100] Goerigk, L.; Grimme, S. Double-hybrid density functionals. *WIREs Comput. Mol. Sci.* **2014**, *4*, 576–600.
- [101] Becke, A. D. Density-functional thermochemistry. III. The role of exact exchange. *J. Chem. Phys.* **1993**, *98*, 5648–5652.
- [102] Lee, C.; Yang, W.; Parr, R. G. Development of the Colle-Salvetti correlation-energy formula into a functional of the electron density. *Phys. Rev. B* **1988**, *37*, 785–789.
- [103] Zhao, Y.; Schultz, N. E.; Truhlar, D. G. Design of Density Functionals by Combining the Method of Constraint Satisfaction with Parametrization for Thermochemistry, Thermochemical Kinetics, and Noncovalent Interactions. *J. Chem. Theory Comput.* **2006**, *2*, 364–382.
- [104] Zhao, Y.; Truhlar, D. G. The M06 suite of density functionals for main group thermochemistry, thermochemical kinetics, noncovalent interactions, excited states, and transition elements: two new functionals and systematic testing of four M06-class functionals and 12 other functionals. *Theor. Chem. Acc.* **2006**, *120*, 215–241.

References

- [105] Parr, R. G.; Yang, W. *Density-Functional Theory of Atoms and Molecules*; Oxford University Press, 1994.
- [106] Cohen, A. J.; Mori-Sánchez, P.; Yang, W. Challenges for Density Functional Theory. *Chem. Rev.* **2012**, *112*, 289–320.
- [107] DiLabio, G. A.; Otero-de-la-Roza, A. In *Reviews in Computational Chemistry*; Lipkowitz, K. B., Ed.; Wiley-Blackwell, 2016; Vol. 29; pp 1–97.
- [108] Otero-de-la-Roza, A., DiLabio, G. A., Eds. *Non-covalent Interactions In Quantum Chemistry and Physics*, 1st ed.; Elsevier, 2017.
- [109] Grimme, S.; Antony, J.; Ehrlich, S.; Krieg, H. A consistent and accurate ab initio parametrization of density functional dispersion correction (DFT-D) for the 94 elements H-Pu. *J. Chem. Phys.* **2010**, *132*, 154104.
- [110] Johnson, E. R.; Becke, A. D. A post-Hartree-Fock model of intermolecular interactions: Inclusion of higher-order corrections. *J. Chem. Phys.* **2005**, *123*, 024101.
- [111] Mori-Sánchez, P.; Cohen, A. J.; Yang, W. Localization and Delocalization Errors in Density Functional Theory and Implications for Band-Gap Prediction. *Phys. Rev. Lett.* **2008**, *100*, 146401.
- [112] Otero-de-la-Roza, A.; Johnson, E. R.; DiLabio, G. A. Halogen Bonding from Dispersion-Corrected Density-Functional Theory: The Role of Delocalization Error. *J. Chem. Theory Comput.* **2014**, *10*, 5436–5447.
- [113] Csonka, G. I.; Johnson, B. G. Inclusion of exact exchange for self-interaction corrected H₃ density functional potential energy surface. *Theor. Chem. Acc.* **1998**, *99*, 158–165.
- [114] Heidrich, D.; Kliesch, W.; Quapp, W. *Properties of Chemically Interesting Potential Energy Surfaces*; Springer-Verlag, 1991; Vol. 56.
- [115] Hratchian, H. P.; Schlegel, H. B. In *Theory and Applications of Computational Chemistry*; Dykstra, C., Frenking, G., Kim, K., Scuseria, G., Eds.; Elsevier, 2005; pp 195–249.
- [116] Frisch, M. J. et al. Gaussian 09, Revision D. 01. 2009.
- [117] Wilson, E. B.; Decius, J. C.; Cross, P. C. *Molecular Vibrations: The Theory of Infrared and Raman Vibrational Spectra (Dover Books on Chemistry)*; Dover Publications, 1980.
- [118] McQuarrie, D. A.; Simon, J. D. *Molecular Thermodynamics*; University Science Books, 1999.

References

- [119] McQuarrie, D. A. *Statistical Mechanics*; University Science Books, 2000.
- [120] Note that Q is actually a function of the number of moles, volume of a system, and temperature. This description, denoted as $Q(N, V, T)$, has been omitted for simplicity.
- [121] Mennucci, B., Cammi, R., Eds. *Continuum Solvation Models in Chemical Physics: From Theory to Applications*; John Wiley & Sons, 2007.
- [122] Marenich, A. V.; Cramer, C. J.; Truhlar, D. G. Universal Solvation Model Based on Solute Electron Density and on a Continuum Model of the Solvent Defined by the Bulk Dielectric Constant and Atomic Surface Tensions. *J. Phys. Chem. B* **2009**, *113*, 6378–6396.
- [123] Ho, J.; Klamt, A.; Coote, M. L. Comment on the Correct Use of Continuum Solvent Models. *J. Phys. Chem. A* **2010**, *114*, 13442–13444.
- [124] McQuarrie, D. A.; Simon, J. D. *Physical Chemistry: A Molecular Approach*; University Science Books, 1997.
- [125] Steinfeld, J. I.; Francisco, J. S.; Hase, W. L. *Chemical Kinetics and Dynamics*, 2nd ed.; Prentice Hall, 1998.
- [126] Truhlar, D. G.; Garrett, B. C. Variational Transition State Theory. *Annu. Rev. Phys. Chem.* **1984**, *35*, 159–189.
- [127] Bell, R. P. *The Tunnel Effect in Chemistry*; Springer Nature, 1980.
- [128] Johnston, H. S.; Heicklen, J. Tunnelling Corrections For Unsymmetrical Eckart Potential Energy Barriers. *J. Phys. Chem.* **1962**, *66*, 532–533.
- [129] Mader, E. A.; Larsen, A. S.; Mayer, J. M. Hydrogen Atom Transfer from Iron(II)-Tris[2,2'-bi(tetrahydropyrimidine)] to TEMPO: A Negative Enthalpy of Activation Predicted by the Marcus Equation. *J. Am. Chem. Soc.* **2004**, *126*, 8066–8067.
- [130] Mahoney, L. R.; DaRooge, M. A. Kinetic and thermochemical study of the reaction of 2,4,6-tri-tert-butylphenoxy radical with substituted phenols. *J. Am. Chem. Soc.* **1970**, *92*, 890–899.
- [131] DaRooge, M. A.; Mahoney, L. R. Reaction of 2,4,6-tri-tert-butylphenoxy radical with unhindered phenols. *J. Org. Chem.* **1967**, *32*, 1–6.
- [132] Howard, J. A.; Furimsky, E. Arrhenius Parameters for Reaction of tert-Butylperoxy Radicals with some Hindered Phenols and Aromatic Amines. *Can. J. Chem.* **1973**, *51*, 3738–3745.

References

- [133] Foti, M.; Ingold, K. U.; Lusztyk, J. The Surprisingly High Reactivity of Phenoxyl Radicals. *J. Am. Chem. Soc.* **1994**, *116*, 9440–9447.
- [134] Chenier, J. H. B.; Furimsky, E.; Howard, J. A. Arrhenius Parameters for Reaction of the tert-Butylperoxy and 2-Ethyl-2-propylperoxy Radicals with some Nonhindered Phenols, Aromatic Amines, and Thiophenols. *Can. J. Chem.* **1974**, *52*, 3682–3688.
- [135] Chenier, J. H. B.; Howard, J. A. A Kinetic Electron Spin Resonance Study of the Transfer of a Hydrogen Atom from α -Tetralin Hydroperoxide to a Tertiary Alkylperoxy Radical. *Can. J. Chem.* **1975**, *53*, 623–627.
- [136] Lucarini, M.; Pedrielli, P.; Pedulli, G. F.; Cabiddu, S.; Fattuoni, C. Bond Dissociation Energies of O-H Bonds in Substituted Phenols from Equilibration Studies. *J. Org. Chem.* **1996**, *61*, 9259–9263.
- [137] Mahoney, L. R.; DaRooge, M. A. Equilibrium reaction of 2,4,6-tri-tert-butylphenol and organic peroxy radicals. *J. Am. Chem. Soc.* **1970**, *92*, 4063–4067.
- [138] Mahoney, L. R.; DaRooge, M. A. Kinetic behavior and thermochemical properties of phenoxy radicals. *J. Am. Chem. Soc.* **1975**, *97*, 4722–4731.
- [139] Korcek, S.; Chenier, J. H. B.; Howard, J. A.; Ingold, K. U. Absolute Rate Constants for Hydrocarbon Autoxidation. XXI. Activation Energies for Propagation and the Correlation of Propagation Rate Constants with Carbon–Hydrogen Bond Strengths. *Can. J. Chem.* **1972**, *50*, 2285–2297.
- [140] Salamone, M.; DiLabio, G. A.; Bietti, M. Hydrogen Atom Abstraction Selectivity in the Reactions of Alkylamines with the Benzyloxyl and Cumyloxyl Radicals. The Importance of Structure and of Substrate Radical Hydrogen Bonding. *J. Am. Chem. Soc.* **2011**, *133*, 16625–16634.
- [141] Pischel, U.; Nau, W. M. Switch-Over in Photochemical Reaction Mechanism from Hydrogen Abstraction to Exciplex-Induced Quenching: Interaction of Triplet-Excited versus Singlet-Excited Acetone versus Cumyloxyl Radicals with Amines. *J. Am. Chem. Soc.* **2001**, *123*, 9727–9737.
- [142] Griller, D.; Howard, J. A.; Marriott, P. R.; Sciano, J. C. Absolute rate constants for the reactions of tert-butoxyl, tert-butylperoxyl, and benzophenone triplet with amines: the importance of a stereoelectronic effect. *J. Am. Chem. Soc.* **1981**, *103*, 619–623.
- [143] Bietti, M.; Martella, R.; Salamone, M. Understanding Kinetic Solvent Effects on Hydrogen Abstraction Reactions from Carbon by the Cumyloxyl Radical. *Org. Lett.* **2011**, *13*, 6110–6113.

References

- [144] Salamone, M.; DiLabio, G. A.; Bietti, M. Reactions of the Cumyloxy Radical and Benzyl Radical with Strong Hydrogen Bond Acceptors. Large Enhancements in Hydrogen Abstraction Reactivity Determined by Substrate/Radical Hydrogen Bonding. *J. Org. Chem.* **2012**, *77*, 10479–10487.
- [145] Malatesta, V.; Scaiano, J. C. Absolute rate constants for the reactions of tert-butoxyl with ethers: importance of the stereoelectronic effect. *J. Org. Chem.* **1982**, *47*, 1455–1459.
- [146] Salamone, M.; Milan, M.; DiLabio, G. A.; Bietti, M. Absolute Rate Constants for Hydrogen Atom Transfer from Tertiary Amides to the Cumyloxy Radical: Evaluating the Role of Stereoelectronic Effects. *J. Org. Chem.* **2014**, *79*, 7179–7184.
- [147] Becke, A. D. Density-functional exchange-energy approximation with correct asymptotic behavior. *Phys. Rev. A* **1988**, *38*, 3098–3100.
- [148] Otero-de-la-Roza, A.; DiLabio, G. A. Transferable Atom-Centered Potentials for the Correction of Basis Set Incompleteness Errors in Density-Functional Theory. *J. Chem. Theory Comput.* **2017**, *13*, 3505–3524.
- [149] Andzelm, J.; Klobukowski, M.; Radzio-andzelm, E.; Sakai, Y.; Tatewaki, H. In *Gaussian Basis Sets For Molecular Calculation*; Huzinaga, S., Ed.; Elsevier, 1984; Valence Scale Factors From John Deisz Of North Dakota State University.
- [150] The Escher program (<https://github.com/aoterodelaroza/escher>) was used to generate a Z-matrix with specific dihedral angles. This geometry was then systematically scanned using simple shell scripts.
- [151] Vydrov, O. A.; Scuseria, G. E. Assessment of a long-range corrected hybrid functional. *J. Chem. Phys.* **2006**, *125*, 234109.
- [152] Vydrov, O. A.; Heyd, J.; Krukau, A. V.; Scuseria, G. E. Importance of short-range versus long-range Hartree-Fock exchange for the performance of hybrid density functionals. *J. Chem. Phys.* **2006**, *125*, 074106.
- [153] Johnson, E. R.; Otero-de-la-Roza, A.; Dale, S. G.; DiLabio, G. A. Efficient basis sets for non-covalent interactions in XDM-corrected density-functional theory. *J. Chem. Phys.* **2013**, *139*, 214109.
- [154] Řezáč, J.; Riley, K. E.; Hobza, P. S66: A Well-balanced Database of Benchmark Interaction Energies Relevant to Biomolecular Structures. *J. Chem. Theory Comput.* **2011**, *7*, 2427–2438.
- [155] Benson, S. W. *Thermochemical Kinetics: Methods for the Estimation of Thermochemical Data and Rate Parameters*, 2nd ed.; Wiley, 1976.

References

- [156] Kojima, T. Potential barrier of phenol from its microwave spectrum. *J. Phys. Soc. Jpn.* **1960**, *15*, 284–287.
- [157] Kim, K.; Jordan, K. Theoretical calculation of the height of the barrier for OH rotation in phenol. *Chem. Phys. Lett.* **1994**, *218*, 261–269.
- [158] Isborn, C.; Hrovat, D. A.; Borden, W. T.; Mayer, J. M.; Carpenter, B. K. Factors controlling the barriers to degenerate hydrogen atom transfers. *J. Am. Chem. Soc.* **2005**, *127*, 5794–5795.
- [159] Dill, K. A.; Bromberg, S. *Molecular Driving Forces: Statistical Thermodynamics in Chemistry & Biology*; Garland Science, 2003.
- [160] Brønsted, J. N.; Pedersen, K. Stöchiometrie und Verwandtschaftslehre. *Z. Phys. Chem.* **1924**, *108*, 185–235.
- [161] Pratt, D. A.; Mills, J. H.; Porter, N. A. Theoretical calculations of carbon-oxygen bond dissociation enthalpies of peroxy radicals formed in the autoxidation of lipids. *J. Am. Chem. Soc.* **2003**, *125*, 5801–5810.
- [162] Panov, G. I.; Parfenov, M. V.; Parmon, V. N. The Brønsted-Evans-Polanyi Correlations in Oxidation Catalysis. *Cataly. Rev.* **2015**, *57*, 436–477.
- [163] van Santen, R. A.; Neurock, M.; Shetty, S. G. Reactivity theory of transition-metal surfaces: a Brønsted-Evans-Polanyi linear activation energy-free-energy analysis. *Chem. Rev.* **2010**, *110*, 2005–2048.
- [164] Bietti, M.; Salamone, M. Kinetic Solvent Effects on Hydrogen Abstraction Reactions from Carbon by the Cumyloxy Radical. The Role of Hydrogen Bonding. *Org. Lett.* **2010**, *12*, 3654–3657.
- [165] Salamone, M.; Martella, R.; Bietti, M. Hydrogen Abstraction from Cyclic Amines by the Cumyloxy and Benzyloxy Radicals. The Role of Stereoelectronic Effects and of Substrate/Radical Hydrogen Bonding. *J. Org. Chem.* **2012**, *77*, 8556–8561.
- [166] Salamone, M.; Milan, M.; DiLabio, G. A.; Bietti, M. Reactions of the Cumyloxy and Benzyloxy Radicals with Tertiary Amides. Hydrogen Abstraction Selectivity and the Role of Specific Substrate-Radical Hydrogen Bonding. *J. Org. Chem.* **2013**, *78*, 5909–5917.
- [167] Salamone, M.; Mangiacapra, L.; Bietti, M. Kinetic Solvent Effects on the Reactions of the Cumyloxy Radical with Tertiary Amides. Control over the Hydrogen Atom Transfer Reactivity and Selectivity through Solvent Polarity and Hydrogen Bonding. *J. Org. Chem.* **2015**, *80*, 1149–1154.

References

- [168] Adam, W.; Grimm, G. N.; Saha-Mller, C. R.; Dall'Acqua, F.; Miolo, G.; Vedaldi, D. DNA Damage by tert-Butoxyl Radicals Generated in the Photolysis of a Water-Soluble, DNA-Binding Peroxyester Acting as a Radical Source. *Chem. Res. Toxicol.* **1998**, *11*, 1089–1097.
- [169] Adam, W.; Marquardt, S.; Kemmer, D.; Saha-Mller, C. R.; Schreier, P. 2'-Deoxyguanosine (DG) Oxidation and Strand-Break Formation in DNA by the Radicals Released in the Photolysis of N-tert-Butoxy-2-pyridone. Are tert-Butoxyl or Methyl Radicals Responsible for the Photooxidative Damage in Aqueous Media? *Org. Lett.* **2002**, *4*, 225–228.
- [170] Jones, C. M.; Burkitt, M. J. EPR Spin-Trapping Evidence for the Direct, One-Electron Reduction of tert-Butylhydroperoxide to the tert-Butoxyl Radical by Copper(II): Paradigm for a Previously Overlooked Reaction in the Initiation of Lipid Peroxidation. *J. Am. Chem. Soc.* **2003**, *125*, 6946–6954.
- [171] MacFaul, P. A.; Ingold, K. U.; Lusztyk, J. Kinetic Solvent Effects on Hydrogen Atom Abstraction from Phenol, Aniline, and Diphenylamine. The Importance of Hydrogen Bonding on Their Radical-Trapping (Antioxidant) Activities 1. *J. Org. Chem.* **1996**, *61*, 1316–1321.
- [172] Valgimigli, L.; Ingold, K. U.; Lusztyk, J. Antioxidant Activities of Vitamin E Analogues in Water and a Kamlet-Taft β -Value for Water. *J. Am. Chem. Soc.* **1996**, *118*, 3545–3549.
- [173] Valgimigli, L.; Banks, J. T.; Lusztyk, J.; Ingold, K. U. Solvent Effects on the Antioxidant Activity of Vitamin E. *J. Org. Chem.* **1999**, *64*, 3381–3383.
- [174] Jovanovic, S. V.; Steenken, S.; Boone, C. W.; Simic, M. G. H-Atom Transfer Is A Preferred Antioxidant Mechanism of Curcumin. *J. Am. Chem. Soc.* **1999**, *121*, 9677–9681.
- [175] Sortino, S.; Petralia, S.; Foti, M. C. Absolute rate constants and transient intermediates in the free-radical-induced peroxidation of γ -terpinene, an unusual hydrocarbon antioxidant. *New J. Chem.* **2003**, *27*, 1563–1567.
- [176] Tanko, J. M.; Friedline, R.; Suleman, N. K.; Castagnoli, N. tert-Butoxyl as a Model for Radicals in Biological Systems: Caveat Emptor. *J. Am. Chem. Soc.* **2001**, *123*, 5808–5809.
- [177] Calculated using the ROCBS-QB3 composite method.
- [178] Hammond, G. S. A Correlation of Reaction Rates. *J. Am. Chem. Soc.* **1955**, *77*, 334–338.

References

- [179] Russell, G. A. In *Free Radicals*; Kochi, J. K., Ed.; Wiley, 1973; Chapter Reactivity, Selectivity, and Polar Effects in Hydrogen Atom Transfer Reactions, pp 275–331.
- [180] Luo, Y.-R. *Handbook of Bond Dissociation Energies in Organic Compounds*; CRC Press, 2002.
- [181] Bordwell, F.; Cheng, J. P.; Harrelson, J. A. Homolytic bond dissociation energies in solution from equilibrium acidity and electrochemical data. *J. Am. Chem. Soc.* **1988**, *110*, 1229–1231.
- [182] Miller, D. C.; Tarantino, K. T.; Knowles, R. R. Proton-Coupled Electron Transfer in Organic Synthesis: Fundamentals, Applications, and Opportunities. *Top. Curr. Chem.* **2016**, *374*, 145–203.
- [183] DiLabio, G. A.; Pratt, D. A.; LoFaro, A. D.; Wright, J. S. Theoretical Study of X-H Bond Energetics (X = C, N, O, S): Application to Substituent Effects, Gas Phase Acidities, and Redox Potentials. *J. Phys. Chem. A* **1999**, *103*, 1653–1661.
- [184] Chan, B.; Radom, L. BDE261: A Comprehensive Set of High-Level Theoretical Bond Dissociation Enthalpies. *J. Phys. Chem. A* **2012**, *116*, 4975–4986.
- [185] Wiberg, K. B.; Petersson, G. A. A Computational Study of RXH_n X–H Bond Dissociation Enthalpies. *J. Phys. Chem. A* **2014**, *118*, 2353–2359.
- [186] Avila, D. V.; Brown, C. E.; Ingold, K. U.; Lusztyk, J. Solvent effects on the competitive β -scission and hydrogen atom abstraction reactions of the cumyloxy radical. Resolution of a long-standing problem. *J. Am. Chem. Soc.* **1993**, *115*, 466–470.
- [187] Avila, D. V.; Ingold, K. U.; Lusztyk, J.; Green, W. H.; Procopio, D. R. Dramatic Solvent Effects on the Absolute Rate Constants for Abstraction of the Hydroxylic Hydrogen Atom from tert-Butyl Hydroperoxide and Phenol by the Cumyloxy Radical. The Role of Hydrogen Bonding. *J. Am. Chem. Soc.* **1995**, *117*, 2929–2930.
- [188] DiLabio, G. A. Using Locally Dense Basis Sets for the Determination of Molecular Properties. *J. Phys. Chem. A* **1999**, *103*, 11414–11424.
- [189] Wright, J. S.; Johnson, E. R.; DiLabio, G. A. Predicting the Activity of Phenolic Antioxidants: Theoretical Method, Analysis of Substituent Effects, and Application to Major Families of Antioxidants. *J. Am. Chem. Soc.* **2001**, *123*, 1173–1183.

References

- [190] Martin, J. M. L.; de Oliveira, G. Towards standard methods for benchmark quality ab initio thermochemistry—W1 and W2 theory. *J. Chem. Phys.* **1999**, *111*, 1843–1856.
- [191] DiLabio, G.; Wright, J. Calculation of bond dissociation energies for large molecules using locally dense basis sets. *Chem. Phys. Lett.* **1998**, *297*, 181–186.
- [192] Wood, G. P. F.; Radom, L.; Petersson, G. A.; Barnes, E. C.; Frisch, M. J.; Montgomery, J. A. A restricted-open-shell complete-basis-set model chemistry. *J. Chem. Phys.* **2006**, *125*, 094106.
- [193] Somers, K. P.; Simmie, J. M. Benchmarking Compound Methods (CBS-QB3, CBS-APNO, G3, G4, W1BD) against the Active Thermochemical Tables: Formation Enthalpies of Radicals. *J. Phys. Chem. A* **2015**, *119*, 8922–8933.
- [194] Simmie, J. M.; Somers, K. P. Benchmarking Compound Methods (CBS-QB3, CBS-APNO, G3, G4, W1BD) against the Active Thermochemical Tables: A Litmus Test for Cost-Effective Molecular Formation Enthalpies. *J. Phys. Chem. A* **2015**, *119*, 7235–7246.
- [195] Petersson, G. A. *Understanding Chemical Reactivity*; Springer Netherlands, 2001; Vol. 22; pp 99–130.
- [196] Pople, J. A.; Head-Gordon, M.; Fox, D. J.; Raghavachari, K.; Curtiss, L. A. Gaussian-1 theory: A general procedure for prediction of molecular energies. *J. Chem. Phys.* **1989**, *90*, 5622–5629.
- [197] Andrienko, G. A. Chemcraft. 2015; <http://www.chemcraftprog.com>.
- [198] Savin, A.; Johnson, E. R. *Topics in Current Chemistry*; Springer International Publishing, 2014; pp 81–95.
- [199] Dorofeeva, O. V.; Mastryukov, V. S.; Allinger, N. L.; Almenningen, A. The molecular structure and conformation of cyclooctane as determined by electron diffraction and molecular mechanics calculations. *J. Phys. Chem.* **1985**, *89*, 252–257.
- [200] Torres, E.; DiLabio, G. A. A (Nearly) Universally Applicable Method for Modeling Noncovalent Interactions User B3LYP. *J. Phys. Chem. Lett.* **2012**, *3*, 1738–1744.
- [201] Valgimigli, L.; Banks, J. T.; Ingold, K.; Lusztyk, J. Kinetic Solvent Effects on Hydroxylic Hydrogen Atom Abstractions Are Independent of the Nature of the Abstracting Radical. Two Extreme Tests Using Vitamin E and Phenol. *J. Am. Chem. Soc.* **1995**, *117*, 9966–9971.

References

- [202] Sheeller, B.; Ingold, K. U. Absolute rate constants for some reactions of the triethylamine-boryl radical and the borane radical anion. *J. Chem. Soc., Perkin Trans. 2* **2001**, 480–486.
- [203] Baignee, A.; Howard, J.; Scaiano, J.; Stewart, L. Absolute rate constants for reactions of cumyloxy in solution. *J. Am. Chem. Soc.* **1983**, *105*, 6120–6123.
- [204] Houk, K. N.; Rondan, N. G. Origin of negative activation energies and entropy control of halocarbene cycloadditions and related fast reactions. *J. Am. Chem. Soc.* **1984**, *106*, 4293–4294.
- [205] Moss, R. A. Adventures in Reactive Intermediate Chemistry: A Perspective and Retrospective. *J. Org. Chem.* **2017**, *82*, 2307–2318.
- [206] Sobek, J.; Martschke, R.; Fischer, H. Entropy Control of the Cross-Reaction between Carbon-Centered and Nitroxide Radicals. *J. Am. Chem. Soc.* **2001**, *123*, 2849–2857.
- [207] Exner, O. *Progress in Physical Organic Chemistry*; John Wiley & Sons, 1973; pp 411–482.
- [208] Blackadder, D. A.; Hinshelwood, C. 555. The kinetics of the decomposition of the addition compounds formed by sodium bisulphite and a series of aldehydes and ketones. Part II. General discussion of energy–entropy relations. *J. Chem. Soc.* **1958**, *0*, 2728–2734.
- [209] Roberts, B. P. Polarity-reversal catalysis of hydrogen-atom abstraction reactions: concepts and applications in organic chemistry. *Chem. Soc. Rev.* **1999**, *28*, 25–35.
- [210] Roberts, B. P.; Steel, A. J. An extended form of the Evans–Polanyi equation: a simple empirical relationship for the prediction of activation energies for hydrogen-atom transfer reactions. *J. Chem. Soc., Perkin Trans. 2* **1994**, 2155–2162.
- [211] Zavitsas, A. A.; Chatgilialoglu, C. Energies of Activation. The Paradigm of Hydrogen Abstractions by Radicals. *J. Am. Chem. Soc.* **1995**, *117*, 10645–10654.
- [212] Zavitsas, A. A. *Encyclopedia of Radicals in Chemistry, Biology and Materials*; John Wiley & Sons, 2012.
- [213] Harding, M. M.; Nowicki, M. W.; Walkinshaw, M. D. Metals in protein structures: a review of their principal features. *Crystallogr. Rev.* **2010**, *16*, 247–302.
- [214] Berman, H.; Henrick, K.; Nakamura, H.; Markley, J. L. The worldwide Protein Data Bank (wwPDB): ensuring a single, uniform archive of PDB data. *Nucleic Acids Res.* **2007**, *35*, D301–D303.

References

- [215] Atkins, P.; Overton, T.; Rourke, J.; Weller, M.; Armstrong, F. *Shriver & Atkins' Inorganic Chemistry*, 5th ed.; Oxford University Press, 2009.
- [216] Karp, G.; Pruitt, N. L. *Cell and molecular biology: concepts and experiments*; Wiley, 1999.
- [217] Ingwall, J. S.; Balschi, J. A. Energetics of the Na⁺ pump in the heart. *J. Cardiovasc. Electrophysiol.* **2006**, *17*, S127–S133.
- [218] da Silva, J. J. R. F.; Williams, R. J. P. *The Biological Chemistry of the Elements*, 2nd ed.; Oxford University Press, 2001.
- [219] Harding, M. M. The geometry of metal-ligand interactions relevant to proteins. *Acta Crystallogr. D* **1999**, *55*, 1432–1443.
- [220] Harding, M. M. The architecture of metal coordination groups in proteins. *Acta Crystallogr. D* **2004**, *60*, 849–859.
- [221] Hsin, K.; Sheng, Y.; Harding, M. M.; Taylor, P.; Walkinshaw, M. D. MESPEUS: a database of the geometry of metal sites in proteins. *J. Appl. Crystallogr.* **2008**, *41*, 963–968.
- [222] Görlich, A.; Bertram, K.; Hudcová, S.; Krizanova, O. Calcium and ROS: a mutual interplay. *Redox Biol.* **2015**, *6*, 260–271.
- [223] Adam-Vizi, V.; Starkov, A. A. Calcium and mitochondrial reactive oxygen species generation: how to read the facts. *J. Alzheimers Dis.* **2010**, *20 Suppl 2*, S413–S426.
- [224] Brookes, P. S.; Yoon, Y.; Robotham, J. L.; Anders, M. W.; Sheu, S.-S. Calcium, ATP, and ROS: a mitochondrial love-hate triangle. *Am. J. Physiol. Cell Physiol.* **2004**, *287*, C817–C833.
- [225] Sullivan, L. B.; Chandel, N. S. Mitochondrial reactive oxygen species and cancer. *Cancer Metab.* **2014**, *2*, 17.
- [226] Bietti, M.; Gente, G.; Salamone, M. Structural effects on the β -scission reaction of tertiary arylcarbonyloxy radicals. The role of α -cyclopropyl and α -cyclobutyl groups. *J. Org. Chem.* **2005**, *70*, 6820–6826.
- [227] Neta, P.; Dizdaroglu, M.; Simic, M. G. Radiolytic studies of the cumyloxy radical in aqueous solutions. *Isr. J. Chem.* **1984**, *24*, 25–28.
- [228] Fukuzumi, S.; Ohkubo, K. Fluorescence Maxima of 10-Methylacridone- Metal Ion Salt Complexes: A Convenient and Quantitative Measure of Lewis Acidity of Metal Ion Salts. *J. Am. Chem. Soc.* **2002**, *124*, 10270–10271.

References

- [229] Reichardt, C.; Welton, T. *Solvents and Solvent Effects in Organic Chemistry*, 4th ed.; Wiley-VCH, 2010.
- [230] Babu, C. S.; Dudev, T.; Lim, C. Differential Role of the Protein Matrix on the Binding of a Catalytic Aspartate to Mg²⁺ vs Ca²⁺: Application to Ribonuclease H. *J. Am. Chem. Soc.* **2013**, *135*, 6541–6548.
- [231] Dudev, T.; Lim, C. Competition among metal ions for protein binding sites: determinants of metal ion selectivity in proteins. *Chem. Rev.* **2014**, *114*, 538–556.
- [232] Siu, F.; Ma, N.; Tsang, C. Alkali metal cation-ligand affinities: Basis set superposition correction for the Gaussian protocols. *J. Chem. Phys.* **2001**, *114*, 7045–7051.
- [233] Corral, I.; Mó, O.; Yáñez, M.; Scott, A. P.; Radom, L. Interactions between Neutral Molecules and Ca²⁺: An Assessment of Theoretical Procedures. *J. Phys. Chem. A* **2003**, *107*, 10456–10461.
- [234] Suárez, D.; Rayón, V. M.; Díaz, N.; Valdés, H. Ab initio benchmark calculations on Ca (II) complexes and assessment of density functional theory methodologies. *J. Phys. Chem. A* **2011**, *115*, 11331–11343.
- [235] Baldauf, C.; Pagel, K.; Warnke, S.; von Helden, G.; Koksch, B.; Blum, V.; Scheffler, M. How cations change peptide structure. *Chemistry—A European Journal* **2013**, *19*, 11224–11234.
- [236] Functions and evolution of selenoprotein methionine sulfoxide reductases. *Biochim. Biophys. Acta* **2009**, *1790*, 1471–1477.
- [237] van Santen, J. A.; Rahemtulla, S.; Salamone, M.; Bietti, M.; DiLabio, G. A. A computational and experimental re-examination of the reaction of the benzoyloxy radical with DMSO. *Comput. Theor. Chem.* **2016**, *1077*, 74–79.
- [238] For a detail description of the RI approximation and explicit correlation, see Ref. 108, Chapter 4.
- [239] Reed, A. E.; Weinhold, F. Natural Bond Orbital Analysis of Near-Hartree-Fock Water Dimer. *J. Chem. Phys.* **1983**, *78*, 4066–4073.
- [240] Reed, A. E.; Weinstock, R. B.; Weinhold, F. Natural Population Analysis. *J. Chem. Phys.* **1985**, *83*, 735–746.
- [241] Glendening, E. D.; Landis, C. R.; Weinhold, F. Natural Bond Orbital Methods. *WIREs Comput. Mol. Sci.* **2012**, *2*, 1–42.
- [242] NBO Version 3.1, E. D. Glendening, A. E. Reed, J. E. Carpenter, and F. Weinhold.

References

- [243] Landis, C. R.; Weinhold, F. In *The NBO view of chemical bonding*; Fernking, G., Shaik, S., Eds.; Wiley-VCH, 2014; Chapter 3, pp 91–120.
- [244] Weinhold, F.; Landis, C.; Glendening, E. What is NBO analysis and how is it useful? *Int. Rev. Phys. Chem.* **2016**, *35*, 399–440.
- [245] Degrève, L.; Vechi, S. M.; Jr., C. Q. The hydration structure of Na^+ and K^+ ions and the selectivity of their ionic channels. *Biochim. Biophys. Acta* **1996**, *1274*.
- [246] Omta, A. W.; Kropman, M. F.; Woutersen, S.; Bakker, H. J. Negligible effect of ions on the hydrogen-bond structure in liquid water. *Science* **2003**, *301*, 347–349.
- [247] Funkner, S.; Niehues, G.; Schmidt, D. A.; Heyden, M.; Schwaab, G.; Callahan, K. M.; Tobias, D. J.; Havenith, M. Watching the low-frequency motions in aqueous salt solutions: the terahertz vibrational signatures of hydrated ions. *J. Am. Chem. Soc.* **2011**, *134*, 1030–1035.
- [248] Heyda, J.; Vincent, J. C.; Tobias, D. J.; Dzubiella, J.; Jungwirth, P. Ion specificity at the peptide bond: Molecular dynamics simulations of N-methylacetamide in aqueous salt solutions. *J. Phys. Chem. B* **2009**, *114*, 1213–1220.
- [249] Slifkin, M.; Allison, A. Measurement of ionization potentials from contact charge transfer spectra. *Nature* **1967**, *215*, 949–950.
- [250] Baldwin, M.; Loudon, A.; Webb, K.; Cardnell, P. Charge location and fragmentation under electron impact. Vthe ionization potentials of (methylated) phosphoramides, guanidines, formamides, acetamides, ureas and thioureas. *J. Mass Spectrom.* **1977**, *12*, 279–282.
- [251] Haynes, W. M., Ed. *CRC Handbook of Chemistry and Physics*, 97th ed.; CRC Press: Boca Raton, Fl, 2016.
- [252] Chatterjee, A.; Dixit, M. K.; Tembe, B. Solvation Structures and Dynamics of the Magnesium Chloride ($\text{Mg}^{2+}\text{Cl}^-$) Ion Pair in Water–Ethanol Mixtures. *J. Phys. Chem. A* **2013**, *117*, 8703–8709.
- [253] Glendening, E. D.; Hrabal II, J. A. Resonance in Formamide and Its Chalcogen Replacement Analogues: A Natural Population Analysis/Natural Resonance Theory Viewpoint. *J. Am. Chem. Soc.* **1997**, *119*, 12940–12946.
- [254] Galano, A.; Alvarez-Idaboy, J. R. A computational methodology for accurate predictions of rate constants in solution: Application to the assessment of primary antioxidant activity. *J. Comput. Chem.* **2013**, *34*, 2430–2445.

References

- [255] Snelgrove, D. W.; Lusztyk, J.; Banks, J. T.; Mulder, P.; Ingold, K. U. Kinetic Solvent Effects on Hydrogen-Atom Abstractions: Reliable, Quantitative Predictions via a Single Empirical Equation1. *J. Am. Chem. Soc.* **2001**, *123*, 469–477.
- [256] HyperChem 5.0, Hypercube, Inc., 1115 NW 4th Street, Gainesville, Florida 32601, USA.
- [257] Marshall, L. A., M. S. amd Burns; Sherrill, C. D. Basis set convergence of the coupled-cluster correction, $\delta_{MP2}^{CCSD(T)}$: Best practices for benchmarking non-covalent interactions and the attendant revision of the S22, NBC10, HBC6, and HSG databases. *J. Chem. Phys.* **2011**, *135*, 194102.
- [258] Řezáč, J.; Hobza, P. Describing Noncovalent Interactions beyond the Common Approximations: How Accurate Is the Gold Standard, CCSD(T) at the Complete Basis Set Limit? *J. Chem. Thoery Comput.* **2013**,
- [259] Iron, M. A.; Oren, M.; Martin, J. M. Alkali and alkaline earth metal compounds: corevalence basis sets and importance of subvalence correlation. *Mol. Phys.* **2003**, *101*, 1345–1361.
- [260] Peterson, K. A.; Adler, T. B.; Werner, H. J. Correlation Consistent F12 Basis Sets: H, He, B-Ne, Al-Ar. *J. Chem. Phys.* **2008**, *128*, 084102.
- [261] Rappoport, D.; Furche, F. Property-optimized gaussian basis sets for molecular response calculations. *J. Chem. Phys.* **2010**, *133*, 134105.
- [262] Perdew, J. P. Density-functional approximation for the correlation energy of the inhomogeneous electron gas. *Phys. Rev. B* **1986**, *33*, 8822–8824.
- [263] Perdew, J. P. In *Electronic Structure of Solids '91*; Zieche, P., Eschrig, H., Eds.; Akademie Verlag, 1991; p 11.
- [264] Becke, A. D. A new mixing of Hartree–Fock and local density-functional theories. *J. Chem. Phys.* **1993**, *98*, 1372–1377.
- [265] Boese, A. D.; Martin, J. M. L. Development of Density Functionals for Thermochemical Kinetics. *J. Chem. Phys.* **2004**, *121*, 3405–3416.
- [266] Yanai, T.; Tew, D. P.; Handy, N. C. A new hybrid exchange–correlation functional using the Coulomb-attenuating method (CAM-B3LYP). *Chem. Phys. Lett.* **2004**, *393*, 51–57.
- [267] Zhao, Y.; Truhlar, D. G. The M06 suite of density functionals for main group thermochemistry, thermochemical kinetics, noncovalent interactions, excited states, and transition elements: two new functionals and systematic testing of four M06-class functionals and 12 other functionals. *Theor. Chem. Acc.* **2008**, *120*, 215–241.

References

- [268] Zhao, Y.; Truhlar, D. G. A new local density functional for main-group thermochemistry, transition metal bonding, thermochemical kinetics, and noncovalent interactions. *J. Chem. Phys.* **2006**, *125*, 194101.
- [269] Schultz, N. E.; Zhao, Y.; Truhlar, D. G. Density Functionals for Inorganometallic and Organometallic Chemistry. *J. Phys. Chem. A* **2005**, *109*, 11127–11143.
- [270] Adamo, C.; Barone, V. Toward reliable density functional methods without adjustable parameters: The PBE0 model. *J. Chem. Phys.* **1999**, *110*, 6158–6169.
- [271] Ernzerhof, M.; Scuseria, G. Assessment of the Perdew-Burke-Ernzerhof exchange-correlation functional. *J. Chem. Phys.* **1999**, *110*, 5029–5036.
- [272] Perdew, J. P.; Burke, K.; Ernzerhof, M. Generalized gradient approximation made simple. *Phys. Rev. Lett.* **1996**, *77*, 3865–3868.
- [273] Tao, J. M.; Perdew, J. P.; Staroverov, V. N.; Scuseria, G. E. Climbing the density functional ladder: Nonempirical meta-generalized gradient approximation designed for molecules and solids. *Phys. Rev. Lett.* **2003**, *91*, 146401.
- [274] Becke, A. D. Density-functional thermochemistry. V. Systematic optimization of exchange-correlation functionals. *J. Chem. Phys.* **1997**, *107*, 8554.
- [275] Chai, J.-D.; Head-Gordon, M. Systematic optimization of long-range corrected hybrid density functionals. *J. Chem. Phys.* **2008**, *128*, 084106.
- [276] Chai, J.-D.; Head-Gordon, M. Long-range corrected hybrid density functionals with damped atom-atom dispersion corrections. *Phys. Chem. Chem. Phys.* **2008**, *10*, 6615–6620.
- [277] Heyd, J.; Scuseria, G. Efficient hybrid density functional calculations in solids: The HS-Ernzerhof screened Coulomb hybrid functional. *J. Chem. Phys.* **2004**, *121*, 1187–1192.
- [278] Heyd, J.; Peralta, J. E.; Scuseria, G. E.; Martin, R. L. Energy band gaps and lattice parameters evaluated with the Heyd-Scuseria-Ernzerhof screened hybrid functional. *J. Chem. Phys.* **2005**, *123*, 174101.
- [279] Kabsch, W. A solution for the best rotation to relate two sets of vectors. *Acta Crystallogr.* **1976**, *A32*, 922–923.
- [280] Calculated using the ROCBS-QB3 method.
- [281] Salamone, M.; DiLabio, G. A.; Bietti, M. Hydrogen Atom Abstraction Reactions from Tertiary Amines by Benzoyloxyl and Cumyloxyl Radicals: Influence of Structure on the Rate-Determining Formation of a Hydrogen-Bonded Pre-reaction Complex. *J. Org. Chem.* **2011**, *76*, 6264–6270.

Appendix

Appendix A

Chapter 3 Additional Data

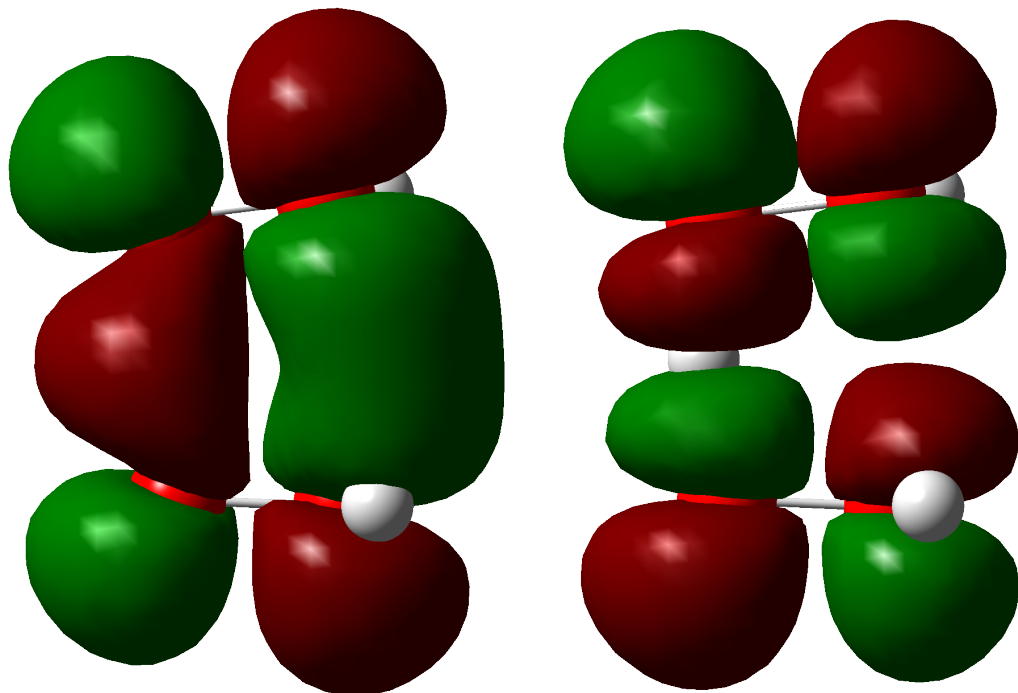


Figure A.1: Molecular orbitals of hydrogen peroxide-peroxyl self-exchange reaction TS complex, demonstrating a PCET mechanism. Left is the HOMO-1 and right is the SOMO. Together they demonstrate a lone pair-lone pair net half bonding interactions, consistent with PCET. MOs are shown with an isovalue of $0.02 e^-/\text{\AA}$.

Appendix B

Chapter 4 Additional Data

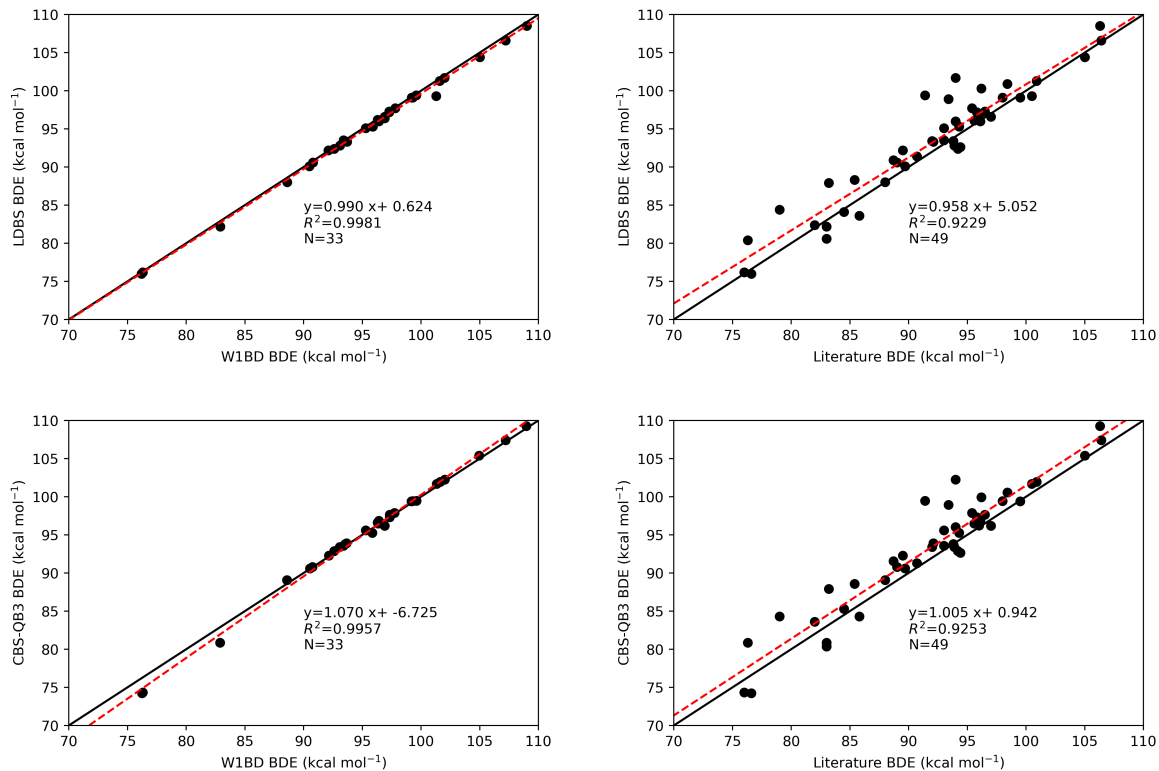


Figure B.1: One-to-one plots of composite methods compared to literature and W1BD.

Appendix B. Chapter 4 Additional Data

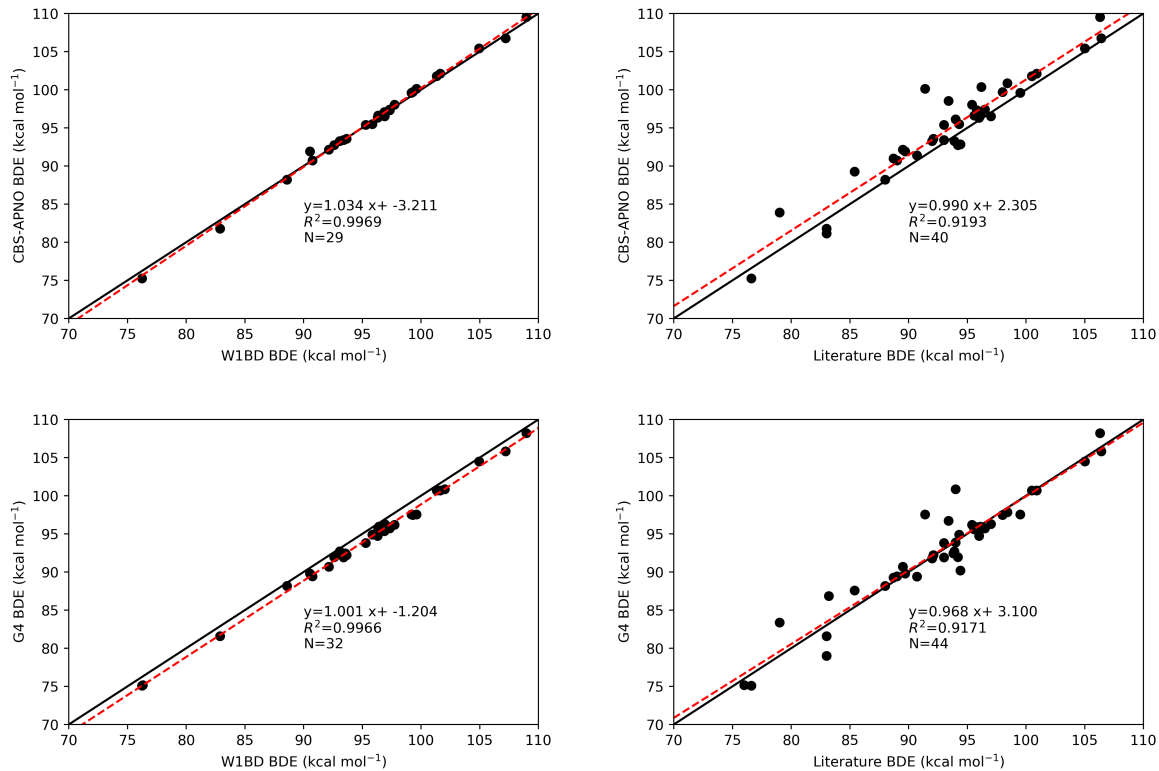


Figure B.1: Continued: One-to-one plots of composite methods compared to literature and W1BD.

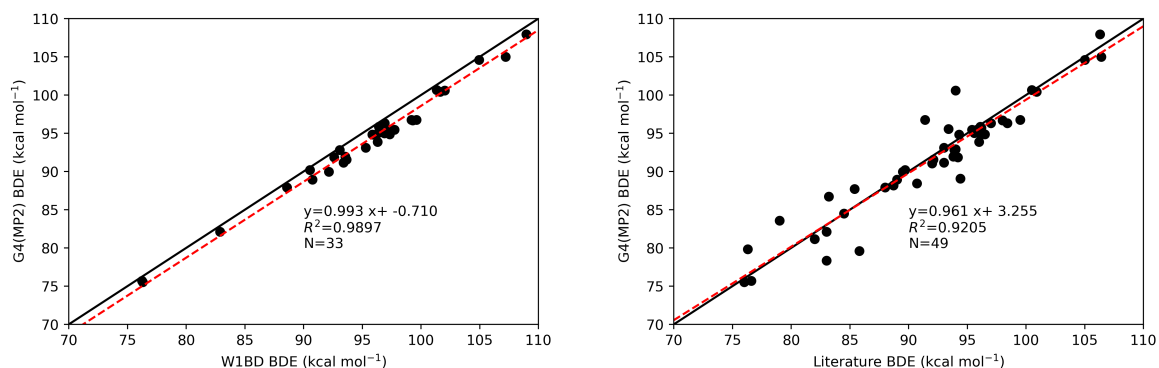


Figure B.1: Continued: One-to-one plots of composite methods compared to literature and W1BD.

Appendix B. Chapter 4 Additional Data

Table B.1: Summary of experimental rate constants ($M^{-1}s^{-1}$) and literature¹⁸⁰ bond dissociation enthalpies (BDEs, kcal mol⁻¹).

Molecule	k_H	Normalized k_H	BDE
1,4-cyclohexadiene	$6.65 \pm 0.02 \times 10^7$	1.66×10^7	76.0
1,4-diazabicyclo-[2.2.2]octane	$9.6 \pm 1.4 \times 10^6$	8.0×10^5	93.4
2,2-dimethylbutane	$9.5 \pm 0.3 \times 10^4$	4.8×10^4	98.0
2,3-dimethylbutane	$5.6 \pm 0.2 \times 10^5$	2.8×10^5	95.4
9,10-dihydroanthracene	$5.04 \pm 0.01 \times 10^7$	1.26×10^7	76.3
Acetone	$< 1 \times 10^4$	2×10^3	96.0
Acetonitrile	$< 1 \times 10^4$	3×10^3	97.0
Adamantane (2°)	6.90×10^6	5.75×10^5	98.4
Adamantane (3°)	6.90×10^6	1.73×10^6	96.2
Benzaldehyde	1.20×10^7	1.20×10^7	88.7
Benzyl alcohol	2.97×10^6	1.49×10^6	79.0
Cumene	$5.6 \pm 0.3 \times 10^5$	5.6×10^5	83.2
Cycloheptane	$2.20 \pm 0.02 \times 10^6$	1.57×10^5	94.0
Cyclohexane	$1.1 \pm 0.1 \times 10^6$	9.2×10^4	99.5
Cyclooctane	$2.98 \pm 0.02 \times 10^6$	1.86×10^5	94.4
Cyclopentane	$9.54 \pm 0.08 \times 10^5$	9.54×10^4	95.6
Dibenzyl ether	5.60×10^6	1.40×10^6	85.8
Diethyl ether	2.6×10^6	6.5×10^5	93.0
Dimethyl sulfoxide	1.8×10^4	6.0×10^3	94.0
Diethylamine	1.10×10^8	2.75×10^7	88.6
Dioxane	8.2×10^5	1.0×10^5	96.5

Appendix B. Chapter 4 Additional Data

Diphenylmethane	$8.71 \pm 0.03 \times 10^5$	4.36×10^5	84.5
Ethylbenzene	$7.9 \pm 0.1 \times 10^5$	4.0×10^5	85.4
Hexamethylphosphoramide	1.87×10^7	1.04×10^6	
Morpholine	5.00×10^7	1.25×10^7	92.0
Piperazine	$2.26 \pm 0.01 \times 10^8$	2.84×10^7	93.0
Piperidine	$1.07 \pm 0.01 \times 10^8$	2.68×10^7	89.5
Pyrrolidine	$1.24 \pm 0.05 \times 10^8$	3.10×10^7	89.0
Tetrahydrofuran	$5.8 \pm 0.1 \times 10^6$	1.5×10^6	92.1
Toluene	$1.85 \pm 0.08 \times 10^5$	6.17×10^4	89.7
Triethylamine	2.1×10^8	3.5×10^7	90.7

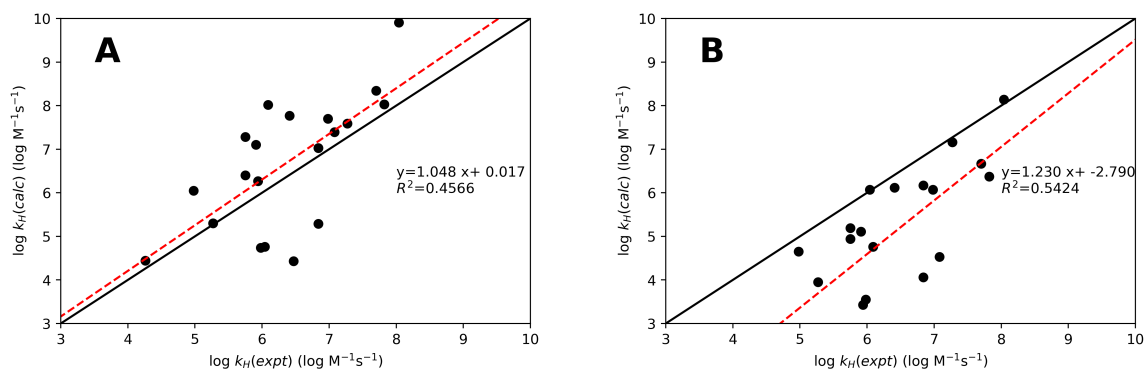


Figure B.2: One-to-one plots comparing experimental and **A** gas-phase calculated and **B** solvent-phase rate constants for HAT reactions between CumO \cdot and various organic substrates.

Appendix C

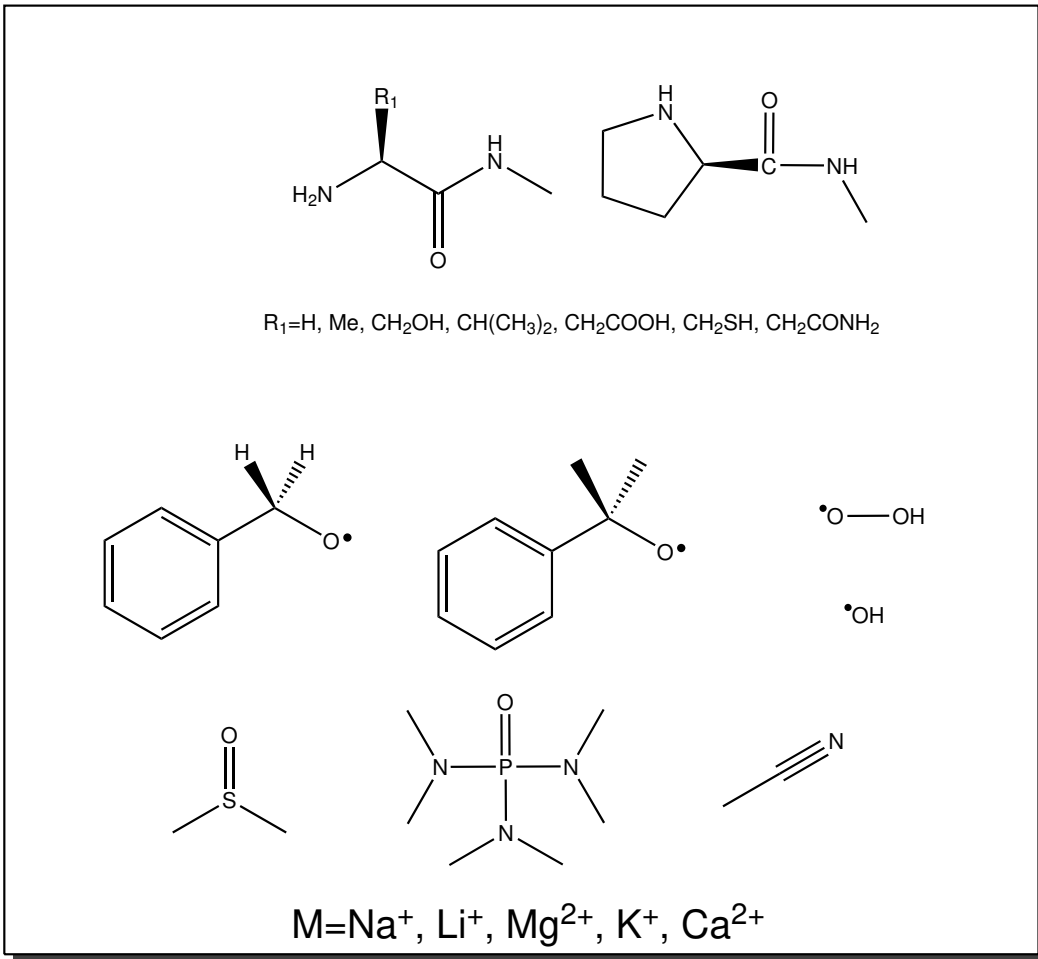
Chapter 5 Additional Data

C.1 Benchmarking DFT based methods for the binding of alkali and alkaline earth metals to organic substrates and oxygen-centred radicals

In order to be confident of the results of quantum mechanical mechanistic studies, the method of choice must be calibrated. While DFT-based methods have been widely applied to these studied, few studies have previously investigated alkali and alkaline earth-metal cation binding to organic substrates.^{232–235} Most importantly, benchmark quality data for a wide variety of metals binding to biologically relevant substrates and oxygen-centred radicals does not exist to calibrate DFT-based methods. Therefore, I performed a benchmark study which incorporated all the biologically relevant alkali and alkaline earth-metal cations, models for dipeptides including amino acid side-chains, oxygen-centred radicals, and solvents which are utilized in the experimental mechanistic studies involved in probing these systems. Unfortunately, due to computational restrictions (*vide infra*), benchmark quality calculations on the originally proposed benchmark set were not possible. Full details of the originally proposed benchmark set are shown in Scheme C.1.

Benchmark quality binding energies are generally calculated using the “gold standard” approach, CCSD(T)/CBS, where correlation consistent basis sets^{257,258} (cc-pV_XZ, X=T,Q,5) developed by Dunning and^{151,152} co-workers are used for complete basis set extrapolation. For the alkali and alkaline earth-metals, Iron et al.²⁵⁹

C.1. Benchmarking DFT based methods



Scheme C.1: Initial proposed benchmark set of substrates/radicals and metal cations. Note this set consists of all combinations of substrates and metal cation, thus there are 75 complexes in the set. Conformational analysis using the Hyperchem package²⁵⁶ to identify the lowest energy conformers of all the substrates was completed using the AM1 semi-empirical approach. Geometry optimizations were then performed without metal cations at the LC- ω PBE-D3(BJ)/6-31+G(2d,2p) level of theory. Several binding sites were investigated and optimized at the same level of theory. Benchmark quality structures have been optimized at the LC- ω PBE-D3(BJ)/6-311+G(3df,3pd) level of theory. I am awaiting computational resources to perform CCSD(T)-F12*/Def2-QZVPPD calculations.

C.1. Benchmarking DFT based methods

demonstrated that additional *d*-type basis functions are necessary to obtain reasonable results. It is also necessary to include core-correlation of at least the first core shell in alkali and alkaline earth metals, thus it would be appropriate to use core valence basis sets such as cc-pCVXZ.⁶⁶ Iron et al.²⁵⁹ also developed core-valence basis sets for the alkali and alkaline earth-metals, however I was not able to obtain these basis sets until very recently.^{vii} These basis sets should be considered for future benchmarking work. Given these difficulties, I originally chose the augmented version of the polarization consistent basis sets of Jensen and co-workers^{67–70} (aug-pc-*N*, *N*=2,3,4), which have been shown to converge to the CBS limit systematically⁸⁴ and are available for all the elements of interest.

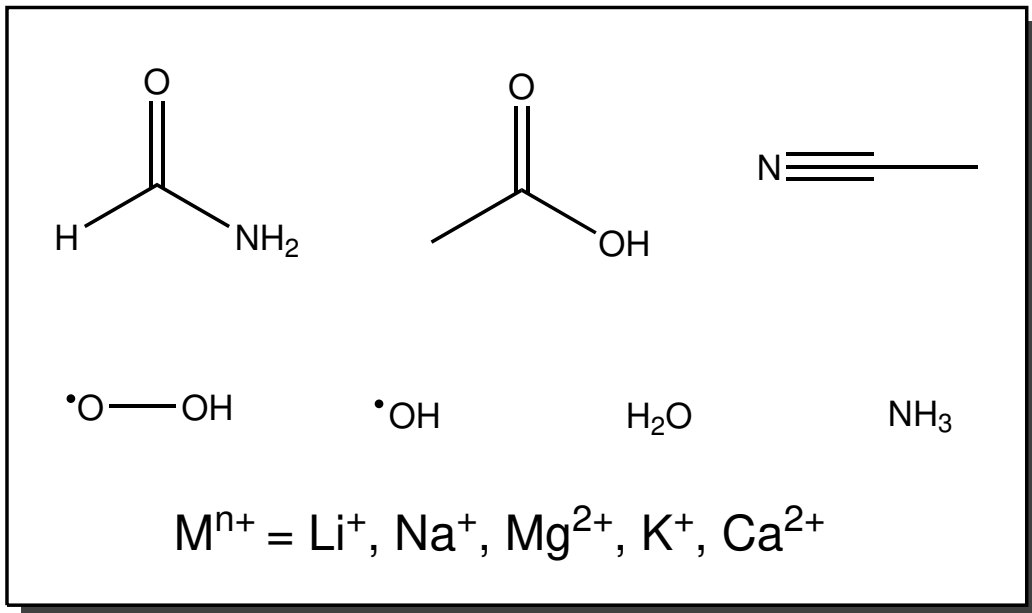
While performing CCSD(T)/CBS calculations, I observed that the metal cations (and neutral metal atoms), did not converge smoothly to the complete basis set limit. As a consequence, complete basis set extrapolation is not feasible. In light of this problem, I decided to re-evaluate the size scope of the benchmark set being used. In order to facilitate future DFT-based work and probe the issue of basis set convergence of alkali and alkaline earth metals, a benchmark set of small substrates was proposed. This new set is shown in Scheme C.2. The new, small benchmark set was selected to include important functional groups and radicals found in biological systems, and one of the most common solvents used in physical organic experiments, acetonitrile.

C.1.1 Metal cation basis set convergence

In order to perform complete basis set (CBS) extrapolation, the total energy of a molecule/atom should converge smoothly to the CBS limit.⁷⁹ However, CCSD(T,Full)/aug-pc*N* (*N*=1,2,3,4) calculations for alkali and alkaline earth-metals convergence of

^{vii}See <http://theochem.weizmann.ac.il/web/papers/group12.html> for the CVNZ basis sets for Li, Be, Na, Mg, K, Ca.

C.1. Benchmarking DFT based methods



Scheme C.2: Revised benchmark set of small substrates and cations. Note this set consists of all combinations of substrates and metal cations, i.e., there are 35 complexes in the set.

poorly to the CBS limit (See Figure C.1). Examining the energy of each ion relative to the smallest basis set, for Li⁺ the value appears to converge reasonably, however this is because there are only 2 electrons in this ion. For all of Na⁺, Mg²⁺, K⁺, and Ca²⁺, there appears to be no convergence to the CBS limit as no asymptote is reached. This is problematic as it means that CBS extrapolation would result in a significant degree of uncertainty in the estimated CBS limit total energy.

The poor convergence was thought to be a result of poorly suited basis sets to full core-correlation. However, the same CCSD(T,Full) calculations using the core-correlation (cc-pCVNZ) basis sets also show unsatisfactory convergence for Na⁺ and Mg²⁺ (See Figure C.2). Therefore, I was tasked with finding a method which would give results which best approximate alkali and alkaline metal binding at the complete basis set limit. I decided to use an explicitly correlated CCSD(T)

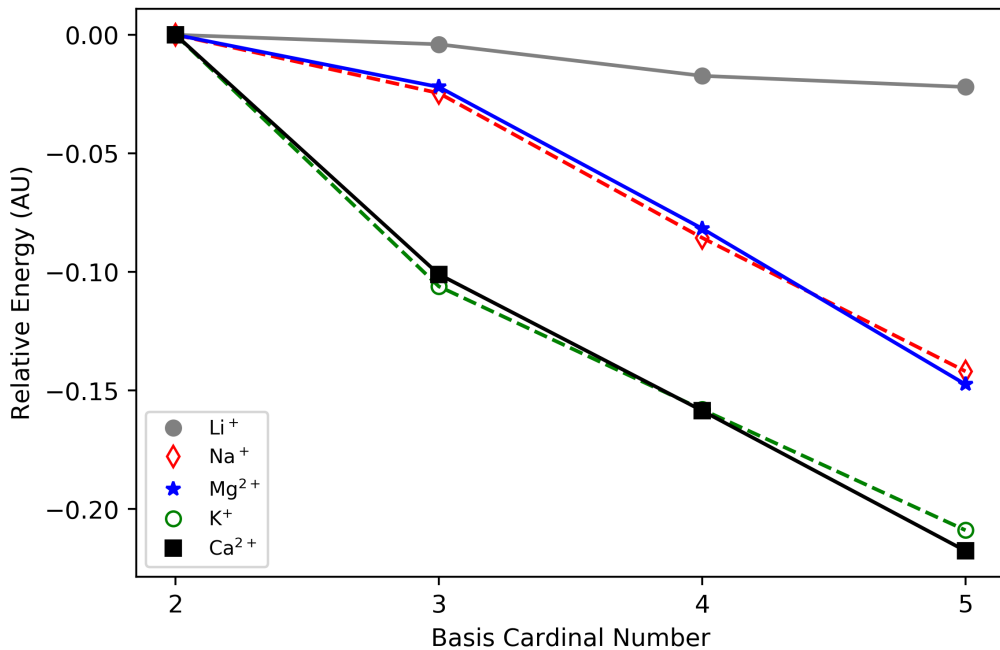


Figure C.1: Basis set convergence of CCSD(T,Full)/aug- $\text{pc-}N$ ($N=1,2,3,4$) for alkali and alkaline earth-metal cations. The relative energy of each basis set relative to the aug- $\text{pc-}1$ for each metal. The cardinal number of the aug- $\text{pc-}N$ basis sets is $X = N + 1$.

C.1. Benchmarking DFT based methods

treatment known as “F12*” to more rapidly approach the CBS limit.⁸⁷ I tested both the core-correlation consistent basis set developed for used with explicitly correlation (cc-pCV X Z-F12),²⁶⁰ and the Ahlrich basis sets (Def2-SVP,-TZVPPD, and -QZVPPD).²⁶¹ Both these basis sets combined with the CCSD(T,Full)-F12* methodology gave satisfactory convergence to the CBS limit for the sodium and magnesium ion (See Figure C.3) for the convergence of all metal ions calculated with the CCSD(T,Full-F12*/Def2-QZVPPD method). Given that Def2-QZVPPD is available for almost every atom on the periodic table, and the observed convergence to the CBS limit, this basis set was selected for benchmark quality binding energies.

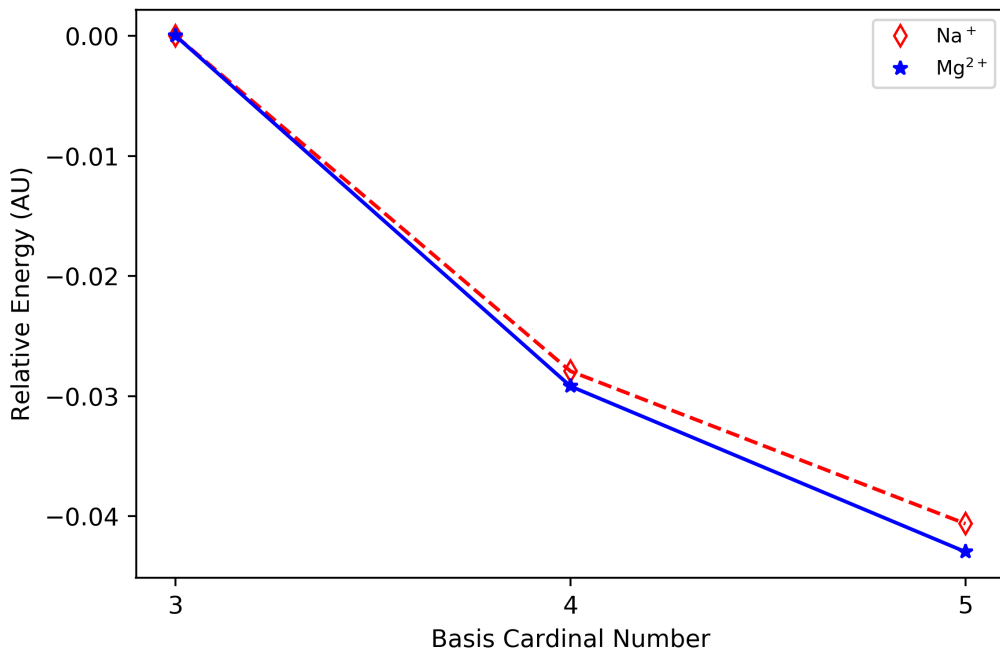


Figure C.2: Basis set convergence of CCSD(T,Full)/cc-pVC X Z ($X=3,4,5$) for sodium and magnesium ions. The relative energy of each basis set relative to the cc-pVCDZ for each metal. The cardinal number of the basis sets is X .

To the best of my knowledge, there is no precedent for extrapolating the Ahlrich

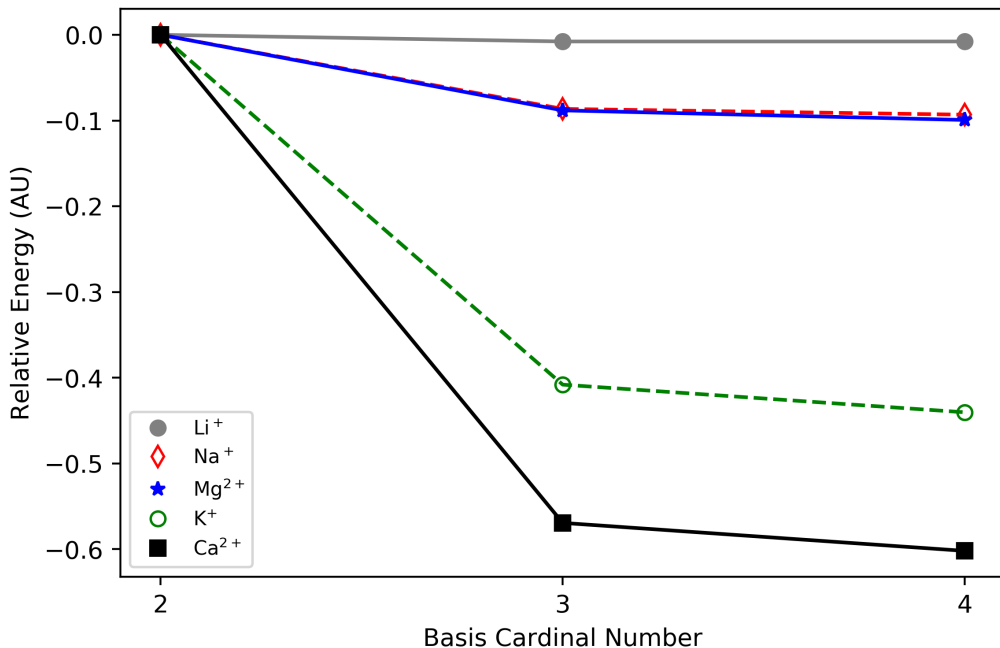


Figure C.3: Explicitly correlated CCSD(T,Full)-F12*/Def2- X ($X=\text{SVP}, \text{TZVPPD}, \text{QZVPPD}$) basis set convergence for alkali and alkaline earth-metal cations. The relative energy of each basis set relative to the Def2-SVP for each metal. The cardinal number of the basis sets is X .

C.1. Benchmarking DFT based methods

basis sets, thus the final benchmark energies are at the CCSD(T)-F12*/Def2-QZVPPD level of theory, without extrapolation. The convergence of the total energies of the cations can be estimated as the sum of the experimental ionization energies of the ions. These results are listed in Table C.1. The calculated values are too high (i.e., not at the CBS limit), and deviate from experiment from 0.16 and 0.66 AU (4.4–18 eV). Deviations of this magnitude are rather significant, and are likely due to the increasing contribution of “relativistic effects” with increasing atomic number. Additionally, there may be cumulative experimental error, as the experimental ionization energies range from 4–5500 eV. Relativistic effects were not considered herein, thus, the calculated binding energies herein are likely the best available approximation to the non-relativistic gas-phase metal-substrate binding energy.

Table C.1: Total energy of alkali and alkaline earth-metal cations from experimental ionization energies²⁵¹ (Expt.) and calculated (Calc.) at the CCSD(T,Full)-F12*/Def2-QZVPPD level of theory. All values are in units of AU.

Ion	Expt.	Calc.
Li ⁺	-7.47798	-7.27983
Na ⁺	-162.43089	-162.24203
Mg ²⁺	-200.32523	-199.49171
K ⁺	-601.93332	-601.77381
Ca ²⁺	-680.19158	-679.53065

C.1.2 High level results and evaluation of various density-functional theory based methods

Table C.2 lists the benchmark binding energy values calculated at the CCSD(T,Full)-F12*/Def2-QZVPPD//LC- ω PBE-D3(BJ)/6-311+G(3df,3pd) level of theory. Some general trends are that alkaline earth-metals bind more strongly than alkali earth-metals. Also, the order of binding follows the Lewis acidity of the metal ions: Mg²⁺ > Ca²⁺ > Li⁺ > Na⁺ > K⁺. The metals all appear to bind most strongly to the

C.1. Benchmarking DFT based methods

amidic oxygen-centre, reflecting the higher Lewis basicity. The metals also bind weakest to the oxygen-centred radicals, with greater binding to HOO^\cdot as compared to HO^\cdot .

Table C.2: Benchmark gas-phase binding energies of alkali and alkaline earth-metals with small organic substrates and radicals. Values are calculated at the CCSD(T,Full)-F12*/Def2-QZVPPD//LC- ω PBE-D3(BJ)/6-311+G(3df,3pd) level of theory. All values are in kcal mol⁻¹.

	Li^+	Na^+	Mg^{2+}	K^+	Ca^{2+}
H_2O	-34.7	-24.4	-82.0	-17.8	-56.8
NH_3	-39.9	-28.2	-98.1	-19.8	-65.3
MeCN	-44.4	-33.0	-113.1	-24.9	-80.7
Formamide	-50.7	-36.9	-128.2	-28.5	-96.1
Formic acid	-38.4	-27.0	-101.9	-20.0	-72.6
HO^\cdot	-21.3	-16.8	-57.0	-12.4	-40.7
HOO^\cdot	-27.1	-19.1	-72.2	-13.9	-49.0

Next, 31 DFT-based methods combined with a moderate basis set (6-31+G(2d,2p)) and a large basis set (6-311+G(3df,3pd)) were tested for their ability to estimate the binding energy between metal cations and substrates. The mean absolute/signed errors (MAE/MSE) and maximum and minimum errors for each method are listed in Table C.3.

Table C.3: Evaluation of DFT-based methods for alkali and alkaline metal binding to organic substrates and radicals. All values are in kcal mol⁻¹. Negative values indicate under-binding.

Method	MAE/MSE	Max./Min	MAE/MSE	Max./Min.
	6-311+G(3df,3pd)		6-31+G(2d,2p)	
B3 ¹⁰¹ LYP ¹⁰²	1.49/1.35	5.12/-0.57	1.59/-0.17	4.67/-7.28
B3P86 ²⁶²	0.94/0.47	3.87/-0.96	1.36/-1.08	1.99/-7.38
B3PW91 ²⁶³	0.95/-0.14	2.74/-1.64	1.89/-1.70	1.47/-8.76
BH+H ²⁶⁴ LYP	1.89/1.84	5.29/-0.59	1.93/0.63	4.65/-5.64

C.1. Benchmarking DFT based methods

B ¹⁴⁷ LYP	1.60/1.07	5.56/-1.51	1.88/-0.75	5.30/-8.80
BMK ²⁶⁵	0.90/-0.70	1.13/-2.40	1.98/-1.93	0.86/-8.75
BP86	1.63/-0.25	4.61/-3.21	2.27/-2.14	1.55/-9.38
CAM-B3LYP ²⁶⁶	2.40/2.40	6.25/ 0.21	1.98/1.04	5.82/-5.25
LC- ω PBE ^{151,152}	0.78/0.58	2.95/-0.73	1.34/-0.74	2.19/-8.00
M05-2X ¹⁰³	1.11/1.11	3.21/ 0.15	1.24/-0.17	2.55/-5.75
M06 ²⁶⁷	1.05/-0.62	2.36/-4.83	1.83/-1.63	1.76/-9.03
M06-2X ²⁶⁷	1.13/1.13	3.68/ 0.11	1.26/-0.07	3.00/-6.63
M06L ²⁶⁸	1.52/-1.14	2.64/-6.94	2.55/-2.48	1.21/-11.2
MOHLYP ²⁶⁹	2.30/-2.02	1.52/-5.40	4.04/-3.96	0.89/-15.2
PBE0 ^{270,271}	1.22/1.18	4.19/-0.31	1.25/-0.34	3.30/-7.25
PBE ²⁷²	1.70/1.46	6.09/-0.87	1.58/-0.46	4.68/-8.15
TPSS ²⁷³	1.38/0.95	4.88/-1.12	1.60/-0.98	2.91/-8.12
B97 ²⁷⁴ D3 ¹⁰⁹	1.50/0.47	5.94/-2.19	1.69/-1.37	2.67/-8.41
ω B97 ²⁷⁵	0.61/0.23	2.13/-1.72	1.41/-0.97	1.78/-7.57
ω B97XD ²⁷⁶	1.12/-0.94	1.02/-4.52	2.24/-2.21	0.65/-8.64
HSEH1PBE ^{277,278}	1.30/1.29	4.28/-0.16	1.23/-0.23	3.45/-6.95
B3LYP-D3(BJ) ^{109,110}	2.86/2.86	7.50/ 0.34	1.92/1.34	7.05/-4.33
BLYP-D3(BJ)	2.89/2.88	8.40/-0.14	1.83/1.06	8.14/-5.30
B3PW91-D3(BJ)	1.47/1.40	5.81/-0.44	1.02/-0.14	3.88/-5.69
BMK-D3(BJ)	1.03/0.80	4.05/-1.06	1.02/-0.43	2.03/-5.49
BP86-D3(BJ)	1.77/1.29	7.78/-1.05	1.26/-0.60	3.96/-6.19
CAM-B3LYP-D3(BJ)	3.19/3.19	7.50/ 0.78	2.27/1.82	7.07/-3.54
LC- ω PDE-D3(BJ)	1.47/1.46	4.07/-0.06	1.33/0.14	3.30/-6.15

C.1. Benchmarking DFT based methods

PBE0-D3(BJ)	1.92/1.92	5.37 / 0.20	1.33/0.40	4.47/-5.74
PBE-D3(BJ)	2.24/2.23	7.57/-0.22	1.44/0.30	5.90/-6.67
TPSS-D3(BJ)	2.03/1.99	6.93/-0.30	1.25/0.06	4.56/-6.03

Given the magnitude of the gas-phase binding energies, the overall agreement between the benchmark values and the DFT-based method values with both moderate and large basis sets is very good. Interestingly, the application of the empirical D3(BJ) dispersion correction systematically decreases agreement with benchmark values as it increases over-binding. Also, going from moderate to large basis sets systematically increases the predicted binding energies, as indicated by an increase in MSE across the board. I chose three of the best performing methods (BMK-D3(BJ), TPSS-D3(BJ), and M05-2X) and performed geometry optimizations with moderate basis sets on the reference structures to determine if the choice of method would significantly impact the minimum energy bound structure. These results are listed in Table C.4.

Table C.4: Comparison of single point (SP on benchmark structure) and relaxed (optimized with method) binding energies for alkali and alkaline metal binding with DFT-based methods and 6-31+G(2d,2p) basis sets. Mean absolute error (MAE) values are in kcal mol⁻¹ and average root mean squared deviation (RMSD)(Root mean square deviation was calculated using the Kabsch algorithm²⁷⁹ as implemented in the rmsd package available on GitHub (Calculate RMSD for two XYZ structures, GitHub, <http://github.com/charnley/rmsd>, accessed Nov. 18, 2016)) of geometry are in Å.

Method	MAE(SP)	MAE(Relaxed)	Average RMSD
BMK-D3(BJ)	1.02	1.24	0.012
M05-2X	1.24	1.17	0.020
TPSS-D3(BJ)	1.25	1.21	0.026

For all the three methods tested, the average of the root mean square deviations (RMSD) from reference structures are very small (0.012–0.026 Å). For BMK-

C.2. HAT reactions involving non-redox active metals

D3(BJ), re-optimization of the structures results in a slight increase in MAE, while for TPSS-D3(BJ) and M05-2X, the opposite is true. As a whole, it seems that DFT-based methods are capable of predicting gas-phase binding energies for alkali and alkaline metal ions with organic substrates and radicals. M05-2X appears to be one of the best performing DFT-based methods. Furthermore, M05-2X is recommended by the QM-ORSA²⁵⁴ method, which outlines “best principles” for calculating accurate HAT rate constants in solution. And finally, M05-2X was previously used by our group in the study of the HAT reaction between DMSO and BnO[•],²³⁷ thus I have selected this method for further study of the effects of alkali and alkaline earth metal cations on the barrier heights of HAT reactions. Note also that M05-2X is a hybrid density-functional with 56% HF-exchange, and thus should not suffer significantly from delocalization error.

C.2 HAT reactions involving non-redox active metals

C.2.1 DMA + HO[•]

I was unsuccessful in performing full optimization calculations in the presence of the metal salt. However, the “guess” TS structures obtained by freezing the hydrogen atom acceptor donor bonds (as described in the Chapter 5 section) herein represent approximated transition state structures and therefore provide an estimate of the effects of metal salts in a more biologically relevant model. The calculated reaction barriers are presented in Table C.5.

For the direct HAT reaction between OH[•] and DMA abstraction occurs primarily from the cis position C–H bond of DMA. The calculated free energy (enthalpic) barrier is 7.9(-2.7) kcal mol⁻¹, which gives a calculated rate constant of 1.0×10^7 M⁻¹s⁻¹, or three orders of magnitude lower than the predicted rate constants of

C.2. HAT reactions involving non-redox active metals

Table C.5: Calculated free energy (enthalpy) barrier ($\Delta G(H)^\ddagger$, kcal mol⁻¹) for direct HAT from different C–H bonds in DMA by HO[•], with and without NaCl. The change in barrier height ($\Delta\Delta G(H)^\ddagger$) is calculated relative to the same abstraction site without the inclusion of NaCl. All barrier heights are relative to separated reactants (or complexed DMA-NaCl) and were calculated at the M05-2X-SMD(MeCN)/6-311+G(2d,2p)//M05-2X/6-31+G** level of theory. *Indicates estimated barrier based on “guess” TS structure.

Reaction	Abstraction Site	$\Delta G(H)^\ddagger$	$\Delta\Delta G(H)^\ddagger$
DMA + HO [•]	trans	8.9(0.0)	
	cis	7.9(-2.7)	
	acetyl	9.9(0.5)	
DMA-NaCl + HO [•]	trans*	13.1(1.3)	4.2(1.3)
	cis*	12.9(0.2)	5.0(2.9)
	acetyl*	16.6(2.0)	7.7(1.5)

1.5×10^{10} M⁻¹s⁻¹. This result is unsurprising given the poor agreement of the calculated values with experiment of HAT reaction between DMA and BnO[•] and CumO[•]. For abstraction by HO[•], the complexation of NaCl to DMA increases the estimated free energy reaction barriers across the board by 4.2–7.7 kcal mol⁻¹. This suggests that if Na⁺ interacts closely with DMA in vivo, then non-redox active metals may have a chemo-protective effect against hydrogen abstraction by HO[•].

For the acetyl position C–H bond of DMA, the enthalpic barrier increases by 1.5 kcal mol⁻¹, even though the calculated BDE decreases slightly upon complexation of NaCl. This can once again be explained by the effects of charge transfer in the TS complex. For the TS structure representing direct HAT between HO[•] the acetyl position of DMA-NaCl, there is a calculated charge transfer from DMA to Na⁺ of 0.02 e⁻, which results in a decrease in charge separation between HO[•] and DMA from 0.26 e⁻ without NaCl to 0.25 e⁻ with NaCl. Although this effect is small, it appears to significantly effect the ability of HO[•] to abstract a hydrogen atom from DMA. The same argument applies to both the cis and trans C–H bond positions of DMA, for which the enthalpic barrier increases by more than the calculated

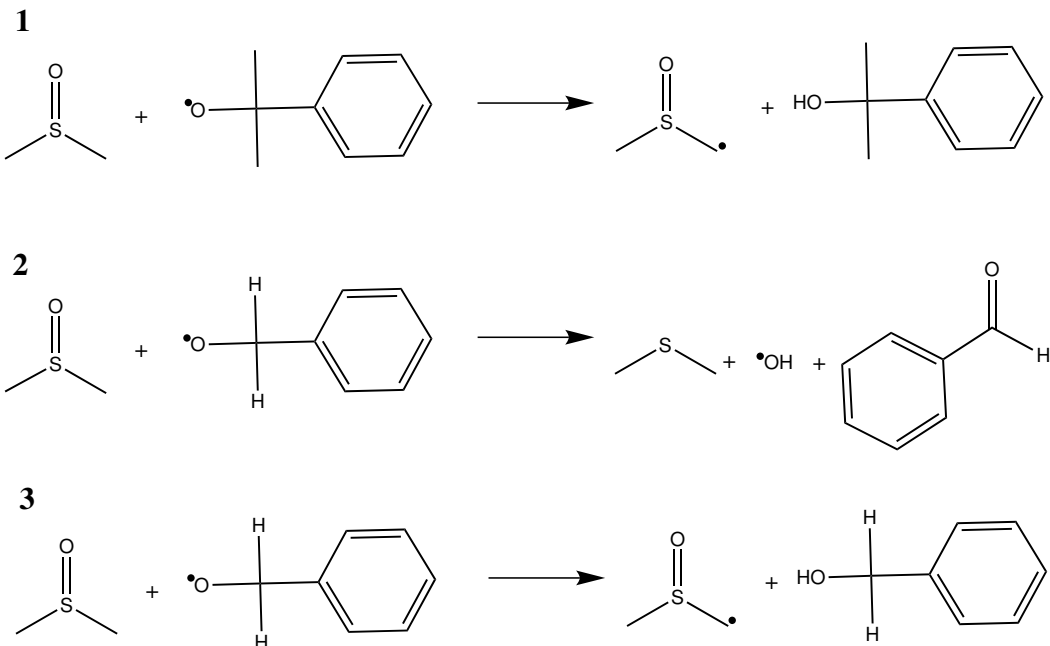
C.2. HAT reactions involving non-redox active metals

change in BDE. For the significantly more reactive HO[•] radical, the metal is less likely to interact with the oxygen centre, thus the effects observed depend only on interactions with DMA. As a result, the reaction barrier increases in all cases upon complexation of NaCl.

C.2.2 Strong hydrogen bond accepting substrates

In the investigation of the effects of metal cations on HAT reactions between DMA and CumO[•] Salamone et al. demonstrated that in DMSO solvent, HAT reactivity is not significantly affected by the addition of metal salts.⁵⁰ This can be explained on the basis of the stronger Lewis basicity of DMSO as compared to DMA, resulting in the competitive binding of Mⁿ⁺ to DMSO over DMA. The rate constant for HAT between DMSO and CumO[•] in DMSO solvent is $1.8 \times 10^4 \text{ M}^{-1}\text{s}^{-1}$ while that for DMSO and CumO[•] is $1.2 \times 10^6 \text{ M}^{-1}\text{s}^{-1}$ in MeCN solvent at 298 K, therefore only small changes in k_{obs} are expected for HAT between CumO[•] and DMA in DMSO solvent with metal salts. I am interested in how metal salts affect the HAT reactivity of DMSO and other related strong hydrogen bond accepting substrates. We previously showed that DMSO and BnO[•] react via a radical H-atom donation reaction, where BnO[•] acts counterintuitively as the hydrogen atom donor rather than acceptor. The net reaction yields benzaldehyde, dimethyl sulfide, and HO[•] as the DMSO-H radical decomposes in a concerted manner following the radical donation of the hydrogen atom by the radical.

An important driving force in this reaction is the formation of benzaldehyde by cleavage of an acidic α -C–H bond. This is not possible in CumO[•] therefore CumO[•] does not react through radical H-atom donation. I have performed computational studies to determine if metal cations could affect this reactivity and if the related (HMPA and TBPO) substrates displayed similar reactivity.



Scheme C.3: The HAT reactions of DMSO with **1** CumO[•], **2** the radical H-atom donation reaction with BnO[•], and **3** the conventional HAT reaction with BnO[•].

Table C.6: Calculated free energy (enthalpy) barrier ($\Delta G(H)^{\ddagger}$, kcal mol⁻¹) for HAT between DMSO and CumO[•], and conventional HAT and radical H-atom donation with BnO[•], with and without NaCl. The change in barrier height ($\Delta\Delta G(H)^{\ddagger}$) is calculated relative to the same reaction without the inclusion of NaCl. All barrier heights are relative to separated reactants (or complexed DMSO-NaCl) and were calculated at the M05-2X-SMD(MeCN)/6-311+G(2d,2p)//M05-2X/6-31+G** level of theory.

Reaction	$\Delta G(H)^{\ddagger}$	$\Delta\Delta G(H)^{\ddagger}$
1	20.9(8.9)	
1 + NaCl	22.4(5.2)	1.5(-3.7)
2	10.4(-2.2)	
2 + NaCl	13.4(-3.4)	2.0(-1.2)
3	22.7(10.4)	
3 + NaCl	22.1(5.2)	-0.6(-5.2)

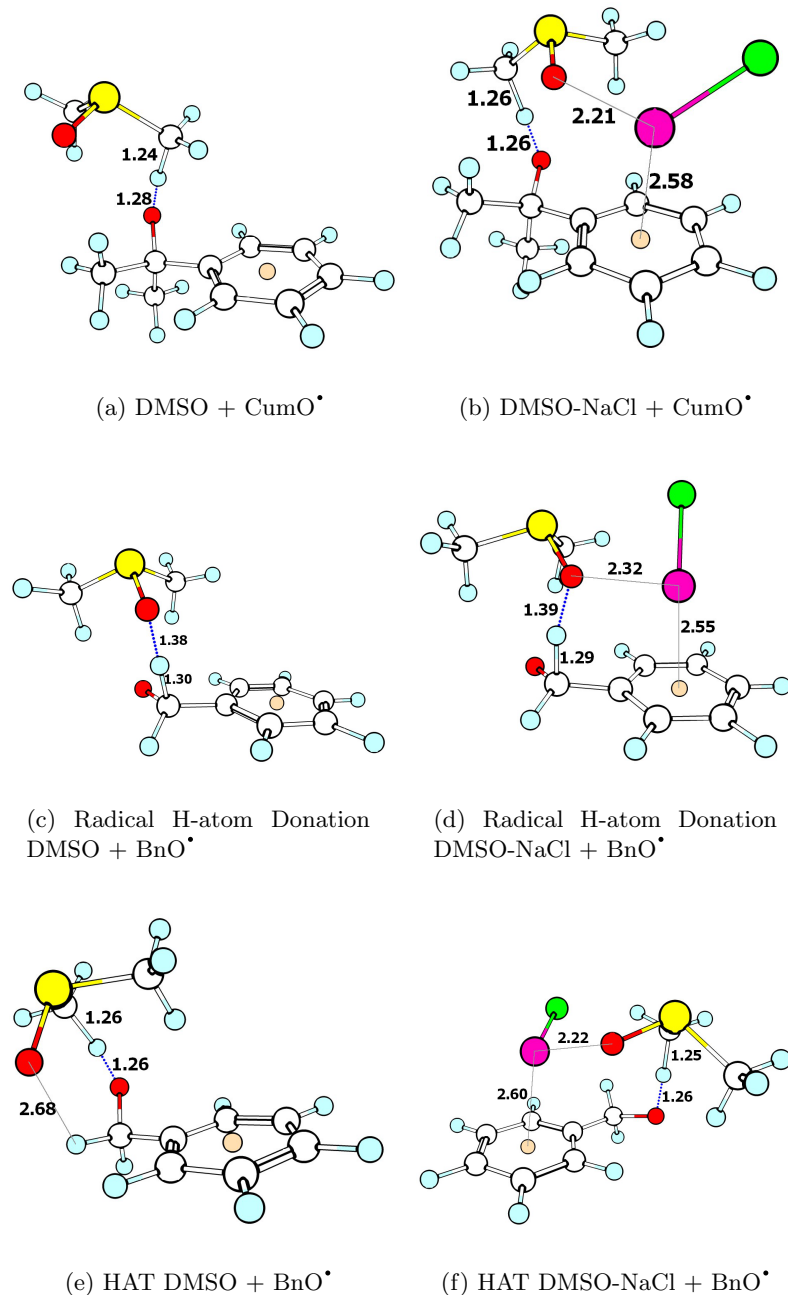


Figure C.4: TS structures of HAT reaction between DMSO and CumO[•], and the conventional HAT and radical H-atom donation reactions reaction with BnO[•] excluding and including NaCl. Key interatomic distances are shown in units of Å. Element colour key: white is carbon, light blue is hydrogen, red is oxygen, yellow is sulfur, purple is sodium, green is chlorine, and peach is a dummy atom in the centre of an aromatic ring.

C.2. HAT reactions involving non-redox active metals

Focussing first of the reactions of DMSO with CumO[·] and BnO[·] in the presence of NaCl. The reactions studied are shown in Scheme C.3 and the calculated free energy (enthalpic) barriers are listed in Table C.6. Also, the TS structures for the reactions in Scheme C.3 are shown in Figure C.4a-f. Firstly, for HAT between DMSO and CumO[·] in the presence of NaCl (Reaction 1, Figure C.4b), the free energy barrier increases by 1.5 kcal mol⁻¹ however the enthalpic barrier decreases by 3.7 kcal mol⁻¹. This can be explained in a similar manner to the reactions of DMA: Na⁺ interacts both with the oxygen of DMSO and the aromatic system of CumO[·], resulting in a stabilization of the TS and a decrease in enthalpic barrier in spite of a predicted increase in C–H BDE. This binding however results in a tighter TS structure, thus the entropic cost increases and so does the ΔG^\ddagger .

Next, the reaction of DMSO with BnO[·] was previously characterized¹⁴⁴ as occurring through the rate determining formation of a strong pre-reaction complex, however, we more recently showed the reaction likely takes place through a reaction in which BnO[·] acts as a hydrogen atom donor, rather than acceptor.²³⁷ For this radical H-atom donation reaction between DMSO and BnO[·] in the presence of NaCl (Reaction 2, Figure C.4d), the free energy barrier increases as a result of NaCl complexation. This appears to be an entropic effect as a result of binding, as ΔH^\ddagger decreases by 1.2 kcal mol⁻¹ due to the interaction of Na with DMSO and the aromatic ring of BnO[·]. In this TS structure excluding NaCl there is some charge separation, however, DMSO (the acceptor) has a partial positive charge and BnO[·] (the donor) has a partial negative charge. This is contrary to typical HAT reactions between oxygen-centred radicals and C–H bonds where in the TS structure, the donor typically has a partial positive charge and the acceptor has a partial positive charge. Therefore, the significant reduction in charge separation from 0.25 e⁻ to 0.11 e⁻ appears to play a lesser role. This may be due to the unusual electronic

C.2. HAT reactions involving non-redox active metals

structure of sulfoxide compounds, which cannot easily be defined using simple Lewis structures. The radical H-atom donation reaction is likely driven by the concerted cleavage of the S=O bond of DMSO-H.

While the conventional HAT reaction between DMSO and BnO^\bullet is unlikely to occur as the barrier is ca. 12 kcal mol⁻¹ higher than the radical H-atom donation reaction, it is still interesting to consider the effect that NaCl has on the reaction barrier height. Figure C.4f shows that in the TS structure for the HAT reaction between DMSO and BnO^\bullet in the presence of NaCl, there is a relatively close interaction with both the oxygen of DMSO and the aromatic ring of BnO^\bullet . As a result, the free energy (enthalpic) barrier decreases by 0.6(5.2) kcal mol⁻¹. NPA estimates a relatively large (as compared to the DMA HAT reactions) 0.10 e^- charge transfer from DMSO to Na, resulting in a decrease in charge separation in the TS structure from 0.27 e^- to 0.21 e^- .

Turning now to the reactions of BnO^\bullet with the substrates HMPA and TBPO, which are closely related phosphine oxide compounds that are commonly used as organic solvents. These two substrates are also closely related to DMSO in that they are strong hydrogen bond accepting substrates, and therefore may undergo a radical H-atom donation reaction in which BnO^\bullet donates an acidic α -C–H hydrogen atom, rather than accepting in the conventional manner. The reaction coordinate diagrams from HMPA with BnO^\bullet and TBPO with BnO^\bullet are shown in Figure C.5a and b, respectively. In the possible radical H-atom donation reactions for both substrates the free energy barrier is lower than the conventional HAT barrier by 6 kcal mol⁻¹ for HMPA and 10 kcal mol⁻¹ for TBPO. However, in both cases the process is energetically uphill, and so is unlikely to occur. For both the radical products HMPA-H and TBPO-H, the cleavage of the P=O bond for the subsequent loss of HO^\bullet in analogy to the reaction of DMSO results in an additional 20 kcal mol⁻¹

C.2. HAT reactions involving non-redox active metals

energy cost owing to the significantly greater strength of P=O bonds as compared to S=O bonds (The BDEs are 86 kcal mol⁻¹ in DMSO vs. 147 kcal mol⁻¹ in HMPA).²⁸⁰ Therefore, radical H-atom donation reactivity of BnO^\bullet to DMSO is likely partially driven by the cleavage of the S=O bond in DMSO.

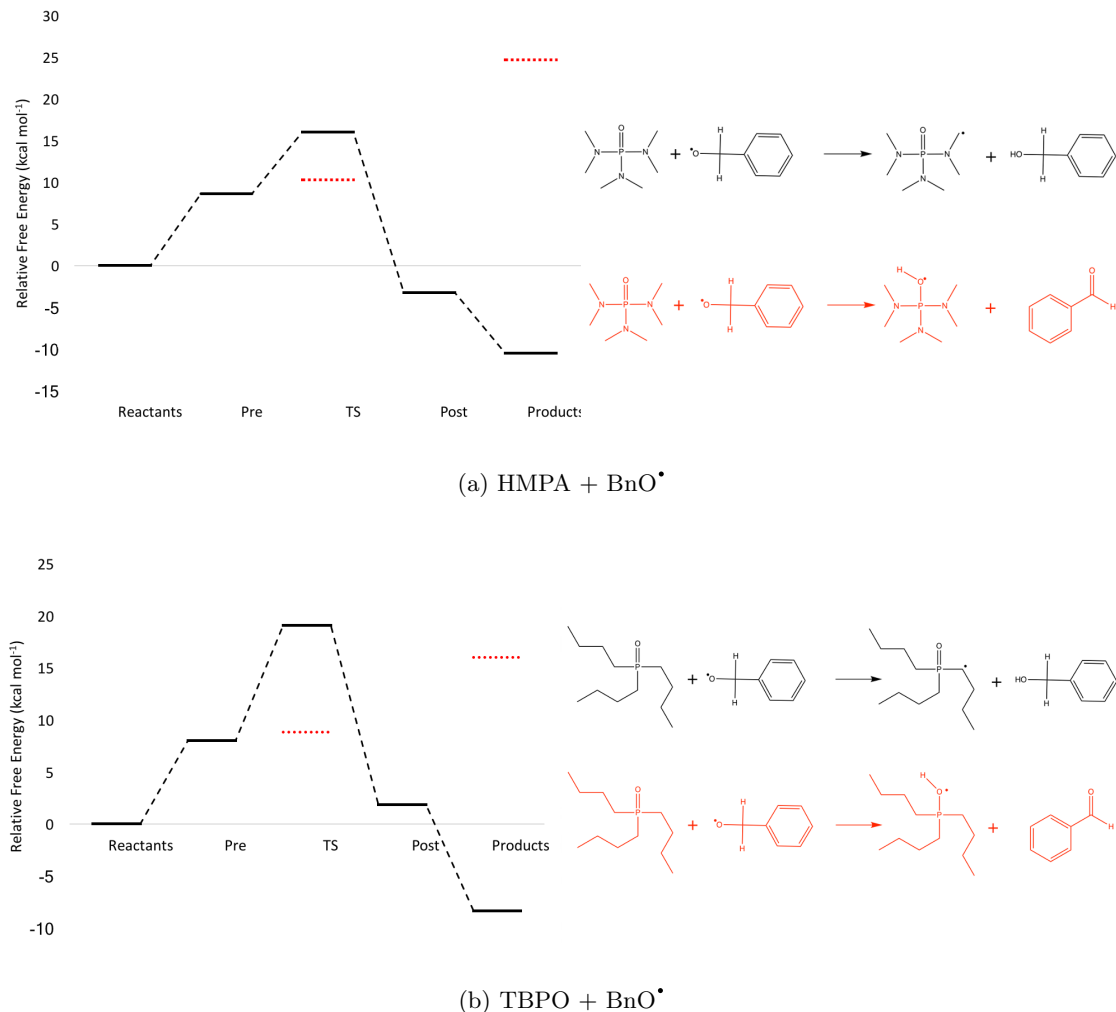


Figure C.5: Reaction profiles for HAT between **a** HMPA with BnO^\bullet **b** and TBPO with BnO^\bullet . Relative free energies in kcal mol⁻¹ are shown for the HAT (black) and radical H-atom donation (red) reactions.

As BnO^\bullet does not donate a hydrogen atom to HMPA or TBPO, I did not seek

C.2. HAT reactions involving non-redox active metals

the determine the effects of NaCl on these reaction barriers. Note also, that unlike DMSO, NBO analysis reveals no strong hyperconjugative overlap between the P=O orbitals and the abstractable C–H bonds of TBPO or HMPA. From an orbital energetic standpoint, this is expected, given the overall higher energy of the P=O bond, as compared to the S=O bond. Therefore, the effects of metal complexation to the phosphine oxygen (where Na will bind) should not significantly affect the C–H bond strengths or enthalpic barrier heights. The HAT reaction barrier heights of NaCl with with HMPA and TBPO for the HAT reaction with CumO[•] are listed in Table C.7. The TS structures for direct HAT reactions between HMPA or TBPO with CumO[•] and BnO[•] including NaCl are shown in Figure C.6.

Table C.7: Calculated free energy (enthalpy) barrier ($\Delta G(H)^{\ddagger}$, kcal mol⁻¹) for HAT between HMPA and TBPO with CumO[•] with and without NaCl. The change in barrier height ($\Delta\Delta G(H)^{\ddagger}$) is calculated relative to the same reaction without the inclusion of NaCl. All barrier heights are relative to separated reactants (or complexed HMPA/TBPO-NaCl) and were calculated at the M05-2X-SMD(MeCN)/6-311+G(2d,2p)//M05-2X/6-31+G** level of theory. *Indicates estimated barrier based on “guess” TS structure.

Reaction	$\Delta G(H)^{\ddagger}$	$\Delta\Delta G(H)^{\ddagger}$
HMPA + CumO [•]	17.4(3.8)	
HMPA-NaCl + CumO [•]	12.8(-1.0)*	-4.6(-4.8)
HMPA + BnO [•]	16.0(2.6)	
HMPA-NaCl + BnO [•]	14.5(1.6)*	-1.5(-1.0)
TBPO + CumO [•]	20.1(6.8)	
TBPO-NaCl + CumO [•]	21.6(6.0)	1.5(-0.8)
TBPO + BnO [•]	19.0(6.9)	
TBPO-NaCl + BnO [•]	19.1(4.8)	0.1(-2.1)

For HMPA with CumO[•] and BnO[•] in the presence of NaCl, the HAT reaction barrier decreases in both cases. For the reaction with CumO[•] (Figure C.6a), this can be explained on the basis of the interaction between Na with both the phosphine oxygen and the aromatic system of CumO[•]. However for the reaction with BnO[•] (Figure C.6b), there is not such interaction with the aromatic system of BnO[•]. In

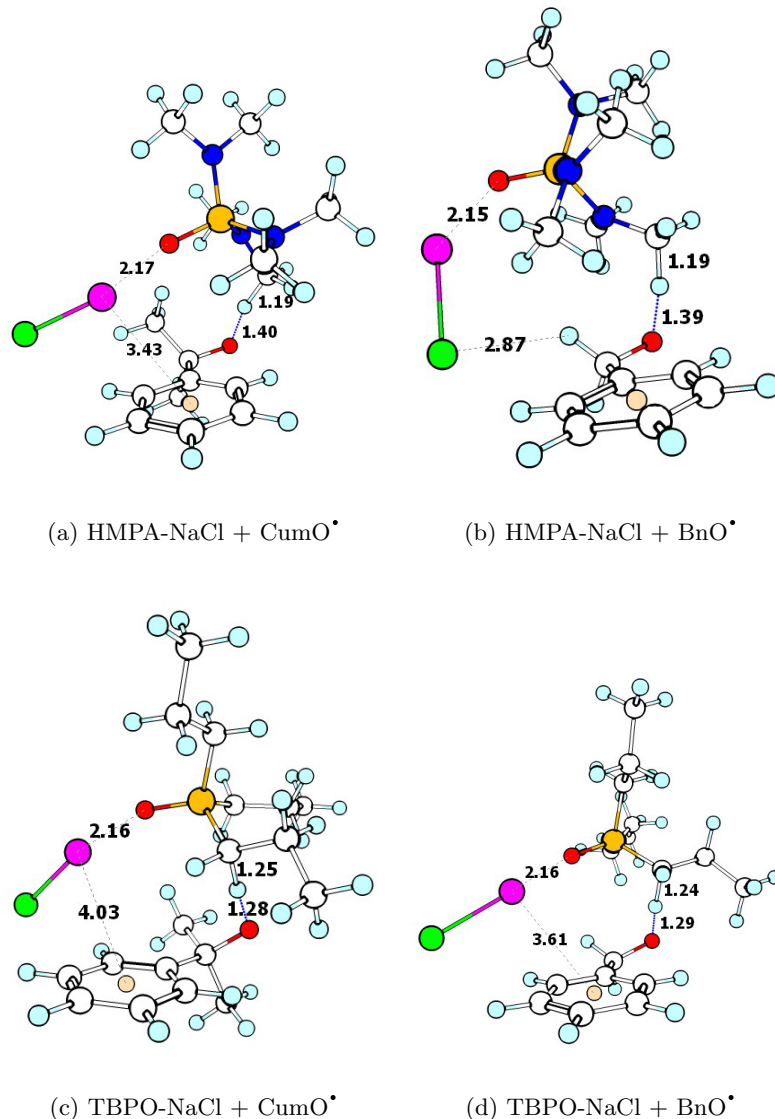


Figure C.6: TS structures of HAT reaction between HMPA and TBPO with CumO[•] and BnO[•] including NaCl. Key interatomic distances are shown in units of Å. Element colour key: white is carbon, light blue is hydrogen, red is oxygen, orange is phosphorous, purple is sodium, green is chlorine, and peach is a dummy atom in the centre of an aromatic ring.

C.2. HAT reactions involving non-redox active metals

in this case, the decrease in reaction barrier can be ascribed to the lack of rotation of the $\text{CH}_2\text{O}^\bullet$ moiety of BnO^\bullet . Previously computational investigations^{144,281} demonstrate a typical rotation of the $\text{CH}_2\text{O}^\bullet$ moiety of BnO^\bullet of about 30 to 45°, while the TS in Figure C.6b has an angle of about 5°. In the HAT reaction between HMPA and BnO^\bullet excluding NaCl, there is a rotation of this moiety by ca. 30°. The complexation of NaCl breaks the hydrogen bond between the α -C–H bond of BnO^\bullet with the oxygen of HMPA, and forms a new interaction between Cl^- and the α -C–H bond of BnO^\bullet . This new interaction stabilizes the TS and allows the oxygen-centre of BnO^\bullet to remain in the plain of the aromatic system.

Finally, for the reactions of TBPO with CumO^\bullet and BnO^\bullet there are long range interactions of Na with the aromatic systems resulting in a decrease in ΔH^\ddagger . The free energy barrier for CumO^\bullet is not significantly affected, while it increases by about 1.5 kcal mol⁻¹ for BnO^\bullet . This is likely due to the longer range interaction of Na with CumO^\bullet as compared to BnO^\bullet (4.0 Å vs. 3.6 Å, respectively).